INVESTIGATION OF PLASMA UPWELLINGS FROM THE EARTH'S UPPER ATMOSPHERE DURING THE INTERNATIONAL POLAR YEAR 2007 CAMPAIGN

Thesis submitted for the degree of

Doctor of Philosophy

at the

UNIVERSITY OF LEICESTER

by

Timothy Wemimo David

Radio and Space Plasma Physics Group

Department of Physics and Astronomy

University of Leicester

September 2017

Abstract

Investigation of Plasma Upwellings from the Earth's Upper Atmosphere During the International Polar Year 2007 Campaign

Timothy Wemimo David

EISCAT Svalbard Radar data, obtained during the IPY-ESR 2007 campaign at a period of deep solar minimum, has been examined to study ionospheric upflow events with fluxes exceeding $10^{13}\,m^{-2}\,s^{-1}$. Ion upflow newly categorized, classifies the upflow events into low, medium and high flux upflows, and the incidence and seasonal distribution of these different classes are discussed. Over 300,000 field-aligned profiles have been considered and analysed. It is observed that, while high upflow fluxes are comparatively rare, low flux upflow events are a frequent phenomenon. Analysis of the ESR data shows that the occurrence frequency of the upward flux maximizes around local noon for all levels of upflow, with occurrence peaks of 31%, 16% and 2% being observed for low, medium and high upflow fluxes respectively during geomagnetically disturbed periods. Analysis of the seasonal distribution reveals that while high-flux upflow has its peak around local noon in the summer, with its occurrence being driven predominantly by high geomagnetic disturbance, the occurrence of low-flux upflow is broadly distributed across all seasons, geomagnetic activity conditions and times of day. The ambipolar electric force drives upflows about seven times more frequently as the Joule heating mechanism. This study finds that, though rare, Poynting flux leads to substantial upflow flux of $4.67 \times 10^{13}\ \mathrm{m^{-2}\ s^{-1}}$ even in the absence of precipitating flux. Upflow occurrence was found to correlate better with solar wind density than speed, and fits better with number density and dynamic pressure below about $20\ \mathrm{cm^{-3}}$ and 5 nPa respectively. Moreover, it was found that occurrence maximizes when the IMF clock angle is southward however, analysis showed a preference for duskward asymmetry of the cusp in comparison to dawnward's. Analysis shows that reconnection is not compulsory for upflow flux, but only enhances its occurrence.

Declaration

I, Timothy W. David, confirm that the research work presented in this thesis is carried out by me. I have referenced information from other sources appropriately.

Dedication

To HIM that utter HIS voice and the Earth melted…

‘The mountains quake at him, and the hills *melt*, and the earth is burned at his presence, yea, the world, and all that dwell therein’ (Nahum 1:5)

‘… the coming of the day of God, wherein the heavens being on fire shall be dissolved, and the elements shall *melt* with fervent heat?’ (2Pet 3:12)

‘The heavens shall pass away with a great noise, and the elements shall *melt* with fervent heat, the earth also and the works that are therein shall be burned up’

(2Pet 3:10)

‘And I saw a new heaven and a new earth… And God shall wipe away all tears from their eyes; and there shall be no more death, neither sorrow, nor crying, neither shall there be any more pain: for the former things are passed away. And he that sat upon the throne said, Behold, I make all things new…’ (Rev. 21:1,4,5)

Acknowledgement

First and foremost, all praises and adoration go to the Almighty God for HIS mercy and blessings on me.

My deepest gratitude goes to ‘olufe-okan-mi’, Oluwakemi, and my children (OreofeOluwa, OluwaSemilogo & OluwaSemiloore) for their perseverance and endurance during the PhD journey.

I would like to specifically thank my supervisor, Dr Darren Wright for his guidance, exceptional support, encouragement and patience starting from my first day at the University of Leicester. Also, my appreciation goes to my second supervisor, Professor Steve Milan for his guidance, support, willingness and ever-ready approach throughout the journey. Prof. Emeritus Stanley Cowley, a teacher per excellence, your encouragement and support throughout is well appreciated. Prof. Mark Lester, the current group head, thank you for statistical expertise. I also appreciate Prof. Timothy Yeoman, my name sake, for his explanations and Dr. Suzie Imber who made available her archived OMNI data. No amount of words is enough to express my gratitude to Ian McCrea and Jackie Davies, the EISCAT experts, for their enlightenment on EISCAT data interpretation.

I am also grateful to all members of the Radio and Space Plasma Physics Group, both teaching and technical staff, for their support. Nigel, your memory lives on!

Also, many thanks go to the Federal Government of Nigeria (TETFUND) for providing financial support to undertake this PhD programme. I am also indebted to the management of Olabisi Onabanjo University for providing the platform for me to access the funds.

My warmest regards to my mums (in Amje & Ijebu), my siblings, the more than one in a million uncle Kunle, Dr. Laoye, My Daddy in the Lord, the HGGM Canaan land parish, and my loving father (Pa Moses Somefun - ‘Baba daada’) that passed on during my 2nd year in the PhD journey.

Finally, I will like to express my sincere appreciation to all my family and friends for the support given to me in the course of this PhD programme.

Table of Contents

CHAPTER 1

Introduction to Space Weather and the Solar-Terrestrial Interactions

1.1. Introduction

In this thesis I focus mainly on the Earth's upper atmosphere and magnetosphere as well as the exchange of plasma between them. The Earth, with a radius (R_E) of about 6,370 km and a dipolar magnetic field, is the third planet from the Sun at a distance of about 1 AU ($\sim 150 \times 10^6$ km). The Earth's atmosphere is made of gases of which nitrogen and oxygen are the major constituents, with other gases constituting a trace of about 1%. The composition of the atmosphere varies with altitude above the planet. Below the homopause, which is at about 100 km altitude, the composition is molecular and also a mixture driven by turbulence, with nitrogen (N_2) to oxygen (O_2) molecules in ratio of around 4:1. Above this region in the upper atmosphere is the heterosphere, where dissociation of molecules takes place, become more independent of each other and the gases adopting a vertical distribution in relation to their scale heights (Brekke, 2013; Nagy et al., 2008). Solar conditions also play an important role in the ion constitution dominance in the upper atmosphere: for instance, the atmosphere above 250 km is dominated by atomic oxygen during solar maximum, while hydrogen ions predominate from above 400 km when the solar activity is minimum (Brekke 2013). The dynamics of the thermosphere, especially through the vertical winds, play a vital role in gases redistribution, enhancing the abundance of heavy ions in regions of upwelling and the lighter ones in downwelling regions (Nagy et al., 2008).

The aim of this preliminary chapter is to introduce the Earth's magnetosphere and its ionosphere as well as the dynamics in the solar wind-magnetosphere-ionosphere system.

1.2. The Sun and Solar Atmosphere

The Sun, which is an effective blackbody with a surface temperature close to six thousand kelvin, is mainly composed of about 90% hydrogen and 10%

helium with trace elements such as carbon, nitrogen and oxygen (Kivelson and Russell, 1995). However, the temperature at the Sun's corona rises dramatically to about two million kelvin, and the Earth's atmosphere is modified by the energy from the solar radiation reaching the Earth. The Sun has a 27-day modulation of activity due to its rotation and an 11-year cycle modulation due to solar cycle variation. During the solar cycle variation, the Sun reaches a period of least sunspot and solar flare activity usually referred to as the solar minimum. On the other hand, a period of solar maximum is also attained in the 11-year cycle, corresponding to peak period of solar activity such as coronal mass ejections (CMEs), solar flares eruption and sunspots. The layers of the Sun are shown in Figure 1.1 with the core being the centre for energy production through nuclear fusion of hydrogen resulting in helium formation. The Sun's temperature falls from the core (15 million kelvin), through absorption of elementary particles during chemical reactions, up to the photosphere (about 4300 - 6400 thousand kelvin) and gradually through the chromosphere, a striking change begins to about 30 thousand kelvin and final to an astonishing value of about 2 million kelvin in the corona (Kivelson and Russell, 1995; Parnell, 1999).

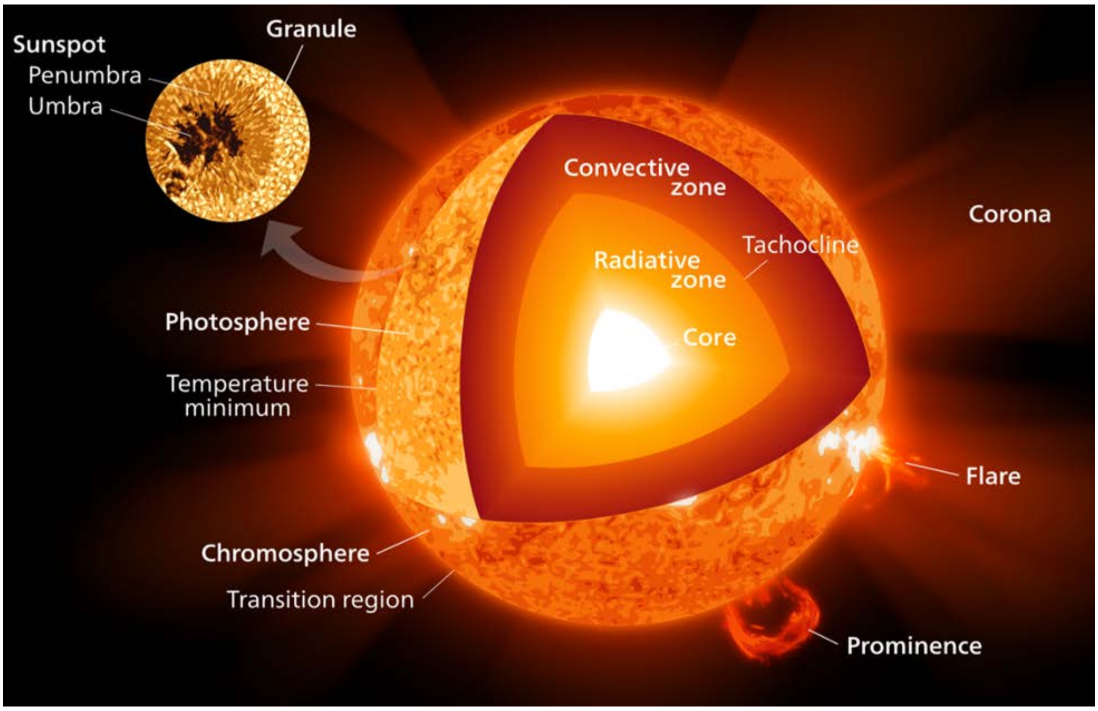

Figure 1.1: A Schematic diagram of Sun's structure. Image credit: Adapted from Wikimedia Commons, 2017.

1.2.1 *The Solar Wind and IMF*

The solar atmosphere is not a vacuum but a region of low pressure. Unlike the Earth's atmosphere which is in hydrostatic equilibrium as a result of the dominance exerts by gravity, the Sun's atmosphere is not static but streams radially into space because of the high temperature by which pressure dominates over gravity (Milan, 2014a). This stream of plasma released from Sun's surface, called the solar wind, is formed by heating the solar gas (to split the electrons and protons apart) at the corona at a temperature above the ionization potential. The average kinetic energy of atoms in a gas is given by:

$$\overline{W} = \frac{3}{2} k_B T \tag{1.1}$$

where $\overline{W}$ is the average kinetic energy,

k_B is the 'Boltzmann constant', and

T is the temperature in kelvin

With the above equation, the required temperature to overcome the ionization potential (say hydrogen) of 13.6 eV is $T > 10^5$ K which is below the solar coronal temperature.

The solar wind consists mainly of proton and electron travelling outward because of the hot corona. There is a constant outflow of the solar wind because the pressure in the local interstellar medium (LISM) which is about 10^{-13} N m^{-2} is not sufficient to balance the pressure of the solar atmosphere which is about 5.5×10^{-3} N m^{-2} at the base of the corona (Milan, 2014a). For this reason, the Sun's atmosphere continues to expand radially outward and fill the interplanetary medium. The conditions in the solar corona determine the solar wind velocity and measurements during spacecraft missions have indicated that the velocity varies between 300 and 700 m s^{-1} (Milan, 2014a). The high solar wind velocity originates from the open field lines around the Sun's pole, referred to as the coronal holes while the slow solar wind emanates from the closed field lines in the lower latitude. As the solar wind streams away from the Sun, it carries along with it the Sun's magnetic field, which is frozen-in to it (a condition in which the plasma and the field move together), and they both permeate the interplanetary space. The solar magnetic field lines dragged by the solar wind extend into the solar system to form the interplanetary magnetic field (IMF). The orientation and strength of the IMF (together with the solar wind plasma particles) has great consequence as it interact with the Earth's magnetic field to cause time-varying conditions known as space weather. The Sun's magnetic field line is inclined at about 45° to the Sun-Earth line (Kivelson and Russell, 1995).

1.2.2 Distortion of the Magnetic Dipole of the Sun

The magnetic field strength is so strong very close to the sunspots that the ratio of the gas pressure to the magnetic pressure is less than 1 up to about two Sun's radius ($R_{\odot}$). Thus, the solar wind cannot pull it and the field remains dipolar very close to the Sun. However after 2 $R_{\odot}$, the energy density of the magnetic field is low compared to that of the solar wind, therefore the gas pressure dominates and the topology of the IMF can be distorted (Milan, 2014a). In the presence of a radially outflowing solar wind at constant speed, the dipolar nature of the Sun's magnetic field is modified as shown in Figure 1.2.

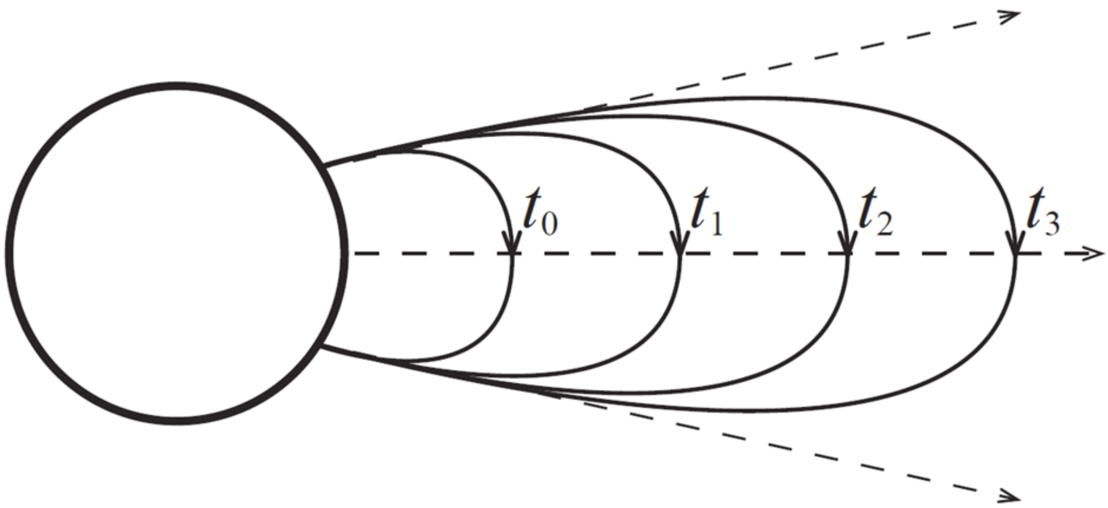

Figure 1.2: A schematic diagram showing magnetic field lines stretched by the radial solar wind at different time interval. Taken from Milan (2014a).

In a dipole field, for example near the Sun, the field is radial and the azimuthal component is zero whereas, it has a non-zero azimuthal away from the Sun. Although the solar wind streams away from the Sun is purely radial, the interplanetary magnetic field lines frozen to it have footprints mapping to fixed locations on the surface of the Sun. As a result of the rotation of the Sun and the Alfvén's theorem (frozen-in flow), the field lines of all plasma parcels having the same source region produce a spiral pattern referred to as Parker spiral as shown in Figure 1.3 (Milan, 2014a).

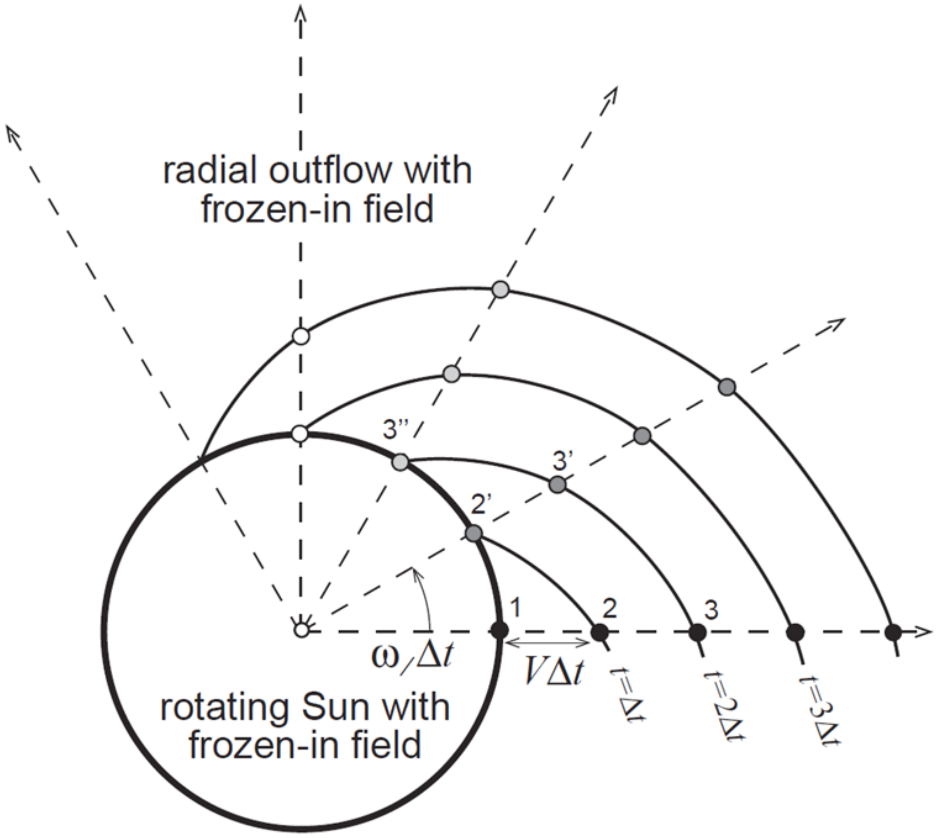

Figure 1.3: A schematic diagram of the Parker spiral pattern of the IMF. Taken from Milan (2014a). The number 1, 2 or 3 indicates plasma elements from the same source region.

1.3. The Earth's Magnetosphere

The Earth's magnetosphere is the region in space, just overlying the ionosphere (Newell et al., 2001), where the dominating influence of the Earth's magnetic field can be felt. The magnetic field of the Earth traps different kinds of charged particles in different locations of the magnetosphere depending on their energy regime. The dynamics of the magnetosphere at both quiet and geomagnetic storm times prevents stability of the charged particles (Liu and Fujimoto, 2011).

1.2.3 Regions of the Magnetosphere

Solar plasma, streams radially into space at high speed (typically 450 km/s or more) and carries the sun's magnetic field with it. The ionized particles and the solar magnetic field that they carry along, is called the interplanetary medium. The outer magnetosphere is the location of dynamic interactions between the sun and earth plasmas. The impact of the solar wind reshapes the dipolar nature of the geomagnetic field by compressing it on the sunward side to a bullet shape and stretching out the night-side magnetosphere into a magnetotail (Figure 1.4). The regions of the magnetosphere can be categorized by the energy as well as the density of the plasma in the regions. The major categories could be arranged in increasing order of energy as the plasmasphere, the ring current, and the Van Allen radiation belts. The energies are typically a few eV, < 100 eV, and > 100 eV respectively. The plasmasphere is a cold, but high density region while the Van Allen belts can harbour particles with very high energy. These regions are coupled with one another and exchange mass and energy with the other regions such as the hot plasma sheet region and the very cold tail lobes (Liu and Fujimoto, 2011). Other regions of the Earth's magnetosphere as shown in Figure 1.5 are (i) the magnetopause, which is the magnetosphere current-carrying boundary that separates the Earth's magnetic cavity from the solar wind, (ii) the polar cusps between the sunward and tail-ward field lines from where particles from solar wind gets into the Earth's upper atmosphere through the magnetic field lines, (iii) the magnetosheath, which is a region of shocked (slowed, compressed and heated) solar wind plasma, (iv) plasma sheet – a region of hot, low density and energetic plasma with a weak field (v) neutral sheet, which is a region of a thin current sheet that separates the plasma sheet along the equatorial plane, (vi) the lobes (north and south) are regions almost bereft of plasma. The very low density and cold plasma here mainly originate from the ionosphere.

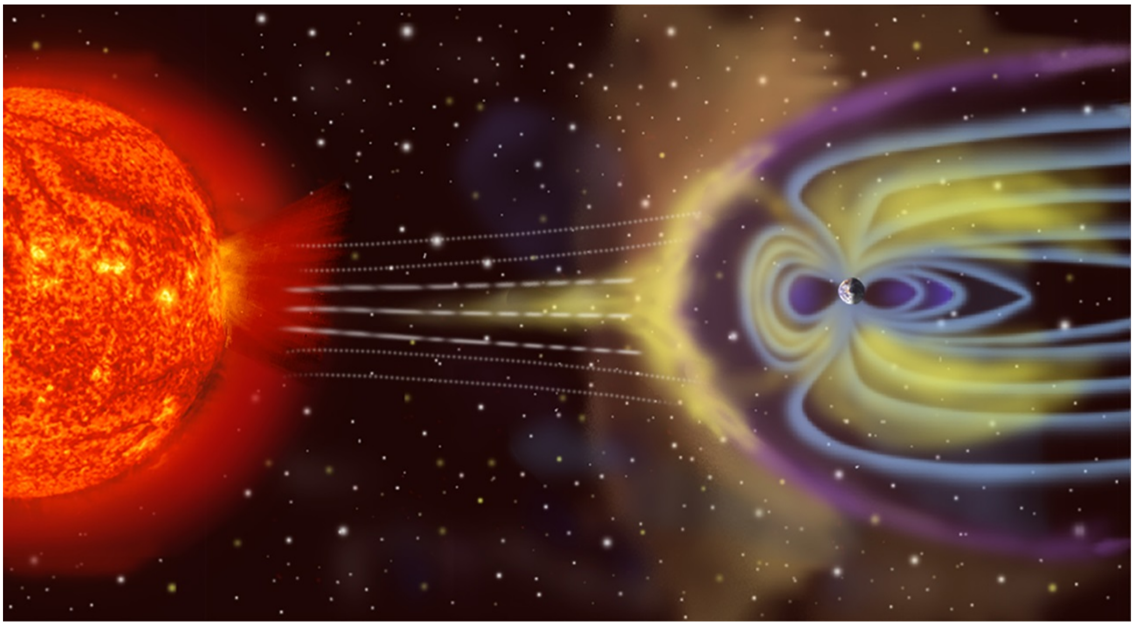

Figure 1.4: A Schematic diagram of shape of the magnetosphere. Image credit: Adapted from NASA, 2015a.

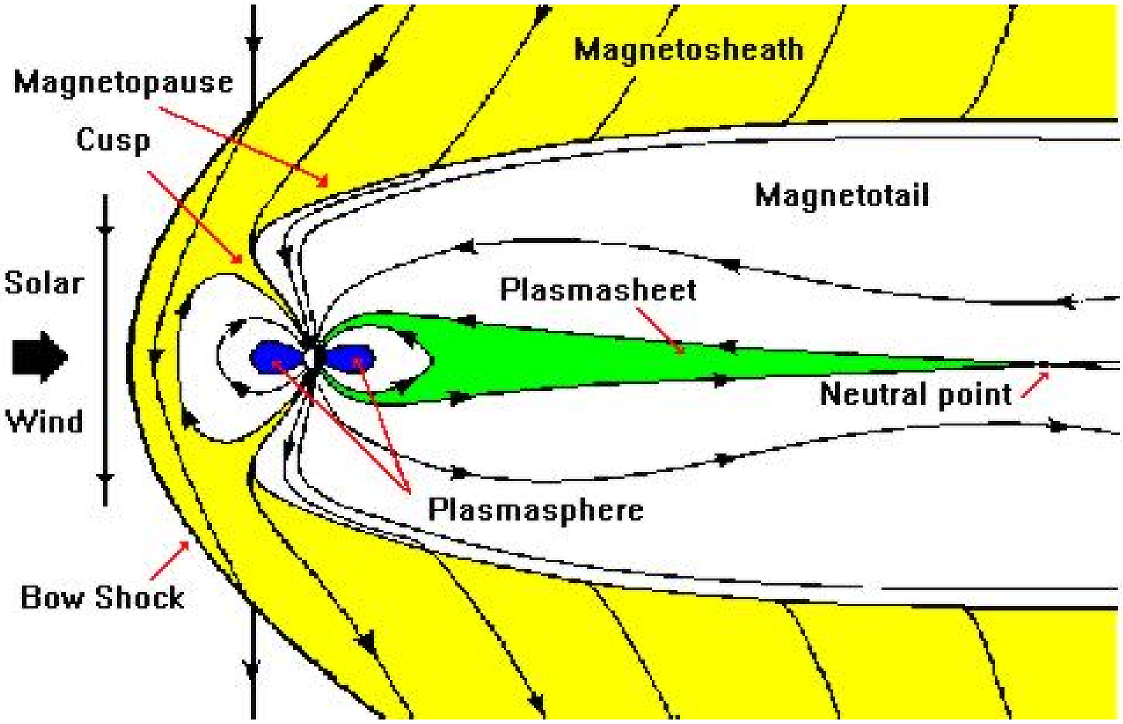

Figure 1.5: A Schematic diagram of regions of the magnetosphere. Image credit: Adapted from NASA, 2014.

1.2.4 Solar Wind – Magnetosphere Interactions

Earth's magnetosphere dynamics are primarily driven by the solar wind, but the precise processes in control of the complex interplay involved are many. These include, inter alia, 'chaotic solar wind plasma and IMF conditions, reconnection, flux transfer events, dynamics in the magnetosheath, and the highly variable nature of Earth's ion foreshock' (University of California, Los Angeles, 2017; Tsurutani et al., 1988; Gonzalez et al., 1989). The magneto-hydrodynamic waves generated by these processes, as a result of impact on the magnetopause, drive plasma convection and modify the background geomagnetic field in every part of the magnetosphere (University of California, Los Angeles, 2017). The current generated at the magnetopause (Figure 1.6) gives rise to a $\mathbf{j} \times \mathbf{B}$ force, which slows the shocked plasma in the magnetosheath and energizes the electromagnetic field (Cowley, 2000).

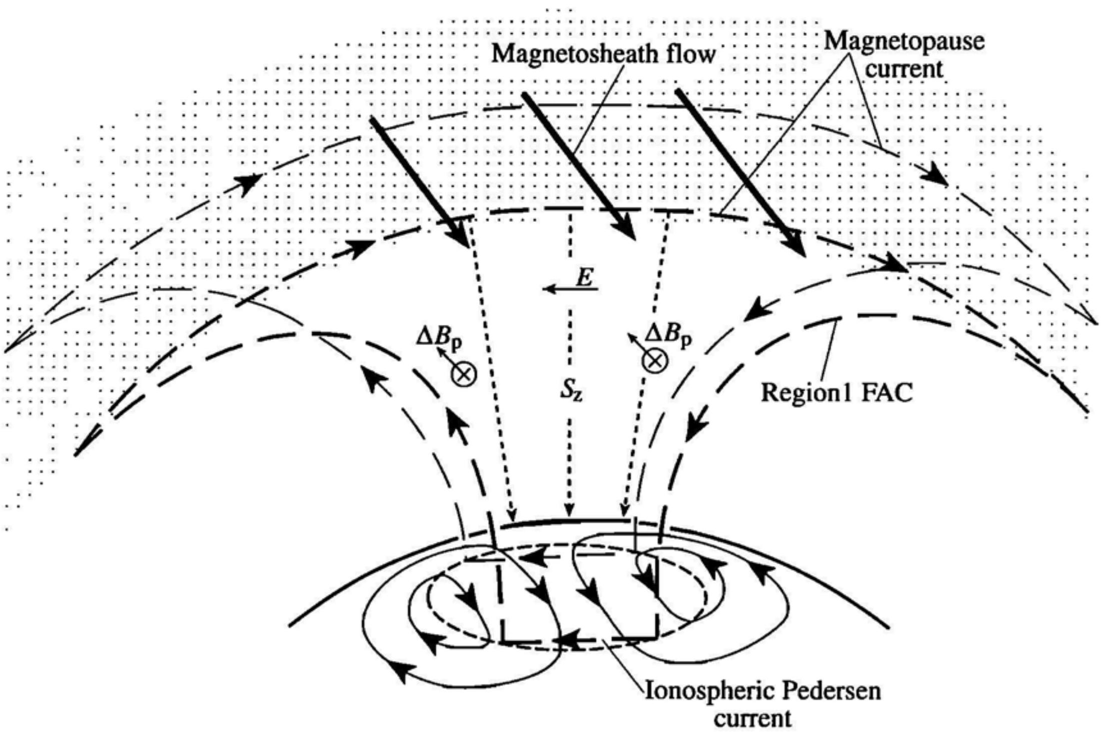

Figure 1.6: A schematic diagram of the polar cap current systems. Taken from Cowley (2000).

The principal means by which energy is transferred from the solar wind to the magnetosphere is a process known as "reconnection" (Dungey, 1961), which occurs when the IMF is oriented anti-parallel to the geomagnetic field lines. This orientation allows the merging of the interplanetary and geomagnetic field lines, resulting in the transfer of energy, mass, and momentum from the solar wind to the magnetosphere (Figure 1.7). Gonzalez et al. (1989) put forward that there is strong evidence that large scale magnetopause reconnection operates during intense storm events. Figure 1.8 shows the schematic of Dungey-cycle flow. However, the orientation of the y-component of the IMF thus affects the shape of the convection pattern. When the condition in the y-component of the IMF is predominantly positive, a duskward "orange-like" shape is usually observed in the convection pattern (Figure 1.9), while negative IMF B_y is commonly characterized with a "banana-like" shaped convection pattern in the duskward side and vice versa for the dawnward side (Cowley, 1981; Liang et al., 2006).

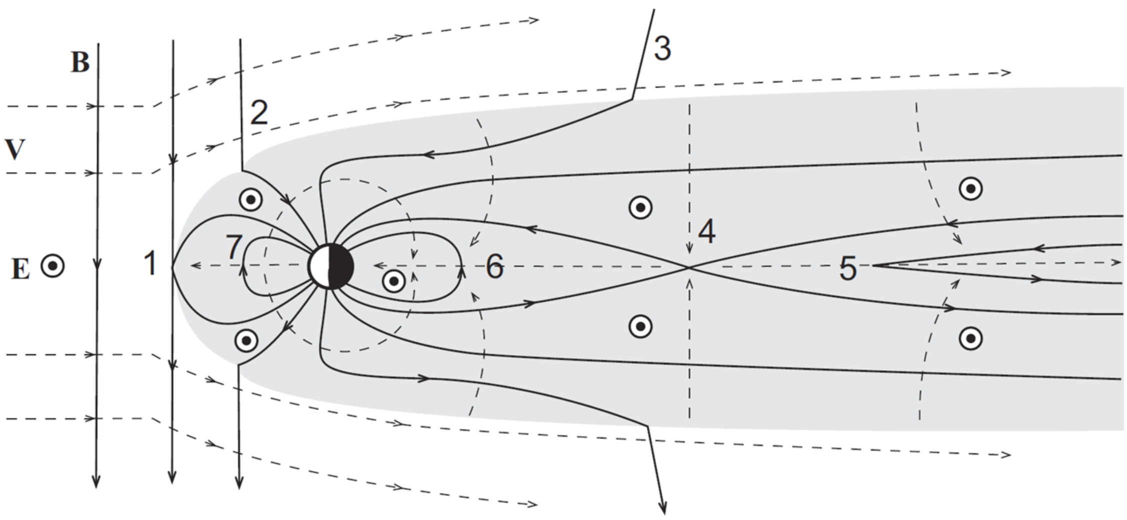

Figure 1.7: A schematic diagram demonstrating magnetic reconnection. Taken from Milan (2014a). (1) and (4) are the dayside and nightside reconnection points respectively.

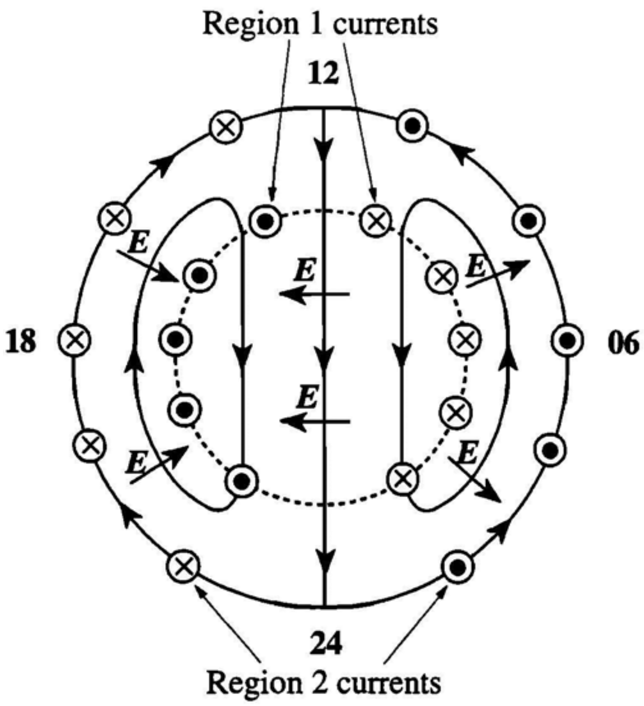

Figure 1.8: A schematic diagram of the Dungey-cycle convection pattern. Taken from Cowley (2000).

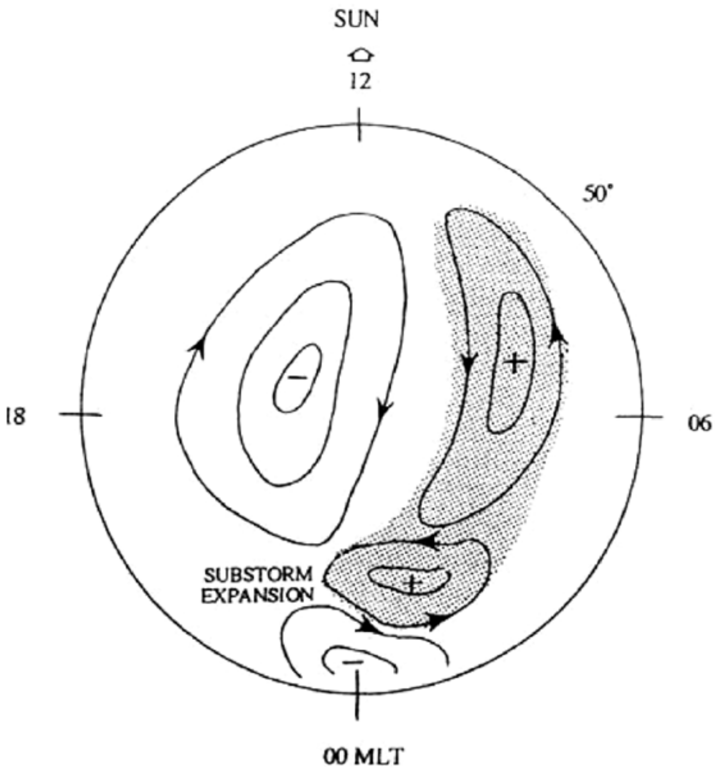

Figure 1.9: A schematic diagram of the convection pattern during asymmetries of IMF $B_y > 0$ for northern hemisphere flow. The “+” and “–” signs denote the signs of the electric potentials. Taken from Liang et al., (2006).

1.4. The Earth's Upper Atmosphere

The Earth's uppermost atmosphere is significantly ionised and the density of the charged particles maximize (up to 10^{12} particles per m^{-3}) around altitude between 250 and 300 km. The ionized region of the Earth's atmosphere is called the ionosphere. The upper limit of the ionosphere is often defined to be 500 – 2000 km, overlapping with the lower magnetosphere (Hultiqvist et al., 1999).

1.3.1 The Ionosphere

The X-rays and extreme ultraviolet (EUV) light ($\lambda \leq 100\ nm$) emanating from the sun interacts with the atoms from the upper atmosphere of the Earth and creates free electrons and ions by photo-ionization. This layer of ionized plasma in the Earth's atmosphere, which can conduct electric charges and be influenced by magnetic field, is called the ionosphere. It is a region in the upper atmosphere that has sufficient electron concentration to influence the propagation of radio waves. The ionosphere underlies the magnetosphere, which is a dynamic region of solar and planetary magnetic fields interaction. The neutral atmosphere and the magnetosphere also have an important role on the electrodynamic behaviour of the ionosphere due to the interaction between the neutrals in the atmosphere and the ionizing agents from the sun. The ionosphere and magnetosphere maintain a system of currents which connects them with the currents in the interplanetary medium, transported by the solar wind plasma (Richmond, 1998).

The main ionospheric altitudes span about 60 to 1000 km, and as a result of its complex coupling system, ionospheric studies are commonly divided into low, mid and high latitudes. Higher latitude regions are coupled to the outer magnetosphere, where interaction with the solar wind is strongest. So, more dynamic effects are observed in the high latitude ionosphere. The main ionospheric layers are D, E, and F layers. The altitude range of the D layer covers 60 to 90 km, E layer fills 90 to 140 km, and the F layer above the E layer extends to the exosphere (Richmond, 1998). The dominant source of ionization for the upper atmosphere are the Lyman alpha ($\lambda \sim 121.6$ nm) and beta ($\lambda \sim 102.6$ nm), X-ray ($\lambda \leq 17$ nm), and extreme ultraviolet (EUV) radiation ($\lambda \sim 17$ - 93 nm) from the sun (Rishbeth, 1988). These radiations are modulated by the 11-year solar cycle variation and the 22-year sun's magnetic cycles. An increase in solar activity in the form of sunspots, coronal mass ejections (CMEs), and solar flares cause sporadic enhancements. Electron precipitation also contributes to the ionization and is subject to variation by disturbances in the magnetosphere (Richmond, 1998; Kivelson and Russell, 1995).

The altitude dependent particle density of the Earth's ionosphere relies on the sun activity and also on the night/day cycle. This cold and tenuous plasma with densities of $n = 10^9 - 10^{12}\ \mathrm{m}^{-3}$ and an altitude dependent chemical composition is as shown in Figure 1.10, which shows the ionospheric layers at various altitudes.

1.3.2 Scale Heights

An important factor used in describing the distribution of ionospheric constituents is the scale height. It describes how ionospheric plasma density gradually becomes less as altitude increases. This quantity falls exponentially such that the density or pressure of the atmosphere drops by a factor of e^{-1} at every scale height as given by equation (1.2) below. The scale height, *H*, shown in equation (1.3) below indicates that the charged particles which are kept close to the planet by gravity, move to a higher altitude as the temperature increases.

$$n(Z) = n_0 e^{-\frac{Z}{H}} \tag{1.2}$$

$$H = \frac{k_B T}{< m > g} \tag{1.3}$$

where *Z* and *H* are the vertical and scale heights respectively,

n is the density,

k_B is the 'Boltzmann constant',

T is the temperature in kelvin,

$< m >$ is the mean molecular mass of dry air, and

g is the 'acceleration due to gravity'.

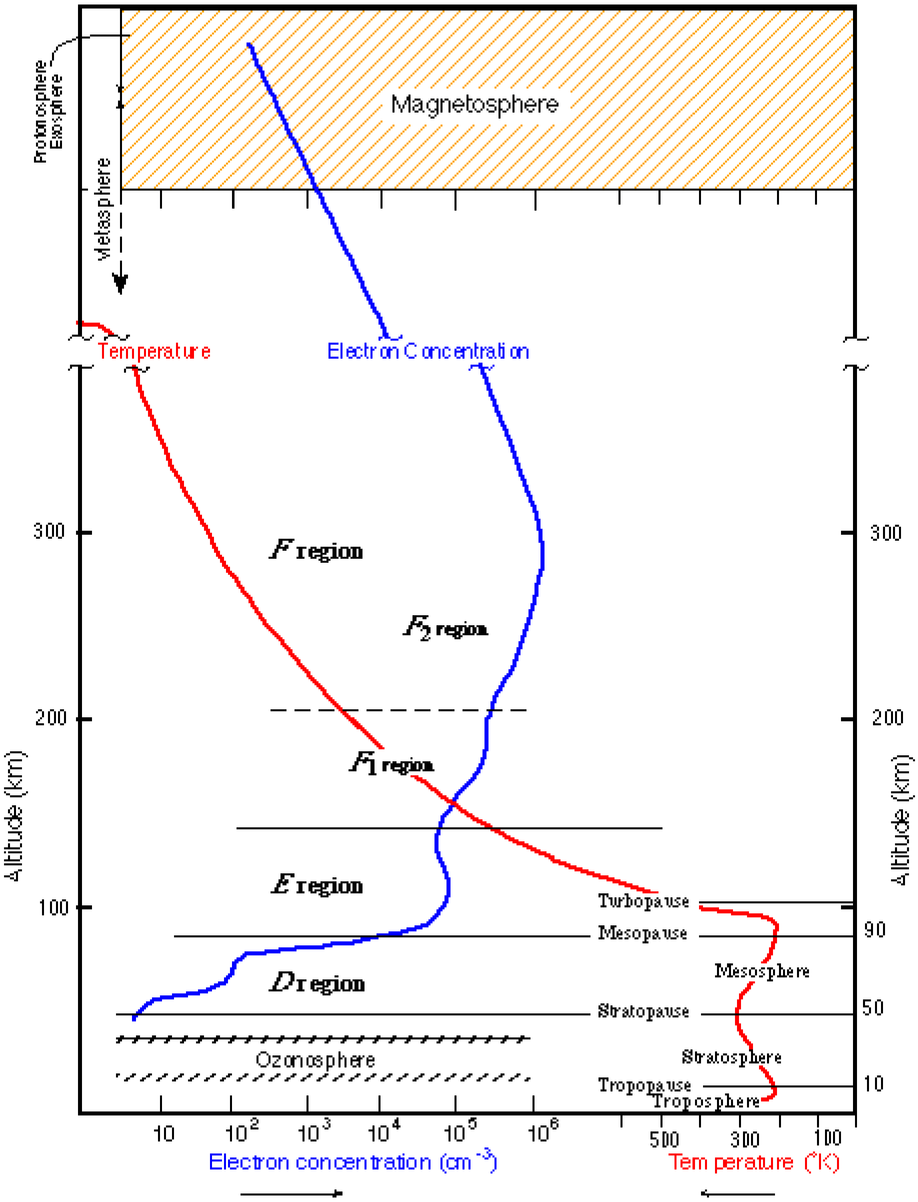

Figure 1.10: A Schematic diagram of electron concentration. From University of Leicester, 2017a.

1.3.3 Magnetosphere – Ionosphere Coupling

The interconnectivity between the plasma of the ionosphere with that of the energetic and highly dynamical magnetosphere is the process known as magneto-ionospheric coupling. The process of interconnectivity is brought about by the Birkeland currents system, outflow mechanisms, wave heating, precipitating particles and electric fields (Figure 1.11). According to Fälthammar (1986), the role of electric field and current from magnetosphere-ionosphere interactions is of great importance in particle energization, plasma convection, as well as chemical separation.

The ionosphere of the earth and the magnetosphere together form a system of plasma, which provides all-encompassing in situ investigation and research. Their densities scope between 10^{12} and $10^{4}\ \mathrm{m}^{-3}$ and respective temperature variation between 10^{3} and 10^{7} K have made them a useful tools in the study of cosmic plasmas. The local plasma is even of more importance because it is the scene of multiplex activities leading to particle energization. These phenomena also occur in astrophysical plasmas everywhere but most easily studied here. Magnetized planetary plasmas have the capability for efficient particle acceleration, which occurs in the near-earth region, and this local plasma permits us to delineate the mechanisms that are accountable for it. The coupling between the magnetosphere and the ionosphere gives room for energy and momentum transfer between them (Fälthammar, 1986). There is a clear difference in the exchange, for instance, the chemical constituent of the plasma from the ionosphere to the magnetosphere is a singly ionized helium (He^{+}) while that from the solar source to the same sink is doubly ionized (alpha particle, He^{2+})

The complexity of the magneto-ionospheric coupling involves electric field and mass movement. The movement can be from either the ionospheric region to the magnetosphere or vice versa. The flow from the magnetosphere causing neighbourhood ionization, heating and auroral activity is brought about by the precipitation of high energy electron and proton. Indeed, ionospheric plasma is found in the magnetosphere during both quiet and active times (Glocer et al., 2009).

The ionospheric plasma found in the magnetosphere can have a tremendous effect on the dynamics in the magnetosphere. Ionospheric outflows add mass to the magnetosphere, leading to decreased Alfvén speed on flux tubes, reduced momentum/energy transfer rates, a slower magnetospheric response time to external drivers, changes in high-latitude magnetospheric dynamics, and magnetosphere-ionosphere coupling via Alfvén waves among others.

Moreover, the presence of heavy ions can modify the ring current in the inner magnetosphere, impacting the D_{st} index and the local plasma beta.

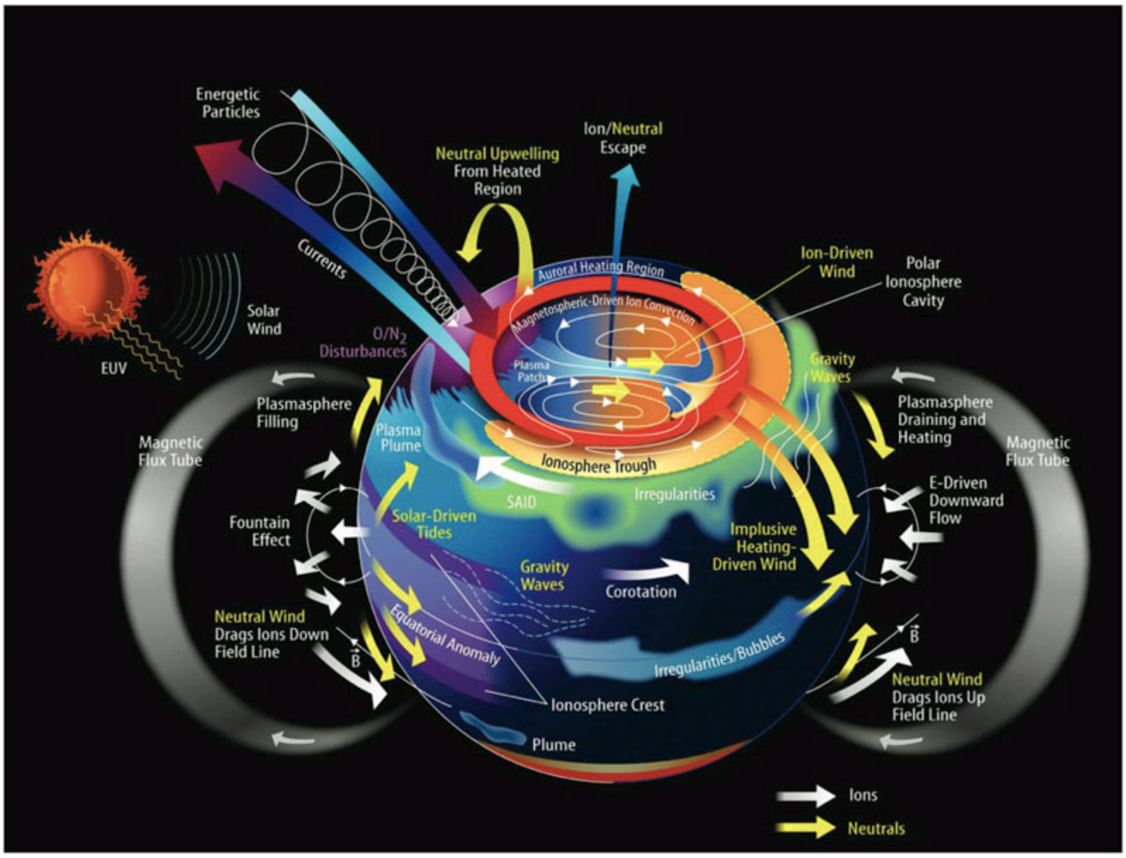

Figure 1.11: A Schematic diagram of magnetosphere-ionosphere coupling. From University of California, Los Angeles, 2013.

1.5. Statement of the Thesis

Ion upflows from the Earth's upper atmosphere, which under the right geophysical conditions and wave activity outflow into the magnetosphere, play a crucial role in solar wind-magnetosphere-ionosphere dynamics. A year-long data set measured by the EISCAT Svalbard Radar (ESR) during the International Polar Year (IPY) 2007 campaign is employed in this study to investigate the driving mechanisms of the ion upflow. In addition, high resolution (1 minute) OMNI data set of solar wind plasma parameters at the bow shock region of the Earth, and also of energetic proton fluxes and geomagnetic activity indices, are used to study the geophysical conditions during the ionospheric upwellings.

Chapter 2 will discuss in detail the current understanding of ion upflow and outflow, which include the ion source and the driving mechanisms. Chapter 3 focuses on the instruments from which data are sourced for this study, while Chapter 4 will discuss the temporal variation of ion upflow as well as the analysis of upflow and downflow as a function of *Kp* index. Chapters 5 and 6 respectively focus on investigating the dominant mechanism of ion upflow energization and the effect of solar wind plasma parameters and geomagnetic indices on ionospheric upwellings. Finally, the summary and conclusions and recommendations for future work will be presented in Chapter 7.

CHAPTER 2

Review of Plasma Outflow in the Earth's Magnetosphere-Ionosphere System

2.1. Introduction

Prior to the investigation performed by Shelley et al. (1972), the solar wind was assumed to be the principal source contributing plasma to the magnetosphere. However their observations by the 1971-089A satellite (in a circular polar orbit at an altitude of about 800 km, with on-board spectrometers taking measurements of ion composition, has revealed that heavy ions of atmospheric source form a significant component of the magnetosphere. Thereafter, it was established that plasma of ionospheric origin could be sufficient to populate the magnetosphere (Waite et al., 1985; Fälthammar, 1986; Chappell et al., 2000). In this Chapter, a review of previous research studies involving ion upflow and outflow from the Earth's upper atmosphere is presented. The review focuses on of the sources and mechanisms of the outgoing ionospheric ions.

2.2. Background Study

Under the right conditions, heavy ions in the upper atmosphere can outflow into the magnetosphere to moderate the dynamics in the solar wind-magnetosphere-ionosphere system. Plasma originating from the ionosphere and entering the magnetosphere forms a substantial part of the plasma that populates the magnetosphere. Strangeway et al. (2005) noted that the Alfvén speed slows down when mass from ionospheric outflows is added to flux tubes. This speed reduction thus affects the way in which the magnetosphere responds to changes in external drivers (Peterson et al., 1994). The upwelling of these heavy ions is also a process that can, over geological timescales, lead to the loss of planetary atmospheres. Landmark papers (Jones et al., 1988; André and Yau, 1997; Yau and André, 1997) claim that the main mechanisms responsible for the initial upflow are the ambipolar electric field, resulting from electron precipitation, and the Joule heating from current closure in the ionosphere as presented in the schematic (in the red boxes) taken from Strangeway et al. (2005) shown in Figure 2.1 below.

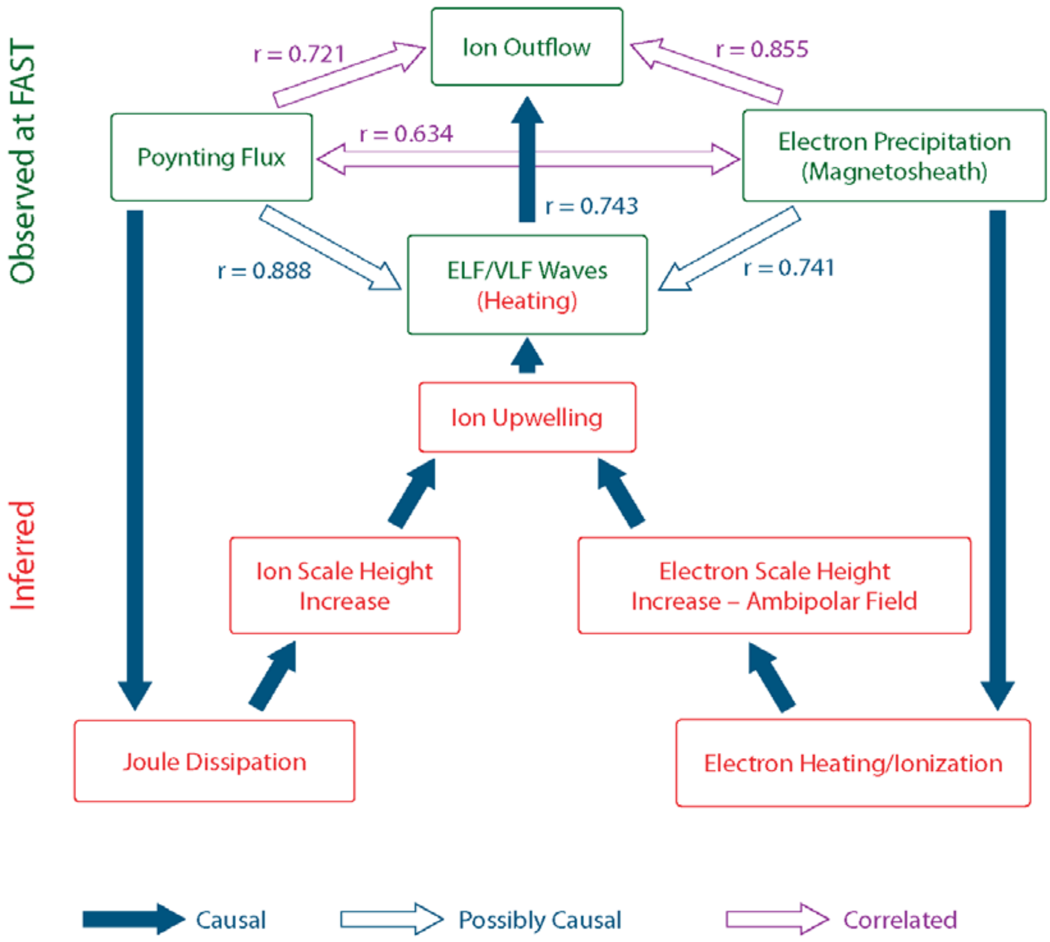

Figure 2.1: A Schematic diagram showing ambipolar field and Joule heating as possible routes to ionospheric plasma upflow (taken from Strangeway et al., 2005).

Dessler and Hanson (1961) were the first to discuss the ionosphere as a source of magnetospheric plasma. They recognised that the terrestrial ionosphere is a large potential source of plasma, especially for light ions at high latitudes outside the plasmasphere. Dessler and Michel (1966) extended this theme, exploring the formation of a steady polar ionosphere outflow into the magnetosphere (see also Moore et. al., 1999 and the references therein). Brinton et al. (1971) and Hoffman et al. (1974) established the ionospheric supply of light ion plasma of polar wind origin to the magnetosphere, using observations from ion mass spectrometer on the Explorer 32 and Isis 2 satellites respectively.

The initial assumption was that the only notable ion outflow from the polar cap ionosphere was the light ion polar wind, first discussed theoretically by Axford (1968). It was envisaged to be made up of H^+ and He^+, with energies of a few electron volts (Shelley et al., 1982). In satellite composition measurements reported by Shelley et al. (1972), it was first observed that heavy ions of atmospheric origin form a significant component of the magnetospheric plasma. These measurements indicated the occurrence of energetic (few keV) O^+ ion fluxes, larger than those of H^+, at the time of geomagnetic storms. Since then, composition measurements from the Geostationary Earth Orbit Satellites (GEOS) 1 and 2, the Spacecraft Charging AT High Altitude (SCATHA) spacecraft, and International Sun-Earth Explorer (ISEE 1), in the high-altitude magnetosphere have shown significant availability of O^+ fluxes throughout the magnetosphere, both in the ring current and the plasma sheet (Yau et al., 1985; Waite et al., 1985; Peterson et al., 1994). It is now well established that the upper atmosphere supplies outflowing ions from the polar ionosphere that might be capable of populating a significant fraction of the plasma in the Earth's magnetosphere, contributing to both the quiet time light ion plasma and the heavy ion plasma characteristic of active times (Chappell et al., 1987; Chappell et al., 2000).

It is believed that wave-particle interactions may be responsible for accelerating upwelling ions, once they reach altitudes above 800 – 1000 km, yet much remains to be understood about this acceleration process (Hultqvist et al., 1999; Skjæveland et al., 2014). Khazanov et al. (1998) explained that in the polar cap ionosphere, the force of the ambipolar electric field causing oxygen ions (O^+) to outflow is weaker than that due to gravity. Thus while light ions generally undergo outflow, heavy ions do not, unless further accelerated.

Intensive investigations into ion upwelling and outflow from the Earth's upper atmosphere have been undertaken in recent years. André and Yau (1997) and Yau et al. (2011) addressed the theories and observations concerning the way the ions are energized. Loranc et al. (1991) and Liu et al. (1995) have attributed the Joule heating effect and ambipolar electric field respectively to be principal driver of ion upflow. The regions in which plasma from the ionosphere is accelerated out into the magnetosphere are the plasmasphere, the auroral regions, and polar cap regions (Glocer et al., 2009). Yau et al. (1985) have shown that between the altitudes of 1.5 and 4 Earth radii (R_E), the occurrence of the oxygen ion, O^+, is dominant in the summer compared to the winter months. Several studies have suggested that the magnetic force, acting upon a toroidal anisotropic ion velocity distribution can result in outflow, the anisotropy resulting from resonant charge exchange that transfers energy via frictional heating to the ion population (Jones et al., 1988; Winser et al., 1988). Howarth and Yau (2008) have shown that the dawn-dusk asymmetry of the interplanetary magnetic field (IMF) determines the part of the plasma sheet that is populated by the ions. According to Moore et al. (2014), the growth of the ambipolar electric field, as a result of higher electron pressure gradients caused by an increasing electron temperature, will saturate at some point and start to decline, resulting in a substantial reduction of the upflowing flux. In addition to the theoretically based proposition by Lemaire and Shunk (1992) that there is a steady transport of cold ions from the plasmasphere through the plasmaspheric wind during a period including extended low geomagnetic disturbance, Dandouras (2013) using data from the Cluster spacecraft, has inferred the erosion of plasmaspheric ions into the magnetosphere during low and medium activities. In addition, a statistical study of solar cycle 23 by Ogawa et al. (2009) has shown that ion upwelling is a general phenomenon that occurs at all local times (LTs). Foster et al. (1998) looked at the diurnal variation of ion upflow as well as its dependence on season and solar cycle, while Endo et al. (2000) have investigated the geomagnetic activity dependence of upflow and downflow, using the data from the vertically pointing CP-7 experiment on the Tromsø EISCAT (European Incoherent Scatter; Rishbeth, 1985) VHF radar.

2.3. Ion Sources

Since the magnetosphere was discovered to contain non-thermal O^+ ions, the ionosphere has been considered as an essential source of plasma that populates the magnetosphere. Outflow from the sunward side of the Earth around cusp is energized by the electrodynamic energy and the ultraviolet (UV) radiation from the sun whereas, nightside auroral substorms immensely contribute to the acceleration processes at the nightside (Yu and Ridley, 2013). Variations in the outflows could result due to seasonal and solar cycle variations that are being modulated by the solar UV. A number of case studies (Yau et al., 1985; Howarth and Yau, 2008) have shown that ion outflows from the ionosphere is strongly related to the level of geomagnetic activities from the solar wind inputs as well as the orientation of the IMF. The ability of the Cluster Ion Spectrometer (CIS) plasma analyzer to probe and ascertain the source of the plasma constituents has provided the opportunity to study and understand different plasma signatures in the magnetosphere (blue labels in Figure 2.2) (ESA, 2013).

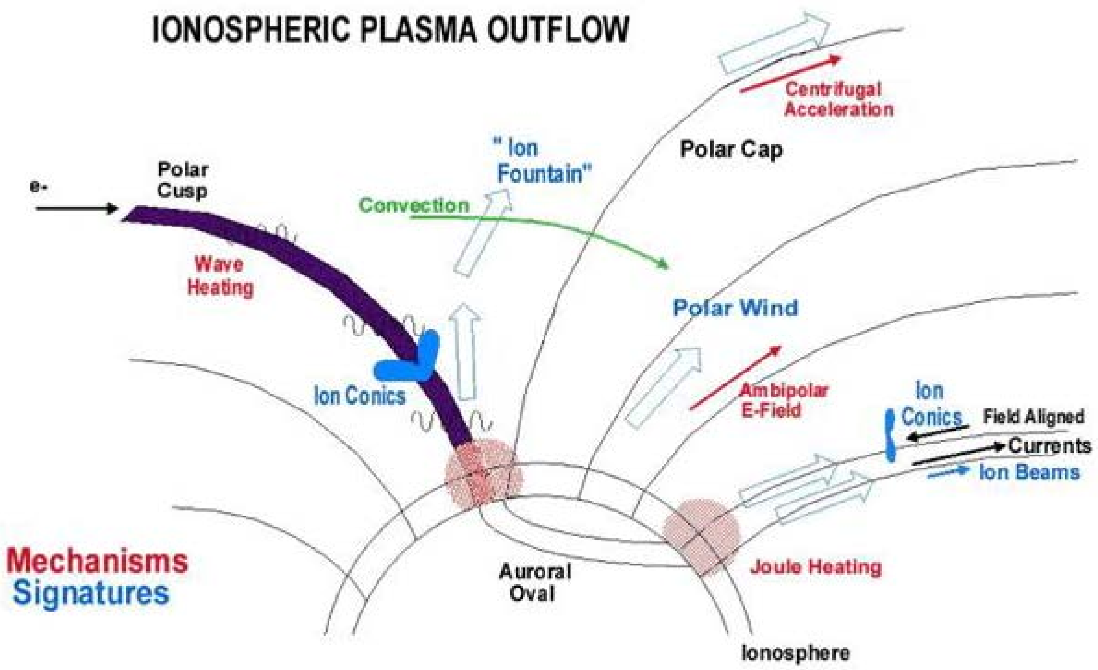

Figure 2.2: A Schematic diagram of ion outflows: Signatures (in blue labels) and Mechanisms (in red labels). From Cluster Ion Spectrometer (ESA, 2013).

Yau and André (1997) reported that diverse processes of ion outflow in the upper-latitude ionosphere have been monitored from spacecraft, rockets, and other instruments that are ground-based in the last thirty years. The outgoing ions through these processes can be classified into two groups, namely; bulk ion upflows of few electron volts (eV) with the collectively ions possessing a characteristic ion velocity, and suprathermal ion flows of greater energies where only a fractional part of the ions are generally energized. The first group comprises the polar wind and the auroral bulk upflow from the topside auroral region while the latter consists of ion conics, transversely accelerated ions (TAI), ion beams and upwelling ions (UWI).

2.3.1 The Polar Wind

The term polar wind was formulated to be an ambipolar outflow of thermal ions originating from the polar region, flowing along the open geomagnetic field lines of the polar cap. The polar wind flow is the result of the energization of the ions through the ambipolar electric field, which is set up by a pressure gradient, and other forces (André and Yau, 1997). This bulk outflow occurs on or near open magnetic field lines, e.g., over the polar cap. The outgoing polar wind results from an ion energization process via the ambipolar electric field, caused by a charge separation, in order to achieve quasi-neutrality with the lighter and fast upflowing electrons (André and Yau, 1997). The ambipolar electric field is set up when electrons in plasma acquire more energy relative to their small mass. The electrons move along the goemagnetic field lines and their energy rise offers sufficient velocity to escape from gravitational pull. Their low mass does not require high kinetic energy from solar UV to overcome the Earth’s gravitational pull and as such, they escape into space. As the number of electrons escaping outward grows, a net positively charged ion is left behind in the ionosphere while the space above the ionospheric altitudes is filled with negatively charged electrons. This charge polarization creates a strong electric field, which resists the movement of the electrons away from the ionosphere. However, the inherent energy increase of the electrons still allows the electric field to be maintained. So, the ions responded to the field by moving out of the ionosphere and quasi-neutrality is achieved. The micro scale level at which this occurs makes it appear as if the two opposite charges move out simultaneously. The ultimate effect is that light ions of H^+, He^+ and heavy O^+ are able to escape from the ionosphere (NASA, 2013).

Planets with strong magnetic field, for example the Earth, retain these outward moving particles even after they gain a few 100 km in height except where other mechanisms release them into interplanetary space (Peterson et al., 1994). These other processes include, plasmaspheric wind, suprathermal energization, Birkeland currents, plasma pressure gradient, $\mathbf{E} \times \mathbf{B}$ convection in a region of curved magnetic field lines, magnetic mirror forces (Lemaire and Schunk, 1992; Dandouras, 2013; Peterson et al., 1994; Waite et al., 1985; Fälthammar, 1986; André and Yau, 1997).

The primary constituents of the polar wind plasma are electrons, and H^+, He^+, and O^+ ions. The F layer is the dominant source of the plasma in the polar wind and its richness in oxygen ions makes the wind dominated by O^+. The origin of a polar wind hydrogen ion occurs when there is an interaction between a hydrogen atom and oxygen ion, resulting in charge exchange during the reaction process, leaving the oxygen species as an energetic neutral atom (ENA) and the newly formed hydrogen ion to be energized perpendicularly to the field and hence, causing the distribution to depart from Maxwellian towards toroidal form. The production of the helium ions on the other hand is brought about when ionospheric helium is photoionized by photons possessing higher energy than helium ionization potential (André and Yau, 1997). The cleft ion fountain described by Lockwood et al. (1985) is a heavy ion (O^+) source which shares the property of the polar wind in that they possess energies ranging between 2 to 20 eV (Yau and André, 1997). These oxygen ions are associated with the polar cusp region from where they are transported by convection into the polar cap (Waite et al., 1985), and during a strong anti-sunward convection could serve as a good source of magnetospheric plasma (Lockwood et al., 1985).

2.3.2 Auroral Bulk Upflow

The main constituent ion of the auroral bulk upflow is the oxygen ion (O^+), and occasionally with substantial amount of nitric oxide ion (NO^+) component. Satellite and radar observation of ions in this upflow showed that they are observed between the altitudinal ranges of about 400 km to around 1500 km (André and Yau, 1997). Ion ouflow related to the bulk ion upflow in the auroral latitudes, especially

O^+, at all local times requires a threshold auroral potential drop of about 10 V (Peterson et al., 1994; Yau et al., 2012).

Frictional heating of O^+ ions at altitudes below about 150 km, where collisions are very important, is one of the important mechanisms that generate auroral upflow. Although the effectiveness of the frictional heating is typically in the F-region (St.-Maurice and Hanson, 1982) but the presence of perpendicular electric fields of several hundred $\mathrm{mV\ m^{-1}}$, capable of generating $\mathbf{E} \times \mathbf{B}$ drifts of the order of few kilometres per second, at the collisional altitudes elevates the ion temperature perpendicularly to the field, which subsequently translate to an increase in the field-aligned component of the temperature. This elevated temperature at collisional altitudes enhances the pre-existing field-aligned pressure gradient drift instability, which convects the ions to a new scale height (André and Yau, 1997; Milan et al., 1997). Sometimes weak electric fields are observed in the auroral precipitation region, yet appreciable upflow, which may be connected with an alternative acceleration process, still occurs (Wahlund et al., 1992; André and Yau, 1997).

Jones et al. (1988) and Winser et al. (1988) introduced the formation of ion-velocity anisotropy to explain the additional process by which the heavy oxygen ions could attain the observed velocity along the parallel magnetic field. They argued that the joint increase in ion scale height and upwelling of the neutral atmosphere are not sufficient to provide the energization for the observed velocity of the ion population. Thus they inferred that when an elevated convection electric field drives the plasma transversely to the magnetic field at a speed above the ion-acoustic speed, energy transfer due to charge exchange between ion and atom would redistributes the ion velocity towards toroidal form such that the velocity perpendicular to the field is greater than the parallel component ($v_{\perp} > v_{\parallel}$), thereby bringing the mirror force into play along the divergent magnetic field.

The bulk upflow could be classified into two groups according to the acceleration processes giving rise to them (Wahlund et al., 1992; Hultqvist et al., 1999):

- Type 1 ion upflows: These are observed when the F region electron density and field-aligned ion velocity are about $\leq 10^{12}\ \mathrm{m}^{-3}$ and $\leq 500\ \mathrm{m\ s}^{-1}$ respectively. They are characterized by periods of elevated ion temperatures as well as high convection electric field. Frictional heating and increased scale height are phenomena of the type 1 upflows. However, no obvious auroral precipitation is observed in this class of upflow, and little or no enhancement is seen in the electron temperature. The anisotropy in the ion temperature at the time of the Joule heating, being influenced by the high convection electric field, is larger in the transverse direction than the parallel. Ion upflow flux of the order $10^{13}\ \mathrm{m}^{-2}\ \mathrm{s}^{-1}$ covering wide range of altitude could be observed.

- Type 2 ion upflows: This class of upflows are particularly prevalent inside auroral arcs. The F region electron density sometimes exceed $10^{12}\ \mathrm{m}^{-3}$ while the field-aligned velocity of the ions occasionally go up to about $1000\ \mathrm{m\ s}^{-1}$. The estimated ion upflow flux in this group can exceeds that of the type 1 and sometimes attain about $10^{14}\ \mathrm{m}^{-2}\ \mathrm{s}^{-1}$. The type 2 upflows are characterized by precipitation down to the E region, strongly elevated electron temperature evident in the F region with less increase in the ion temperature. In contrast to the type 1 upflows, upward displacement in altitude is not evident in the F region. Anisotropic electron temperature is observed in this upflow class with preference to the temperature in the perpendicular direction to the field. The perpendicular electric field in the type 2 upflows is moderate compared to the type 1 yet, their occurrence frequency is higher and likewise their upflow flux strength most times.

In the absence of further energization, the two upflow categories discussed above will not attain the escape velocity and hence, ion downflow might occur. Different kinds of ion energization processes promote the formation of suprathermal and energetic outgoing ions resulting from the initial upflow from the auroral and polar cap ionosphere. These suprathermal upflowing ions are discussed in the following section from 2.3.3 to 2.3.5.

2.3.3 Ion Conics and Transversely Accelerated Ions

Outflow of the heavy ions species relates to the energization of the ionospheric ions in a transverse direction to the magnetic field. Energetic ions ranging from a few eV to a few keV are responsible for forming upflowing ion distributions and an onward movement along the geomagnetic field lines to form conics in velocity space (André and Yau, 1997). The flux distribution of ion conics is peaked at an oblique angle to the upward geomagnetic field direction. A range of frequency oscillation of the perpendicular component of electric fields is generally responsible for this kind of energization. When magnetic activity is low, conics are evenly distributed above 2000 km altitude, whereas during increasing geomagnetic activity its occurrence increases with altitude. There is reduction in occurrence probability of ion conics with low energy as the altitude increases from above 15,000 km. The high energy ion conics are a source of ring current ions (André and Yau, 1997; Hultqvist et al., 1999).

The Transversely Accelerated Ion (TAI) distributions are a peculiar case of ion conics, in which the ion velocity is nearly or completely perpendicular to the field thereby having a pitch angle close to or about 90°. The magnetic mirror force at this point is yet to reverse the velocity component along the field. On the dayside, TAI are observed down to altitude of about 3000 km while on the nightside, they are most common at a much lower altitude between 1400 km and 1700 km. During high auroral activity, they can be observed with the aid of sounding rockets down to lower altitude as low as about 400 km (Yau and André, 1997; Hultqvist et al., 1999).

2.3.4 Ion Beams

Both ion beams and conics are at times referred to as upflowing ions (UFI), but in contrast to ion conics, the flux distribution of ion beam is peaked along the parallel geomagnetic field line. However, in comparison to the conics, the energization of the ion beams is also brought about in the direction perpendicular to the magnetic field and both are usual phenomenon as they occur frequently on some occasions above 50% up to about altitude of one earth radius and above. In general ion beams, unlike conics, are restricted above about 5000 km altitude. Ion conics can evolve into ion beams as at higher altitudes as they become more aligned to the field as a result of not being strongly energized perpendicularly enough to the field and hence, the divergent magnetic field changes the motion into field-aligned. Occurrence probability of ion beams with low energy increases with altitude, up until close to about 4 R_E but in contrast, the occurrence probability of ion conics with low energy reduces as the altitude increases from above 15,000 km. Both species of outgoing ion are dominated by hydrogen and oxygen ions from energy range between 10 and a few keV (Yau and André, 1997; Hultqvist et al., 1999; Yau et al., 2011).

2.3.5 Upwelling Ions

Ion outflows as mentioned earlier usually originate from the dayside cusp as well as the nightside auroral region (Yu and Ridley, 2013). The upwelling ions (UWI) are dayside outflows that exhibit the characteristics of being energized from about one to tens of eV both transversely and along the field (Hultqvist et al., 1999). Equatorward of the polar cap and the dawn sector of the auroral oval are the major areas where the upwelling ions are being observed. They are most frequent almost everywhere in the morning sector, but at different locations. However, due to ionospheric convection, UWI can appear parallel to the magnetic field at other local times. Observation of UWI events shows that the ion velocities and that of the satellite making the observation are almost the same. At higher altitudes, UWI tends to move to higher invariant latitude and the flow becomes more field-aligned. It is somewhat difficult to easily distinguish between UWI and conics of low energy however, UWI in comparison to conics in the same perpendicular energy regime have higher average kinetic energy and are more upward moving. The most common outflow in the UWI is usually the O^+ even though all other species (both light and heavy ions) experience the same energization. Of the entire suprathermal ion outflow, the UWI events are mostly related to the cleft ion fountain (Yau and André, 1997; Hultqvist et al., 1999; Yau et al., 2011).

2.4. Upflow and Outflow Mechanisms

The initial ion upflow from the ionosphere and its eventual outflow under the right conditions are brought about by different energization processes/drivers. Some of these drivers or mechanisms, which operate at different altitudes, are discussed in this section. The CIS plasma analyser (ESA, 2013) helps in identifying the outflow drivers and also to distinguish between plasma from different regimes. The schematic of the upflow-outflow mechanisms is as shown in Figure 2.2 (red labels). According to Yau et al. (2011), one single process is not sufficient to bring about ion outflow from the Earth's upper atmosphere. Multiple processes including the initial acceleration of the bulk upflows consisting of polar wind and auroral bulk upflow, suprathermal energization of the bulk upflow, and acceleration by variety of different wave modes are part of the intrinsic processes that culminate in ion outflow.

2.4.1 Ambipolar Electric Field

One of the constitutive elements of all polar wind theories is the ambipolar coupling of electron energy to the ion plasma, which is caused by a slight charge separation in the plasma (André and Yau, 1997). The charge separation polarizes the plasma distribution and as a result, an ambipolar potential drop is set up with a sufficient strength to balance the flow rate of escaping electrons and ions in conjunction with the precipitating electrons into the system so that quasi-neutrality phenomenon is not breached. Tam et al. (1995) estimated that sufficient electrons are needed at higher altitude for appreciable flux of O^+ to escape. Khazanov et al. (1997) subsequently working on the assumption that sufficient electrons will be readily present, verified the result of Tam et al. (1995).

2.4.2 Centrifugal Effect

Cladis (1986, cited in Hultqvist et al., 1999) proposed that the centrifugal force in the frame where the plasma convects across the polar cap contributes immensely to O^+ energization process, which Horwitz et al. (1994) suggested would give the heavy ion a sufficient acceleration to escape. In the work of Demars et al. (1996), the strong influence of centrifugal acceleration on the O^+ was ascertained, but added that it was of great importance at altitudes above few earth radii. The implication of this is that other acceleration mechanism, for example, frictional heating is necessary at lower altitude. A way by which the centrifugal acceleration achieves its high contribution is that it raises the parallel component of the velocity in preference to the transverse flow, making the ions go down the magnetospheric tail lobes (Moore and Delcort, 1995).

2.4.3 Ion Acceleration by Auroral Low-Energy Electron Precipitation and Currents

Plasma pressure gradient along the field line is modified by processes which preferentially heats the ionospheric thermal electron population. This subsequently leads to elevated polarisation electric field, which in turn results in an ion outward energization and outflow (Hultqvist et al., 1999). Using a simple fluid approach to describe the ionospheric plasma, Blelly et al. (1996) in their numerical simulation of ion outflow have modelled the radar-inferred downward topside electron heat flow observation of EISCAT-VHF (Blelly and Alcaydé, 1994). Blelly et al. (1996) have shown how the ionosphere responds to the perturbation caused by such heat flux. Their model found a good agreement with the observed time-dependent ionospheric structure and dynamics, with O^+ outflow velocity attaining 800 m s^{-1}, which is associated with elevated electron temperature. Their results also suggested that during large scale heat flow perturbation, and elevated ion and electron temperatures, currents arising from electron precipitation and $\mathbf{E} \times \mathbf{B}$ drifts inside the auroral arcs can occur simultaneously and hence, basics acceleration mechanisms. Analysis of EISCAT data by Caton et al. (1996) on the influence of upflow mechanisms in the F region and topside ionosphere also showed that the combined effect of the soft auroral precipitation and the electron heat flux are of great significance to the upflow compared with the effect from the frictional ion heating.

2.4.4 Ion Acceleration by Frictional Heating

Large currents circulating at the E region altitudes and intense $\mathbf{E} \times \mathbf{B}$ convection drifts greatly influence the ionosphere above the auroral and polar regions. As plasmas moves through the neutral atmosphere in the E region, the electrons move under the effect of the $\mathbf{E} \times \mathbf{B}$ drift, whereas the ion, as a result of high ion-neutral collision frequency, undergoes substantial frictional heating (Hultqvist et al., 1999; Milan et al., 1997). The plasma heating takes about a few seconds to minutes while the neutral atmosphere, itself being heated, takes a time constant of a few hours (Hultqvist et al., 1999). The possible outcome of such frictional, or Joule, heating, is an increase in the ion temperature, which under the influence of the field-aligned plasma pressure gradients will set up an upward motion of the ions that could be sufficient to overcome the gravitational pull. The expansion of the neutral atmosphere will also contribute to an increasing scale height of the upwelling ions. St.-Maurice and Schunk (1979, cited in Hultqvist et al., 1999) and Lockwood et al. (1987, cited in Hultqvist et al., 1999) explained that extreme frictional heating transverse to the geomagnetic field will consequently heats the ions preferentially in the transverse direction, resulting in ion temperature anisotropies. This plasma anisotropy as stated before, can subject the plasma to a mirror force in the presence of divergent geomagnetic flux tube with increasing altitude. The combined effect of the forces due to mirroring and the upward pressure gradient accelerates the major ion species (O^+) up to hundreds of m s^{-1} (Hultqvist et al., 1999).

2.4.5 Heating by Broadband Low Frequency Waves

Waves have the characteristic property of particle scattering by heating. A typical example of such waves is the broadband low frequency (f_{LB}) waves with a frequency range of $0 < f_{LB} < 100$ Hz, which Chang et al. (1986) suggested could cause transverse energization of the ions and effective heating of the ions with preference for the O^+ over H^+ . This they posited could to be a good reason for O^+ dominance in the plasma sheet. The gyrofrequencies of the outflowing ions are within this band-width at altitudes from about 1000 km up to a few R_E (André and Yau, 1997; Hultiqvist et al., 1999). For the waves to optimally heat the ions, two assumptions have to be made:

- The perpendicular vector of the wave is far less than the reciprocal of the ion gyroradius.

- The ions are being heated by the left-hand polarized part of the waves.

With these assumptions, Chang et al. (1986) and Hultiqvist et al. (1999) expressed the heating rate as

$$\frac{dW}{dt} = \frac{q^2}{2m} S_L \quad (2.1)$$

where q and m are the charge and mass of the ion, and

S_L is the 'field spectral density at the ion gyrofrequency'.

Equation (2.1) yields best results when the heating rate is estimated from the observed spectral densities (André and Yau, 1997; Hultiqvist et al., 1999). Different observations by sounding rocket in the cleft region have shown that ions are energized by broadband low-frequency waves, and a noticeable depletion in the ions densities is a clear indication of the energization (Kintner et al., 1996; Moore et al., 1996).

2.4.6 Lower Hybrid and EMIC Wave Heating

Waves in the neighbourhood of the lower hybrid frequency (f_{LH}), which is the result from mixture of two frequencies , can also energize ions (Hultqvist et al., 1999). Some of the events analysed by André and Yau (1997) showed that the strength of the waves close to f_{LH} is more than that of waves near O^+ and H^+ cyclotron frequencies (f_{O^+} and f_{H^+}) and is believed to be the major mechanism for ion energization (André and Yau, 1997; Yau et al., 2011). Waves close to the ion cyclotron frequencies are essential for pre-heating the ions to acquire sufficient velocities to make them resonate with the waves around the lower hybrid frequency, but the latter is responsible for most of the energization (Hultqvist et al., 1999; Yau et al., 2011). Electromagnetic ion cyclotron (EMIC) waves can also be generated through electrons from auroral precipitation. The EMIC waves below the ion cyclotron frequency according to Ball (1989) can, in theory, heat ions of greater gyrofrequency by the transverse energization brought about by the double cyclotron absorption mechanism, but may at most times be of less practical importance (Ball and André, 1991). However, the ion cyclotron frequency of some ions may be below the EMIC waves of another heavy ion, for instance, the emissions may occur between f_{H^+} and f_{O^+}. It is also likely for the EMIC emissions above f_{O^+} to heat oxygen ions in such a way as waves above lower hybrid frequency (Hultqvist et al., 1999).

2.5. Basic Theory

2.5.1 Ambipolar electric force and the Joule heating

The ambipolar electric force produces a field-aligned force that redistributes the particles along the field lines. It arises from the ambipolar electric field, which is caused by charge separation along the magnetic field as explained in detail under section 2.3.1. The polarization of the plasma distribution as a result of the charge separation results in a large ambient electric potential that contributes to ion upwelling in order for quasi-neutrality to be maintained. The Joule heating on the other hand results from current closure in the ionosphere. Heating results from ion-neutral friction arising from the Pedersen current that is being driven by an enhanced electric field. This leads to the Joule heating of the neutrals, causing an upwelling of the neutral gas that also drag ions up the field lines. Also, when strong electric field drives ion population through the neutral atmosphere, the ions are specifically heating giving rise to the term called ion frictional heating. While the Joule heating is electromagnetic in nature, the ambipolar electric force is kinetic.

Equation (2.2) is the plasma momentum equation, which shows the forces that contribute to the overall motion (Milan, 2014b).

$$\rho \frac{d\mathbf{V}}{dt} = \rho\mathbf{g} - \nabla P + \rho_q \mathbf{E} + \mathbf{j} \wedge \mathbf{B} \qquad (2.2)$$

where $\mathbf{V}$ is the plasma bulk velocity,

ρ *and* ρ_q are the mass and charge density respectively,

$\mathbf{g}$ is the acceleration due to gravity,

P is the isotropic plasma pressure and

E and **B** are the electric and magnetic field respectively.

By applying the law of conservation of momentum and treating electrons and ions separately, equation (2.2) could be written in terms of plasma constituents, and electron and ion momentum equations can be derived as shown below:

$$\sum final\ momentum = \sum initial\ momentum$$

$$(\Sigma m_e + \Sigma m_i)\mathbf{V} = N_e m_e \mathbf{V}_e + N_i m_i \mathbf{V}_i$$

$$M\mathbf{V} = (n_e m_e \mathbf{V}_e + n_i m_i \mathbf{V}_i)d\tau \qquad ; where\ N = nd\tau$$

Dividing through by $d\tau$ (a volume element) and taking the time derivate of both sides, we have:

$$\frac{M}{d\tau}\frac{d\mathbf{V}}{dt} = n_e m_e \frac{d\mathbf{V}_{\boldsymbol{e}}}{dt} + n_i m_i \frac{d\mathbf{V}_{\boldsymbol{i}}}{dt}$$

$$\rho \frac{d\mathbf{V}}{dt} = n_e m_e \frac{d\mathbf{V}_{\boldsymbol{e}}}{dt} + n_i m_i \frac{d\mathbf{V}_{\boldsymbol{i}}}{dt}$$

$$\rho \frac{d\mathbf{V}}{dt} = \rho_e \frac{d\mathbf{V}_{\boldsymbol{e}}}{dt} + \rho_i \frac{d\mathbf{V}_{\boldsymbol{i}}}{dt}$$

where $\rho = \frac{M}{d\tau} = nm$ is the mass density,

subscripts $e\ and\ i$ indicate electron and ion respectively,

n is the number density and m is the mass,

N indicates the number of particles in the volume

M is the total mass of every specie.

Substituting the parameters above into equation (2.2) and assuming quasi-neutrality $(n_e \approx n_i)$ and singly-charged ions so that $\rho_q = en_i - en_e$ and $\mathbf{j} = en_i\mathbf{V}_i - en_e\mathbf{V}_e$, we have:

$$\rho_e \frac{d\mathbf{V_e}}{dt} = n_e m_e \mathbf{g} - \nabla P_e - e n_e \mathbf{E} - e n_e \mathbf{V}_e \wedge \mathbf{B} \tag{2.3}$$

$$\rho_i \frac{d\mathbf{V_i}}{dt} = n_e m_i \mathbf{g} - \nabla P_i + e n_e \mathbf{E} + e n_e \mathbf{V}_i \wedge \mathbf{B} \tag{2.4}$$

Since I am interested in the ion momentum equation and the ion motion along the parallel magnetic field, I concentrate on equation (2.4). Bearing in mind that the vector product of two parallel vectors vanishes, the $\mathbf{j} \wedge \mathbf{B}$ force which is the last term in equation (2.4) vanishes along the field, and we have:

$$\rho_i \frac{d\mathbf{V_{i//}}}{dt} = n_e m_i \mathbf{g} - \nabla P_i + e n_e \mathbf{E}_{//} \tag{2.5}$$

The 1st, 2nd and 3rd terms on the RHS (right hand side) of equation (2.5) indicate respectively the gravitational force, the pressure gradient and electric force on the ions in the direction along the field line. Assuming that field perpendicular gradients in E are small, gradient in the parallel electric field is taken to be the derivative of $E_{//}$ along the field line (Cowley, 2016);

$$\text{i.e.,} \qquad \nabla E_{//} = \frac{\boldsymbol{\partial} E_{//}}{\boldsymbol{\partial s}} \tag{2.6}$$

During the International Incoherent Radar School sponsored by EISCAT and NSF (2016), the equation governing the ambipolar electric field was sourced and was given by Roger (2016) as in equation (2.7) below. It was later found that under the assumption of a steady state and $m_e \approx 0$, equation (2.7) can be derived from equation (2.3) for field-aligned motion.

$$E_{//} = -\frac{1}{e n_e} \nabla_{//} \left(n_e K_B T_e\right) \tag{2.7}$$

Substituting equations (2.6) and (2.7) into (2.5), we have:

$$\rho_i \frac{d\mathbf{V}_{\boldsymbol{i}//}}{dt} = n_e m_i \mathbf{g} - \boldsymbol{\nabla} P_i - \frac{\boldsymbol{\partial}}{\boldsymbol{\partial s}}(n_e K_B T_e) \qquad (2.8)$$

where K_B is the Boltzmann constant,

T_e is the field-aligned electron temperature,

$\frac{\boldsymbol{\partial}}{\boldsymbol{\partial s}}$ indicates the differential operator with respect to altitude.

The 3rd term on the RHS of equation (2.8) will be used throughout Chapter 5 to plot and discuss the ambipolar electric force. To estimate the value of Joule heating for the events, the electric field component transverse to the magnetic field is required to calculate the Pedersen current, but the ESR 42 m dish, which is our primary instrument for sourcing data, is fixed and field-aligned. In the absence of perpendicular electric field or velocity component, ion temperature enhancement is used as a proxy to infer Joule heating as event driver, because the relative motion between ions and neutrals generates frictional heating which raises the ion temperature (Buchert et al., 2004; Skjæveland et al., 2014). Since the field-aligned T_i is measured by the ESR 42 metres dish, $-\boldsymbol{\nabla} P_i$ (i.e., the ion pressure gradient) from equation (2.8), which is equal to $-\frac{\partial}{\partial s}(n_e K_B T_i)$, is used as the proxy for the Joule heating. The balance force, which is the algebraic sum of all the RHS terms in equation (2.8) is also investigated to show the direction of flow of the ions, either upflow, downflow or at equilibrium.

2.5.2 Plasma temperature

The electron plasma frequency is the characteristic frequency of the plasma, owing to the fact that the frequency with which the ion oscillates is lower than that of the electron because frequency is a function of mass of the particle – the higher the mass of the particle, the lower the oscillating frequency. Equations (2.9) and (2.10) describe the electron and ion plasma frequencies respectively.

$$\omega_{pe} = \left(\frac{n_o e^2}{m_e \varepsilon_0}\right)^{1/2} \qquad (2.9)$$

$$\omega_{pi} = \left(\frac{n_o e^2}{m_i \varepsilon_0}\right)^{1/2} \tag{2.10}$$

where ω_{pe} and ω_{pi} are the electron and ion frequencies respectively,

n_o is the equilibrium density,

e is the electronic charge,

ε_0 is the permittivity of free space, and

m_e *and* m_i are the respective electron and ion masses.

Temperature, which is a measure of random motion of particles around the bulk motion, has a direct relationship with particle velocity for conservation of the particle distribution function (PDF), f, at any point as expressed in equations (2.11) and (2.12) below. The consequence is that temperature is related to particle plasma frequency. Therefore, since the electron plasma frequency is the characteristic frequency of the plasma, it is expected that the electron temperature will bear more semblance with the plasma temperature than the ion temperature. Equation (2.11) is the PDF behaviour in a drifting isotropic Maxwellian distribution while equation (2.12) represents anisotropic temperature distribution (Cowley, 2014).

$$f = f_o \exp\left(\frac{-m}{2k_B T}\left(v_x^2 + (v_y - V)^2 + v_z^2\right)\right) \tag{2.11}$$

$$f = f_o \exp\left(\frac{-m v_\perp^2}{2k_B T_\perp}\right) \exp\left(\frac{-m v_\parallel^2}{2k_B T_\parallel}\right) \tag{2.12}$$

where f *and* f_o are the instantaneous and initial particle distribution function respectively,

m is the mass of particle,

v_x, v_y *and* v_z are the respective x, y and z components of particle velocity,

$v_\perp$ *and* $v_\parallel$ are the perpendicular and field-aligned particle velocities respectively

$T_\perp$ and $T_\parallel$ are the perpendicular and field-aligned particle temperatures respectively

V is the bulk speed (isotropic about v_y), and

k_B is the Boltzmann constant.

2.6. Summary

Outflow of heavy ions is a process leading to loss of planetary atmospheres. It plays a crucial role in determining the mass and energy density of the overlying magnetosphere. It was first observed that heavy ions of atmospheric origin form a significant component of the magnetospheric plasma through the composition measurements of Shelley et al. in 1972. Heavy ions mainly originate from the dayside cusp and the nightside auroral region, and the main mechanisms responsible for the initial upwellings are ambipolar electric field and the Joule heating. Several wave modes including, inter alia, broadband low frequency waves, lower hybrid frequency waves, and Electromagnetic ion cyclotron waves are responsible for suprathermal energization of the ions to outflow from the planet's gravitational barrier.

CHAPTER 3

Instrumentation and Data Sources

3.1. Introduction

The data used for this research study are obtained from ground-based instruments that employ either incoherent or coherent scatter, and also from space-based instruments in the Medium Earth Orbit (MEO) and Geosynchronous Earth Orbit (GEO). This chapter discusses the remote sensing ground-based and the in situ spacecraft instruments used for data source in this thesis.

3.2. Ground-based Instruments

The remote sensing ground-based radars employed in this research that measure the flow of plasma in the Earth's upper atmosphere as a result of wave activities are the European Incoherent Scatter (EISCAT; Rishbeth, 1985) radar and the Super Dual Auroral Radar Network (SuperDARN; Greenwald et al., 1995) working on the principles of incoherent and coherent scatter respectively. The incoherent scatter (IS) theory and technique employed in EISCAT measurements are addressed, in particular, in this section as it is the primary source of data.

3.2.1 Theory of Incoherent Scatter and the Radar Technique

When charged particles move through plasmas, detectable random fluctuations in electron density, which can be seen as EM waves scattering, is triggered. This type of scattering is referred to as incoherent scattering (Bowles, 1961; Alcaydé, 1997; Akbari et al., 2017). The term incoherent scattering does not mean the waves phase is not definite, but rather, a term referring to a phenomenon meaning radio waves are randomly scattered by ionospheric electrons (EISCAT and NSF, 2016). The simple approach of incoherent scatter radar theory first proposed by Gordon (1958) was later reviewed and modified by contributions from landmark papers. These include, inter alia, the spectral broadening correction by Bowles

(1958), the effects of electron-ion temperature ratio on the total backscatter spectral shape by Farley (1966), correction of the independent free electron scattering (Dougherty and Farley, 1960), and the effect of the electrostatic Coulomb force on the scattering coefficient (Fejer, 1960). Owing to the signal backscatter caused primarily by electrons, the initial thought which hinged on electrons as independent scatterers assumed the returned signal resulted from Thomson scattering. However, the particle distribution function of the returned spectrum is modified from the expected Gaussian distribution by the more massive ions because they are electrostatically coupled to the electrons. The incoherent scatter comes from a cloud of electrons that are thermally in random motion and as a result of the ions influence, a spectrum of frequencies in the neighbourhood of the transmitted signal that obeys Bragg scattering is returned as the ion lines (Akbari et al., 2017).

The theory on which the incoherent scatter is based is applicable to powerful radars which can detect the weakly scattered radio waves, Doppler shifts encompassing frequency spread of the received backscatter, echos caused by the ionospheric electrons, and the role of the ions in the backscatter especially when the radar wavelength is much greater than the Debye length (Gordon, 1958; Evans, 1969). The generalized scattering coefficient per unit volume, which tends to Gordon's approximation ($\sigma = \sigma_e N$) at a very small value of the exploring wavelength, is given by equation (3.1) (Fejer, 1960). However, at the radio wavelength, which as expected is usually greater than the Debye length, the mean scattering cross section coefficient becomes half of the Gordon's approximation (Fejer, 1960; Dougherty and Farley, 1960) as shown in equation (3.2).

$$\sigma = \sigma_e N \left(\frac{\left(4\pi\lambda_D \sin(\frac{\theta}{2})\right)^2 + \lambda^2}{\left(4\pi\lambda_D sin(\frac{\theta}{2})\right)^2 + 2\lambda^2} \right) \tag{3.1}$$

$$\sigma = \frac{1}{2}\sigma_e N \qquad\qquad (for\ \lambda \gg \lambda_D) \tag{3.2}$$

$$\sigma_e = \left(\frac{\mu_0 e^2}{4\pi m} sin\psi \right)^2 \tag{3.3}$$

where σ is the ‘scattering coefficient per unit volume’,

σ_e is the ‘single electron scattering cross section’,

N is the ‘electron number density’,

λ is the ‘wavelength of the incident radio wave’,

λ_D is the ‘Debye length’,

θ is the ‘scattering angle’,

μ_0 is the ‘permeability of free space’,

e and m are the respective ‘charge and mass of the electron’, and

ψ is the ‘polarization angle’.

3.2.2 The Incoherent Scatter Radar Spectrum

The electromagnetic pulses transmitted from the radar interact with the ionospheric plasma, and the latter emits a fractional part of the exploring signal as scattering. The backscatter frequency spectrum received (referred to as the incoherent scatter (IS) spectrum) provides a great deal of information regarding the ionosphere (Rishbeth and Williams, 1985). From the IS spectrum a number of basic ionospheric parameters can be derived such as the electron density, ion and electron temperatures, and the ion drift velocity across the Earth’s upper atmosphere (Gordon, 1958; Dougherty and Farley, 1960; Evans, 1969; Alcaydé, 1997). When the radar wavelength is larger in comparison to the Debye length (as is the case in ISR experiments), notable features of resonance lines as shown in Figure 3.1 below are observed in the IS spectrum. Figure 3.2 shows a magnified ion line and how parameters are estimated from it. The ratio of the electron to ion temperature is estimated from peak to trough, while the full width at half maximum of the spectrum gives the ion temperature to ion mass ratio. The electron density is measured from the total area of the spectrum and the Doppler frequency shift observed in the ion line is a measure of the ion drift velocity.

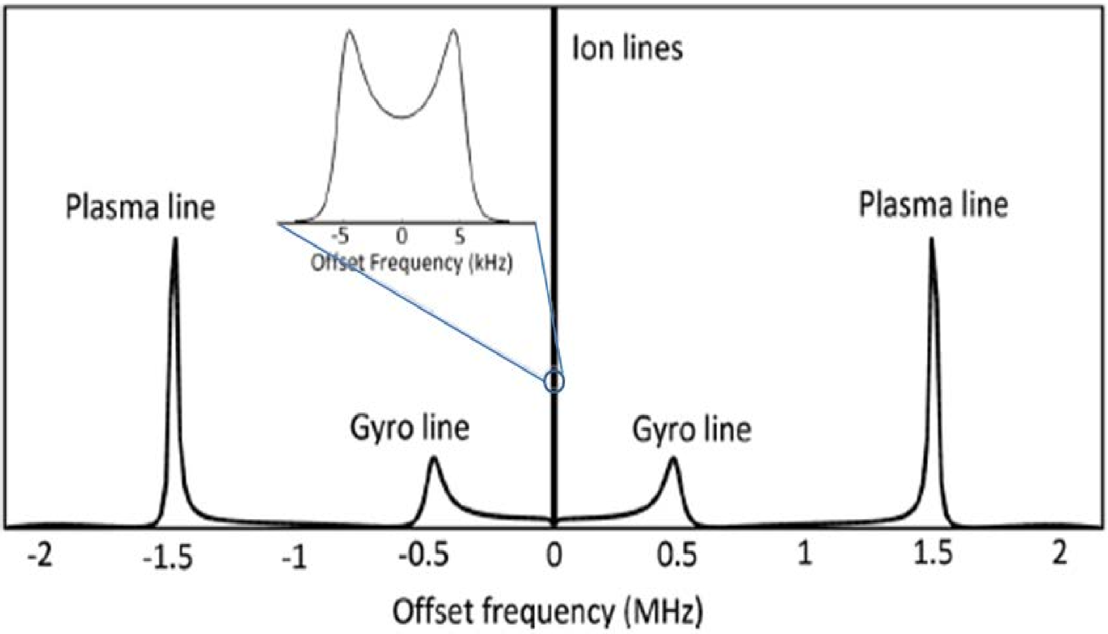

Figure 3.1: A Schematic diagram showing the resonance lines from an ideal incoherent scatter spectrum. From Akbari et al., 2017.

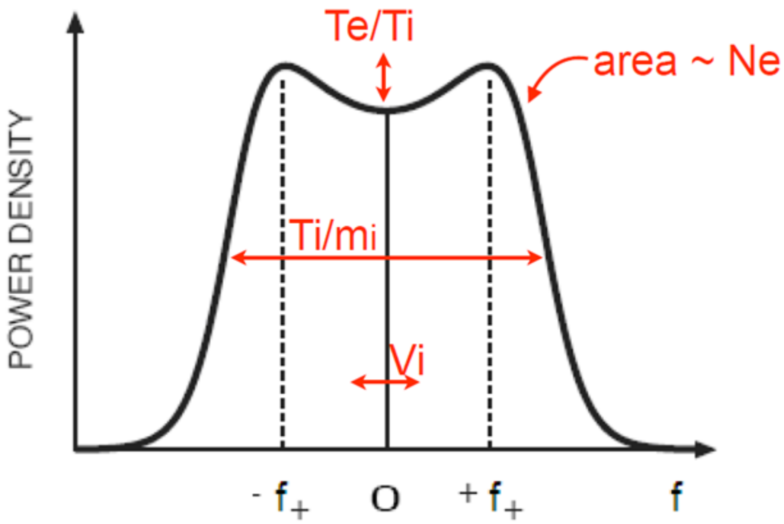

Figure 3.2: A Schematic diagram showing the derived parameters from incoherent scatter spectrum. Taken from EISCAT and NSF, 2016.

3.2.3 The European Incoherent Scatter (EISCAT) Scientific Association

The EISCAT Scientific Association is a body set up to carry out research, using the ISR technique to probe the ionosphere as well as the different divisions (from lower to upper) of the atmosphere. Its heating facility could also be used to modulate the ionosphere for experimental purposes (EISCAT, 2016; Fu et al., 2015).

There are six associate countries of the EISCAT Scientific Association, which include China, Finland, Japan, Norway, Sweden and the United Kingdom. The host countries of the EISCAT facilities are Finland, Norway and Sweden. Other affiliate countries are Russia, Ukraine, France and South Korea (EISCAT and NSF, 2016). All the countries and their status are shown in Figure 3.3.

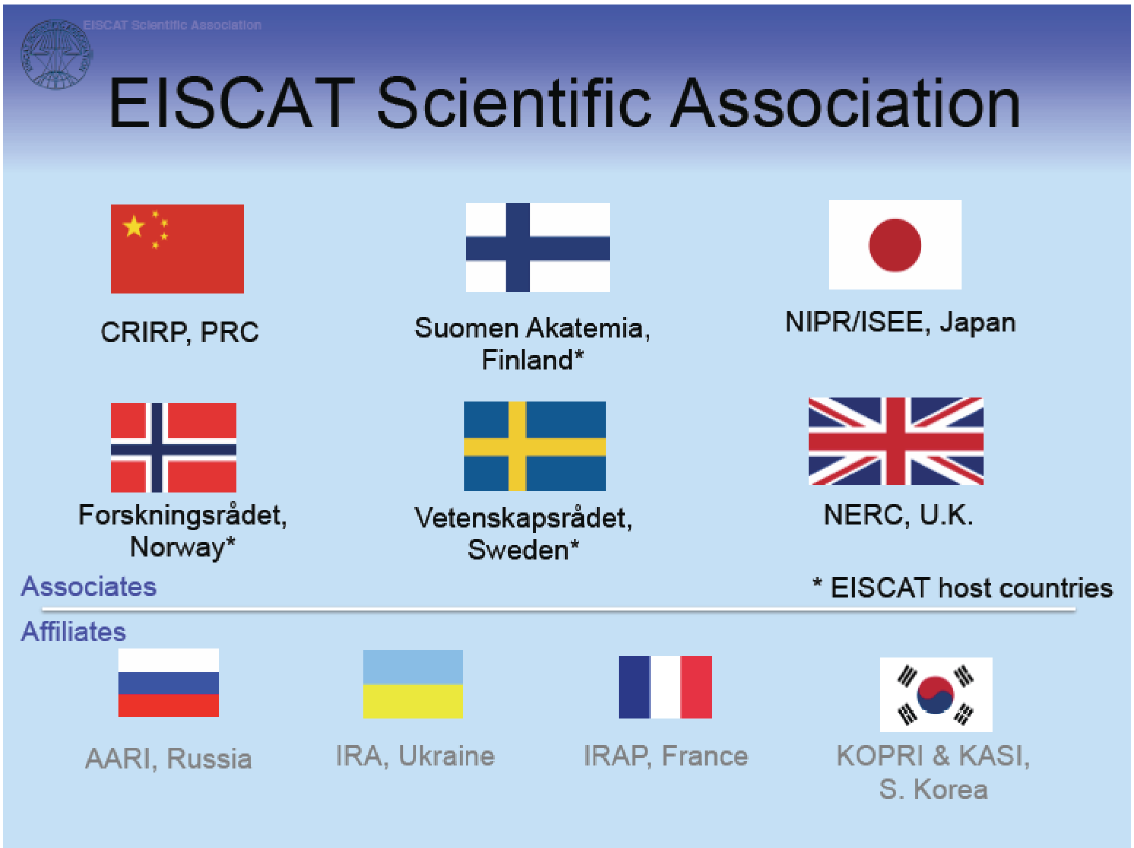

Figure 3.3: The EISCAT countries and their status. From EISCAT and NSF, 2016.

3.2.3.1 EISCAT Facilities

Eleven Incoherent Scatter Radars (ISRs) are fully operational in the world of which, EISCAT runs three of the highest-standard facilities, six by the National Science Foundation (NSF), USA and one each by Ukraine and Russia.

There are three other additional radars that work on the same principle – The Japanese Middle and Upper (MU) atmosphere radar and Equatorial Atmosphere Radar (EAR) which are fully operational though were really designed for lower altitudes, but are powerful enough to get at least some scatter from the ionosphere, while the Chinese radar at Qujing has been constructed, but it is not yet fully operational (EISCAT, 2016).

The present study is focussed on the EISCAT Svalbard radar (ESR; Figure 3.4), situated close to Longyearbyen, Svalbard at a geographic coordinate $78^{\circ}09'11''\mathrm{N}$ and $16^{\circ}01'44''\mathrm{E}$ (Vlasov et al., 2011). The frequency of operation is in the 500 MHz band and it is being transmitted at maximum power of 1.0 MW. In 1994, a facility credited for its very high gain and low noise performance fully steerable parabolic dish antenna of 32 m diameter was completed, and the ESR was officially launched on August 22, 1996 (Wannberg et al., 1997). Also in 1999, another fixed field-aligned antenna of higher sensitivity (42 m diameter) was added. The aim of locating this facility at high latitude is to foster in particular, the studies of the cusp and polar cap region (EISCAT, 2016). The work carried out in this research used the data from the 42 m field-aligned ESR dish.

The EISCAT Svalbard Radar uses the ISR technique (Williams, 1995) and with it, measure some basic plasma parameters of the ionosphere, including; electron density, n_e, from the total scattered energy, ion temperature, T_i, and electron temperature, T_e, from the spectrum shape which is usually double peaked, and the ion drift velocity, v_i, from the ion line Doppler shift. The ESR 42 m diameter fixed dish measures the ion drift velocity along the local geomagnetic field line with a data resolution of 1 minute.

Figure 3.4: The fixed 42m dish of the EISCAT Svalbard Radar. From EISCAT, 2015.

3.2.3.2 EISCAT Programmes

There are a number of experimental modes available for EISCAT common programmes based on the pointing direction(s) of the antenna in conjunction with the characteristic time spent in each direction. The available common programmes given by Tjulin (2017) are as follows:

- Common Programme 1 (CP-1): This employs a fixed transmitter that points along the field line.
- Common Programme 2 (CP-2): The design of the CP-2 enables the transmitter to use a 4-position scanning mode.
- Common Programme 3 (CP-3): This is designed to cover a range of 10° latitude in the F-region to about $74^{\circ}N$. It swings positions up to 17 scans in a 30 minutes duty cycle.
- Common Programme 4 (CP-4): This uses a low elevation scan to take measurements up to $80^{\circ}N$ and provides measurements for field-aligned and vertical observations.

- Common Programme 6 (CP-6): The design of the CP-6 is to make observations of low altitude areas for mesospheric studies.
- Common Programme 7 (CP-7): The aim for the CP-7 is to probe vertically flow at high altitudes in order to study the polar wind.

The Common Programme is commonly/frequently run from time to time for the purpose of long term database for statistical studies. There are other special programmes run occasionally by the EISCAT community. One of such is the IPY (international polar year) mode, from which the data for the study throughout this research is sourced. The reason for selecting the IPY 2007 campaign, which is the most recent (even though it is at solar minimum), was to get a better data coverage than previously achieved (albeit only for a year) and because other data sets existed due to the coordinated nature of the campaign.

3.2.3.3 EISCAT Pulse Code Experiments

EISCAT experiments are routines which pass information to the transmitters, receiving antennas, and digital signal processing units on action to be carried out at a particular time (Tjulin, 2017). The pulse code to be chosen in an experiment needs to put into consideration, the range span, time resolution, range gate size, and spectral range among others, which fits into the region of the ionosphere to be investigated. Figure 3.5 shows some examples of ESR experiments such as manda, ipy, beata, tau7, and folke employed during Common Programmes. Table 3.1 summarises the characteristics of the pulse codes used for the IPY observations presented in this thesis.

Table 3.1: ESR-IPY pulse code experiment summary.

Code length (bit)	Baud length (μs)	Sampling rate (μs)	Range span (km)	Time resolution (s)	Spectral range (kHz)	Spectral resolution (kHz)
30	30	15	77 - 470	60	± 33	1.11 - 1.63

There range gate size varies: increasing from about 3 to 14 km, 15 to 20 km and 20 to 30 km for altitudes 100-200 km, 201-300 km and > 300 km respectively.

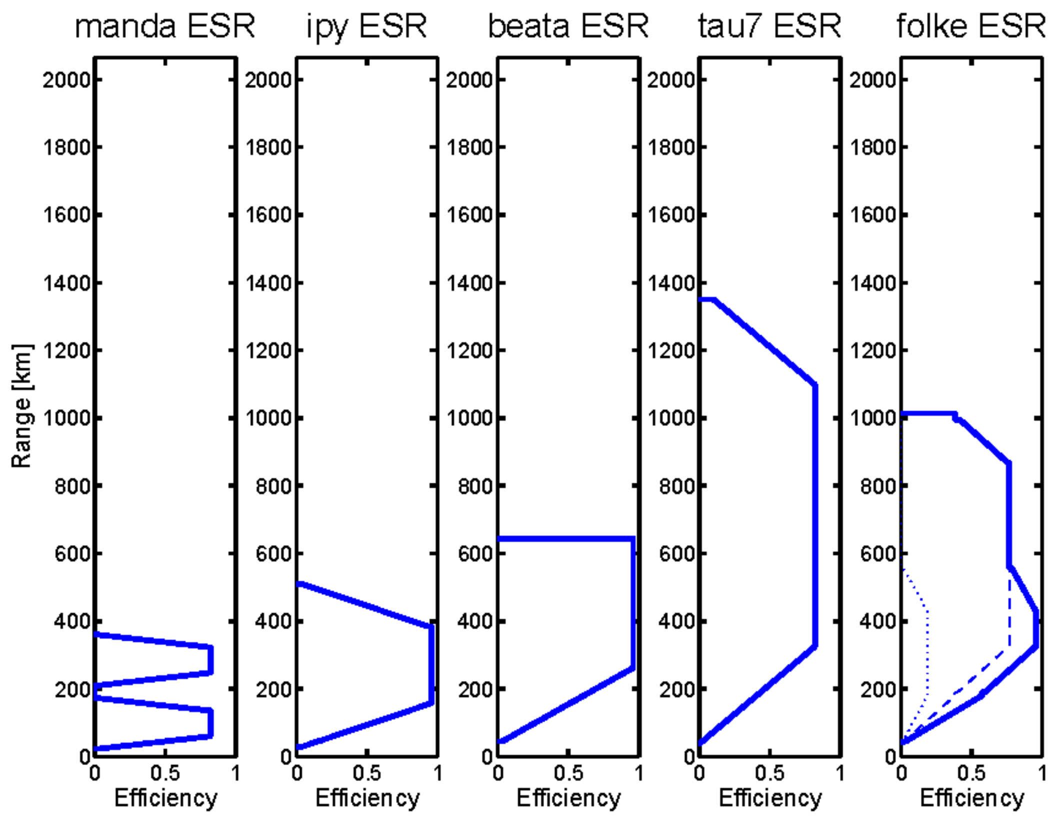

Figure 3.5: A Schematic diagram showing the ranges covered by the EISCAT Svalbard Radar (ESR) for different experiments. From Tjulin, 2017.

Manda is the pulse code used specifically for the D-layer and middle atmosphere. It has high resolution with ion line, but no plasma line. The IPY pulse code was employed during the international polar year. It spans a range of up to about 28 – 509 km and capable of showing both ion and plasma lines. Beata experiment has many characteristic features like the IPY, but extends to higher altitude of about 645 km. Tau7 experiment has the longest baud length and extends up to the topside ionosphere at about 1350 km. Folke pulse code is a dual antenna experiment available only at Svalbard, where the 32m and 42m dishes span between a range of 43 – 1014 km and 43 – 555 km respectively. However, plasma line is only available with the 42m dish (Tjulin, 2017). Other EISCAT pulse code experiments on Common Programmes are arc_slice (85 – 481 km), tau0 (53 – 1297 km), steffe (34 -1021 km), taro (47 – 830 km), hilde (34 – 917 km), and bella (63 – 1344 km).

The ESR-IPY 2007 pulse code covers a range of about 75 to 500 km in altitude. The average number of data points for each unique time covers the D, E and F regions at an average ratio of 2:5:9 respectively. An upper limit of 470 km is imposed on the geodetic altitude to avoid the noise associated with Incoherent Scatter Radars (ISRs) at high altitude, and I use returns from above 100 km, in order to allow for investigation only in the upwelling region.

3.2.4 The Super Dual Auroral Network (SuperDARN)

The SuperDARN is a worldwide chain of high frequency (HF) radars which monitor plasma dynamics of the ionospheric E and F layers above the high and middle latitude regions (Ribeiro et al., 2013a; 2013b). The SuperDARN has been in operation since its inception over 20 years ago (Greenwald et al., 1995; Gillies et al., 2012) and it is a ground-based tool that has made a considerable success in investigating both ionospheric and magnetospheric dynamics as well as the neutral atmosphere. The SuperDARN consists of several radars that employ coherent-scatter radars (CSRs) technique operating in the HF band with a superposed fields-of-view that envelope the ionosphere above the poles in both hemispheres. The radar network has the principal objective of studying and measuring ionospheric convection, but has also achieved significant success at the magnetospheric altitudes (Chisham et al., 2007). The radars return measurements from plasma irregularities flowing up to several km s^{-1}, detectable to a range of thousands of kilometres, and the line-of-sight velocity, spectral content, and intensity can be derived (Ribeiro et al., 2013a; 2013b) from autocorrelation functions (ACFs) formed from the raw data samples.

3.2.4.1 The CUTLASS Radars

The two SuperDARN radars employed in this study are the bistatic pair of the SuperDARN radars network called CUTLASS (‘Cooperative UK Twin Located Auroral Sounding System’; Milan et al., 1997). CUTLASS is a system that has frequency agility, operating in the 8–20MHz band-width and comprises stations at Pykkvibær, Iceland and the other at Hankasalmi, Finland (Milan et al., 1997; Wright et al., 2004). The CUTLASS radars shown in Figure 3.6

consists of two arrays of log-periodic antennas, a main array of 16 antennas that both radiate and receive the radio signal, and an interferometer array of 4 antennas acting as a receiver only and for determining the angle of the arriving backscatter signal. The radars have fields of view enveloping wide area including the ESR facility (Figure 3.7), which is the area being considered under the present study (Milan et al., 1997; Wright et al., 2004). There are 16 azimuthal pointing directions in each of the CUTLASS radars, of which the northward directed beam 9 of the Finland radar and beam 5 of the Iceland radar overlay the ESR facility (Milan et al., 1997; Yeoman et al., 2010), and are employed in this study as they pass through the coverage area of the EISCAT Svalbard Radar. The geographic co-ordinates of the Finland and Iceland radars are (62.32°N, 26.61°E) and (63.86°N, 19.20°W) respectively (Milan et al., 1997; Lester, 2013).

Figure 3.6: The main and interferometer antennas of CUTLASS Iceland radar at Pykkvibaer. From University of Leicester, 2017b.

3.2.5 The SuperMAG Magnetometer Array

The SuperMAG global ground-based magnetometer database is an international cooperation of organizations and national agencies, currently operating over 300 ground-based magnetometers spread across the world (Gjerloev, 2009; 2012). It uses a common baseline technique to provide measurements for geomagnetic field perturbations of all stations with similar coordinate system and its vast number of magnetometers allows for a robust global average. SuperMAG focuses on providing easy access to measurements needed to validate ionosphere-magnetosphere studies from many and well-distributed stations (Gjerloev, 2012).

The SuperMAG upper and lower electrojet indices (SMU and SML) are obtained from the readings based on magnetic perturbation in the northward direction from about 300 ground-based magnetometers positioned at different local time zones. The SMU is the average northward magnetic perturbation caused by the eastward electrojet at any given instant, while the SML is estimated from the southward field disturbance resulting from the westward electrojet.

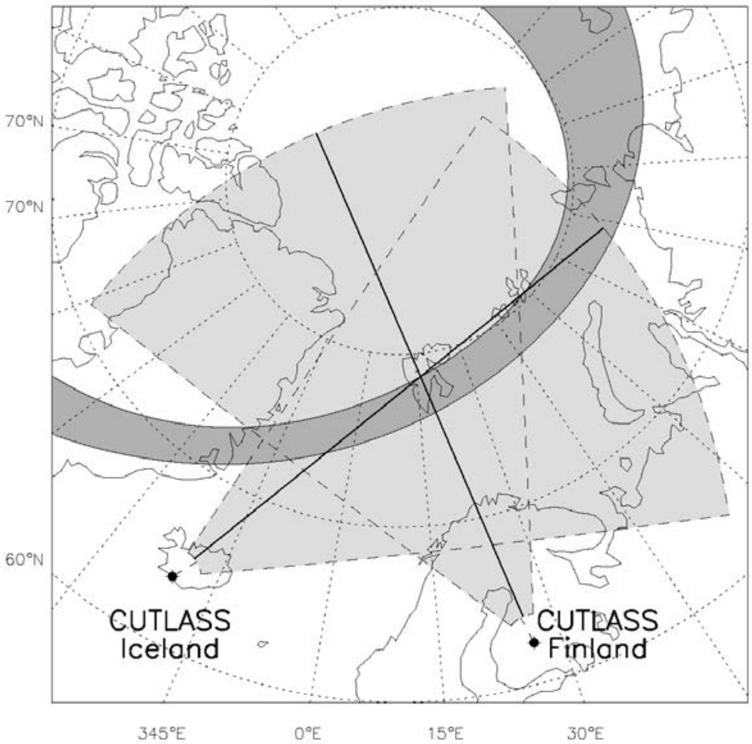

Figure 3.7: The fields of view of the Pykkvibær, Iceland and Hankasalmi, Finland CUTLASS radars over ESR.

3.2.6 *The IMAGE Magnetometer Network*

The International Monitor for Auroral Geomagnetic Effects (IMAGE) magnetometer network launched with the aim of studying auroral electrojets consist of 35 magnetometer stations, covering latitudes between 54 to 79˚. The ionosphere above Svalbard, where the ESR radar is located is under the field of view (FOV) of IMAGE network coverage, and it presents a localised data rather than the global average from other networks. The X-component of the IMAGE magnetometer data is employed in this study and it measures the northward perturbation of the Earth's magnetic field. A positive value of the X-component indicates that the magnetic field is pointing in the northward direction, while its negative value implies a depletion (southward pointing).

3.3. Spacecraft Instruments

The Fast Auroral SnapshoT (FAST) spacecraft and the Advanced Composition Explorer (ACE) discussed below are the in situ spacecraft instruments explored in the study.

3.3.1 The Fast Auroral SnapshoT (FAST) Satellite

The Fast Auroral SnapshoT (FAST) satellite shown in Figure 3.8 is one of the Small Explorer (SMEX) missions by National Aeronautics Space Agency (NASA; Baker et al., 1991; Harvey et al., 2001). The multiplex spacecraft was configured to take high resolution in situ measurements above the Earth's auroral regions. The FAST spacecraft measures the acceleration of particles and takes readings that would assist in the understanding of the auroral processes. It completed a revolution in about 2¼ hours, with an apogee altitude of a little above 4000 km, it was able to venture high into the territory of the particles that create the aurora (Pfaff et al., 2001; Ergun, 2001; Carlson et al., 2001). The FAST spacecraft was put into orbit on 21st August, 1996, at a respective apogee and perigee of 4175 km and 350 km.

The spacecraft database has assisted scientists in reviewing theories about the nature of Earth's auroral. The FAST mission has helped in addressing key questions on the mechanisms responsible for particle acceleration, auroral formation, pitch-angle distribution of energetic auroral particles, and associated processes relating to the suprathermal energetic upflowing ions from the auroral ionosphere, which includes ion beams, ion conics and upwelling ions (Carlson et al., 1998; 2001; Pfaff et al., 2001).

It is worthy of note that FAST normal operations ended on May 1st, 2009, so, FAST is no longer gathering routine data (University of California, Berkeley, 2017).

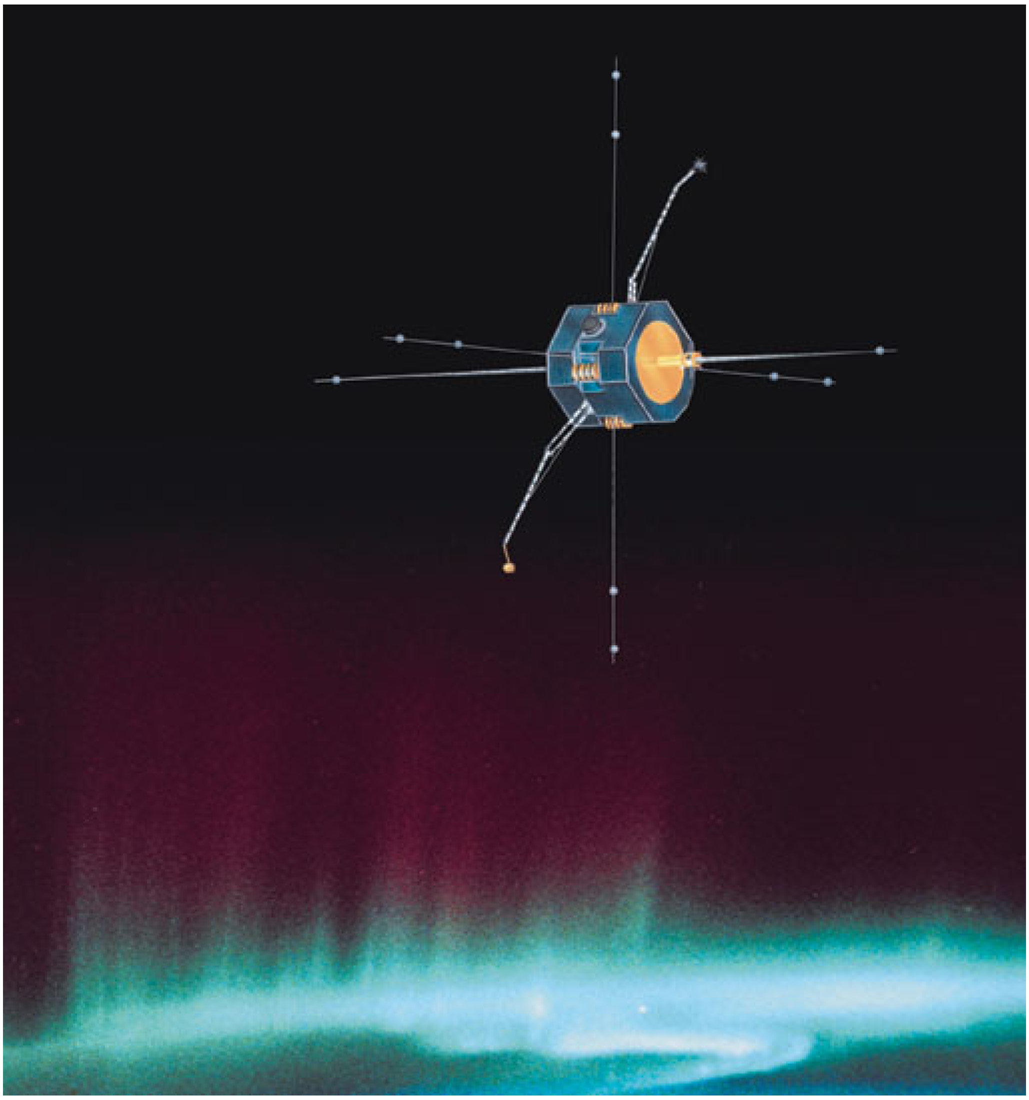

Figure 3.8: The Fast Auroral SnapshoT (FAST) satellite. From NASA, 2015b.

3.3.2 The Advanced Composition Explorer (ACE)

The Advanced Composition Explorer (ACE) is another mission embarked upon by NASA in order to study energetic particles of sun, interstellar and galactic origins. In 1997, the spacecraft was placed into orbit around the L1 Lagrangian point where it can remain at equilibrium with respect to both the Sun and Earth's gravity. The L1 location (about a ratio of 1 to 99 of the astronomical unit in the Earth-Sun distance) assists the ACE to have a prime view of the solar wind plasma parameters and also of accelerated particles in the interstellar medium. The solar wind upstream data monitored by the ACE spacecraft are delayed by a time appropriate to the solar wind speed and the distance between the spacecraft and the Earth to indicate the conditions at the magnetopause in the same time frame as the other data to be discussed in this study. The time delay has been taken care of in the OMNIweb database. High resolution OMNI data set of solar wind plasma parameters at the bow shock region of the Earth, and also of energetic proton fluxes were employed in this study.

3.4. Data Sources

The data for the work in this thesis are both ground-based and satellite origins. Data from each source are summarized below.

3.4.1 Ground-based data source

The four basic ionospheric parameters, namely electron density, electron and ion temperatures, and the field-aligned ion velocity are from the ESR 42 m dish while the line-of-sight velocity of the plasma along the meridian is sourced from beams 5 and 9 of the Iceland and Finland CUTLASS radars respectively. Data for local magnetic perturbation around Svalbard peninsula are obtained from IMAGE magnetometer network array while the global average geomagnetic activity indices are obtained from SuperMAG (SML and SMU) and OMNIweb (AL, AU and Sym-H) database. The lower and upper auroral electrojet indices (AL and AU), obtained from the OMNIweb database, are the equivalent version of the SML and SMU explained under section 3.2.5. In contrast to the SuperMAG indices, the AL and AU are averaged from a fewer number of magnetometers in comparison to the SML and SMU. The ring current index (Sym-H) is the high resolution version of the mean values (compared to Dst, an hourly average) of the northward horizontal H-component of the Earth's magnetic field obtained at low-latitude observatories. Since the ring current is westward, it most often causes a depletion of the Earth's dipole field. The Sym-H evaluates the amount of energy injected into the ring current during a geomagnetic storm (Baumjohann and Treumann, 1997).

3.4.2 Spacecraft-based data source

In this thesis, for one study the FAST spacecraft measurements when ESR observed ion upflow at the time the FAST satellite simultaneously detected ion outflow are investigated. Also solar wind plasma parameters, namely the solar wind speed, v_{sw}, the solar wind number density, n_{sw}, the solar wind pressure, P_{sw}, and the IMF components, B_x, B_y and B_z, are obtained from measurements by the ACE.

CHAPTER 4

A study of observations of Ionospheric upwelling made by the EISCAT Svalbard Radar during the International Polar Year campaign of 2007

4.1. Introduction

In Chapter 2, I have discussed the significance of the ionospheric heavy ions in moderating the solar wind-magnetosphere-ionosphere dynamics. The main aim of this chapter is to investigate the diurnal and seasonal variability of the ion flux at various levels of geomagnetic activity (determined by the *Kp* index), as observed at E and F region altitudes by the EISCAT Svalbard Radar (ESR), an Incoherent Scatter Radar (ISR) operated by the European Incoherent Scatter Scientific Association, in order to make contributions to the knowledge of upwelling ions from the Earth's upper atmosphere. In this study, I restrict my attention to events with ion fluxes above a threshold of $10^{13}\ \mathrm{m}^{-2}\ \mathrm{s}^{-1}$ which have the potential to become an outflow (Wahlund and Opgenoorth, 1989; Wahlund et al., 1992). The data set comprises the results obtained by the ESR during the Third International Polar Year (IPY) campaign. This campaign ran from 2007 to 2009, during which time the ESR 42 m dish was run continuously for about 300 days, measuring 312,444 field-aligned plasma parameter profiles from March 2007 to February 2008, during a period of deep solar minimum. This period is shown in Figure 4.1, where I plot the time series of the daily total (black line) and yearly smoothed (red line) sunspot numbers. The interval studied here is indicated by the pair of vertical dashed lines. It can be seen that the period of the IPY 2007 campaign corresponds to solar minimum conditions, with yearly smoothed sunspot numbers of 18 for 2007 and 5 for 2008.

Below, the source of data and the filtering technique employed to separate the real signal from noise will be discussed. Then I will discuss the analysis of upflow and downflow as a function of *Kp* index, followed by an analysis of seasonal occurrence.

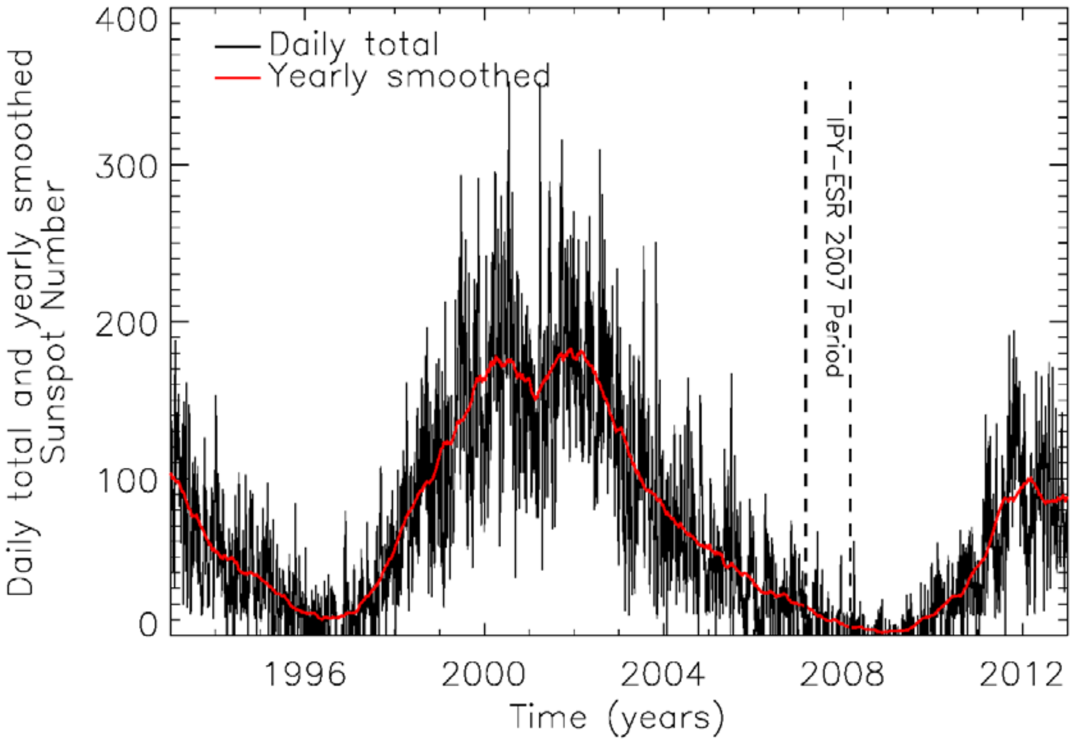

Figure 4.1: Plot showing the time series of the daily total (black line) and yearly smoothed (red line) sunspot number.

4.2. Data source and criteria for data selection

4.2.1 Source of Data

The primary source of data for this study is the ESR 42 m diameter dish, which has a fixed and field-aligned antenna, measuring the ion drift velocity along the local geomagnetic field line. The data is contained and extracted from an online database called Madrigal containing all the ESR-IPY data.

The IPY 2007 provided a long campaign of data measurements, which allowed us to perform a statistical analysis over a long-term of ionospheric variations. During the campaign, data were recorded for 81% of the 366 days, while measurements are available for about 70% of the 8784 hours. November and December 2007 suffered many data gaps due to operational problems (Vlasov et al., 2011).

4.2.2 Data Filtering

To distinguish between good data (real signal) and measurements adversely affected by noise, I formulated some criteria which are incorporated into a routine code, in addition to the quality flag embedded in the data set from the Madrigal database, to filter the data as follows:

a) The flux at an altitude immediately below or above an observation point in the vertical profile of any time resolution must not change by a factor greater than 10;

b) The minute corresponding to the geodetic altitude before and after the point being observed must satisfy the condition in (a) above;

c) The fitted geodetic altitude of an observation point must be at least 100 km;

d) The 0.05% of the data extending beyond 470 km have been expunged because the signal to noise ratio drops dramatically; Vlasov et al. (2011) set a cut-off of 450 km when studying travelling ionospheric disturbances for the same set of data.

The unfiltered data contains sporadic, unphysical velocity values in excess of $10\ \mathrm{km\ s^{-1}}$, which is in contrast to existing literature (Jones et al., 1988; Winser et al., 1988; Wahlund and Opgenoorth, 1989; Blelly et al., 1996) that set the ion drift velocity of the upwelling ions below a thousand meters per second ($v_i < 1000\ \mathrm{m\ s^{-1}}$). The incorporation of the filter described above, removed single noisy data points and 99.8% conform to the required result. Previous studies in the field chose the ion velocity as the basis for the filter, but in this work, I have chosen the ion flux because in a steady state it is a conserved quantity along the flux tube. Alternatively the ratio of the ion flux to the magnetic field strength is constant in a steady state.

$$f_{ion} \times A = constant \tag{4.1}$$

$$\frac{f_{ion}}{B} = constant \tag{4.2}$$

where A is the cross sectional area of the flux tube in the ionosphere,
B is the field strength, and
f_{ion} is the ion flux.

Following the assumption that quasi-neutrality holds for ionospheric plasma ($n_i \approx n_e$), the ion flux is calculated from the ESR data using equation (4.3) and any observation by the ESR that satisfies the conditions set out in the filter above is taken as a valid data point.

$$f_{ion} = n_e \times v_i \tag{4.3}$$

Ion upflow has been defined as a flux with a minimum threshold of 10^{13} m^{-2} s^{-1} (Wahlund and Opgenoorth, 1989; Keating et al., 1990; Foster et al., 1998) and in addition, a field-aligned velocity > 500 m s^{-1} could make it have the potential of becoming an outflow (Wahlund and Opgenoorth, 1989). A filter that constrained negative values and fluxes below 10^{13} m^{-2} s^{-1} is imposed on the flux and the result is further classified as presented in Table 4.1 below. Any data point that satisfies the threshold is regarded as an event and this may be more than one data point of geophysical observation along field-aligned profiles. There are 32 data points in a vertical profile and the average number of data points for each unique time covers the D, E and F regions at an average ratio of 2:5:9 respectively. A total of 1,832,559 and 93,793 data points and event points are obtained respectively after filtering. It is worth to note that uncertainties are negligible in this study.

Table 4.1: The classifications of ion upflow flux.

	Ion Flux	**Class interval**
i.	Low	1.0×10^{13} m^{-2} s^{-1} $\le f_{ion} <$ 2.5×10^{13} m^{-2} s^{-1}
ii.	Medium	2.5×10^{13} m^{-2} s^{-1} $\le f_{ion} <$ 7.5×10^{13} m^{-2} s^{-1}
iii.	High	$f_{ion} \ge 7.5 \times 10^{13}$ m^{-2} s^{-1}

4.3. Results and Discussion

Figure 4.2 shows a scatter plot of the local time (LT) dependence of flux over all our observations and the frequency of upflow in each category shown in Table 4.1. The local time is used throughout this study in order to underscore the cusp and midnight events at the ESR location. The Figure shows the scatter plot of the ion fluxes, which is colour coded as black, blue and red representing the class categories from low to high flux in Table 4.1 respectively. It appears that all categories of flux are general LT phenomenon. The density increases at noon and there is a prominent dip mainly around 16:00 – 20:00 LT. The high flux is clearly indicated in Table 4.2 to be a rare occurrence while the low class is a frequent phenomenon. About 88% of the upflow flux are in-between $1.0 \times 10^{13}\ \mathrm{m}^{-2}\ \mathrm{s}^{-1}$ and $2.5 \times 10^{13}\ \mathrm{m}^{-2}\ \mathrm{s}^{-1}$, while the remaining ~12% is shared between the medium and high fluxes at about ratio 9:1 respectively.

Figure 4.3 shows an event commencing at 22:00 LT on March 15, 2007, which is a typical example of an ESR parameter plot during the IPY-ESR campaign. The five panels shown in Figure 4.3 are electron density, electron temperature, ion temperature, ion drift velocity and the ion flux respectively. The plot begins with a weak typical night time electron density in the E region (below 150 km) from 22:00 LT until around 23:20 LT. However, immediately after this time, an intermittent intense electron precipitation down to the E region occurs until around midnight. At the same time, an enhancement of T_e follows from the electron precipitation, which would lead to the creation of an ambipolar electric field, setting up an increase in the ion scale height and ion upwelling as a result. Though intermittently elevated ion temperatures are indicated in the third panel, the electron temperature appears to be the dominant driver of the upwelling ion flux in the fifth panel. The peak upwelling ion flux in the class intervals around this period of 23:20 LT until midnight is the high category, where $f_{ion} \geq 7.5 \times 10^{13}\ \mathrm{m}^{-2}\ \mathrm{s}^{-1}$, and it occurs at altitudes from above 200 km. However, between 23:35 – 23:40 LT, the ion flux is predominantly below the threshold and this corresponds to weak electron density and ion drift velocity at this time in panels one and four respectively. The event is associated with moderate substorm from OMNI data analysis of the upper and lower electrojets during the period.

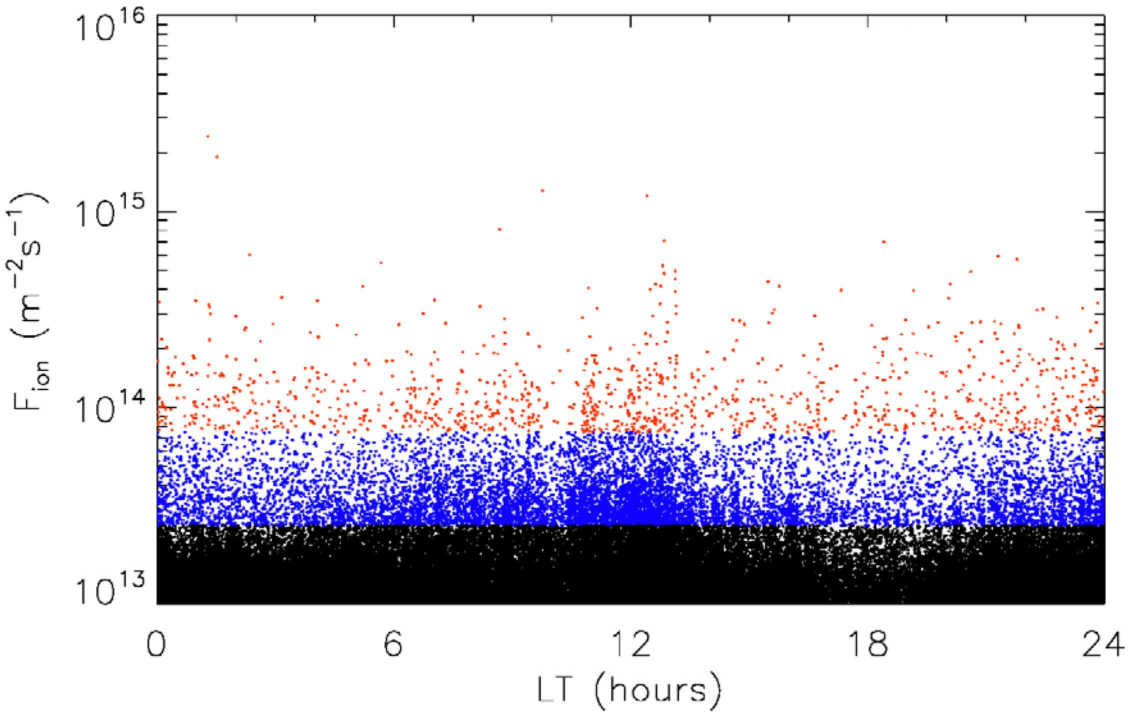

Figure 4.2: Plot showing the scatter plot of the ion flux. Black, blue and red indicate the low, medium and high upflow flux in Table 4.1 respectively.

Table 4.2: The frequency of the ion flux categories

	Ion Flux	**Class frequency (%)**
i.	Low	88.3
ii.	Medium	10.5
iii.	High	1.2

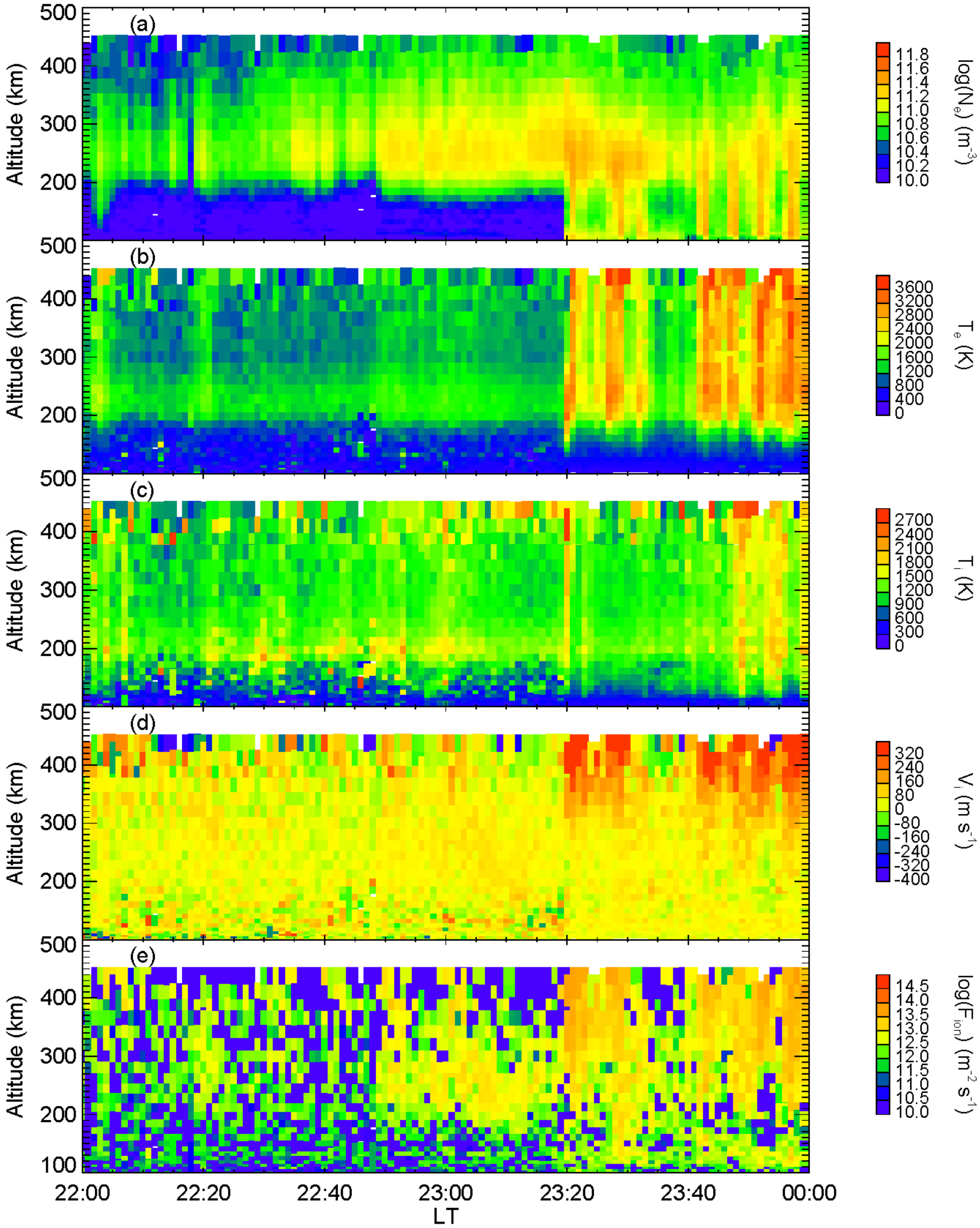

Figure 4.3: Plot showing a typical example of ESR parameter plot for the 42 m dish during the IPY-ESR campaign from 22:00 - 00:00 LT on 15th March, 2007: The five panels are (a) electron density, (b) electron temperature, (c) ion temperature, (d) ion drift velocity, and (e) the ion flux respectively.

Figure 4.4 shows the flux distribution observed by the EISCAT Svalbard Radar during the IPY-ESR 2007 campaign with respect to local time (2 hours ahead of UT) at Longyearbyen for all data. Figure 4.4a shows the total number of data points observed by the radar per hour throughout the period under observation during the campaign, while Figure 4.4b shows the number of event points (showing upward flux) per hour during the same period. Figure 4.4c is the percentage ratio of panel (b) to panel (a) of Figure 4.4. The percentage occurrence of the upflow shows a distinct maximum around local noon which appears consistent with the observational report by Ogawa et al. (2009). However, the occurrence level is lesser in magnitude (about three quarters) compared to their previous work, which could be as a result of the period under present observation study – deep solar minimum. Furthermore overall outgoing ion flux is observed for 2 – 13% of the time in comparison to about 3 – 17% they observed during a complete solar cycle.

4.3.1 Kp Index Analysis of Upflow

Figure 4.5 indicates the local time (LT) distribution of upflow flux in conjunction with the Kp index, a measure of geomagnetic activity, where $Kp < 2$, $2 \leq Kp < 4$, and $Kp \geq 4$ denote low, medium and high disturbance respectively in this study. Panels a to c of Figure 4.5 show the number of events in each local time interval throughout the period under investigation for low, medium and high categories of flux in Table 4.1 respectively. It is clear from Figure 4.5 that the number of upflow events for low flux is skewed to the nightside while the medium and high fluxes are central around local noon (albeit there is a small peak at noon for low flux). The low flux peaked between 21:00 – 22:00 LT (6200 events) while the medium and high classes peaked around noon (for 1050 and 105 events respectively). Furthermore, it can be seen in Figure 4.5 that high disturbance events are predominantly in the pre-noon sector especially for the medium and high flux categories.

Figure 4.6 indicates the percentage occurrence of the various classes of upflow in Table 4.1, and its relationship with the levels of geomagnetic disturbances. Panels (a), (b) and (c) of Figure 4.6 show the low, medium and high classes of flux in a respective order. Figure 4.6 is computed from the ratio of the event points in each LT bin with respect to the Kp index level and class, to the total number of data points at respective LT interval and magnetic conditions. In Figure 4.6, the geomagnetic conditions are also shown in green, amber and red colours for the low, medium and high Kp index respectively. In Figure 4.6a, where low flux upflow is investigated, the maximum occurrence is below 5% during low geomagnetic conditions ($Kp < 2$), and there is no obvious peak across the local time. However, when Kp is either medium or high, a distinct occurrence peak is conspicuous around local noon. The highly disturbed periods ($Kp \geq 4$) record a peak of about 31% while the maximum occurrence during medium disturbance ($2 \leq Kp < 4$) is ~23%. Another phenomenon that is observed in this class of flux is the dawn and nightside occurrence spikes, which occur during active geomagnetic periods between 5 - 6 LT and 21 - 22 LT. The medium flux is investigated in Figure 4.6b and analysis shows that the occurrence frequency increases in magnitude with respect to the level of disturbance as is also the case with the low flux. However, the occurrence magnitude for the medium flux is drastically reduced, with a peak of about 16 and 5 during high and medium Kp respectively, and negligible occurrence during low disturbance. Figure 4.6c is focused on influence of geomagnetic disturbances on high flux events, and just like the previous classes, its occurrence peak is observed around local noon, with low values indicating that it is a rare phenomenon. The occurrence peak during high disturbance is about 2%, while at other geomagnetic conditions are below 0.5%. A small enhancement in all three classes of flux event is observed during high Kp between 5 - 6 LT, indicating a possible pre-noon asymmetry. However, the peaks observed at the night sector of the low flux are not evident in the high and medium flux upflows. The occurrence peaks during high flux and high Kp index at dawn, noon and nighttime are 0.24%, 2.09% and 0.03% respectively, which is equivalent to a percentage ratio of about 10:89:1. Similarly, the low and medium classes have a respective ratio of 23:56:21 and 15:83:2. This indicates that most upflows in high and medium classes are concentrated around local noon. An inference from this is that the low flux could either be cusps or nightside aurora related, while the high and medium fluxes are predominantly cusps related.

The occurrence peaks in each of the classes of flux is between 10 - 11 LT for the high *Kp* while it occurs between 11 - 12 LT for the medium disturbance. The peak total occurrence during high disturbance, summing over the three classes of upflow events, is about 50%, which is almost double the peak total occurrence during medium *Kp*. This is in contrast to the data studied by Ogawa et al. (2009), where the occurrence peak during high disturbance is lower compared to periods of medium geomagnetic conditions. The difference in the pattern of the ion upflow occurrence at different levels of geomagnetic disturbances during the previous and present study could be as a result of the former being distributed well, over a whole solar cycle (700 days from 11 years; 97,000 field-aligned profiles) while the current study uses a near-continuous year-long dataset (300 days from one year; 312,444 field-aligned profiles) at solar minimum. Further observation reveals that as expected, the upflow occurrence across all LT is lower in the present study compared to previous studies that on average are more solar active. The only exception is the upflow occurrence around the cusp, which is greater by a factor of 2.5 in the present study during high geomagnetic activity ($Kp \geq 4$). The reason for this is yet unclear, but still open to future research whether the increase is as a result of the difference in selection method or is based on a different definition of high *Kp* used in the previous study.

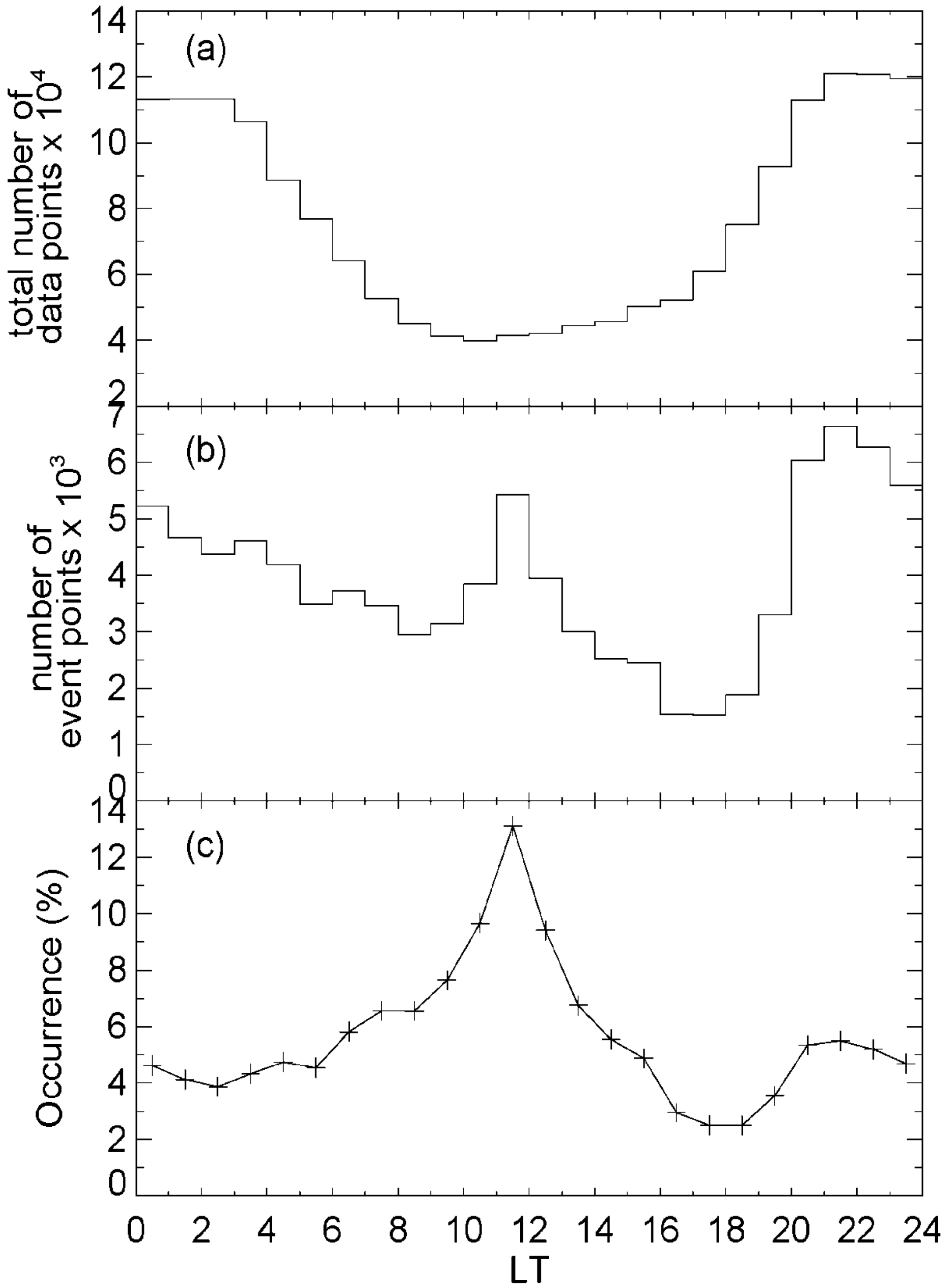

Figure 4.4: Plot showing the local time distribution of number of ion fluxes observed during the IPY-ESR 2007 campaign: (a) all data points observed by the radar during the period under investigation, (b) events points – data points that satisfy the threshold of $1.0 \times 10^{13}\ \mathrm{m}^{-2}\ \mathrm{s}^{-1}$, and (c) percentage of flux that meet the required threshold, i.e., $(b)/(a)$.

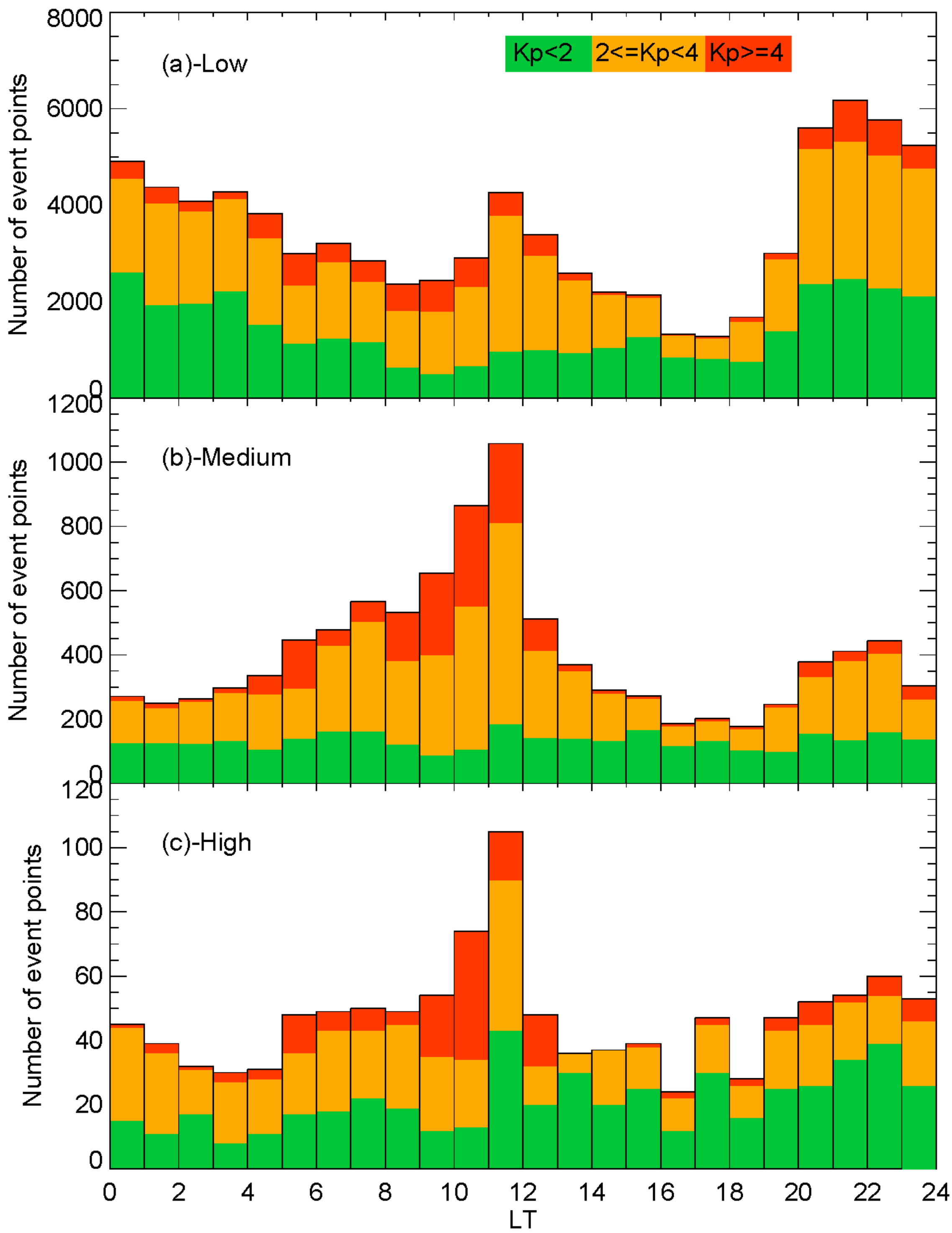

Figure 4.5: Plot showing the histogram of ion flux upflow observed for different levels of geomagnetic index (Kp), when flux is: (a) low, (b) medium, and (c) high. Red fill indicates $Kp \geq 4$, amber indicates $2 \leq Kp < 4$, while green shows plots for $Kp < 2$.

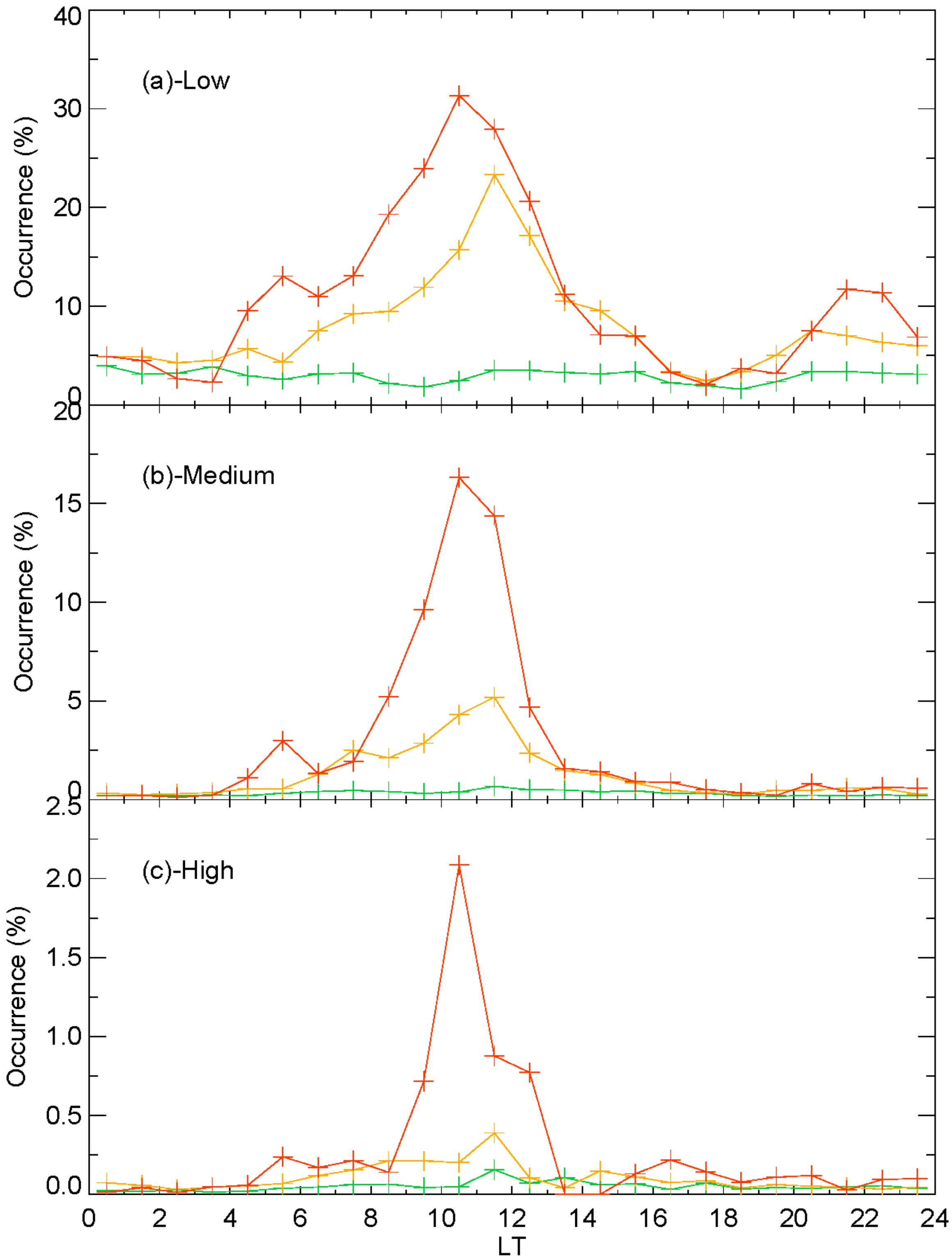

Figure 4.6: This shows the plot over the ESR local time for the upflow occurrence in each class in Table 1. This is the percentage ratio of events points to all data points in each local time bin with respect to Kp index level and class. Red line indicates $Kp \geq 4$, amber indicates $2 \leq Kp < 4$, while green shows plots for $Kp < 2$: (a) low flux occurrence, (b) medium flux occurrence, and (c) high flux occurrence.

4.3.2 Kp Index Analysis of Downflow

The upwelling ions, unless they have enough energy to escape, will ultimately experience a downflow due to gravity. In addition, particle precipitation during magnetic reconnection can lead to the injection of particles from either the cusp or nightside which can also add to the number of the downflow flux from ballistic return of upflows (Skjæveland et al., 2014). I have defined a downflow event in this study as one that in addition to satisfying the filtering conditions in section 2.2 also reaches a threshold of $|f_{ion}| \geq 10^{13}\ \mathrm{m^{-2}\ s^{-1}}$ arising from a negative (down-going) velocity. Figure 4.7 presents the downflow-upflow distribution for the IPY-ESR 2007 data. Figure 4.7a shows the velocity distribution of the flux magnitude where negative and positive values in the horizontal axis refer to the downward and upward motion of the ions indicated by the dashed and dotted lines as marked respectively. Some symmetry is seen in Figure 4.7a, but it is clear that the number of upflow begins to dominate slightly above $|f_{ion}| \geq 10^{13}\ \mathrm{m^{-2}\ s^{-1}}$ which agree with previous studies (Endo et al., 2000; Ogawa et al., 2009) on the point that upflow events are more commonly observed than downflows. It can also be seen that close to $|f_{ion}| = 10^{15}\ \mathrm{m^{-2}\ s^{-1}}$, a few scattered downflows are observed more than the upflows. One explanation to this is that those could be due to precipitation from particle injection from the either cusp or nightside. Panel (b) of Figure 4.7 presents the occurrence of downflow flux which is computed from the ratio of the downflow event points in each LT interval with respect to the *Kp* index level, to the total number of data points at respective LT interval in conjunction with the same *Kp* index range. The green, amber and red colours show the low, medium and high geomagnetic conditions in a respective order. Figure 4.7b shows predominantly that there is not much clear change in the downflow occurrence with respect to increase in disturbance level before noon and after dusk. However, between 13 – 18 LT, a clear *Kp* dependence is observed where downflow occurrence increases with increasing disturbance level. The downflow occurrence per local time bin on average is 1.34%, 1.39% and 1.55% respectively for the low, medium and high disturbance level.

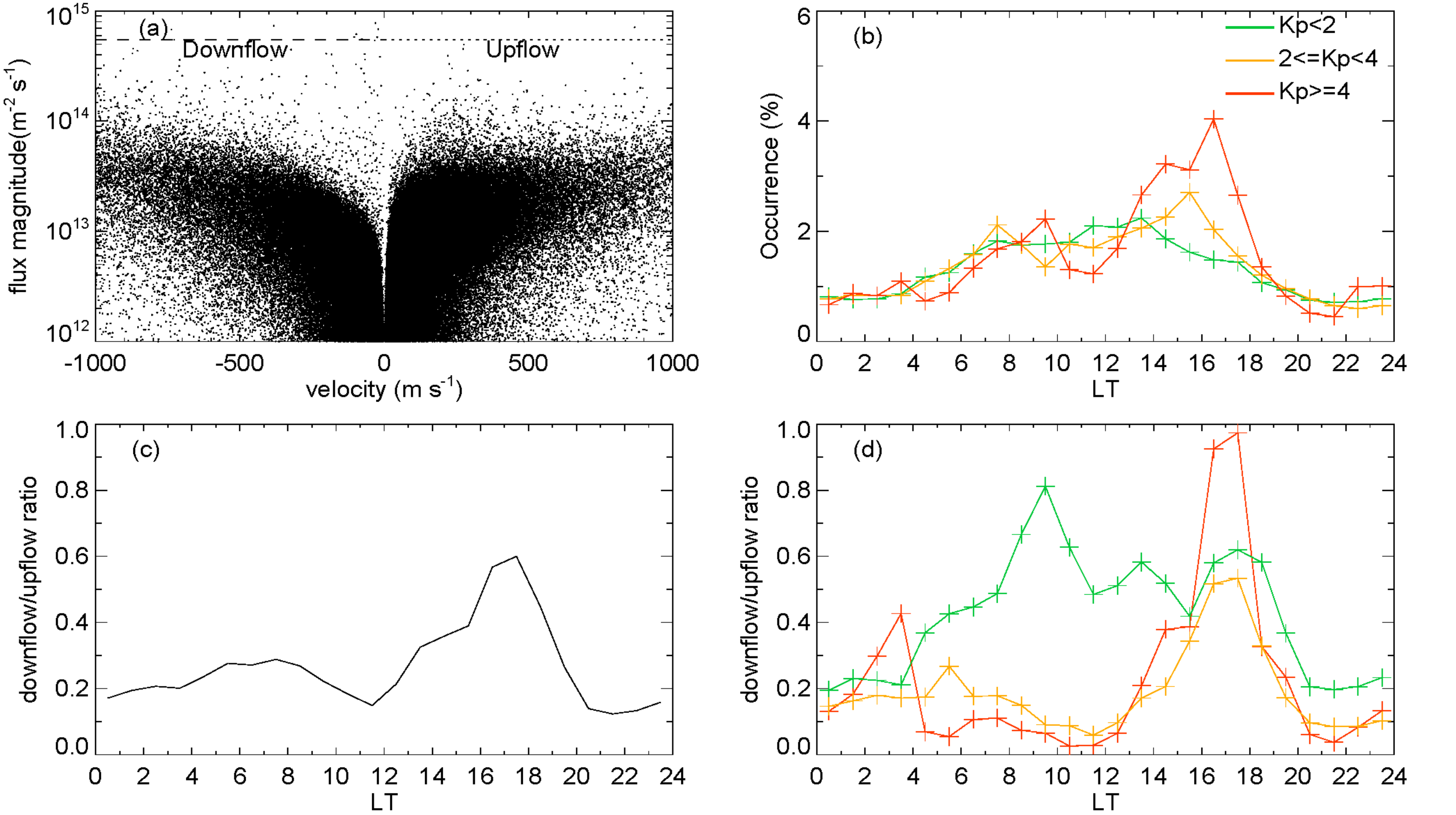

Figure 4.7: Plot showing (a) velocity distribution of ion flux (b) local time variation of ion downflow occurrence, when: (i) $Kp < 2$ – green line, (ii) $2 \leq Kp < 4$ – amber line and (iii) $Kp \geq 4$ – red line (c) local time variation of total downflow-upflow ratio and (d) hourly variation of ion downflow-upflow ratio, when: (i) $Kp < 2$ – green line, (ii) $2 \leq Kp < 4$ – amber line and (iii) $Kp \geq 4$ – red line.

It is also seen that a flip in Kp dependence is noticed around the cusp between 10 – 13 LT. This inverse relationship between downflow occurrence and Kp levels at these periods is precisely the interval in which it has already been shown that greater magnetic activity tends to increase the number of ion upflow events (Figure 4.6). In Panel (c) of Figure 4.7, local time distribution of the ratio of the total number of downflow to upflow for $|f_{ion}| \geq 10^{13}\ \mathrm{m}^{-2}\ \mathrm{s}^{-1}$ shown in panel (a) is presented. It can be seen that the general trend observed in the 2007 extreme solar minimum data shows that the ratio of downflow to upflow occurrence has a peak of about 60% (Figure 4.7c). This agrees with previous studies conducted during periods of higher solar activities (Endo et al., 2000; Ogawa et al., 2009) that showed that the ratio is predominantly less than 1 across all LTs. Minimum points are observed at dawn, local noon and local midnight which, are periods corresponding to increase upflow incidence in Figure 4.6a (representing about 88% of the upflow). Figure 4.7d shows the downflow-upflow ratio, split into different *Kp* levels, where the geomagnetic disturbances are shown in green, amber and red colours for the low, medium and high *Kp* index respectively. It is also clear that the downflow-upflow ratio for all levels of *Kp* is less than 1 across all LTs. However, downflow-upflow ratio due to low *Kp* predominantly dominate across all LTs except between 2 – 4 LT and 16 – 18 LT where the ratio due to high *Kp* dominates. A sharp increase in downflow-upflow ratio is seen in the pre-midnight sector when the geomagnetic disturbance level is high at which point the upflow and downflow flux almost balanced out. This may be explained as period of intense particle precipitation being injected from the nightside (during substorms) coupled with the downflow due to Earth's gravitational pull. The downflow-upflow ratio with respect to geomagnetic disturbances seems not to be a linear relationship because on average over all LTs, the values are 42%, 19% and 22% with respective low, medium and high *Kp*. In general, just like the ion upflow, the downflow are also a perpetual LT phenomenon and can take place during quiet, moderate and active geomagnetic conditions. The downflow occurrence in Figure 4.7b is concurrent in trend with the study by Ogawa et al. (2009), showing that Kp dependence pattern is the same irrespective of solar activity, but of smaller magnitude before the formation of the ionosphere during low and medium *Kp* at solar minimum.

4.3.3 *Seasonal Analysis of Results*

Given its geographic location, there is obviously a very strong seasonal variation in the solar flux and ionisation rate above the EISCAT Svalbard Radar. This might intuitively be expected to lead to a seasonal variation in ion upflow events, due to the modulation of electron density. In searching for such a seasonal variation, however, we must take into account the fact that the radar data are often of lower quality during the winter months, due to low Signal to Noise ratio; hence a smaller fraction of the ESR data satisfies the filtering criteria which we specified earlier.

Panels a-d of Figure 4.8 show the seasonal variability in the scatter plots of the upflowing ion flux with respect to season, with the low, medium and high fluxes respectively coded in black, blue and red. The flux of upwelling ions from the ionosphere for the summer and winter periods of the IPY 2007, as observed using the ESR, indicates that clear seasonal dependencies are apparent. Local time variation is observed to be higher in the summer months than in winter. A general LT phenomenon with small variation is observed in the ion upflow in winter while summer shows a dawn-to-noon (06 – 14 LT) predominance for the high and medium classes and postdusk-to-dawn (20 – 08 LT) for the low flux. Lower occurrence of fluxes around 16:00 – 20:00 LT is also a seasonal phenomenon however; it is less pronounced in winter but higher in autumn than in other seasons.

Table 4.3 indicates the seasonal frequency in each of the classes of the ion upflow. The highest frequency for the low flux occurs in summer (~94%), followed by spring (~89%), while winter leads the medium and high fluxes with respective ~24% and ~5%, followed by autumn which is about half and fifth in winter respectively. The occurrence of the flux in winter for the medium and high fluxes is about 4 and 9 times higher respectively than the one in summer. This could partly be due to the smaller dataset in winter compared to summer as shown in Figure 4.9, as a consequence of reduced solar activity due to large zenith angle and hence, low background electron content and less plasma ionosphere (Vlasov et al., 2011). I can conclude from Table 4.3 that the most often observed class of the ion upflow flux across all seasons is the low flux.

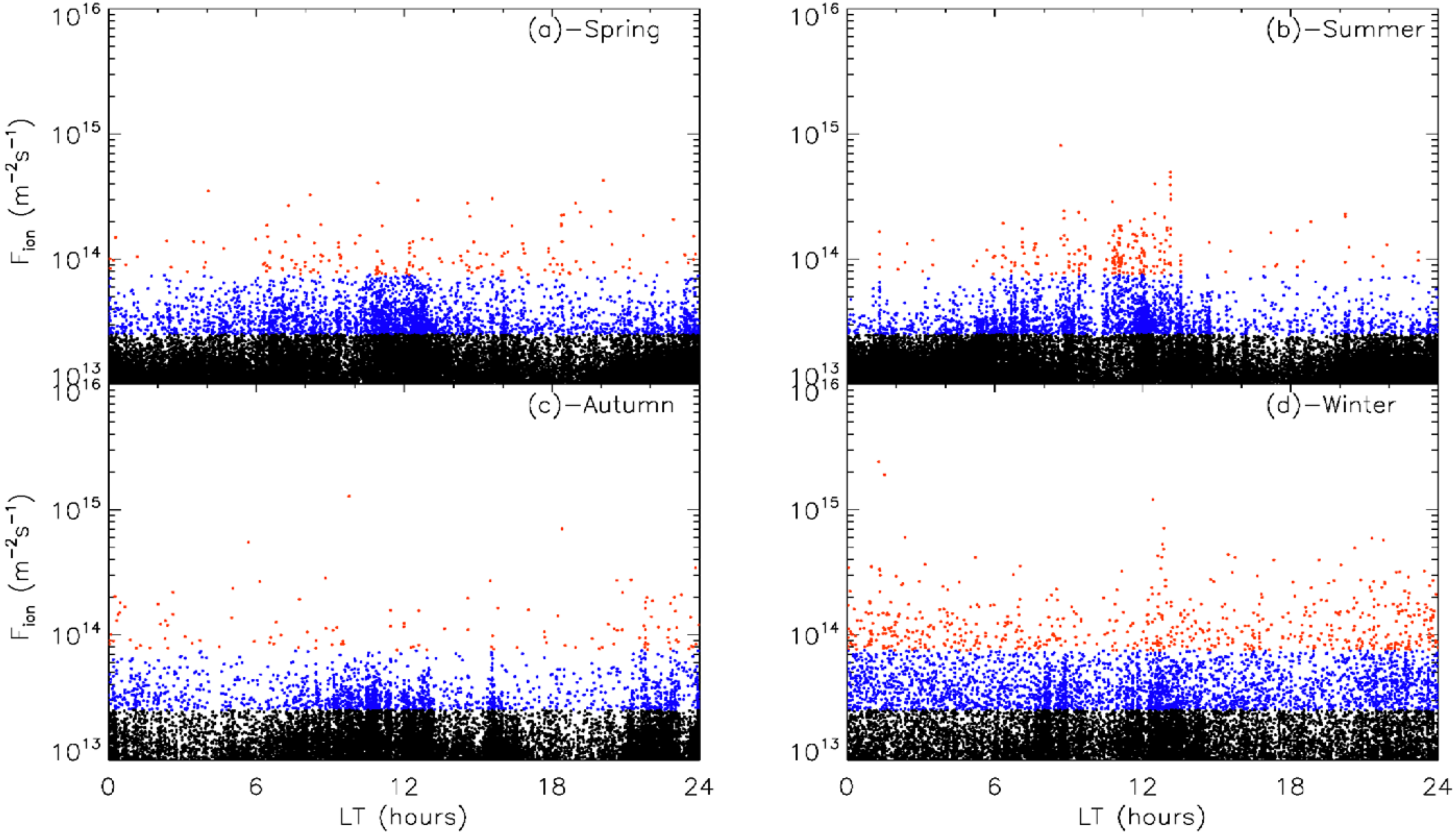

Figure 4.8: Plot showing the scatter plot for the seasonal ion upflow classification. Panels a-d represent the spring, summer autumn and winter respectively, and the colour format is the same as outlined in Figure 4.2.

Table 4.3: The seasonal frequency of ion flux categories

	Ion Flux	Class frequency (%)			
		spring	**summer**	**autumn**	**winter**
i.	Low	88.86	93.63	86.76	71.32
ii.	Medium	10.50	5.83	12.32	23.77
iii.	High	0.64	0.54	0.92	4.91

Figure 4.9 shows the number of data points observed in each local time bin during the four seasons of the IPY-ESR 2007 campaign, where I plot the local time distribution for all Kp data (black line), $Kp < 2$ (green line), $2 \leq Kp < 4$ (amber) and $Kp \geq 4$ (red line). It can be seen that the number of data points is greatest in summer then, spring, and observations are predominantly at the night sector.

Figures 4.10 – 4.12 show the local time distribution of the number of ion upflow events that satisfies the threshold value at different levels of Kp (low, medium and high) for each of the seasons. Figure 4.10 presents the low flux category, while Figures 4.11 and 4.12 present the medium and high classes respectively. In addition, the green, amber and red colours indicate low, medium and high disturbed conditions respectively, and panels (a) – (d) of the Figures represent the spring, summer, autumn and winter seasons respectively. It can be seen from the low flux in Figure 4.10 which is ~88% of the total events that more events are observed in summer and spring, which may be partly owing to larger total number of data points observed at the periods (Figure 4.9) or more solar flux and low zenith angle than in autumn and winter. However, any level of geomagnetic disturbance is observed to be appropriate to trigger the low class of upflow at any time of the seasons. Figure 4.11 indicates that the medium class of flux is well distributed across the seasons than any other class. It is also the only class of flux that shows a distribution with central peak across all seasons. The low flux almost depicts a central peak across the seasons except for summer. It is clear from Figure 4.12 that the high flux is a rare event with a peak less than 60, which is about a seventh of the medium class and a seventieth of the low flux, occurring and mostly driven by high geomagnetic disturbance around local noon in summer. It is also clear from Figure 4.12 that despite fewer data points in winter than in any other season (Figure 4.9), the overall number of high flux events occurs predominantly in winter. This may be connected with volume clutter in winter. Furthermore, Figure 4.12(d) shows that all levels of geomagnetic disturbances play an active role in ion upwelling during winter and the events occurs at all LTs. On the other hand, high disturbance events in all classes (Figure 4.10 − 4.12) are predominantly pre-noon to post-noon in summer and autumn while it is predominantly all local times event in spring, and post-noon to pre-noon in winter.

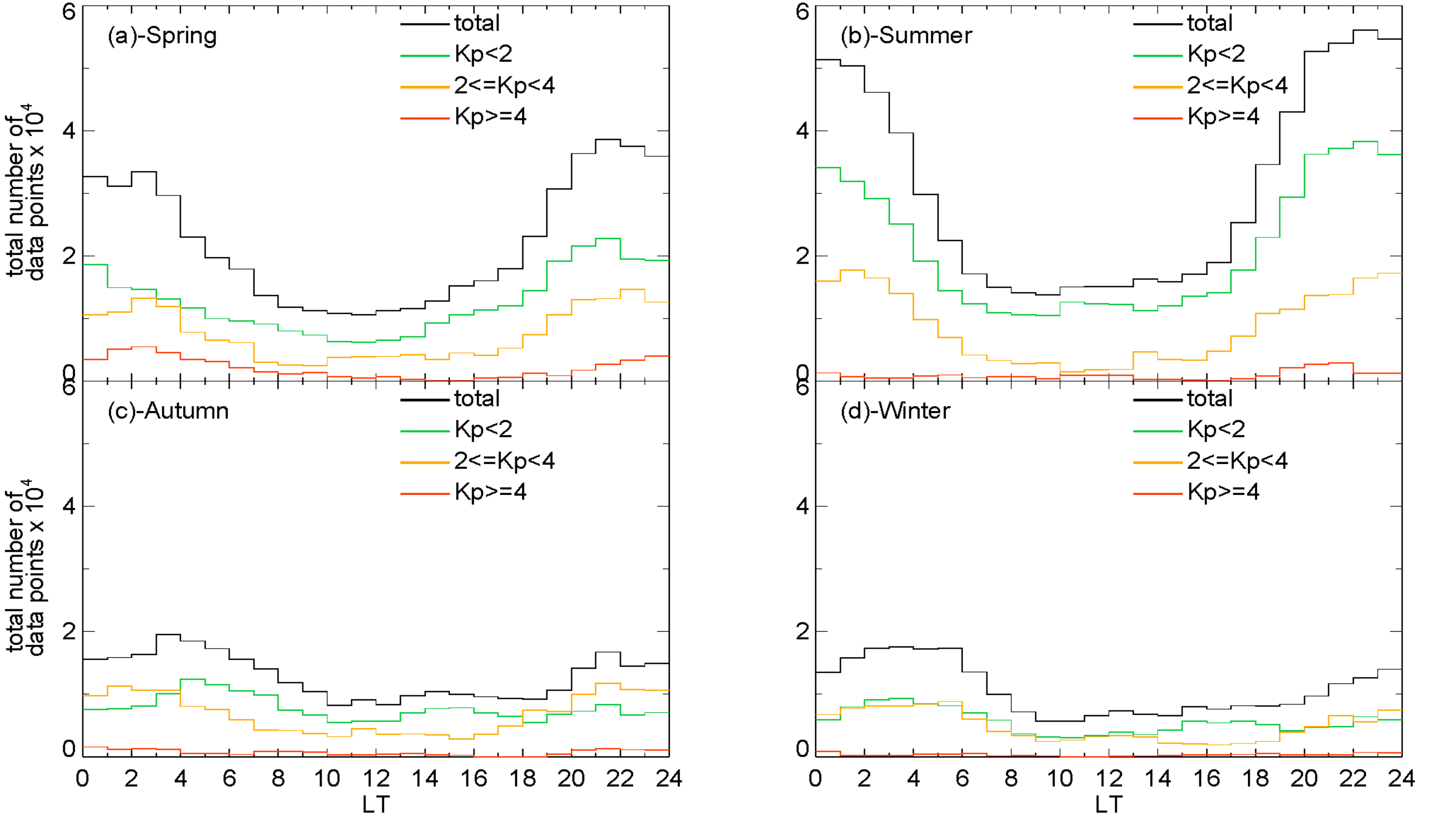

Figure 4.9: Plot showing the seasonal local time distribution of total number of data points observed by the radar for all *Kp* data (black line), low *Kp* (green line), medium *Kp* (amber line) and high *Kp* (red line) during (a) spring, (b) summer, (c) autumn, and (d) winter.

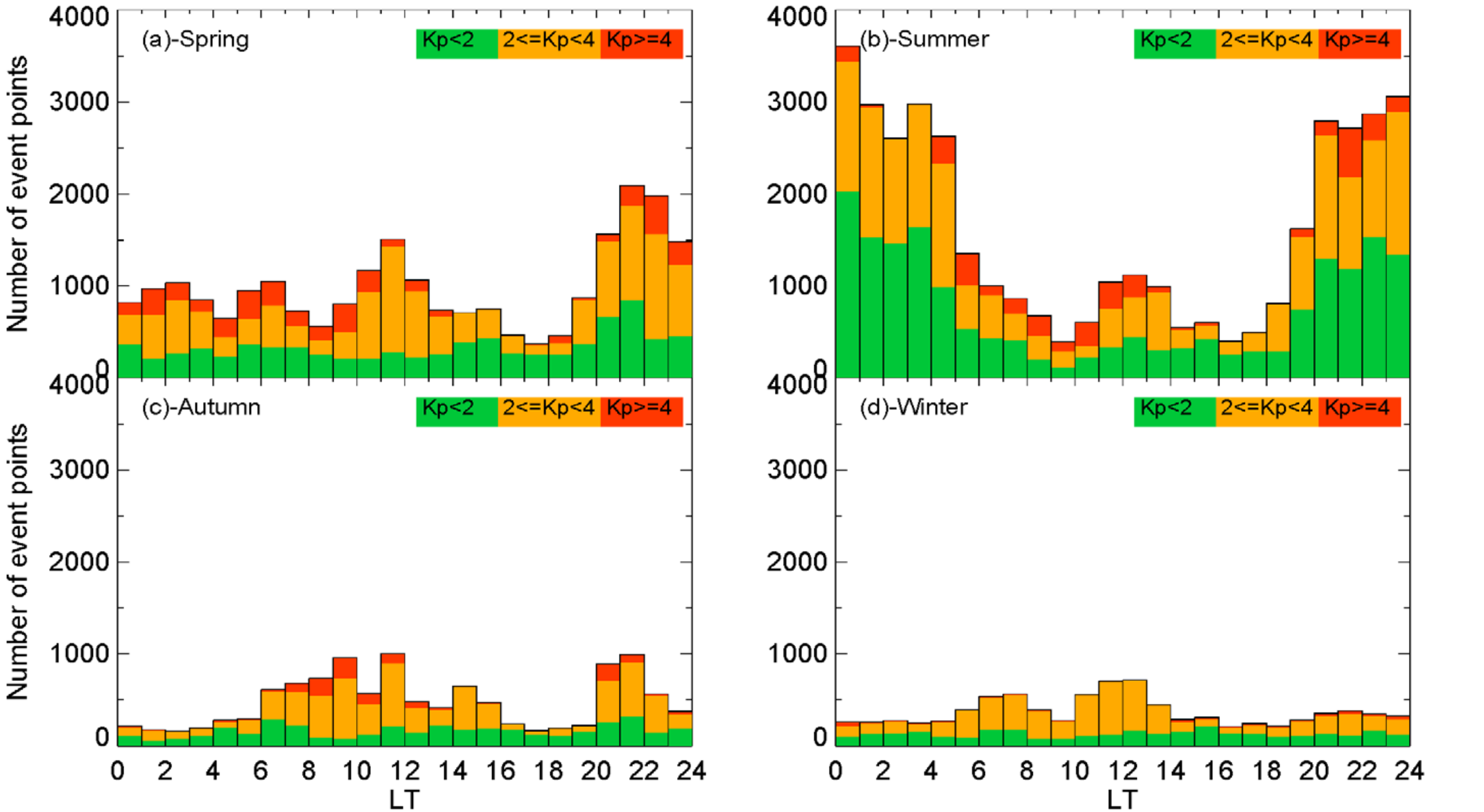

Figure 4.10: Plot showing the histogram of event points for low upflow flux observed for different levels of geomagnetic index, Kp during (a) spring, (b) summer, (c) autumn, and (d) winter. Red indicates $Kp \geq 4$, amber indicates $2 \leq Kp < 4$, while green shows plots for $Kp < 2$.

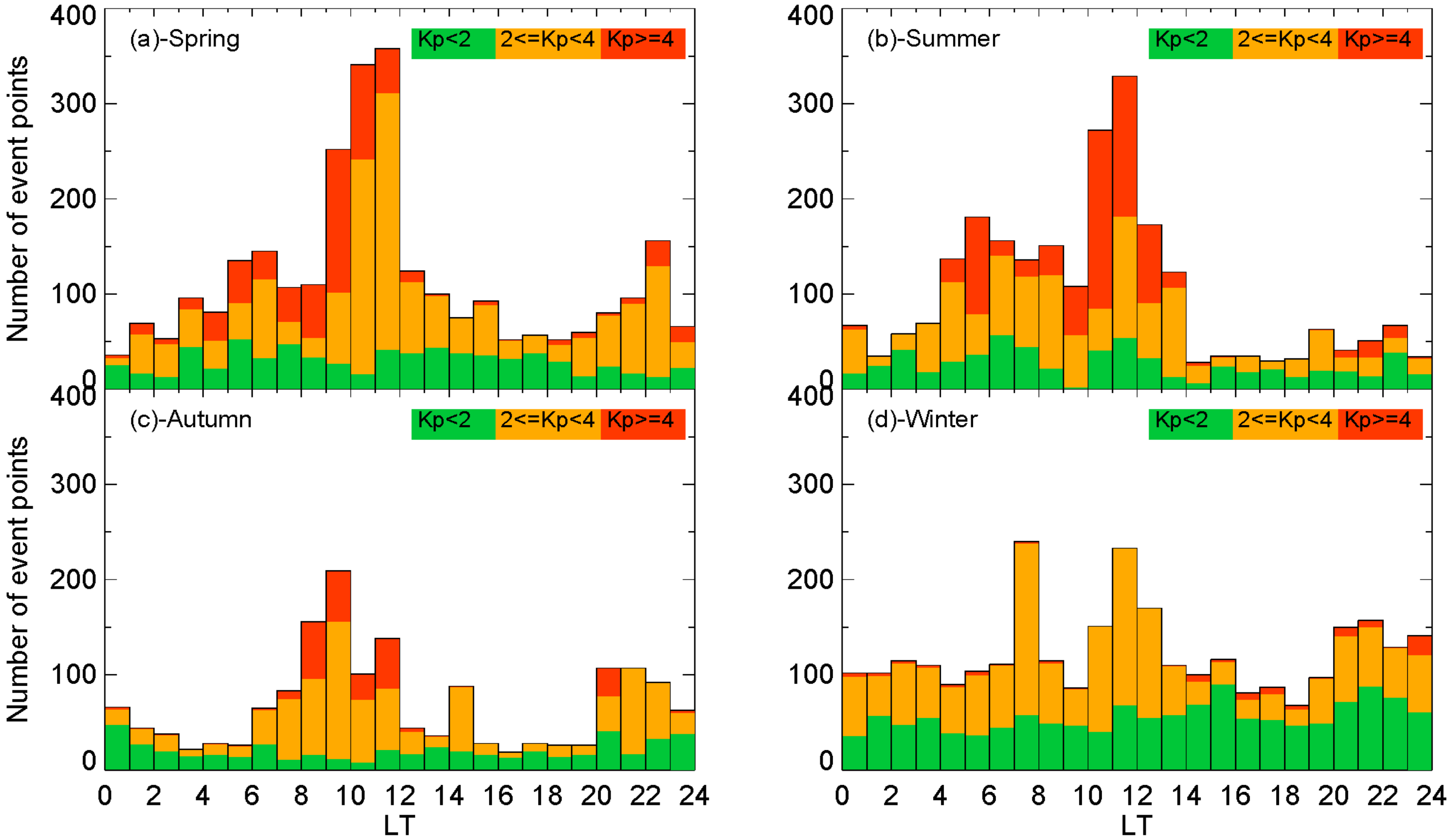

Figure 4.11: Plot showing the histogram of event points for medium upflow flux observed for different levels of geomagnetic index, *Kp*. The panel and colour format are the same as outlined in Figure 4.10.

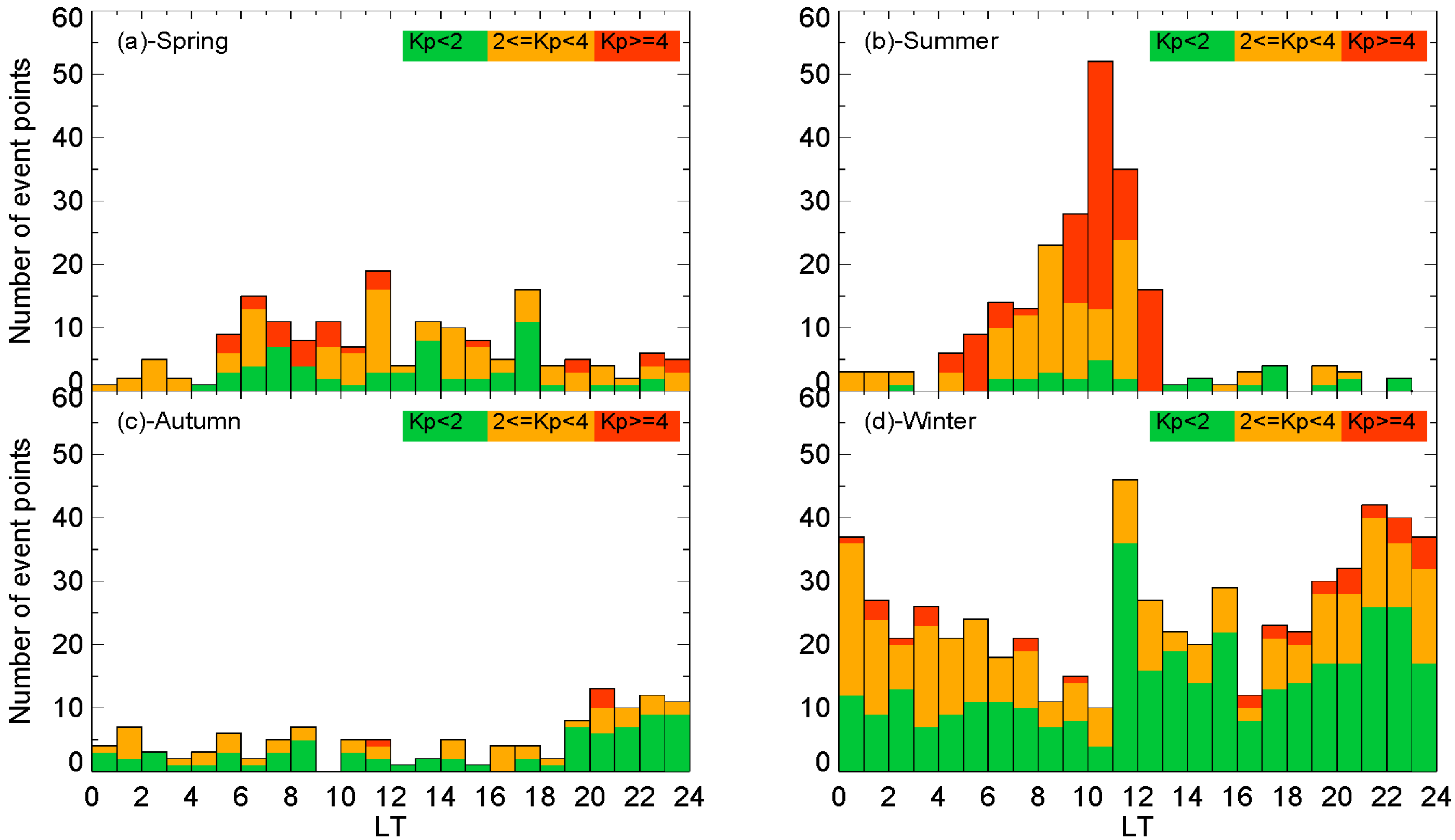

Figure 4.12: Plot showing the histogram of event points for high upflow flux observed for different levels of geomagnetic index, *Kp*. The panel and colour format are the same as outlined in Figure 4.10.

In Figures 4.13 − 4.15, seasonal occurrences of the upflow for the low, medium and high classes of flux are respectively shown. This is calculated as percentage ratio of the height of each colour in the colour coded histogram in each LT bin in Figures 4.10 − 4.12 with respect to the corresponding colour, LT and season in Figure 4.9. The panels (a-d) refer to the spring, summer, autumn and winter months respectively while red, amber and green colours indicate the respective high, medium and low geomagnetic conditions. Figure 4.13 shows the seasonal outlook of the upflow occurrence for low flux class. Analysis shows that during quiet conditions, there is no obvious occurrence peak across the seasons and local time. However, distinct occurrence maxima stand out in all the seasons when geomagnetic conditions are either medium or high. Higher occurrence is predominantly observed with high *Kp* around the cusp in all season except winter, which may be due to approximately less or no direct production in winter. It is also clear that the summer is highly spiky and dominates the occurrence frequency plot during high geomagnetic disturbance (Figure 4.13b). This could be related to the formation of the ionosphere for longer periods at summer and the degree of the drivers' strength. In addition, occurrence peaks that are mainly due to high *Kp*, are observed for the low class pre-midnight in all seasons –this could possibly be an effect associated with occurrence of nightside aurora. Figure 4.14 present the seasonal medium flux, and it can be seen that the occurrence frequency due to low *Kp* is insignificant except in winter where, though there is no obvious peak but, about 2% bump is noticeable around noon. It is also clear that occurrence frequency increases predominantly with an increase in disturbance level as in low flux, however, this is not definitive in winter of medium upflow. Moreover, unlike the broad peak due to high *Kp* in low flux at summer, all peaks in the medium upflow are distinct. Futhermore, the occurrence magnitude is lower in all season of the medium flux compared to the low flux class across all LTs and disturbance level. For example, the peak occurrence around local noon during high disturbance is between 35-40% in low flux, whereas, it has reduced to 13-22% in the medium class. The winter season is not included in the above range as it can been seen that high *Kp* upflow seldom occurs around local noon during the period. In Figure 4.15, the seasonal occurrence plot for the high flux is shown, and analysis reveals that the occurrence peak has dropped below 5 and 2.2% in summer and other seasons respectively, which implies that the phenomenon is rare across all seasons. The high upflow flux associated with low and medium disturbances in spring and autumn appears to be almost negligible while the ones associated with high disturbance also indicate predominantly a period of little or no occurrence except small intermittent bumps. The bumps around local noon and $19-21$ LT are below 1% and could be cusp or aurora related respectively. However, there are visible peaks for the high class of upflow occurrence by high Kp during summer and winter, and while the occurrence is from pre-noon till afternoon in summer, it is predominantly a pre-noon and post-noon phenomenon in winter. Furthermore, Figure 4.15 reveals that high geomagnetic disturbance is a sufficient condition for high flux occurrence in all seasons, however, a peak of about 1% can still be triggered in summer and winter by medium and low disturbance respectively.

In general, it is clear that upflow occurrence increases with an increase in geomagnetic activity, whereas, it decreases with the magnitude of the upflow flux. While, in general, all seasons contain examples of low, moderate and high geomagnetic activity across all local times, the winter observations are sufficiently sparse that some local time bins have no examples of high Kp conditions ($Kp \geq 4$). Hence the red traces in the wintertime (lower right) panels are not continuous.

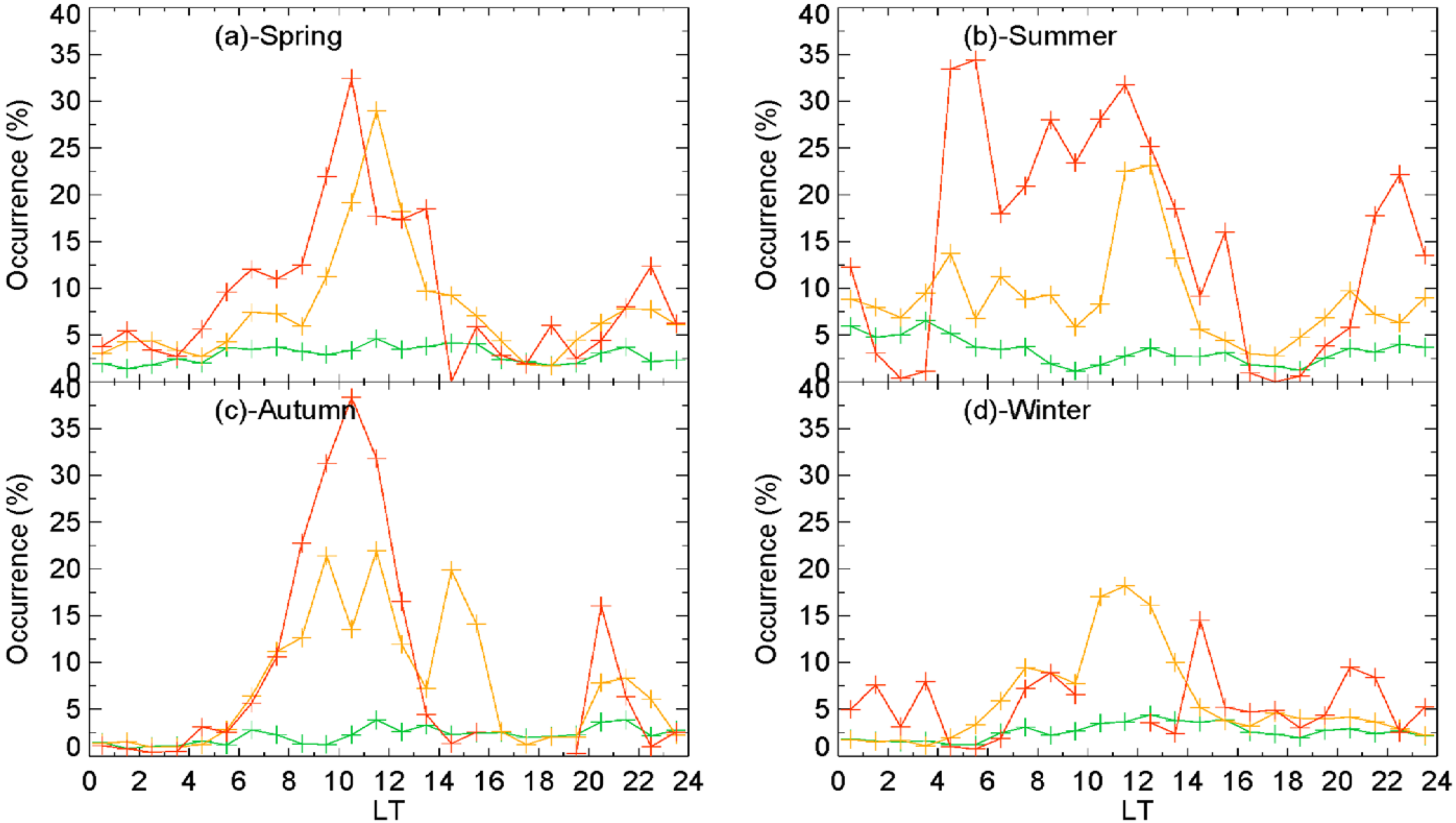

Figure 4.13: Plot showing the seasonal occurrences of the low upflow in Figure 4.10. This is the percentage ratio of Figure 4.10 to Figure 4.9 with respect to the corresponding colour, LT and season. Red line indicates $Kp \geq 4$, amber indicates $2 \leq Kp < 4$, while green shows plots for $Kp < 2$. Panels (a) – (d) represent the respective spring, summer, autumn and winter.

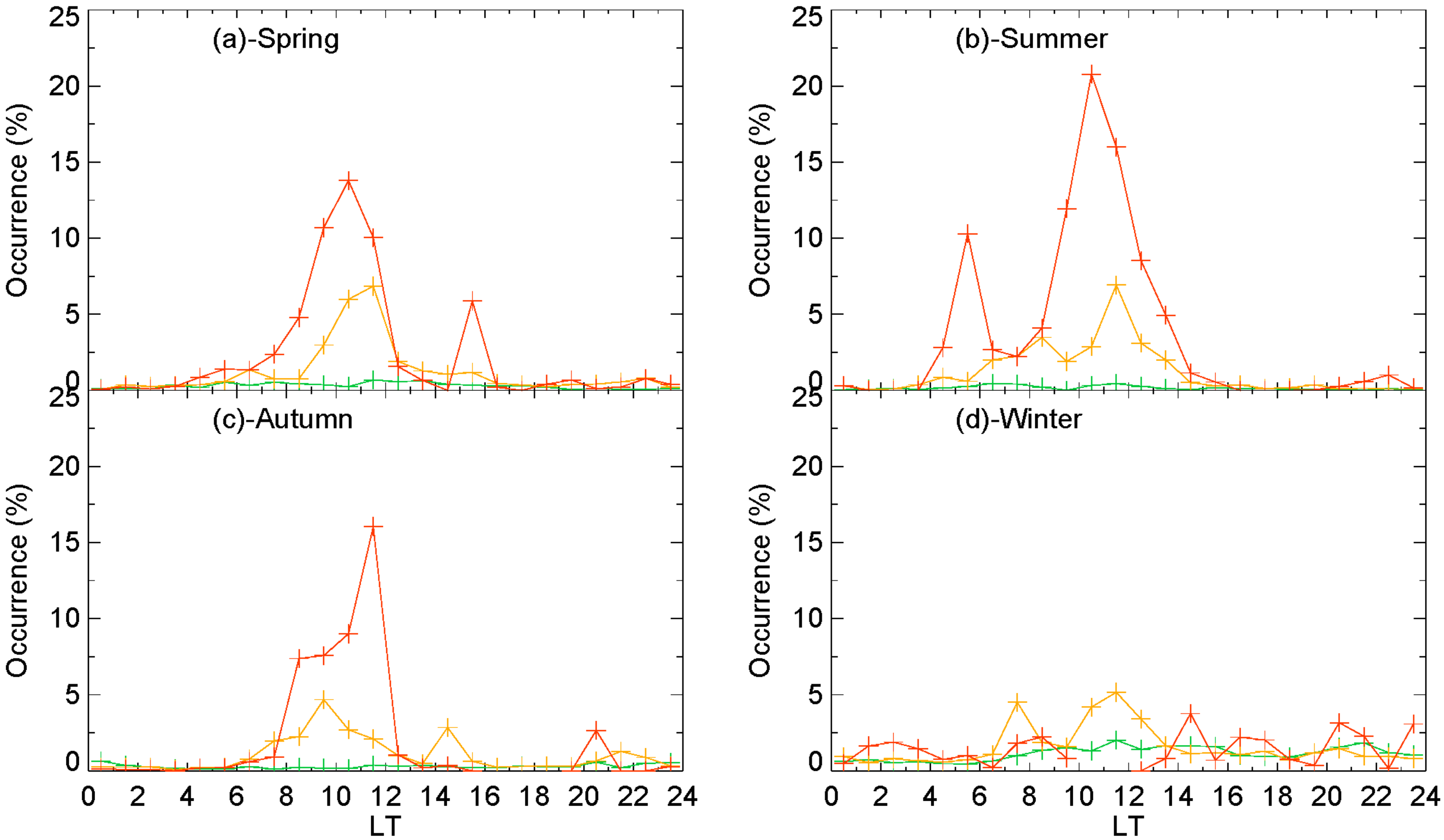

Figure 4.14: Plot showing the seasonal occurrences of the medium upflow in Figure 4.11. This is the percentage ratio of Figure 4.11 to Figure 4.9 with respect to the corresponding colour, LT and season. The panel and colour format the same as outlined in Figure 4.13.

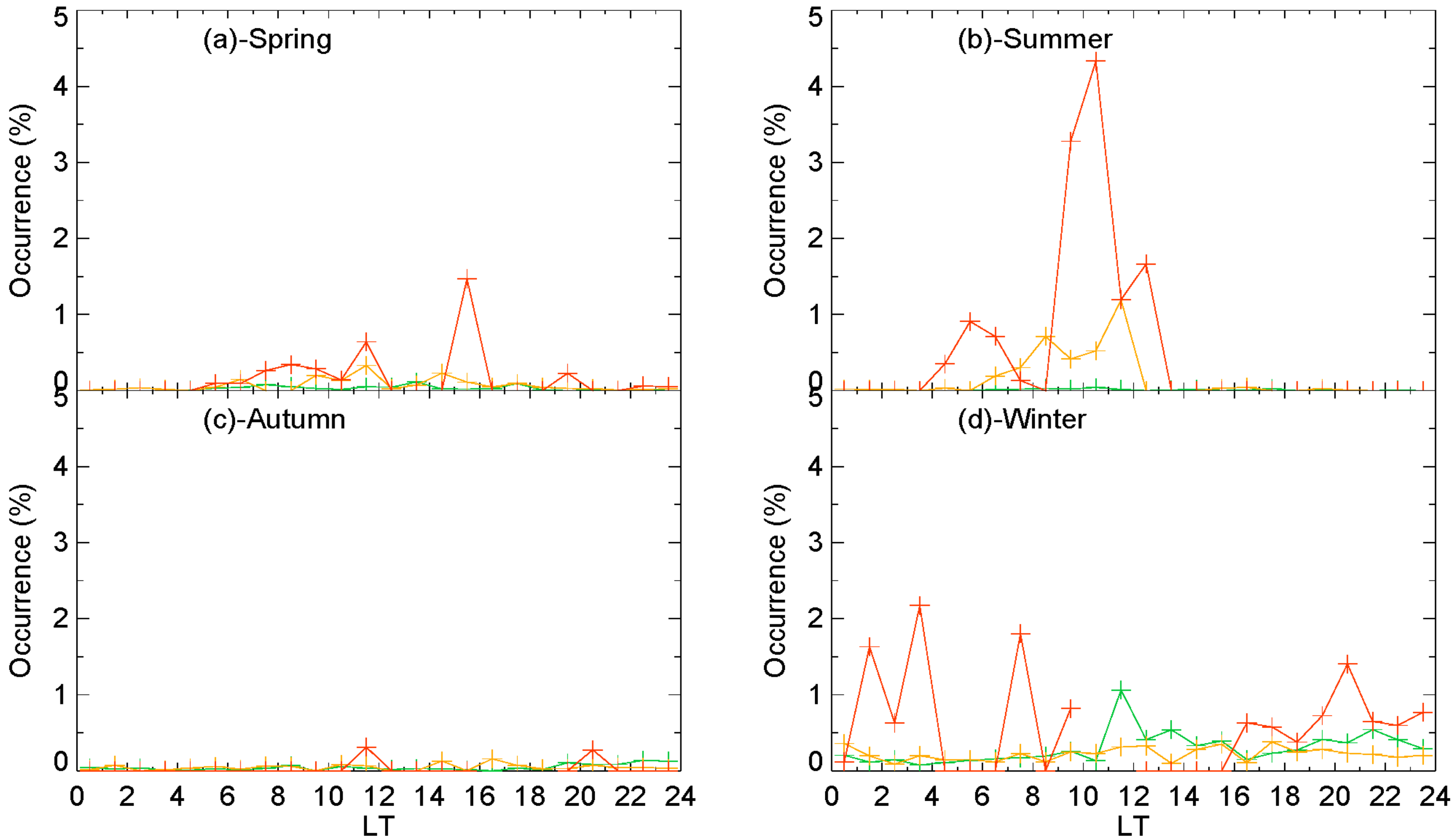

Figure 4.15: Plot showing the seasonal occurrences of the high class upflow in Figure 4.12. This is the percentage ratio of Figure 4.12 to Figure 4.9 with respect to the corresponding colour, LT and season. The panel and colour format the same as outlined in Figure 4.13.

4.4. Summary and Conclusions

I have investigated the ionospheric upwellings observed by the EISCAT Svalbard Radar (ESR) during a deep solar minimum campaign of collaborative effort of the international community to research the polar regions in 2007. Previous studies in the field chose the ion velocity as the basis for the filter, but in this work, I have chosen the ion flux because it is a conserved quantity along the flux tube (for approximately constant magnetic field strength). The summary of the main results are as follows:

- The upgoing flux ($\geq 10^{13}$ m^{-2} s^{-1}) has been shown to have different characteristics as the flux magnitude increases. Although this is expected, the confirmation comes up for the first time in this study.

- The upflow occurrence maximizes around local noon, however, the peak upflow flux distribution is skewed toward earlier times for the low flux. Although there is an increase in upflow occurrence in the nightside of the low flux, the peak occurrence for the class is still around local noon.

- A lower magnitude of upflow flux and occurrence has been observed during solar minimum in comparison to the magnitude of previous studies on half and complete solar cycle, and the downflow occurrence also follows similar pattern during low solar activity. In agreement with previous studies, where the ratio of downflow to upflow occurrence is less than 1 (Endo et al., 2000; Ogawa et al., 2009), downflow occurrence is observed to be less than the upflow occurrence at all LTs.

- Ion upflow and downflow are common phenomenon and can take place during low, medium and high activity in geomagnetic conditions. This is in good agreement with previous studies from EISCAT VHF radar data at Tromsø (Endo et al., 2000) and ESR data (Ogawa et al., 2009).

- Occurrence increases in all classes of ion upflow as the level of geomagnetic disturbance increases, whereas there is little or no significant change on the average in the downward flux occurrence frequencies as the *Kp* level changes. Although it is observed that the relationship between geomagnetic activity and downflow-upflow ratio is not exactly linear, a higher ratio of downflow to upflow events is generally observed when *Kp* is low.

- The most frequent class of ion upflow flux is the low category between $1.0 \times 10^{13}\ \mathrm{m}^{-2}\ \mathrm{s}^{-1}$ and $2.5 \times 10^{13}\ \mathrm{m}^{-2}\ \mathrm{s}^{-1}$, followed by the medium class which is 10 times the high class. The low flux is about 7.5 times the other classes put together. Meanwhile, on the seasonal outlook, the most often observed class across all seasons is still the low flux, which peaks in summer. However, there is a higher occurrence of medium and high fluxes in winter than any other season

- Local time variation is observed to be higher in the ion upflow scatter plot during summer than winter. However distinct minimum in upflow flux is clearly shown around 16 – 20 LT. This dip in flux around 16 – 20 LT is also a general seasonal phenomenon however, less pronounced in winter, but higher in autumn than in other seasons.

- While the high upflow flux is a rare event with its peak occurring around local noon in summer and its occurrence frequency depending predominantly on high geomagnetic disturbance across the seasons, the low flux is predominantly in spring and summer, however, any level of geomagnetic disturbance is observed to be appropriate to trigger the low class of upflow at any time of the day. The medium flux however, indicates a good distribution across the seasons and a centrally peaked occurrence driven by high *Kp*.

- Upflow occurrence decreases with increase in magnitude of the upflow flux across all seasons.

- All the seasons indicate pre-midnight occurrence peak for the low-flux upflow.

- Distinct occurrence maxima stand out in all the seasons when geomagnetic conditions are either medium or high.

The temporal analysis showed the diurnal variation of the upflow flux and its occurrence in relation to conditions in geomagnetic activity. It was found that upflow flux was prevalent at the nightside, but its occurrence was peaked around local midday. Increase in geomagnetic activity was found to enhance the occurrence frequency of ion upflow in all classes of flux. Ion upflow was observed to take place over a wide range of geomagnetic conditions, with downflow occurrence being lower than upflow occurrence. In contrast to previous observations, however, the upflow occurrence was greater around noon during highly disturbed geomagnetic condition than medium geomagnetic condition.

Analysis of the seasonal distribution revealed that while high-flux upflow had its peak around local noon in the summer, with its occurrence being driven predominantly by high geomagnetic disturbance, the occurrence of low-flux upflow was broadly distributed across all seasons, geomagnetic activity conditions and times of day. The medium-flux upflow events, although distributed across all seasons, showed an occurrence peak strongly related to high *Kp*. Furthermore during highly disturbed conditions, the low-flux and medium-flux upflow events showed a minimum occurrence during the winter, whereas minimum occurrence for the high-flux upflow events occurred in autumn. It was also observed that, across all seasons, upflow occurrence decreased with increase in magnitude of the upflow flux.

CHAPTER 5

A study of ambipolar electric field and ion frictional heating in ionospheric upflow during the IPY-ESR 2007 observations

5.1. Introduction

As discussed under the review of plasma outflow in Chapter 2, ionospheric outflow is preceded by upflow from the upper atmosphere, which under the right geophysical conditions results in an outflow into the overlying magnetosphere. Landmark papers claim that several mechanisms responsible for these upflows and outflows are caused by some types of heating for ionospheric upwelling and suprathermal energization by wave activity to create ion outflows (André and Yau, 1997; Hultiqvist et al., 1999; Yau et al., 2011). Here several periods of ion upflow are identified from observations by the EISCAT Svalbard Radar (ESR) during the international polar year (IPY) campaign of 2007.

The main focus of this chapter is to investigate the dominant mechanism that is responsible for driving the ion upflow around the noon and midnight sectors, during the period under investigation. The two leading mechanisms are an ambipolar electric field (resulting from electron precipitation) and ion frictional heating (resulting from current closure in the ionosphere) (André and Yau, 1997; Yau et al., 2011; Moore et al., 2014). Any observation by the ESR that satisfies the conditions set out in the data filter described in Chapter 4, section 4.2.2, and in addition an ion flux threshold of $10^{13}\ \mathrm{m}^{-2}\ \mathrm{s}^{-1}$ for a duration of at least 10 minutes interval is regarded as an event in this chapter. In this study, I have identified 683 events from the ESR parameter plots, which correspond to periods of noticeable velocity upflow and/or activity in the electron precipitation in conjunction with enhancement in electron and/or ion temperature(s) as observed by the ESR during the IPY-ESR 2007 campaign. Figure 5.1 shows the histogram of event durations, where about 42.5% of the events do not last beyond one hour.

In this chapter, equation (2.8) arrived at in the review section, Chapter 2, is employed to generate the ion momentum plots. Other subdivisions investigated for the two leading upflow mechanisms (the ambipolar electric field and Joule heating) include events relationship with B_y asymmetry, southward and northward B_z, classes of geomagnetic storm, substorm onset and events duration.

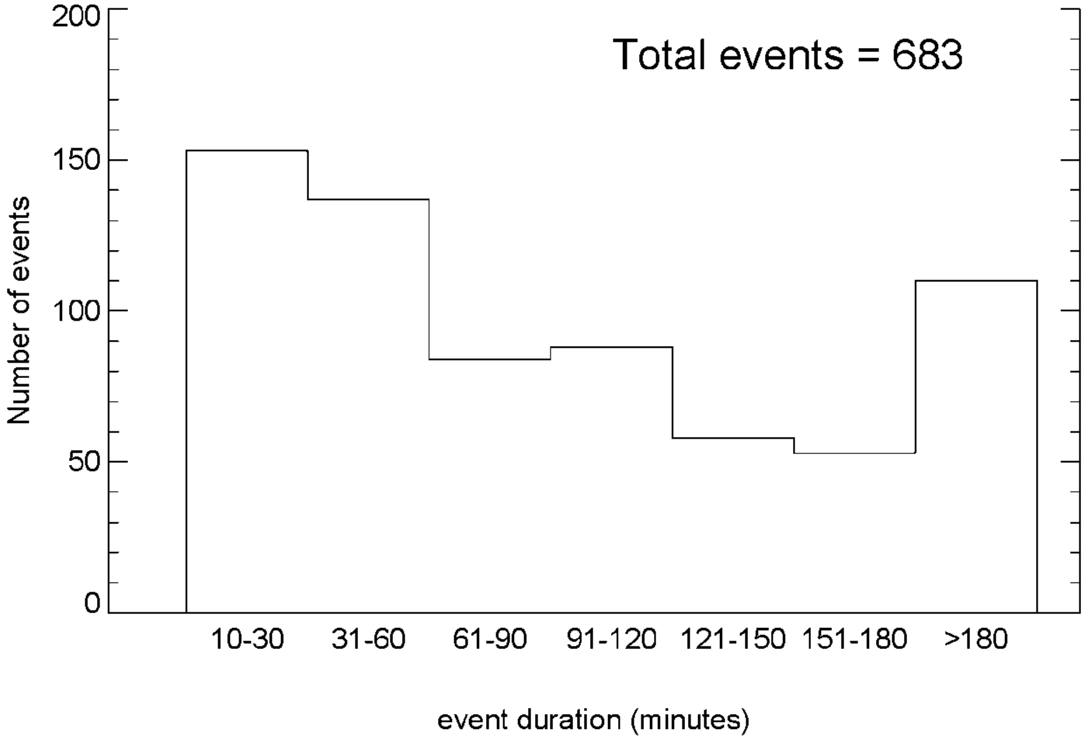

Figure 5.1: Plot showing the number of events and the corresponding time intervals it lasted.

5.2. Case Study 1: Events driven by ambipolar electric field

5.2.1 Instruments and data source

The basic ionospheric parameters data used in this study are derived from the EISCAT common programme 1 (CP-1) scan pattern / ipy_60 pulse code experiment on the ESR 42 m dish during the IPY 2007 collaboration. The CUTLASS Finland radar of the SuperDARN family of radars has sixteen radar beams covering a wide range field-of-view of which beam 9 passes through the ESR facility (Yeoman et al., 2010). Data from beam 9 is used to investigate the perpendicular flow of plasma across the field, while the high resolution OMNI data set of solar wind plasma parameters at the bow shock region of the Earth, and also of energetic proton fluxes and geomagnetic activity indices from OMNIweb, is utilised to generate the OMNI plot for this section. Chapter 3 of this thesis presents a comprehensive description of the instruments.

5.2.2 Results and Discussion

5.2.2.1 ESR parameter plot

Each of the ESR parameter plots in this section consists of five panels, which are electron density (n_e), electron temperature (T_e), ion temperature (T_i), ion velocity (v_i) and the ion flux (f_{ion}) respectively. The plots show variations in the above parameters with respect to altitude ranging from 100 km to around 500 km. It is worth noting that positive values of velocity from the ESR data represent upward flow away from the radar.

- **20070614 dayside event**

Figure 5.2 presents a dayside/cusp event on June 14, 2007, which indicates precipitation, inferred from an elevated n_e in the electron density profile below the E-region (below 150 km), throughout the period under investigation from 09:00 LT until around 15:00 LT. The precipitation goes down to the lower E-region (100 km) from 13:30 UT until the rest of the period. A period of elevated electron temperature is observed above 200 km from the start to the end of the noon sector, with strongest enhancements in three successions around 09:30 – 10:50 LT, 11:10 – 12:30 LT and 13:00 – 13:50 LT. A period of moderate ion temperature dominates the entire sector with few intermittent enhancements especially during the first session of strong T_e enhancement. High flow in ion velocity is observed in the fourth panel around the time corresponding to moment of strong T_e elevation. The last panel indicates that ion flux upflow that satisfies the threshold value and conditions to be regarded as an event also corresponds to the periods of strong T_e enhancement. The maximum fluxes from the first to third session of strong increase in T_e are 9.93×10^{13}, 1.61×10^{14} and $1.78 \times 10^{14}\ \mathrm{m}^{-2}\ \mathrm{s}^{-1}$ respectively, which correspond to class of high flux upflow mentioned in Chapter 4. The altitude of the ion upflow flux during the first session is predominantly from 300 km, while the second and third sessions cover from above 250 km and 200 km respectively.

- **20070315 nightside event**

Figure 5.3 is a nightside event that occurs on March 15, 2007. The electron density profile in the first panel also indicates an intermittent intense precipitation down to the lower E-region from 23:20 LT until around the first few minutes of the following morning (00:15 LT). However, the ionosphere appears to be quite low in electron concentration a few hours before and after the event. The second panel shows an elevated electron temperature at the time of event, which could create an ion-electron charge separation, setting up an ambipolar electric field, whereas moderate ion temperature with few intermittent enhancements is observed in the third panel. The period of event coincides with high upward flow predominantly above 300 km, and throughout the six-hour period, the ion flux that satisfies the threshold condition shown in the last panel occurs only during the period of event. The peak ion upflow throughout the period is $8.45 \times 10^{13}\ \mathrm{m}^{-2}\ \mathrm{s}^{-1}$, which occurs at 300 km altitude at about three and a half minutes past midnight, and this also corresponds to the high flux category.

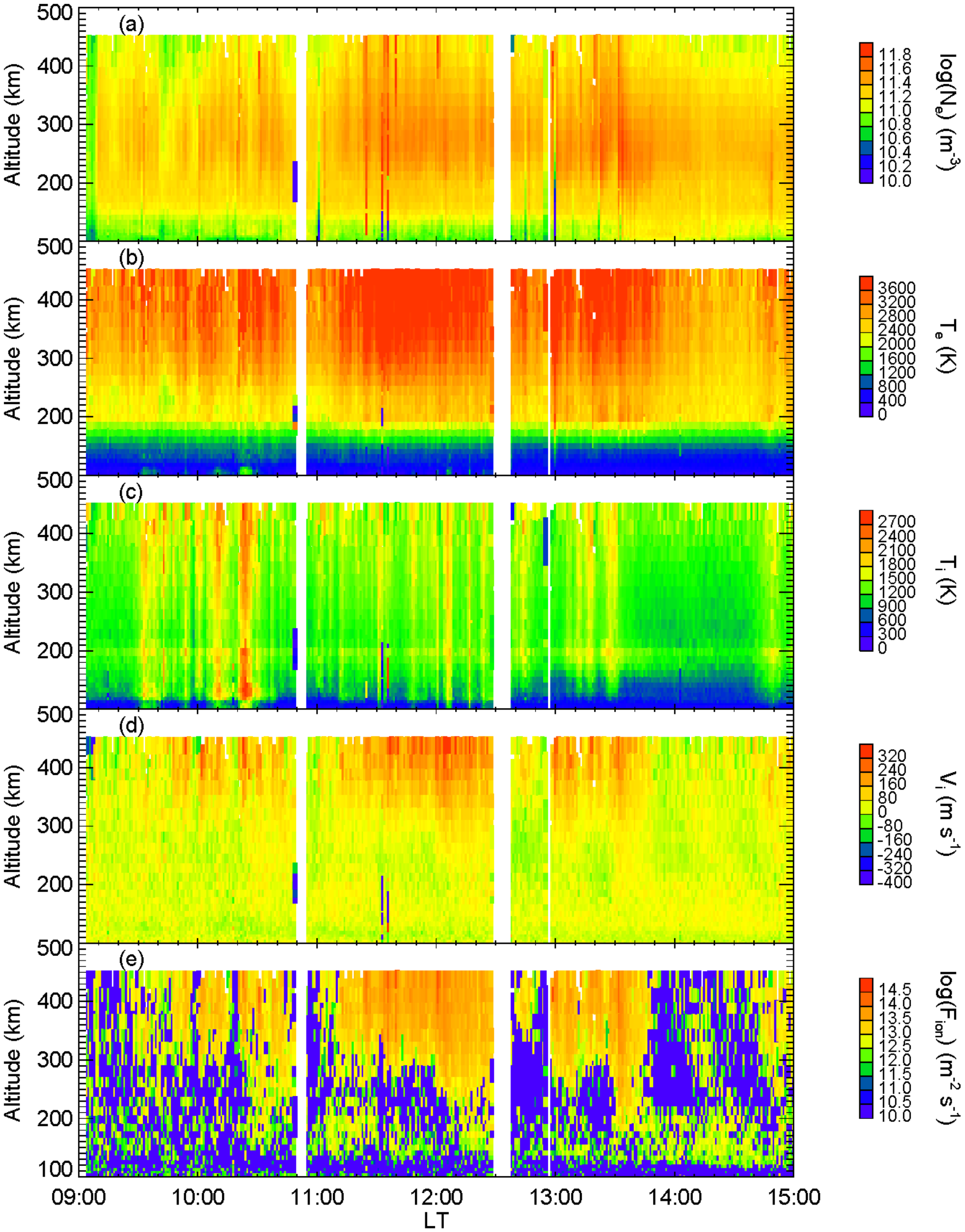

Figure 5.2: Plot showing the June 14, 2007 ESR parameter plot for the 42m dish during the IPY-ESR campaign from 09:00 - 15:00 LT. The five panels are the (a) electron density, (b) electron temperature, (c) ion temperature, (d) ion drift velocity, and (e) ion flux respectively.

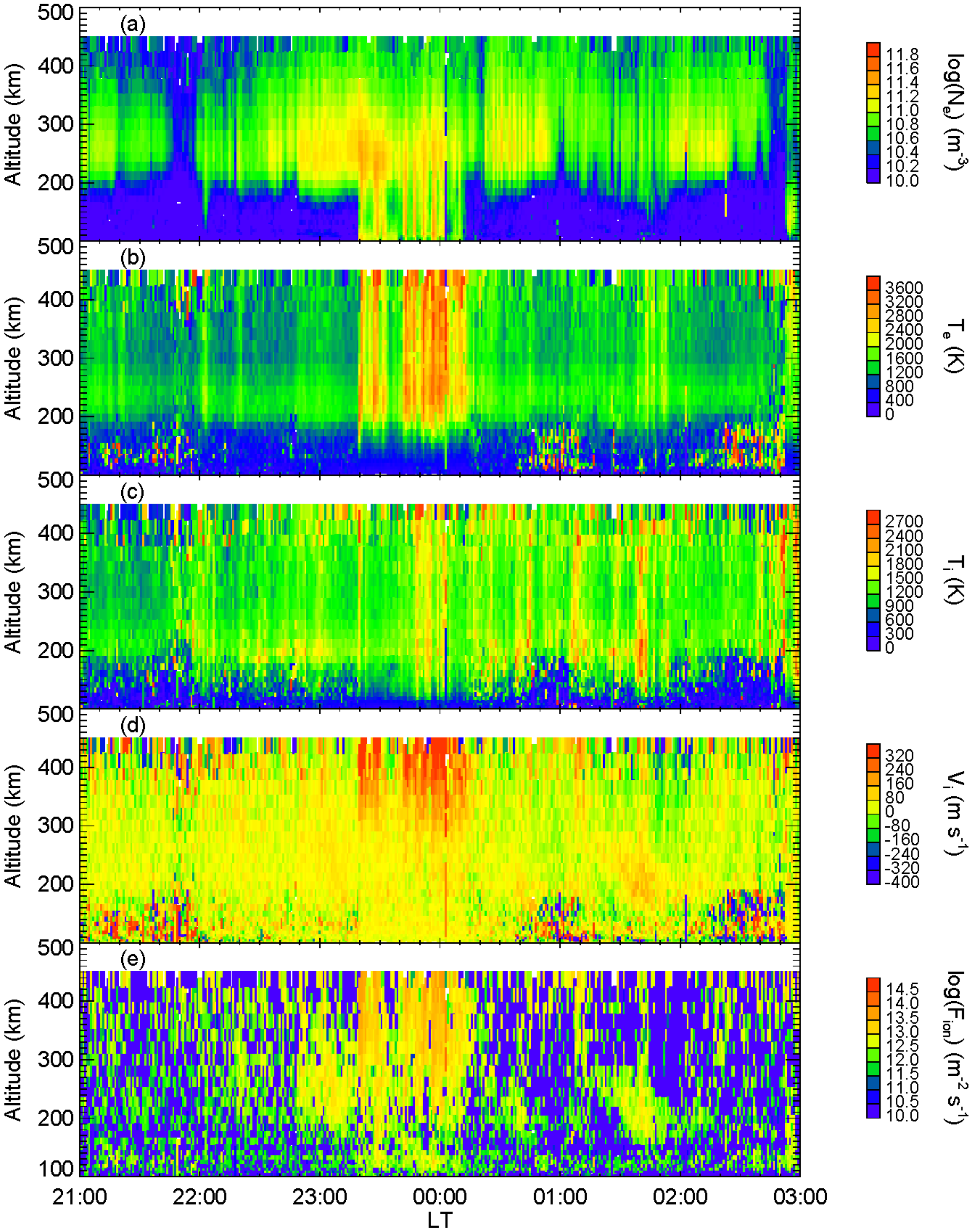

Figure 5.3: Plot showing the March 15, 2007 ESR parameter plot for the 42m dish during the IPY-ESR campaign from 21:00 - 03:00 LT. The panels' format is the same as outlined in Figure 5.2.

5.2.2.2 OMNI measurements

The plots in this section comprises eight panels, namely, the Sym-H ring current index, the lower auroral electrojet (AL) and upper auroral electrojet (AU) indices, the solar wind number density, the dynamic pressure, the solar wind speed V_{sw}, B_y, and B_z components of the IMF, and the magnitude of the IMF, B_{mag}, respectively. The plots span six hours from 09:00 – 15:00 LT for the dayside event and from 21:00 – 03:00 LT for the nightside event.

- **20070614 dayside event**

The OMNI record of the June 14 2007 dayside event due to electron precipitation is present in Figure 5.4. The first panel of the event shows that the ring current index, Sym-H, indicates a weak to quiet period of geomagnetic storm, where $-35\text{ nT} < \text{Sym-H} \leq 0\text{ nT}$ throughout the six-hour duration. The minimum ring current for the period occurs during the first session of the elevated T_e (described in section 5.3.2.1), and at about 10:50 LT, which corresponds to the end of the first T_e enhancement interval, there is a sharp upward turning in Sym-H to about -5 nT around 11:15 LT. Thereafter, the ring current remains ≥ -15 nT for the rest of the period. It worth mentioning here that according to ring current classification (Vieira et al., 2001; Gonzalez et al., 2001; David, 2013), the ring current index does not indicate any period of intense geomagnetic storm during the IPY 2007 campaign. However the quiet, weak and moderate periods are about 96.6%, 3.1% and 0.3% respectively. This is due to the sun being at solar minimum during the period of present study. The excursion of AL and AU indices on the second panel indicates significant global energy input between 12:00 LT and 13:00 LT corresponding to the period of second T_e enhancement. The third and fourth panels show the plasma density and dynamic pressure, which are fluctuating predominantly between $n = 10.0 \pm 2.0\text{ cm}^{-3}$and $P_{dyn} = 4.0 \pm 1.5\text{ nPa}$ respectively. However, a steady increase is observed in the solar wind plasma velocity starting from around 400 km s^{-1} at 09:00 LT and reaching a maximum of about 500 km s^{-1} towards the end of the noon sector. The last three panels present the orientation and the strength of the IMF. B_y indicates that the cusp is predominantly duskward during the first and second sessions of T_e enhancement, whereas the impinging solar wind causes the cusp to move duskward and dawnward during the third T_e enhancement at 13:00 – 13:50 LT. Reconnection on the dayside is shown to be enhanced by southward B_z for about half of the period and this dominates the second session of T_e enhancement between 10:50 – 12:50 LT. However, the last interval seems to be triggered by a sudden switch to B_z northward just before 13:00 LT.

- **20070315 nightside event**

The first panel of Figure 5.5 shows a weak perturbation in the ring current between 21:00 LT on March 15, 2007 until 03:00 LT on March 16, 2007. However, a strong perturbation in the westward electrojet indicated by AL on the second panel, commencing from around 23:00 LT, signals substorm onset for the nightside ion upflow discussed in section 5.3.2.1. The solar wind speed is about 600 km s^{-1} at 21:00 LT and decreases gradually until it reaches 570 km s^{-1} at about 22:45 LT. Thereafter, a sharp increase in the speed magnitude to above 610 km s^{-1} is observed at the commencement of the event, and fluctuating between $600 \pm 20 \text{ km s}^{-1}$during the time of event. Duskward turning of B_y dominates during the time of event and predominantly duskward throughout the six-hour period, while B_z component of the IMF begins from a northward position during the time of event and turns southward around 23:40 LT to reach a weak minimum of about -4 nT in the midst of the event around 23:45 LT. The last panel indicates that the magnitude of the interplanetary magnetic field experiences a sharp decrease in magnitude whenever there is a sudden change at the end of the IMF B_z southward orientation excursion. This is particularly pronounced around 22:00, 23:00, and 23:50 LT, which correspond to periods of end of southward and beginning of northward turning in B_z.

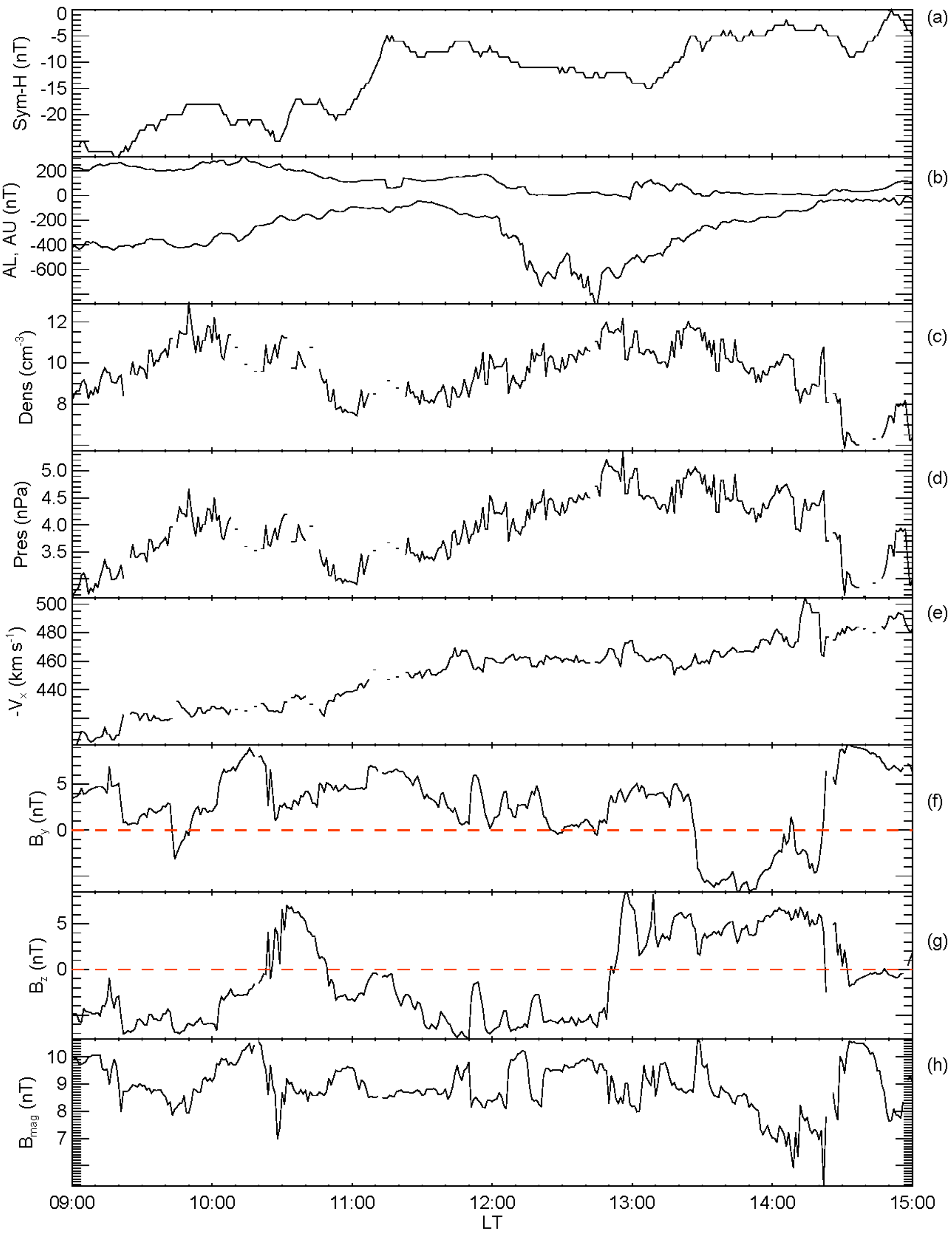

Figure 5.4: Plot showing the OMNI measurements for the cusp event on June 14, 2007. The eight panels are the (a) Sym-H, (b) upper and lower auroral electrojet indices, AU and AL, above and below zero respectively, (c) solar wind density, (d) dynamic pressure, (e) solar wind speed in the GSE coordinate, (f) IMF B_y, (g) IMF B_z, and (h) magnitude of the IMF respectively.

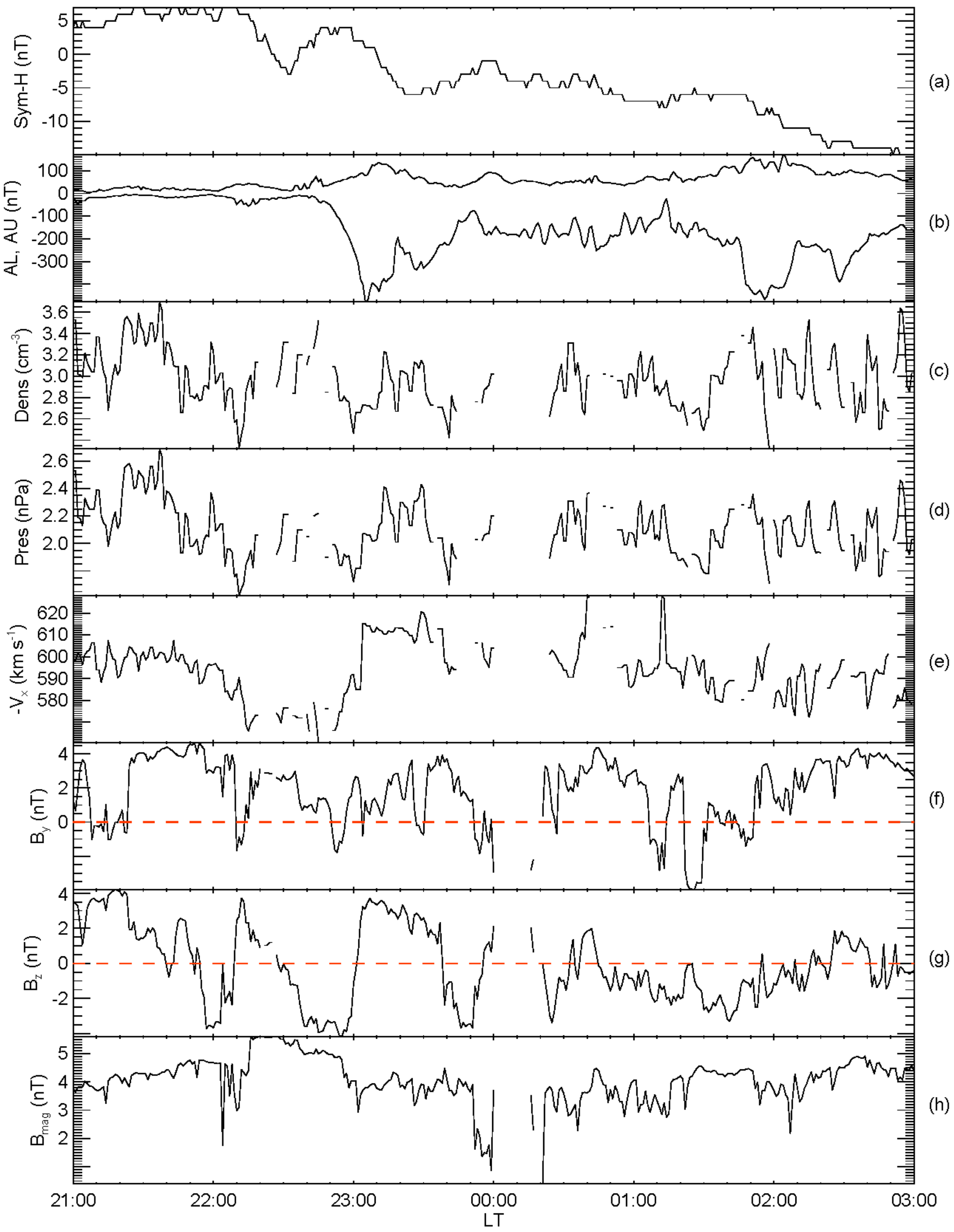

Figure 5.5: Plot showing the OMNI measurements for the midnight event on March 15, 2007 from 21:00 - 03:00 LT. The panels' format is the same as outlined in Figure 5.4.

5.2.2.3 Ion momentum plot

The Figures in this section comprise six panels, of which the first five describe the ambipolar electric force $(en_iE_{//})$, ion pressure gradient $(-\boldsymbol{\nabla}P_i)$, the balance force (F_{net}) arising from the algebraic sum of all the forces in the RHS of equation (2.8), the line-of-sight velocity (v_{los}) beam 9 of CUTLASS Finland radar, and the average value of ion upflow flux along the field-aligned profile $(< F_{ion} >)$ respectively. The last panel during the dayside event shows the IMF B_z while for the nightside presents the AL and AU indices.

Table 5.1 below lists some values obtained around 320 km from the ion momentum plot on June 14, 2007 (Figure 5.6). The table presents some examples of the ambipolar electric force, ion pressure gradient and gravitation force from which the balance force (F_{net}) is calculated.

Table 5.1: Some examples of the values of terms in the ion momentum equation at altitude 320 km between 12:00 LT – 12:10 LT

Time (LT)	$en_iE_{//}$ $(\times 10^{-14}$ N m$^{-3})$	$-\boldsymbol{\nabla}P_i$ $(\times 10^{-14}$ N m$^{-3})$	$F_{gravity}$ $(\times 10^{-14}$ N m$^{-3})$	F_{net} $(\times 10^{-14}$ N m$^{-3})$
12:005	2.47	3.42	-5.88	0.00414
12:015	4.76	3.61	-5.18	3.19
12.025	1.17	1.76	-5.96	-3.03
12:035	4.98	2.97	-5.60	2.34
12:045	7.43	3.26	-6.72	3.98
12:055	6.13	3.58	-6.83	2.88
12:065	4.54	2.67	-6.03	1.17
12:075	-2.52	1.48	-5.40	-6.44
12:085	0.0755	1.51	-5.49	-3.90
12:095	2.38	1.49	-5.57	-1.70

- **20070614 dayside event**

The topside of the F layer as shown in the first panel of Figure 5.6 indicates a predominantly strong upward ambipolar force for the six-hour period. It is especially stronger during the periods corresponding to the second and third session of elevated T_e and high upflow described in section 5.3.2.1 at 11:10 – 12:30 LT and 13:00 – 13:50 LT respectively. This is due to the electron precipitation which, it is suggested, leads to the creation of an ambipolar electric field, an increase in the ion scale height and ion upwelling as a result. In addition, the ambipolar electric field is caused by a pressure gradient in the electrons driving them up the field, and because the electrons being light are not gravitationally bound (but ions are), the differential motion between the two sets up an electric field which then acts to restrain the electrons and pull up the ions as a result. So the higher the T_e, the greater the electron pressure and the larger the ambipolar field becomes. The ion pressure gradient shown on the second panel is weaker than the ambipolar force at all LT under investigation especially at altitudes ≥ 300 km, where the ion upflows predominantly occur during the event. The balance force from the third panel indicates that there is sufficient upward net force to drive an upflow at the period when ion upflows are observed as shown in the fifth panel. The SuperDARN plot on the fourth panel shows a paucity of data before 11:00 LT and after 13:00 LT at the ESR magnetic latitude (75.18°N). However, there is fast anti-sunward flow away from the radar indicated by the Hankalsami, Finland radar between 11:00 – 13:00 LT, which is a signature of the ionospheric cusp (Milan et al., 1998). The fifth panel shows a three-step event corresponding to periods of enhanced ambipolar electric force, with maximum flux peak increasing from first to third. However the second step, which occurs between 11:10 – 12:30 LT, lasted longer than the other two and has highest overall bulk upflow flux. The fifth and last panels of Figure 5.6 show that the first step of upflow flux occurs when the IMF B_z is southward for half of the period, that is, 09:50 – 10:20 LT and northward for the remaining half time (10:20 – 10:50 LT), whereas the second and third steps show a complete southward and northward excursion of B_z respectively. An upsurge in average ion flux is observed during sharp turnings from southward to northward B_z as seen from the first and last steps of the event, and also during further southward turning of B_z in the middle step. Pham et al. (2016) has explained the effect of northward B_z on both reconnection and viscous interactions as disrupting magnetospheric plasma flow, and causing a mixture of configuration topology during southward to northward B_z excursion. Detailed analysis which include, inter alia, B_y and B_z effect, clock angle and coupling function will be looked into in Chapter 6.

- **20070315 nightside event**

The ambipolar electric force in the first panel of Figure 5.7 is predominantly at equilibrium for altitude above 230 km. However, the time interval between 23:20 LT on March 15 and 00:10 LT on March 16, 2007, indicates a strong upward directed ambipolar force which, exceeds $4 \times 10^{-14}\ \mathrm{N\ m^{-3}}$. The ion pressure gradient on the second panel appears to be lesser at all times in comparison to the force due to the ambipolar electric field. The third panel shows that the balance force from the ion momentum equation indicates dominance from the gravitational pull on the ion, leading to downwelling except at the interval where the ambipolar force exceeds $4 \times 10^{-14}\ \mathrm{N\ m^{-3}}$. The data gap from CUTLASS beam 9 Finland radar limits comment on what the V_{los} is doing during the six-hour period, however, the green patch of scatter from 23:00 – 23:40 LT implies a small equatorward expansion of the auroral oval/polar cap. From the fifth panel which shows the average upflow flux along the field line, upflow occurs mainly at the period corresponding to elevated ambipolar electric force and this suggest ambipolar electric field as the driver of the March 15, 2007 event. Moore et al. (2014 and references therein) explained that the process of heating the ionosphere through differential electron pressure moves the electrons up the field line by the energy acquired and as a result, sets up an ambipolar electric field. As the ambipolar field becomes more and more elevated through an increasing pressure gradient, a corresponding ion flux breaks loose from the gravitational pull to retain their electrostatic coupling with the electrons and thus preserving quazi-neutrality. A moderate substorm onset reaching a minimum value of about $-500\ \mathrm{nT}$ precedes the ion upflow as shown in the last panel of Figure 5.7, indicating additional westward current from substorm to the usual electrojet current system from AL and AU. It is right to posit here that there are periods of ion upflow at the midnight sector without substorm occurrence and vice versa, however, the latter is a rare occurrence. Section 5.3 presents an example of ion upflow event without being associated with any substorm occurrence.

5.2.3 Summary

Electron precipitation down to the lower E-region is observed and elevation in electron temperature dominates over ion temperature during the June 14 and March 15, 2007 events. High upward flow is observed above 300 km in both events, whereas the ion upflow flux extends down to 200 km during the cusp event on June 14, 2007. Furthermore, the peak ion upflow flux around cusp on June 14, 2007, is more than the peak around midnight during the March 15, 2007 event, however, both attained the high-flux upflow explained in Chapter 4. The June 14, 2007 event is a cusp related event as ascertained by the SuperDARN plot and moreover, it is a three-step event. On the other hand, the March 15, 2007 event is substorm related as shown by large enhancement in AL over AU around 23:00 LT and it is a single-step event in contrast to the June 14, 2007 cusp event. Further analysis shows that about 21.7% of the total events occur around local noon, of which 80.4% are cusp related, while about 30.2% occur around midnight, of which 65.5% are related to substorm activity. It is also observed that ion upflow can occur both during southward and northward excursion of IMF B_z. The major driver for the two events is the ambipolar electric field, which grows as the electron pressure gradient increases. More on the statistic of all events follows in section 5.6.

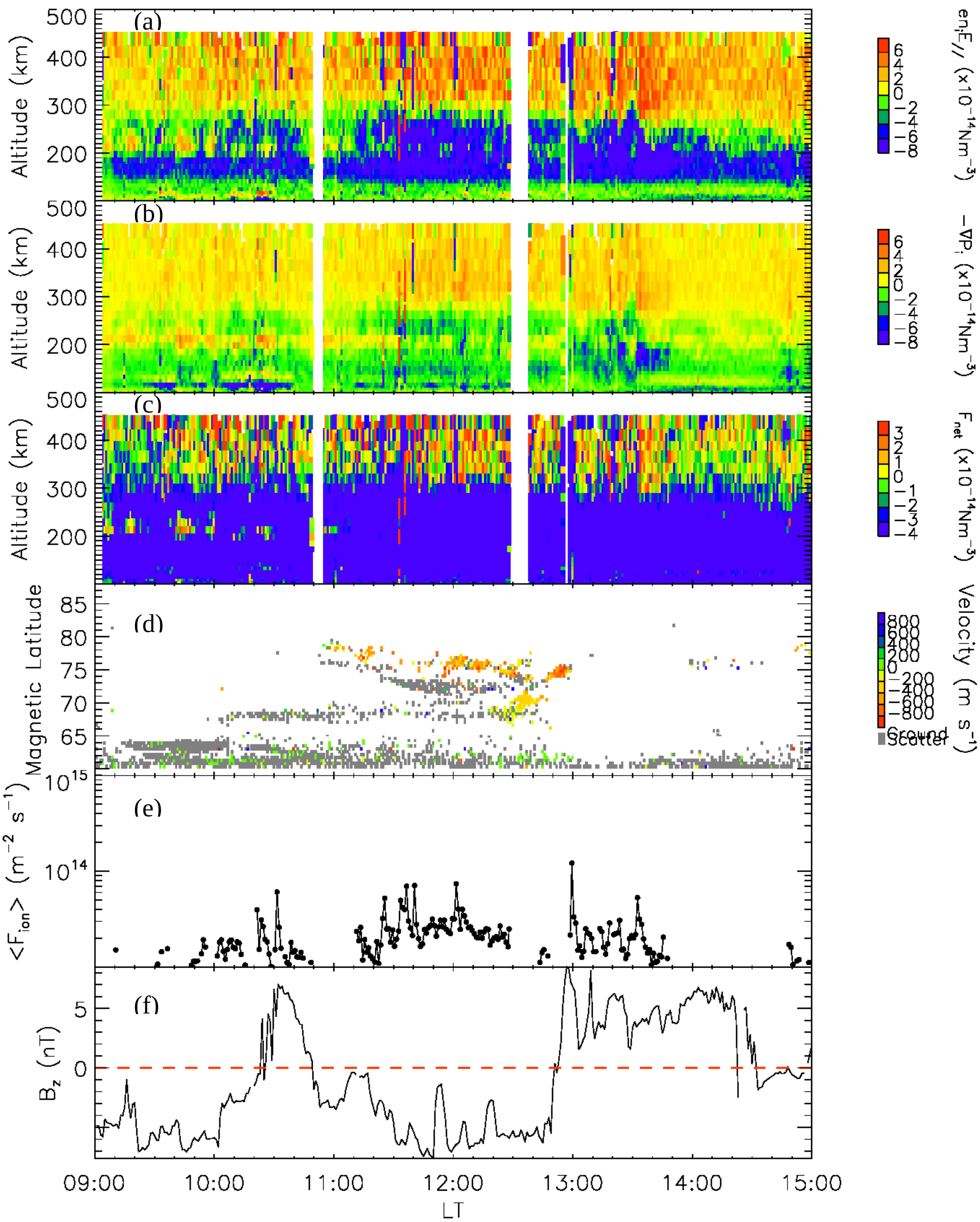

Figure 5.6: Plot showing the ambipolar electric force as the dominant driver of the ion upflow driver during the June 14, 2007 event. The six panels are the (a) ambipolar electric force $\left(en_iE_{//}\right)$, (b) ion pressure gradient $(-\nabla P_i)$, (c) balance force (F_{net}), (d) line-of-sight velocity (v_{los}) beam 9 of CUTLASS Finland radar, (e) average value of ion upflow flux along the field-aligned profile $(< F_{ion} >)$, and (e) IMF B_z respectively.

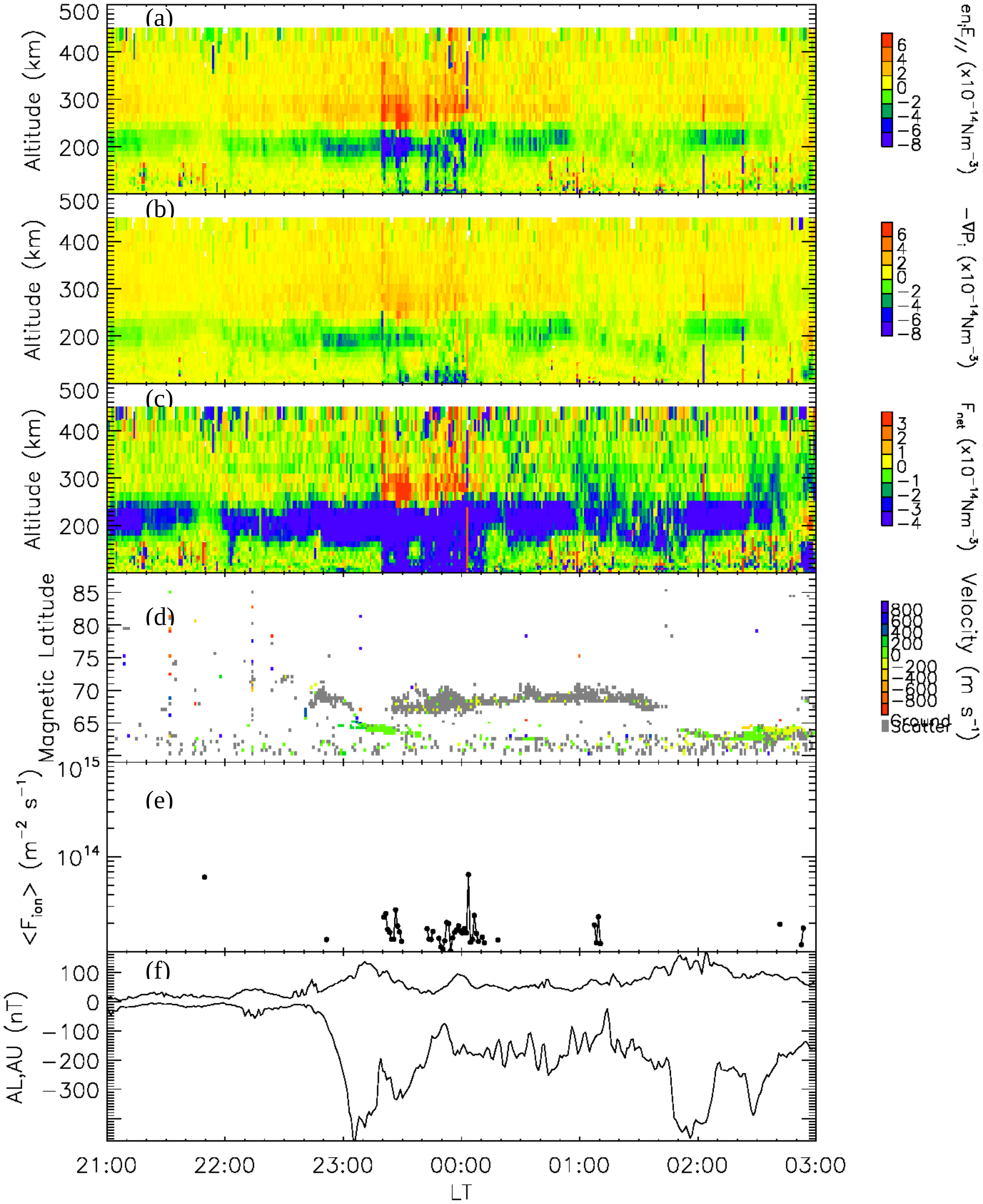

Figure 5.7: Plot showing the ambipolar electric force as the dominant driver of the ion upflow during the March 15, 2007 event. The first five panels have the same format as outlined in Figure 5.6. The last panel during the midnight event shows the AL and AU indices.

5.3. Case Study 2: Event driven by Joule heating

Unlike in Case Study 1 where two events, one on dayside and the other on the nightside, are presented, only one event is presented in this section because an isolated T_i enhancement was rarely observed by the ESR especially around noon. Throughout the IPY 2007 campaign there is no event on the dayside with an isolated T_i enhancement. There are very few occurrences in the nightside lasting between 10 and 15 minutes. A peculiar occurrence that spans about an hour is considered in this section. It is possible to get Joule heating both from an increase in conductivity as well as during increase in the magnitude of the relative velocity between ions and neutrals, $|v_i - v_N|$ (Aruliah, 2016). It is possible to have the latter without the former, where relative velocity between ions and neutrals causes friction and as a result frictional heating is generated, which is the case to be presented in this section. An event starting around 23:30 LT on September 11, 2007, is considered for studying the Joule heating effect as a mechanism for driving ion upflow. Although, the September 11 event, shows four different sessions of elevated ion temperature when there is no precipitation, but only the time interval for the second enhancement will be focused in the section because of its longer duration.

5.3.1 Instruments and data source

In addition to the EISCAT, SuperDARN and OMNI data mentioned in section 5.3.1, data from International Monitor for Auroral Geomagnetic Effects (IMAGE) ground magnetometer and SuperMAG are also investigated in this section. The ionosphere above Svalbard, where the ESR radar is located is under the field of view (FOV) of IMAGE network coverage, and it presents a localised data instead of the global average from other networks. Furthermore, beam 5 of the CUTLASS Iceland radar, which points North and East and passes through the ESR facility (Yeoman et al., 2010), is also investigated in this section because there is paucity of data for beam 9 of CUTLASS Finland radar at the time interval when the event occurs.

5.3.2 Results

5.3.2.1 ESR parameter plot

- **20070911 nightside event**

The ESR parameter plot for the September 11, 2007, nightside event is shown in Figure 5.8. The first panel showing the electron density indicates that there is no electron precipitation throughout the six-hour period around midnight except one that appears very weak between 23:10 – 23:30 LT. The evacuation of the ionosphere is noticeable at all altitudes between 100km and 200 km and extended to around 280 km altitude between 23:50 UT – 00:00 LT. The electron temperature, T_e, on the second panel shows a predominantly low electron temperature profile at all altitudes. The brief moment of slight enhancement in the electron temperature corresponds to the period of weak precipitation mentioned in the first panel. The ion temperature (T_i) panel shows that periods of strong frictional heating are indicated on the third panel by the ESR around 22:30 – 22:40 LT, 23:30 – 00:30 LT, 01:15 – 01:30 LT and also 02:05 – 02:20 LT. I have chosen to focus on the time interval corresponding to the second T_i enhancement because of its longer time duration in comparison to the other time intervals. The strong ion temperature increase, which becomes significantly enhanced through ion frictional heating, results in high flow around the periods of each T_i enhancement as shown on the fourth panel of Figure 5.8. This agrees with existing theory that there is a clear relationship between large ion velocities and ion temperature elevation as shown on the third and fourth panels (St.-Maurice and Hanson, 1982). The heating is most effective in the F-region altitude, modifying the plasma pressure gradient and resulting in field-aligned ion acceleration. It is evident that the dominant mechanism for ion flux indicated on the last panel at these periods is the Joule heating, as there is no indication of electron precipitation and the enhanced T_e that can cause an increasing gradient in electron pressure, which would lead to an ambipolar electric field as a result. According to the upflow classification in Chapter 4, the classes of ion flux observed during the event are low and medium upflow flux. The ion upflow driven by the elevated T_i is predominantly at altitude ≥ 300 km which, peaked at 4.67×10^{13} m^{-2} s^{-1} above 300 km around 00:10 LT.

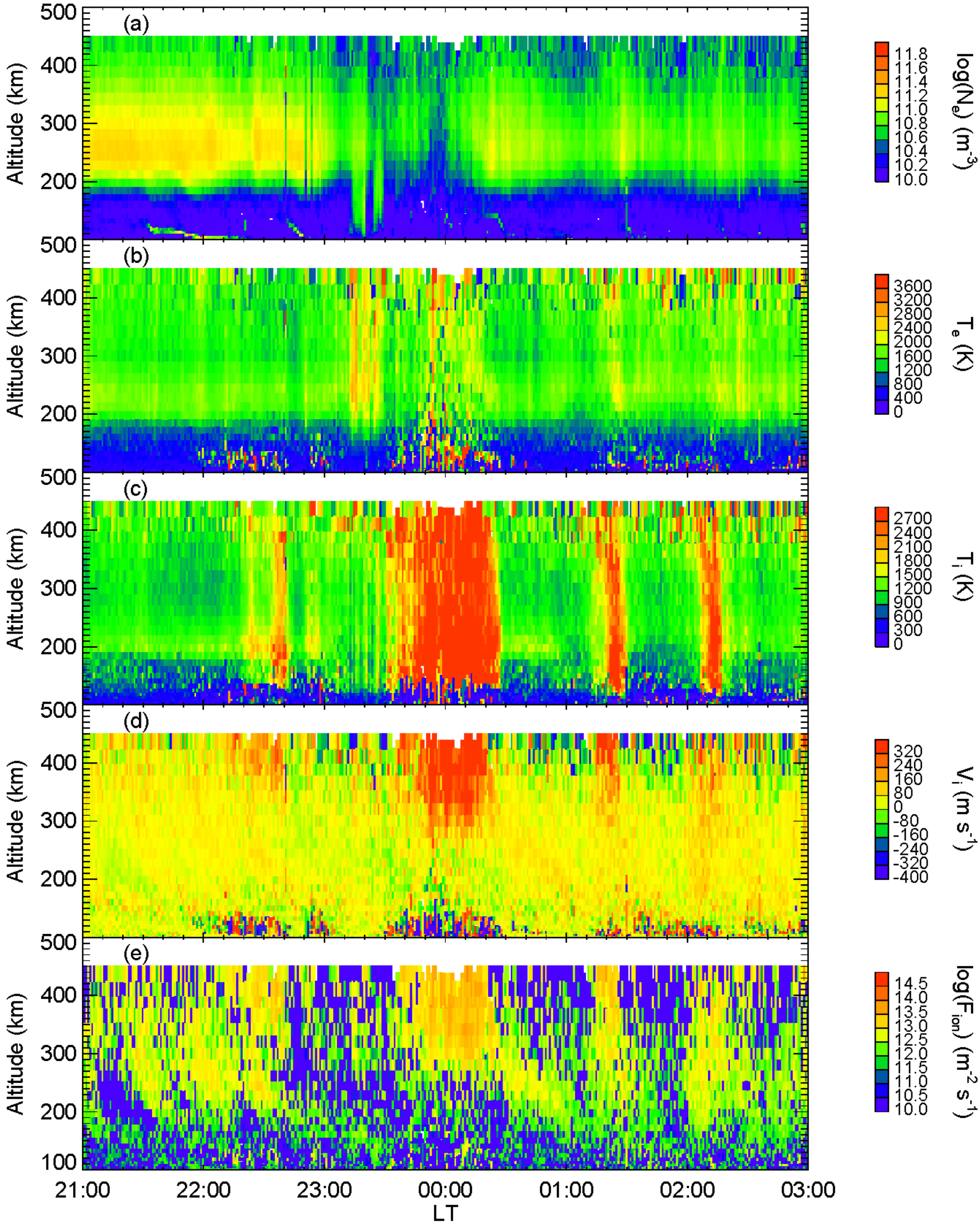

Figure 5.8: Plot showing ion upflow around midnight, during low conductivity and high ion-neutral relative motion, observed by the ESR 42 m dish on September 11, 2007. The panels' format is the same as outlined in Figure 5.2.

5.3.2.2 OMNI measurements

- **20070911 nightside event**

The OMNI measurements cover six hours between 21:00 – 03:00 LT. The ring current on first panel of Figure 5.9 shows a barely negative perturbation throughout the six-hour period under investigation. However, the perturbation is very weak and insignificant with a minimum value of about -7 nT which falls in the quiet range for ring current classification. The blocky Sym-H indicates that there is no geomagnetic storm throughout the six-hour period. Furthermore, the difference between the magnitude of the upper and lower magnetic field perturbations recorded by ground-based magnetometers array, ranges between $13\ \mathrm{nT}\ \leq |AU| - |AL| \leq 28\ \mathrm{nT}$ which, indicates that there is no signature of substorm onset and substorm occurrence during the time interval. The dynamic pressure and the upstream velocity on the fourth and fifth panels indicate a low pressure and slow solar wind speed that ranges between about $0.95 \pm 0.25\ \mathrm{nPa}$ and about $300 \pm 10\ \mathrm{km\ s^{-1}}$ respectively. The flow speed that begins around $300\ \mathrm{km\ s^{-1}}$ at about 21:00 LT fluctuates and decreases gradually until it reaches about $290\ \mathrm{km\ s^{-1}}$ around midnight. Thereafter, there are intermittent sharp increases within half an hour until it reaches a peak of about $307\ \mathrm{km\ s^{-1}}$ indicating a fairly slow solar wind for the period. The orientation of IMF B_y from the sixth panel shows a duskward orientation throughout the time interval while on the seventh panel, B_z orientation remains southward within the same period with a peak minimum of around -3.0 nT. However, the total magnitude of the IMF on the last panel does not indicate any significant strength at the periods of T_i elevations compare to other periods within the time interval.

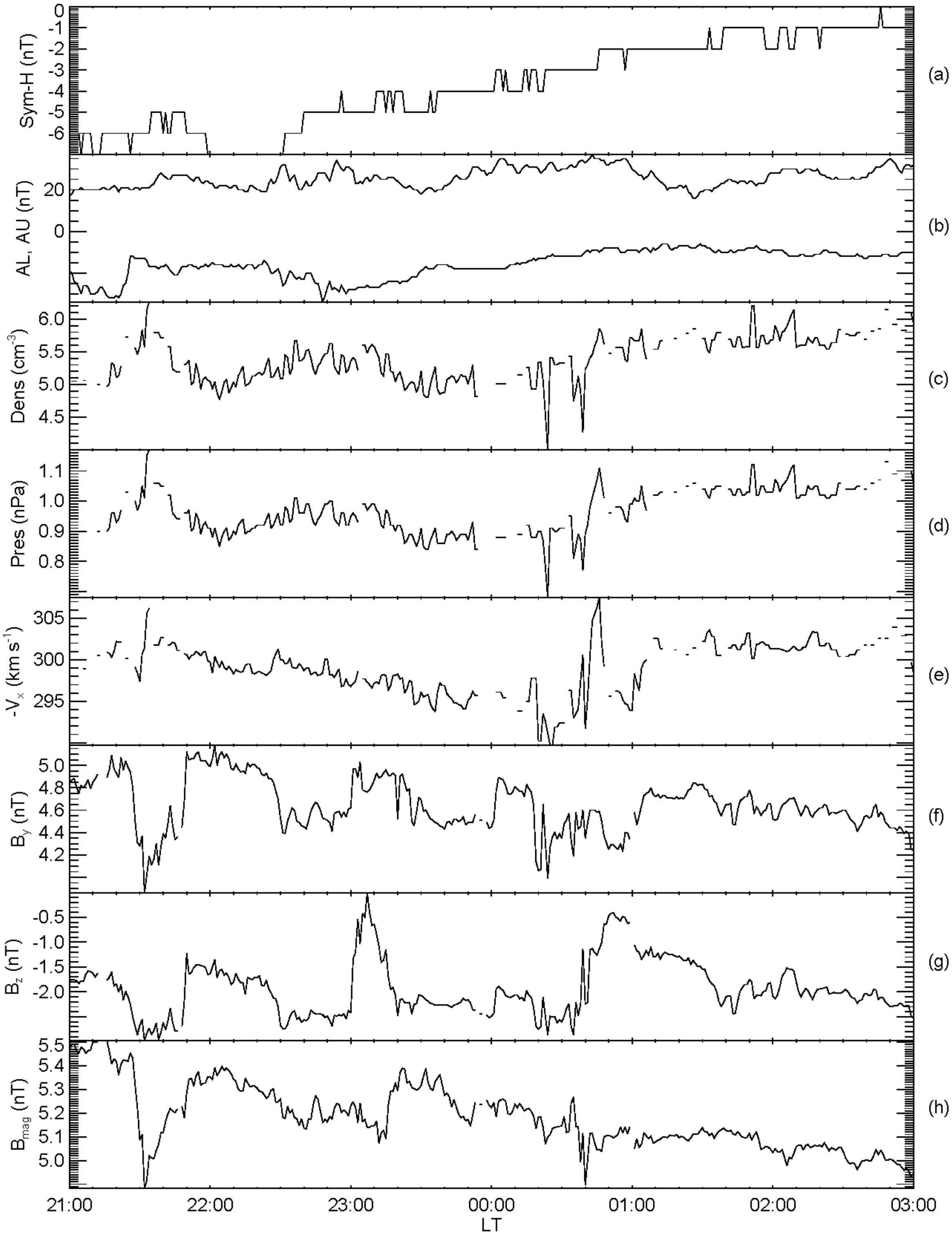

Figure 5.9: Plot showing the OMNI measurements for the midnight event on September 11, 2007 from 21:00 - 03:00 LT. The panels' format is the same as outlined in Figure 5.4.

5.3.2.3 Ion momentum plot

Figure 5.10 is presented in this section for the ion momentum plot of the September 11, 2007 event, and it has the same format as outlined in section 5.3.2.3. An additional plot, Figure 5.11, is added in an attempt to investigate and validate the processes leading to the ion upflow during the September 11, 2007 event.

- **20070911 nightside event**

As earlier mentioned, attention is focussed on the event that happens between 23:30 LT on September 11, 2007, until 00:30 LT the following day. During the aforementioned period, the first panel of Figure 5.10 shows that the ambipolar electric force is predominantly negative. Thereafter, from 00:30 LT until the rest of the LT interval being investigated, downward ambipolar force dominates the altitudes below E and lower F layers, while the upper parts of the F layer remain predominantly at equilibrium. The ion pressure gradient presented in the second panel, though a bit weak, is stronger than the ambipolar electric field the period within the 23:30 – 00:30 LT window. The balance force on the third panel is predominantly negative between 23:30 – 00:10 LT, an indication that the gravitational pull is dominant over the pressure gradients in equation (2.8), whereas the fifth panel on the figure indicates that ions are outgoing within the time interval. With this I can draw a conclusion that there is another mechanism other than the kinetic-induced ambipolar force arising from precipitation, which is responsible for the upwelling within the time interval. This other force, Joule heating, is electromagnetic in nature (Moore et al., 2014). The CUTLASS Finland radar shows a paucity of data during the six-hour period and it is difficult to tell if there is any high perpendicular flow to the field during the period. In addition, the last panel of Figure 5.10 shows that a weak current system is set up in the lower and upper electrojet, giving rise to weak magnetic perturbation as indicated by the AL and AU indices. The excursion of the AL and AU indices shows that there is no indication of substorm onset during the period.

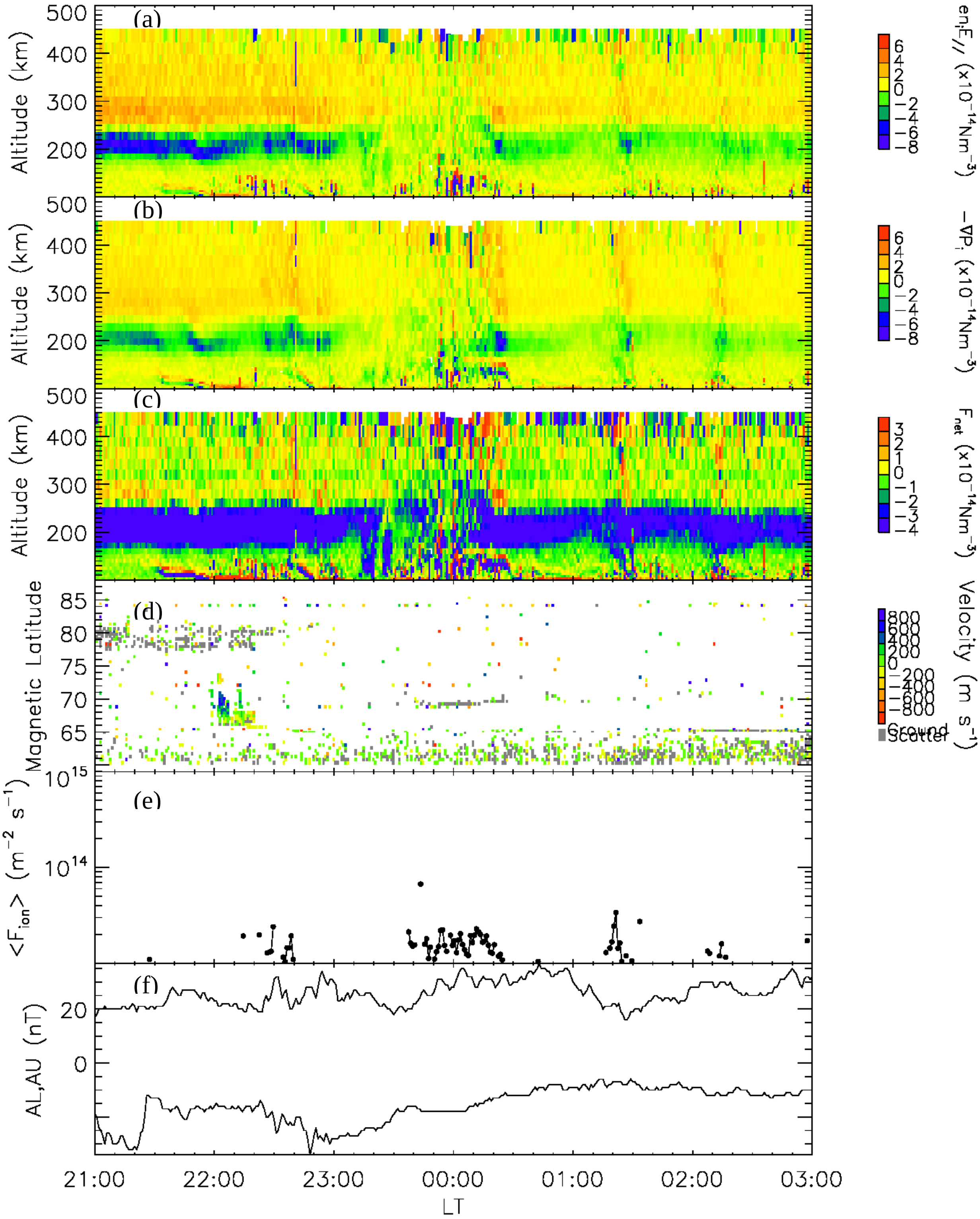

Figure 5.10: Plot showing the Joule heating as the dominant driver of the ion upflow during the September 11, 2007 event. The first five panels have the same format as outlined in Figure 5.6. The last panel shows the AL and AU indices.

Figure 5.11 comprises five panels, of which the first three show the plots from IMAGE magnetometer data for Ny-Ålesund (nal), Longyearbyen (lyr) and Hornsund (hor) stations respectively. The three stations are all high latitude stations, which are located within the Island of Norway in the Svalbard peninsula, around the polar region. Panel 1 shows that Ny-Ålesund at magnetic latitude (75.25°N) records a variation of about -20 nT to 20 nT from the baseline magnetic field, whereas on the second panel, the perturbation from baseline at Longyearbyen, which is the location of the ESR facilities, ranges between about -25 nT $\leq$ X ≤ 26 nT. The third panel shows that the magnetic perturbation at Hornsund (74.13°N), whose magnetic latitude is located slightly below that of Longyearbyen, is larger and has a maximum excursion to about -40 nT. The fourth panel of Figure 5.11 shows the velocity plot perpendicular to the magnetic field from line-of-sight velocity (v_{los}) beam 5 of CUTLASS Iceland radar which points North-East over Svalbard. The plot indicates plasma convection towards the radar between 21 – 23 LT, and also from 23:30 LT onward. However, high flow, away from the radar, dominates the period from midnight until around 03:00 LT. Moreover, a shear in velocity, which is pronounced between 00:20 – 00:30 LT as a result of convection reversal, the Harang discontinuity, is observed from magnetic latitude $70 - 75^{\circ}$N. The plot on the last panel of Figure 5.11 is the SuperMAG Upper and Lower (SMU, SML) auroral electrojet indices from SuperMAG global ground-based magnetometer database. The plot shows a weak enhancement in the SML before and after midnight. The peak difference in perturbation caused by the substorm electrojet is about 90 nT during the SMU and SML six-hour excursion period. The perturbation shown by the SuperMAG plot in Figure 5.11 is greater than that shown by the AU and AL indices from Figure 5.10. The reason for the difference could be as a result of differences in baseline technique being used, uncertainty in data, and above all, more robust network (over 300) of ground-based magnetometers covered by SuperMAG for better statistical average.

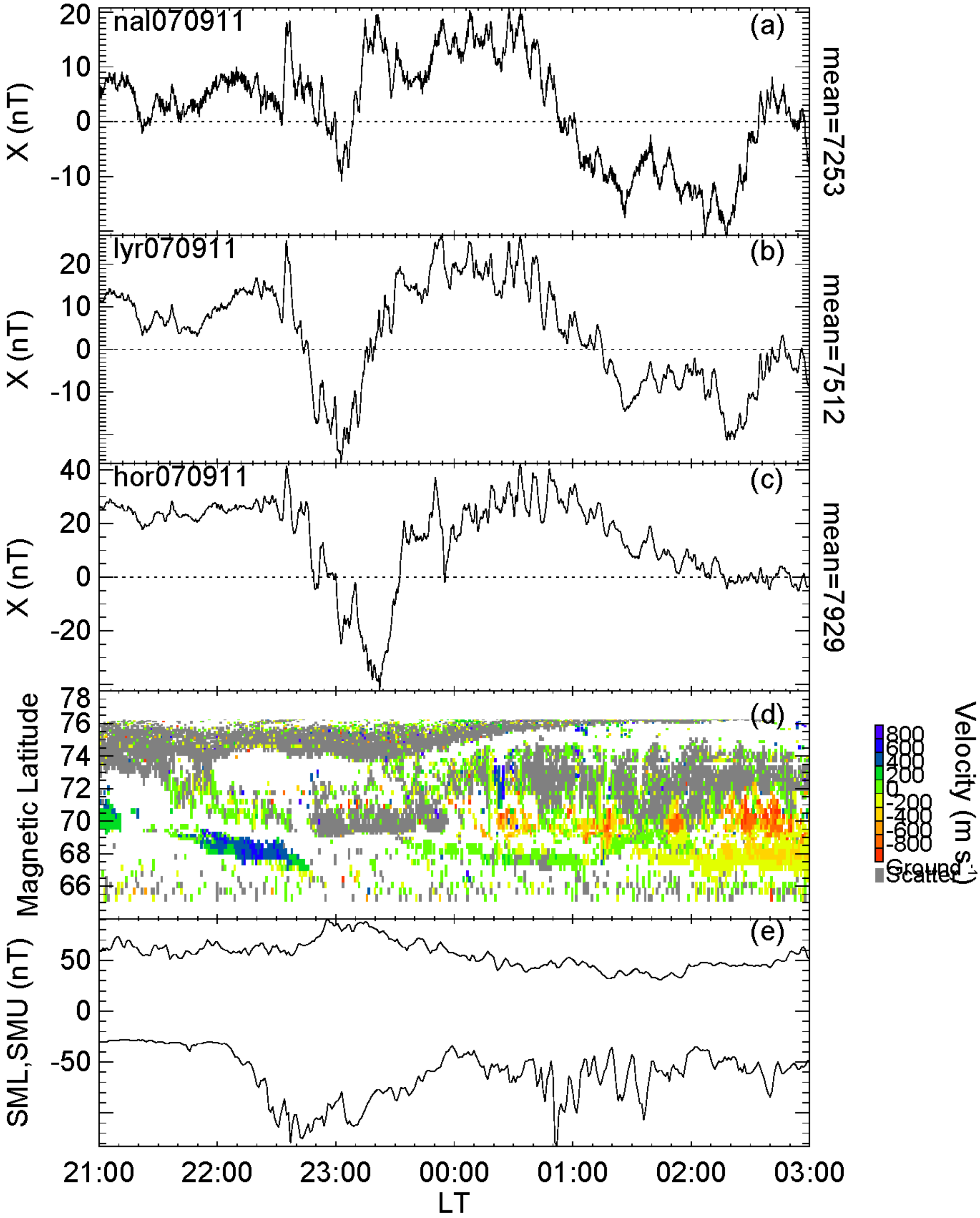

Figure 5.11: Plot showing additional parameters to validate that the September 11, 2007 event, is due to friction between ion and neutral other than substorm occurrence. The first three panels show magnetic perturbation observed by the IMAGE ground magnetometer at (a) Ny-Ålesund, (b) Longyearbyen, and (c) Hornsund, while the last two show the (d) beam 5 from CUTLASS Iceland radar, and (e) SuperMAG upper and lower auroral electrojet indices respectively.

5.3.3 Discussion

It is unlikely to have magnetospheric loading of energetic particles that can intensify the ionospheric currents above the ionosphere at Longyearbyen, Svalbard and other neighbouring high latitudes due to the insignificant magnetic perturbations measured around the time interval. Furthermore, the global auroral electrojet average from OMNI data and SuperMAG also indicate that there are either no or weak substorm activities that could increase conductivity during the period. However, IMAGE magnetometer data indicates wave activity in the magnetic field, which can scatter particles and energize them into the Earth's polar region. The Iceland radar indicates a shear in velocity as a result of convection reversal observed from magnetic latitude $70 - 75^{\circ}$N, which occurs from 00:10 – 01:30 LT (pronounced between 00:20 – 00:30 LT). The implication of this according to Lockwood et al. (1988) is that regions of elevated T_i would be generated as the boundary of the polar cap moves as a result of ion-neutral friction, and probably leading to outgoing ions resulting from velocity higher than that at the boundary. As can be seen from the fourth panel of Figure 5.11, the plasma convection is towards the radar between 00:20 – 00:30 LT at magnetic latitudes around $70 - 72^{\circ}$N and away from the radar at magnetic latitudes around $72 - 75^{\circ}$N at about the same time interval, with a perpendicular flow magnitude between $600 - 800 \text{ m s}^{-1}$ in both cases. As a result of the velocity shear indicating an ions and neutrals anti-parallel flow, T_i elevation occurs in the equatorward part of the boundary (Lockwood et al., 1988 and references therein) and drives the Joule heating effect. The ambipolar electric force from Figure 5.10 predominantly shows a downflow at the time of event, which indicates that the ion upflow driver for the September 11, 2007 event could not be due to ambipolar force. I can conclude that the increase in T_i as seen from Figure 5.8 could only be brought about by electromagnetic energy through wave activity that drives the ion-neutral relative motion through the Poynting flux (Moore et al., 2014), which leads to high flow speed perpendicular to the geomagnetic field and conversion to Joule heating as a result. Attenuated ionosphere observed from the electron density in the first panel of Figure 5.8 and high T_i from the third panel can only occur during high perpendicular flow speed ($\text{v}_{\perp}$), which gives rise to faster recombination of the particles (a reduction in plasma density and ion to carry current) and hence, reduced conductivity. Increase in velocity perpendicular to the field implies an increase in the perpendicular electric field, which is proportional to the square root of the Joule heating rate.

$$Q_J = \Sigma_p E^2 \tag{5.1}$$

where Q_J is the Joule heating,

Σ_p is the ionospheric conductivity, and

E indicates the ionospheric electric field strength.

The Joule heating arising from the $v_\perp$, would initial show an increase in the perpendicular temperature ($T_\perp$), which will later translate to an increase in temperature parallel ($T_{//}$) to the field as particles scatter and return the plasma to isotropy (Cowley, 2017). Cai et al. (2014) and references therein have mentioned that increase in ion temperature could be the result of the Joule heating effects on the dynamics of magnetosphere-ionosphere coupling. Furthermore, the relative motion between ions and neutrals generates frictional heating which raises ion temperature (Skjæveland et al., 2014).

The September 11, 2007 event is indeed a rare occurrence and has revealed a contrary opinion to the submission that there cannot be any remarkable outflow irrespective of the amount of the Poynting flux as long as we have zero precipitating flux (Moore et al., 2014). Throughout the period of IPY 2007 campaign, this is the only event that is caused by high increase in T_i without precipitation flux or substorm occurrence and lasted for about an hour with sufficient upflow. Similar phenomenon driven by T_i without electron precipitation during the campaign is seldom (say, 10 events ~ 1.4% of total events) as observed by ESR, and only lasted between 10 – 15 minutes. This could be due to the deep solar minimum period that coincides with the campaign. A future campaign for at least a year around solar maximum would be suggested for collaborative effort of the international scientific community to research the polar regions.

Most of the short duration periods, where there is an increase in the Poynting flux, but no precipitation flux, ended up with little or no outgoing ions as claimed by Moore et al. (2014). The ESR parameter plots in Figures 5.12 and 5.13 show examples of periods without electron precipitation during a short duration increase in T_i around 01:35 – 01:45 LT on March 27, and December 22, 2007 respectively. The latter indicates that about $< 2.5\%$ of the data points around the time interval satisfy the upflow threshold while the upflow flux in the former is insignificant. The peak flux observed during the March 27, and December 22, 2007 events are $8.67 \times 10^{12}\ \mathrm{m^{-2}\ s^{-1}}$ and $3.79 \times 10^{13}\ \mathrm{m^{-2}\ s^{-1}}$ respectively. It is importance to note that such events with an increase in T_i with reduced number density, which indicates an evacuated atmosphere leading to reduction in conductivity, is observed only at the nightside during the IPY 2007 campaign. There is no dayside event where there is an increasing T_i without precipitation flux.

5.3.4 Summary

The September 11, 2007 event has shown a period of little or no conductivity and a case where the ionosphere is attenuated during a high increase in ion temperature between 23:30 – 00:30 LT. Outgoing flux reaching a peak of about $4.67 \times 10^{13}\ \mathrm{m^{-2}\ s^{-1}}$ above 300 km around 00:10 LT is observed during the event. IMF B_y shows a duskward asymmetry while B_z is southward throughout the time interval being investigated. Global and local ground-based magnetometers data indicate weak or no substorm occurrence. The ambipolar electric force is predominantly weak and negative during the period of event that begins around 20:30 LT and likewise the ion momentum balance force. However, a velocity shear is indicated by beam 5 of CUTLASS Iceland radar around 00:20 LT on September 12, 2007, suggesting ion-neutral friction causing initial enhancement in the temperature perpendicular to the field, which will later translate to elevated ion temperature along the parallel magnetic field. The period of increase in ion temperature (T_i) during the interval, which indicates an increase in the magnitude of the relative velocity between ions and neutrals, $|v_i - v_N|$, the absence of strong upwelling ambipolar electric force and also coupled with the velocity shear in the plasma convection, suggests Joule heating as the driver of the September 11, 2007 event. The event is indeed a rare occurrence and has revealed a contrary opinion to the submission that there cannot be any remarkable outflow irrespective of the amount of the Poynting flux as long as there is no precipitating flux (Moore et al., 2014).

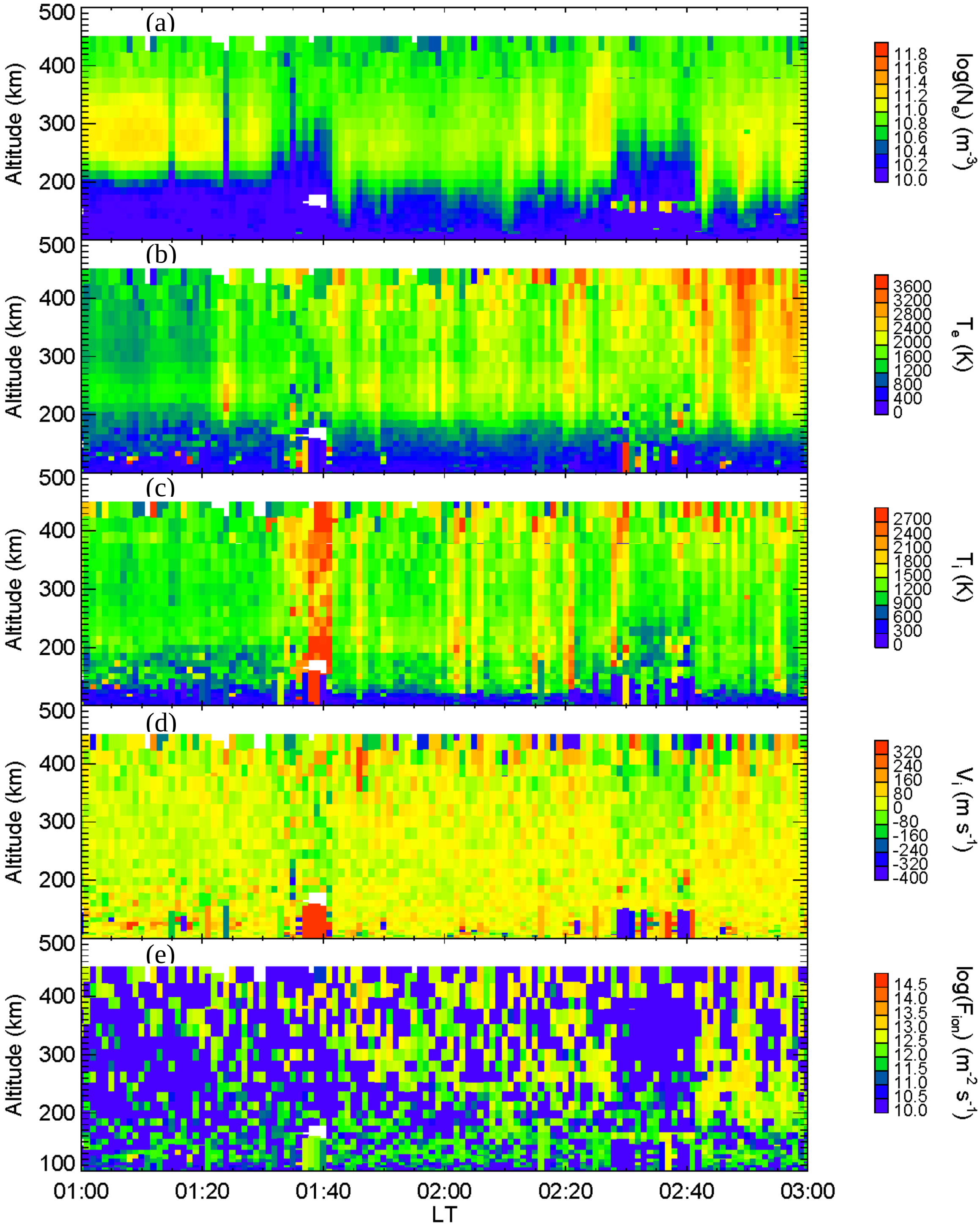

Figure 5.12: ESR parameter plot showing an example of events with insignificant ion upflow during low conductivity and elevated ion temperature observed on March 27, 2007. The panels' format is the same as outlined in Figure 5.2.

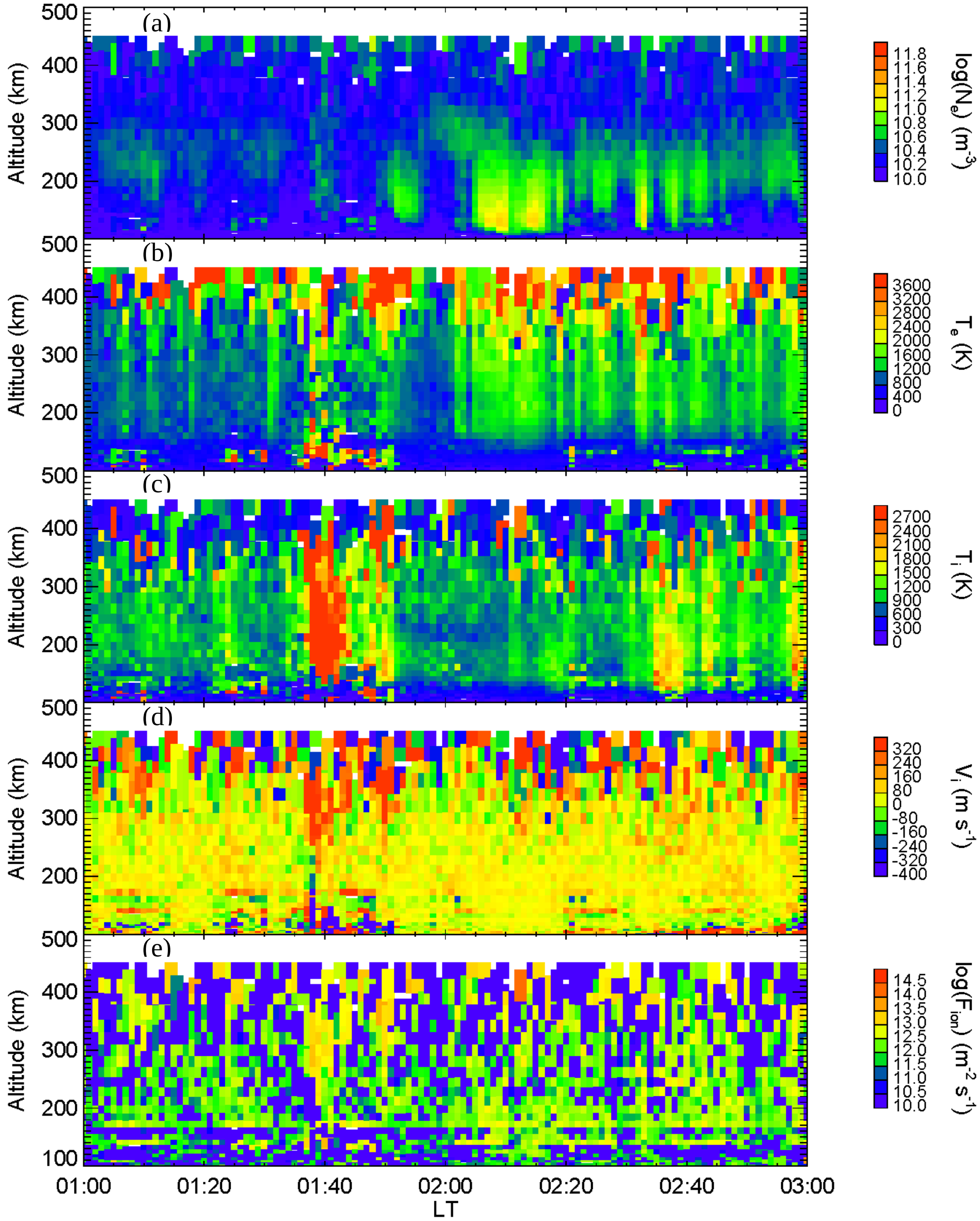

Figure 5.13: ESR parameter plot showing an example of events with very little ion upflow during low conductivity and elevated ion temperature observed on December 22, 2007. The panels' format is the same as outlined in Figure 5.2.

5.4. Case Study 3: Events driven by both ambipolar electric field and Joule heating

5.4.1 Results and Discussion

5.4.1.1 ESR parameter plot

- **20070929 dayside event**

The September 29, 2007 event is a dayside event which shows intermittently strong precipitation in the electron density profile panel of Figure 5.14. The electron precipitation covers all the six-hour duration around noon from 09:00 – 15:00 LT, and predominantly extends down to 100 km altitude throughout the period. Elevated electron temperature, T_e, is observed on the second panel predominantly at altitudes ≥ 200 km almost throughout the time interval. Since an increase in either or both conductivity as well as magnitude of the relative velocity between ions and neutrals can lead to ion heating, the ion temperature, T_i, on the third panel indicates a positive response across all altitudes to highly variable conductivity implied by the first panel. However unlike the electron temperature, the elevated T_i discontinues at about 13:30 LT. The fourth Panel shows high flow along the field lines predominantly above 200 km altitude. At the time of simultaneously elevated electron and ion temperatures around 09:00 – 13:10 LT, the field-aligned velocity is higher than when T_i discontinues. This is translated to the features observed in the upflow flux on the last panel of Figure 5.14, where the ion upflow flux reaches a peak of 7.58×10^{13} m^{-2} s^{-1} between the time interval of simultaneous elevated T_e and T_i, while the peak upflow is reduced to 6.29×10^{13} m^{-2} s^{-1} when only the increase in electron pressure gradient drives the upflow (Figure 5.18). During the conjunction of elevated T_e and T_i, about 11% of the data points exceed the upflow threshold mentioned in Chapter 4, while only about 1.7% do in the session without elevated T_i. Furthermore, the ion upflow covers more altitude in the former than the latter probably due to the wider coverage of T_i.

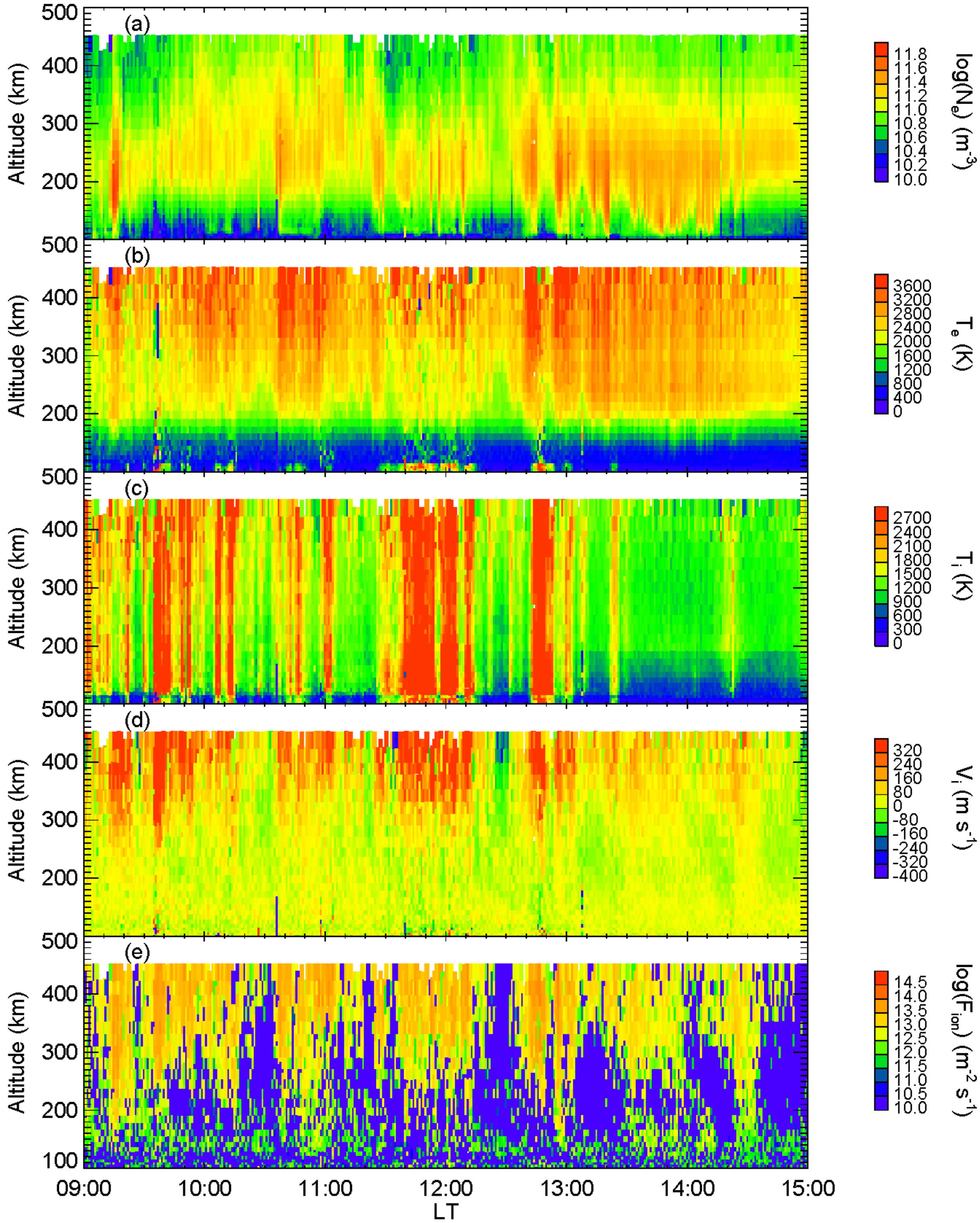

Figure 5.14: ESR parameter plot showing an example of events with ion upflow around cusp, during simultaneous increase in electron and ion temperatures, observed on September 29, 2007. The panels' format is the same as outlined in Figure 5.2.

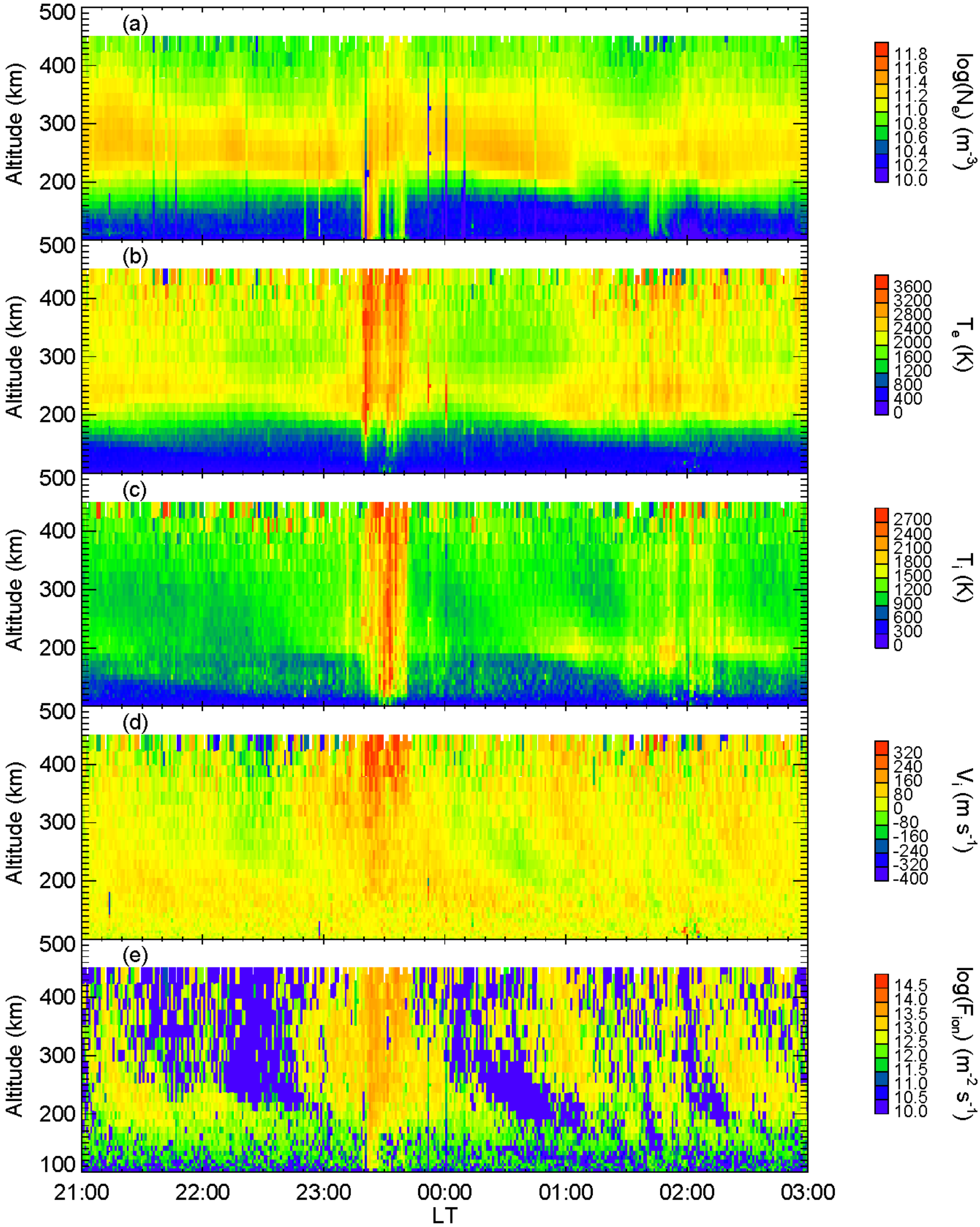

Figure 5.15: ESR parameter plot showing an example of events with ion upflow around midnight, during simultaneous increase in electron and ion temperatures, observed on April 18, 2007. The panels' format is the same as outlined in Figure 5.2.

- **20070418 nightside event**

Figure 5.15 presents the nightside event on April 18, 2007, which begins with a weak electron density in the region below 200 km until around 23:20 LT when a strong precipitation extending to 100 km altitude takes place. Although the intense precipitation is short-lived (less than 10 minutes), it is immediately followed by a moderate precipitation also extending to 100 km until around 23:40 LT. Thereafter, the ionosphere goes back to its former state as at begin of the interval. The time interval between 23:20 – 23:40 LT corresponding to time of electron precipitation is observed to coincide with enhanced electron and ion temperatures as shown on the second and third panels respectively. The simultaneous increase in T_e and T_i does give rise to high field-aligned flow within the same time interval as shown on the fourth panel. The last panel showing keogram-like plot of the ion flux indicates ion upflow within the time interval of simultaneous increase in n_e, T_e, T_i and v_i. The ion upflow during this event cut across wide range of altitudes (from above 100 km), which may likely be driven by nightside auroral substorms as will be seen in section 5.5.2.3. The peak upflow derived from the basic ESR parameters attains the high upflow category at a value around $1.09 \times 10^{14}\ \mathrm{m^{-2}\ s^{-1}}$ at about 23:20 LT, during the time of wide intense precipitation extending to 100 km altitude, and furthermore, about 34% of the data points meet the upflow threshold criterion of $10^{13}\ \mathrm{m^{-2}\ s^{-1}}$.

5.4.1.2 OMNI measurements

- **20070929 dayside event**

The ring current index on the first panel of Figure 5.16, begins with a weak perturbation of about -35 nT and decrease to peak minimum value of about -52 nT for the six-hour observation around 10:00 LT. Thereafter, a slow and varying recovery follows until it attains a quiet Sym-H value of about -22 nT. The AL and AU indices indicate that substorms occurrence dominates over half of the six-hour period. AL is observed to reach the peak minimum of the period at about 10:28 LT with a value less than -1000 nT and this coincides with a period of electron precipitation down to about 100 km, with an intense density around 100 km as shown in Figure 5.14. The third and fourth panels of Figure 5.16 show a low density and dynamic pressure regime coming from the solar wind plasma. The ram pressure throughout the six-hour duration ranges between 2.5 ± 1.0 nPa, indicating a weak compression of the terrestrial magnetic field on the dayside magnetopause. However, high speed upstream flow of the solar wind plasma is observed to fluctuate on the fifth panel, reaching a minimum and maximum value of about 600 km s^{-1} and 680 km s^{-1} respectively. The solar wind speed is an important parameter to estimate the quantity of energy coupled from the solar wind into the magnetosphere, and the reconnection rate bears a direct relationship with four-third of its power (Milan et al., 2012). In the light of the above, the precipitation observed on Figure 5.14 might be connected with the high flow speed that dominates the entire six hours. The panel showing the IMF B_y indicates a swing between dawnward and duskward position of the cusp until around 11:00 LT, thereafter, it remains predominantly duskward until around 14:00 LT. This affects the convection pattern as the time around 11:10 – 12:00 LT and 12:40 – 14:00 LT show periods of long duration of strong precipitation to the E-region in Figure 5.14 coinciding with periods when the B_y is predominantly stable in the duskward orientation as shown in Figure 5.16. On the seventh panel is the B_z component of the interplanetary magnetic field, which begins from southward orientation and turns gradually northward. However, further analysis of the data shows that about 70% of the area under the curve indicates southward B_z throughout the period. This accounts for the long duration of precipitation as a result of reconnection between the earth's magnetic field and the interplanetary magnetic field on the dayside. The last panel of Figure 5.16 indicates that geo-effectiveness of the IMF during the first half of the time interval is higher than in the second half, which might be connected with much of ion upflow observed in the first half than second half of the period.

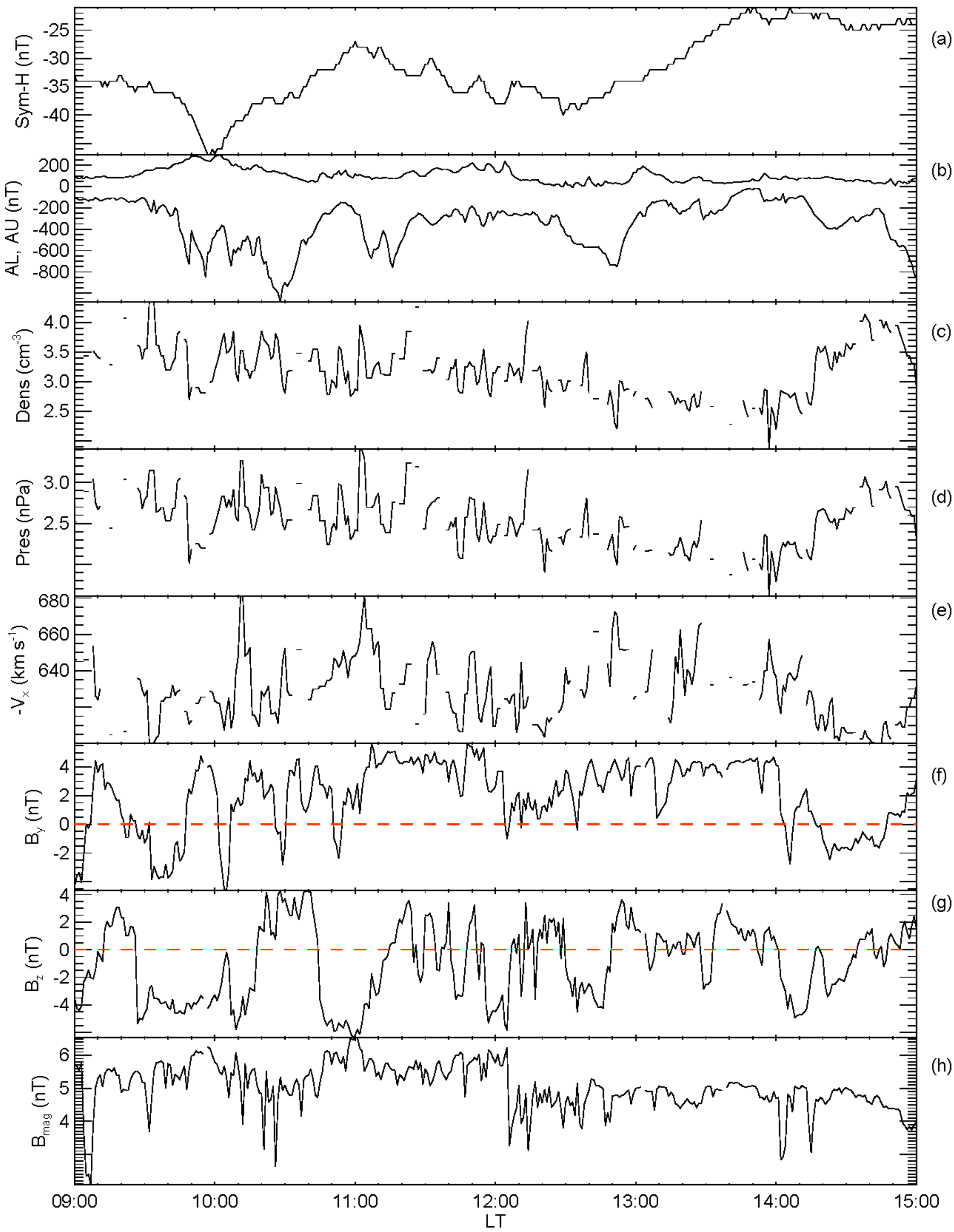

Figure 5.16: Plot showing the OMNI measurements for the cusp event on September 29, 2007 from 09:00 - 15:00 LT. The panels' format is the same as outlined in Figure 5.4.

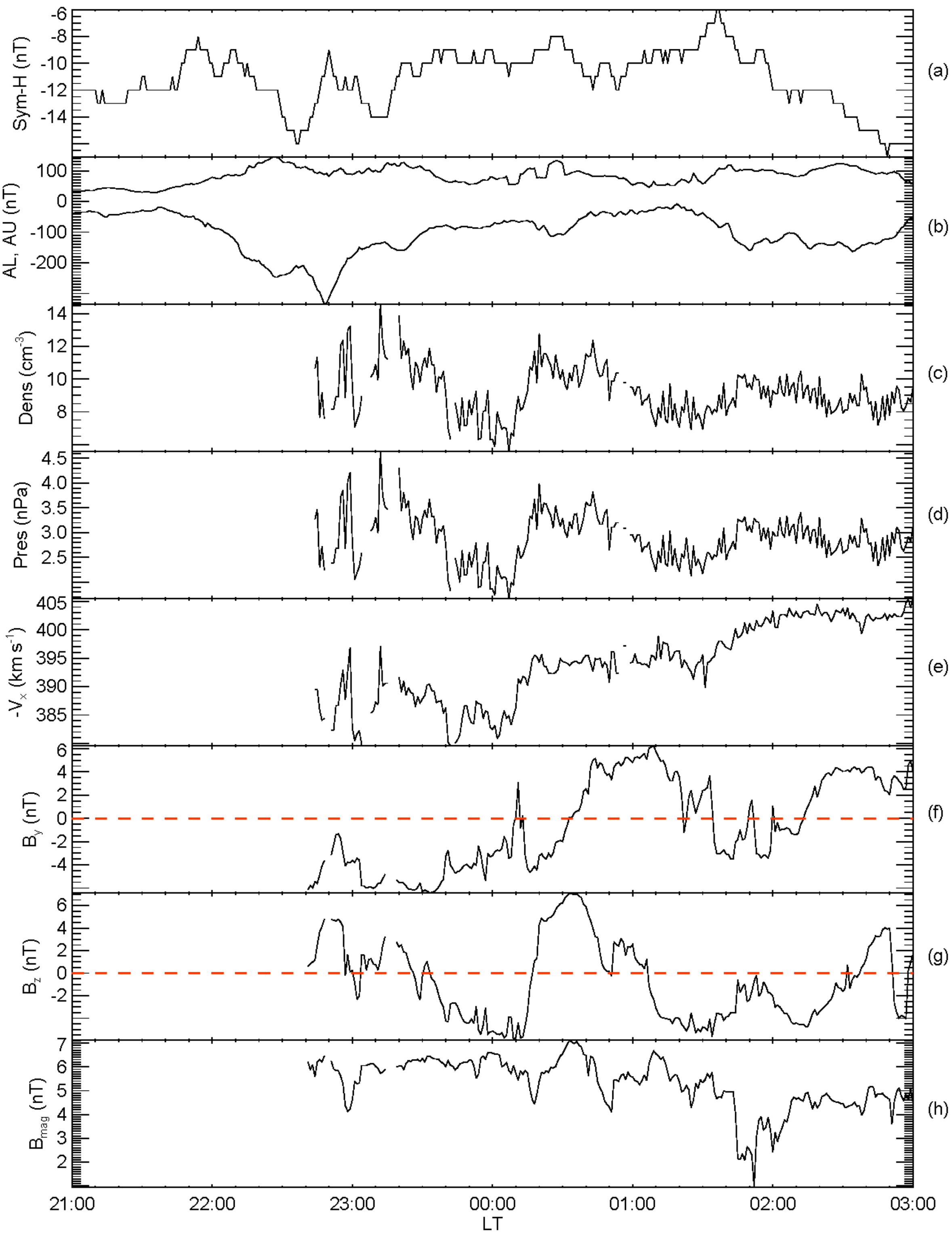

Figure 5.17: Plot showing the OMNI measurements for the midnight event on April 18, 2007 from 21:00 - 03:00 LT. The panels' format is the same as outlined in Figure 5.4.

- **20070418 nightside event**

Quiet ring current values greater than -17 nT span the entire six-hour time interval around midnight on Figure 5.17, however, substorm onset is observed in the AL and AU indices on the second panel around 22:50 LT on April 18, 2007. Moderate substorm occurrence, where AL magnitude is greater than 300 nT as a result of the contribution from the substorm current electrojet, precedes the April 18, 2007 event. At about the time of commencement of event around 23:10 LT, the solar wind density and the ram pressure attain their respective maxima of about $14.5\ \mathrm{cm}^{-3}$ and 4.6 nPa for the period. It is logical to infer that about 10^7 per cubic meter dense solar wind will facilitate more precipitation due to reconnection, which is observed at the nightside, signalled by the substorm expansion in the second panel. Moreover, Milan et al. (2012) suggested that pressure does not affect the dayside reconnection rate, however high solar wind pressure can lead to the onset of nightside reconnection. This is due to pressure compressing the tail and causing substorm onset, but does not directly affect the level of precipitation. At about 23:00 LT the solar wind speed decreases sharply to about $380\ \mathrm{km\ s}^{-1}$ and thereafter, at about the time coinciding with period of maximum density and pressure, a sudden increase in the solar wind speed to about $397\ \mathrm{km\ s}^{-1}$ is observed. A dawnward B_y asymmetry is observed on the sixth panel throughout the short interval that the event takes place. On the part of B_z, however, a southward turning begins immediately at the time of commencement of event until it reaches about -4 nT around 00:10 LT the following day. The last panel indicates that the magnitude of the IMF is above the period average at the time of event.

5.4.1.3 Ion momentum plot

- **20070929 dayside event**

The first panel showing the ambipolar electric force on Figure 5.18 indicates a period of strong upward force from altitudes predominantly above 250 km throughout the time interval. However, at about 09:10 LT, the strong ambipolar electric force extends to around 200 km altitude as a result of wider coverage of strong precipitation observed in Figure 5.14 around $120 - 300$ km altitude. On the other hand the ion pressure gradient on the second panel, which is our proxy for the Joule heating, shows effectiveness from about 200 km altitude whenever it is strongly elevated. This is because the Joule heating as a result of current closure in the ionosphere occurs in the Pedersen layer. Conjunctions of enhanced ambipolar electric force and ion pressure gradient are observed around 09:10 – 09:20, 09:35 – 09:45, 11:40 – 12:10 and 12:40 – 13:20 LT and these time intervals show periods of enhanced upward net force on the third panel of Figure 5.18. The balance force on the third panel also indicates enhancement between 13:40 – 14:20 LT, but does not have wide altitudinal coverage as in the case of periods of conjunction of ambipolar electric force and Joule heating and as a result, the ion upflow flux average on the fifth panel between 13:40 – 14:20 LT is not as much as at the periods of conjunction. The line-of-sight velocity plot of beam 9 CUTLASS Finland radar in the fourth panel begins with a moderate flow of magnitude at about 400 m s^{-1} away from the radar around the ESR magnetic latitude. At about 09:30 LT, the perpendicular flow to the field becomes sufficiently enhanced and attains a magnitude between $800 - 1000$ m s^{-1}. The fast flow continues until about 12:30 LT around the ESR magnetic latitude, and thereafter, there is paucity of data. The available data from the CUTLASS Finland radar indicates strong cusp signature during the September 29, 2007. Again as observed under Case Study 1, the fifth and sixth panels of Figure 5.18 confirm that ion upflow is possible during both southward and northward orientation of IMF B_z. However, the upflow occurrence seems to be higher on average during southward B_z as shown at the intervals between 09:30 – 10:20 LT and 10:40 – 11:10 LT in comparison to intervals between 11:10 – 11:40 and 12:50 – 13:20 LT, which are predominantly associated with northward B_z.

- **20070418 nightside event**

The first three panels of Figure 5.19, namely the ambipolar electric force $\left(en_iE_{//}\right)$, ion pressure gradient $(-\nabla P_i)$ and the balance force (F_{net}), show that during the time interval of the April 18, 2007 event being investigated, 23:20 – 23:40 LT, the three forces show enhancement in the upward direction across altitudes predominantly from about 250 km to over 400 km, whereas the gravity exerts pressure on the electron and ion pressure gradients at other time intervals and as a result, keeps their enhancement below 300 km altitude. The fourth panel on Figure 5.19 presents the line-of-sight velocity plot of beam 5 CUTLASS Iceland radar, where moderate velocity shear is observed at magnetic latitude below 70°N at the time of the event which can cause ion-neutral friction as explained in detail under section 5.3.3. Significant ion upflow flux is observed on the fifth panel during the time interval 23:20 – 23:40 LT than at any other time and in addition, further analysis reveals that about 69% of the upflow occurs during the short duration corresponding to period of event. Moreover, the peak upflow flux during the conjunction of ambipolar electric force and Joule heating indicated by elevated T_i and increasing ion pressure gradient around 23:20 – 23:40 LT is about $1.09 \times 10^{14}\ \mathrm{m}^{-2}\ \mathrm{s}^{-1}$, whereas it is about $3.48 \times 10^{13}\ \mathrm{m}^{-2}\ \mathrm{s}^{-1}$ and $1.73 \times 10^{13}\ \mathrm{m}^{-2}\ \mathrm{s}^{-1}$ around 01:00 LT and 02:30 LT respectively. The last panel on Figure 5.19 shows a similar trend on the excursion of AL and AU indices from 21:00 LT until around 22:10 LT when the auroral electrojet causes a further perturbation in the lower envelope covered by the AL index. The additional perturbation signals commencement of substorm onset, which attains peak minimum around 22:50 LT, a few minutes before the commencement of the April 18, 2007 event. Magnetometer data in Figure 5.20 shows that the contribution from Longyearbyen, the ESR location, to the magnetic perturbation observed to trigger the substorm occurrence takes place at about the exact time that the event commenced – 23:20 LT. The April 18, 2007 event is strongly correlated with the magnetometer spike at Longyearbyen around 23:20 LT in Figure 5.20 which coincides with the time a southward turning of B_z commenced (Figure 5.17), and a short burst of North-Eastward flow seen by the Iceland radar. All these and the global average indicated by the SuperMAG data in Figure 5.20 confirm that the April 18, 2007 outgoing event is triggered by substorm onset.

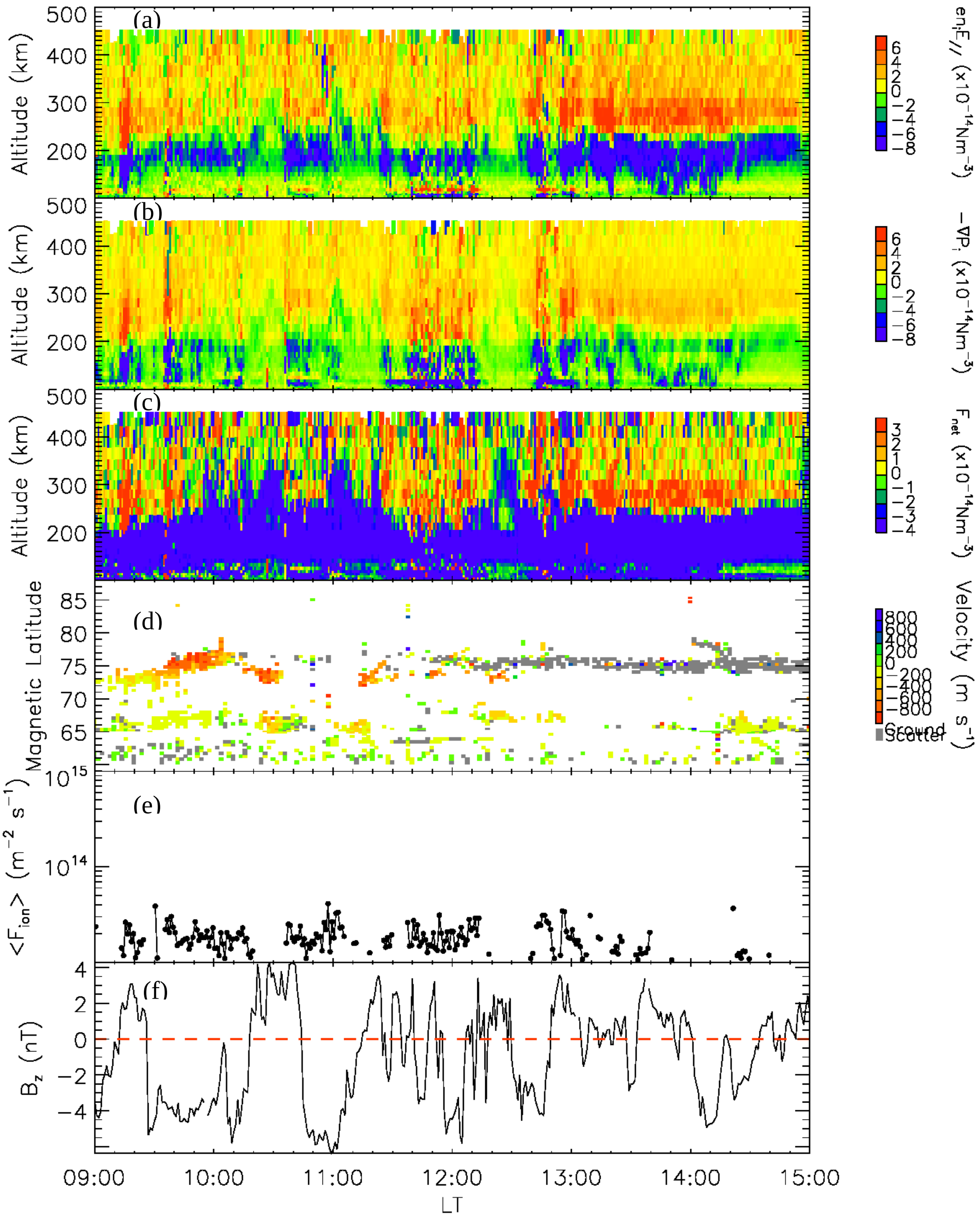

Figure 5.18: Plot showing ion upflow around cusp during simultaneous enhancement of the ambipolar electric force and Joule heating for the September 29, 2007 event. All the panels have the same format as outlined in Figure 5.6.

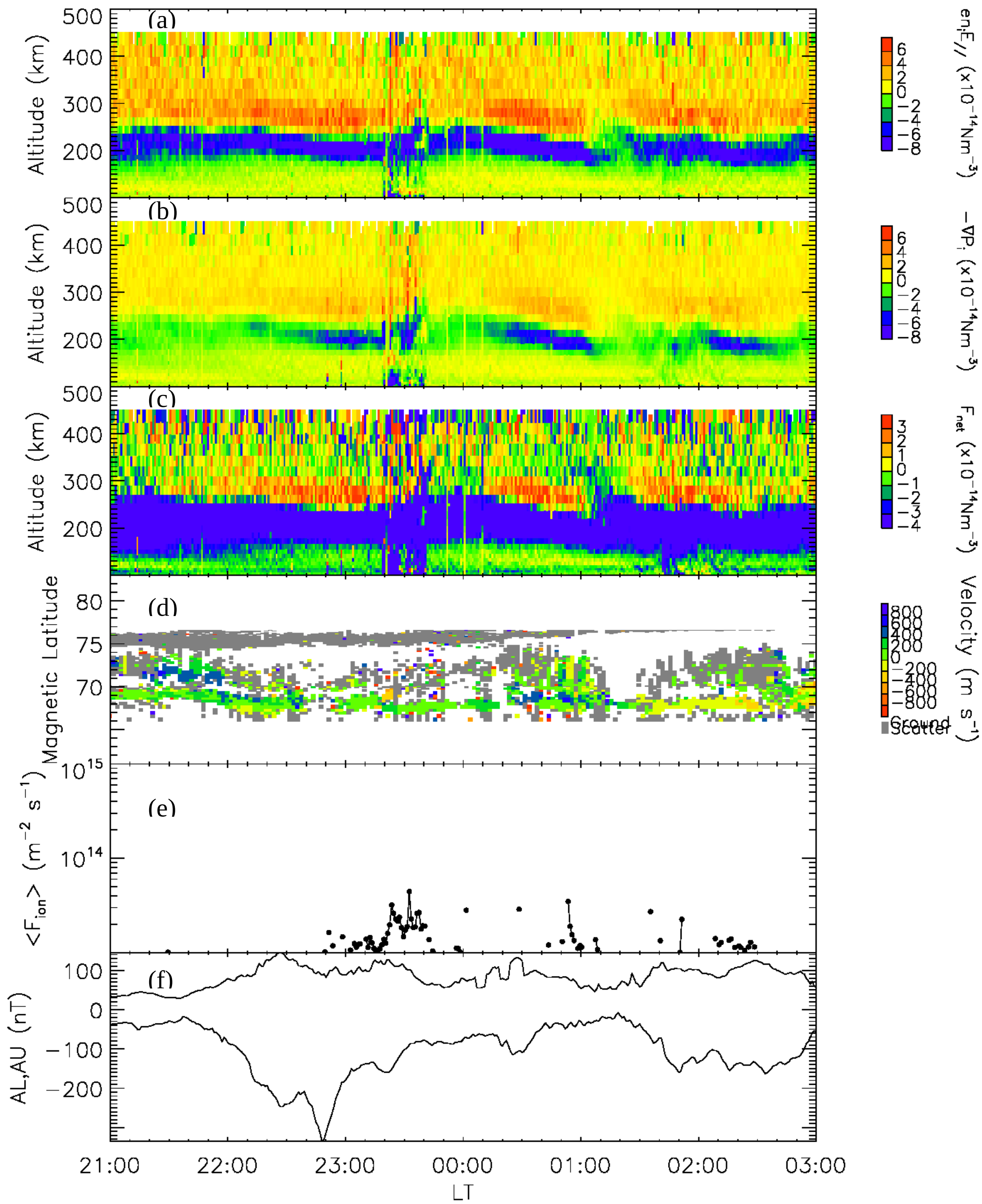

Figure 5.19: Plot showing ambipolar electric force and the Joule heating simultaneously driving the ion upflow during the midnight event on April 18, 2007. The six panels are the (a) ambipolar electric force $\left(en_iE_{//}\right)$, (b) ion pressure gradient $(-\nabla P_i)$, (c) balance force (F_{net}), (d) line-of-sight velocity (v_{los}) beam 5 of CUTLASS Iceland radar, (e) average value of ion upflow flux along the field-aligned profile $(< F_{ion} >)$, and (e) IMF B_z respectively.

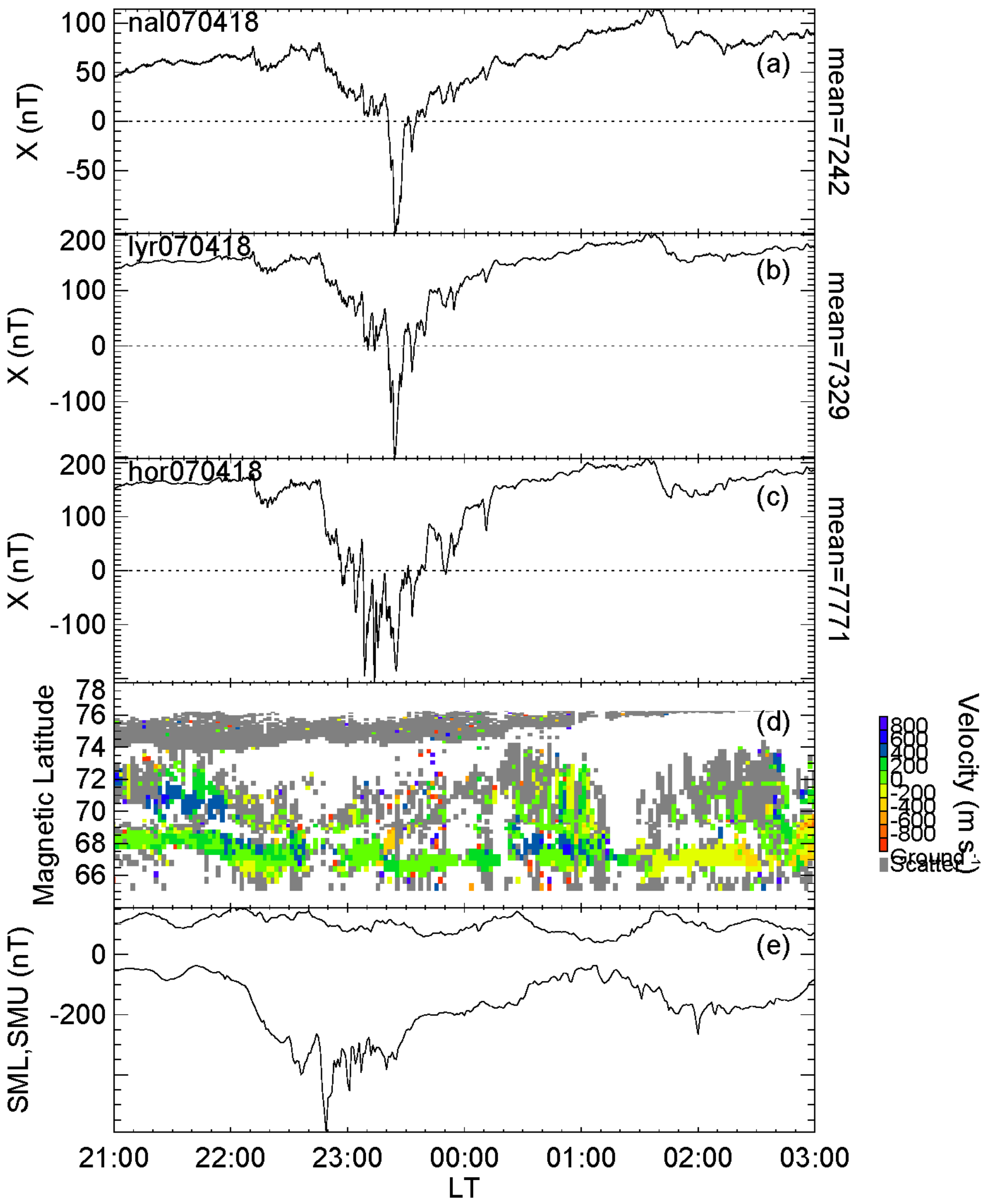

Figure 5.20: Plot showing the contribution from Longyearbyen to the global substorm occurrence during the April 18, 2007 event. The panels' format is the same as outlined in Figure 5.11.

5.4.2 Summary

The dayside event on September 29, 2007, ascertained by the SuperDARN plot to be cusp related, has shown a period when simultaneous elevation in electron and ion temperatures drive the ion upflow. It is observed that upflow happens at a respective ratio of $13 : 2$ during the simultaneous enhancement of T_e and T_i, and when T_i discontinues leaving only T_e to drive the upflow thus, suggesting a higher energization when electrons and ions are simultaneously heated. In addition, the peak upflow flux is higher in the former than the latter. On the other hand, the April 18, 2007 event, substorm-related, shows ion upflow from above 100 km, covering a wide range of altitude during a period of intense electron precipitation. While the dayside event on September 29, 2007, is characterized by high flow speed that can facilitate the enhancement of energy coupling at the magnetopause, the April 18, 2007 nightside event is described by high electron density in the solar wind, which under the right conditions can facilitate increasing number density during precipitation and hence, enhancing the ion flux. Furthermore, varying average ion upflow occurrence is observed during northward and southward orientations of IMF B_z with preference to the latter during the dayside event. For the nightside event, magnetic perturbation from baseline measured by the IMAGE ground-based magnetometers at Longyearbyen, where the ESR facilities is located, and other nearby high latitude station in the Svalbard peninsula shows a southward perturbation during the event time interval and a moderate substorm occurrence is indicated by both OMNIweb and SuperMAG data. A period of ambipolar electric force and Joule heating is observed in both events, and the peak upflow flux at conjunction exceeds the peak upflow driven by only one mechanism in both cases. The study found out that conjunction of ambipolar electric force and Joule heating leading to ion upflow can occur during both dayside and nightside events.

5.5. Case Study 4: Duration of upflow events

The time taken for an event is categorized under three classes, namely short, medium and long duration. Events that occur between 10 – 60 minutes are regarded as short duration events, while medium and long duration events are allotted the time interval range of 61 – 120 minutes and > 120 minutes respectively. It can be seen from Figure 5.1 that short duration events are frequent, covering about 42.5% of the histogram, while the medium and long duration events cover 25.2% and 32.4% respective areas of the histogram. Here the dayside and nightside occurrence for each of the classifications with respect to events' duration as well as the driving mechanism for each classification are investigated.

5.5.1 Results and Discussion

Figure 5.3 and 5.8 show examples of short duration events on the nightside. However, Figure 5.21 shows an example of short duration dayside events that occurs on April 12, 2007. A typical ionosphere is observed from 09:00 LT until around 11:50 LT when the electron density is raised, leading to an elevated electron temperature. No increase is observed in the ion temperature around this time, indicating the ambipolar electric force as the major driver of the event. The fourth panel shows an increase in the ion velocity about the same time from 11:50 LT until around 12:25 LT. Ion upflow corresponding to the same time interval is observed on the last panel with a maximum flux upflow of about $8.27 \times 10^{13}\ \mathrm{m^{-2}\ s^{-1}}$ around 10:05 LT.

Dayside and nightside examples of medium duration events are respectively presented in Figures 5.22 and 5.23. The dayside event on June 17, 2007, shown in Figure 5.22 indicates an increase in electron density in the ionosphere at about 13:20 LT until the rest of the noon period. The second panel shows an elevated T_e at about the same time with intermittently strong T_i on the third panel. High flow in the ion velocity becomes substantial around the same time interval of 13:30 – 15:00 LT. Ion upflow flux on the last panel reaches a maximum value of $6.22 \times 10^{13}\ \mathrm{m^{-2}\ s^{-1}}$ at the commencement of the event. The medium duration nightside event on April 14, 2007, commences from around 01:40 until about 03:00 LT as shown in Figure 5.23. The electron density panel indicates electron precipitation down to the E-region around the time of event and elevated electron and ion temperatures are observed on the second and third panels respectively within the same interval of time. The ion velocity and the upflow flux are observed to be highly raised at periods corresponding to strong enhancement in T_i as a result of joint contribution from the electron and ion pressure gradients. At about 00:30 LT, the ion upflow attains its maximum value of $6.05 \times 10^{13}\ \mathrm{m^{-2}\ s^{-1}}$ for the period. It could the inferred that both ambipolar electric force and the Joule heating contribute to the respective dayside and nightside events of June 17 and April 14, 2007.

The September 29, 2007 event presented in Figure 5.14 and explained in detail under section 5.4.1 is a long duration dayside event. However, a nightside event that also spans a long duration is presented in Figure 5.24 below. The August 6, 2007 event shows a predominantly moderate precipitation on the first panel from 21:00 LT until around 23:40 LT and thereafter, an intermittently strong precipitation follows until around 01:10 LT after which, it switches back to moderate precipitation for the rest of the period. The second panel shows an enhancement in T_e during the period corresponding to strong precipitation time interval, while the third panel indicates a strong intermittent enhancement in the ion temperature few minutes after the intense precipitation discontinues. Little contribution is observed from the T_i in addition to the intense T_e around 23:40 until about 00:45 LT and this probably results in time interval of maximum ion velocity and ion upflow flux observed in the fourth and fifth panels respectively. The dominant driver of the upflow flux during the periods of intense precipitation and afterward, could be inferred to be the ambipolar electric force and the Joule heating respectively. The peak upflow flux during the former driver is $6.05 \times 10^{13}\ \mathrm{m^{-2}\ s^{-1}}$ at about 23:56 LT, while the peak during the latter is $5.74 \times 10^{13}\ \mathrm{m^{-2}\ s^{-1}}$ around 02:15 LT on the following day.

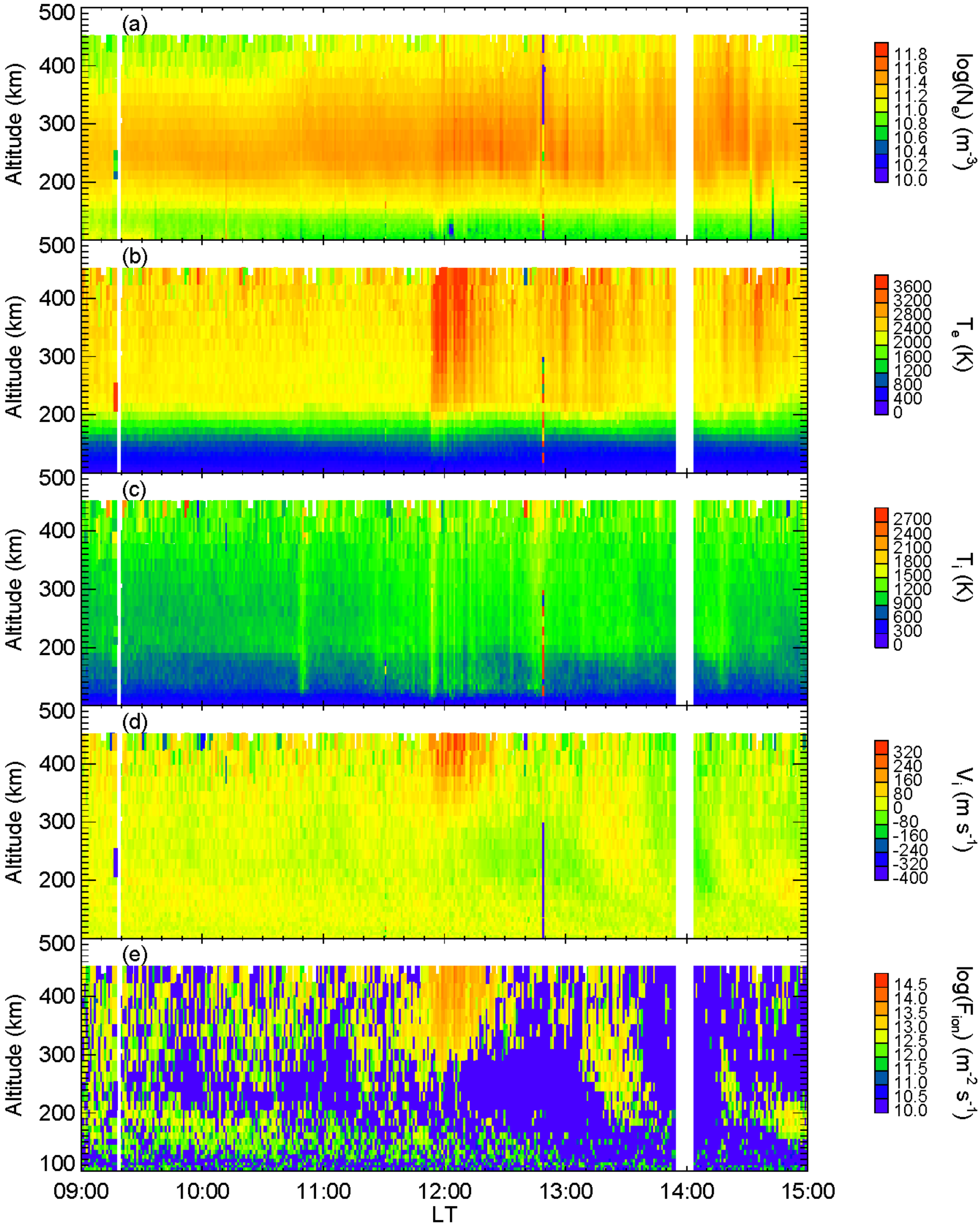

Figure 5.21: ESR parameter plot showing an example of short duration ion upflow events observed on the dayside on April 12, 2007. Figures 5.3 and 5.8 are examples of nightside equivalent. The panels' format is the same as outlined in Figure 5.2.

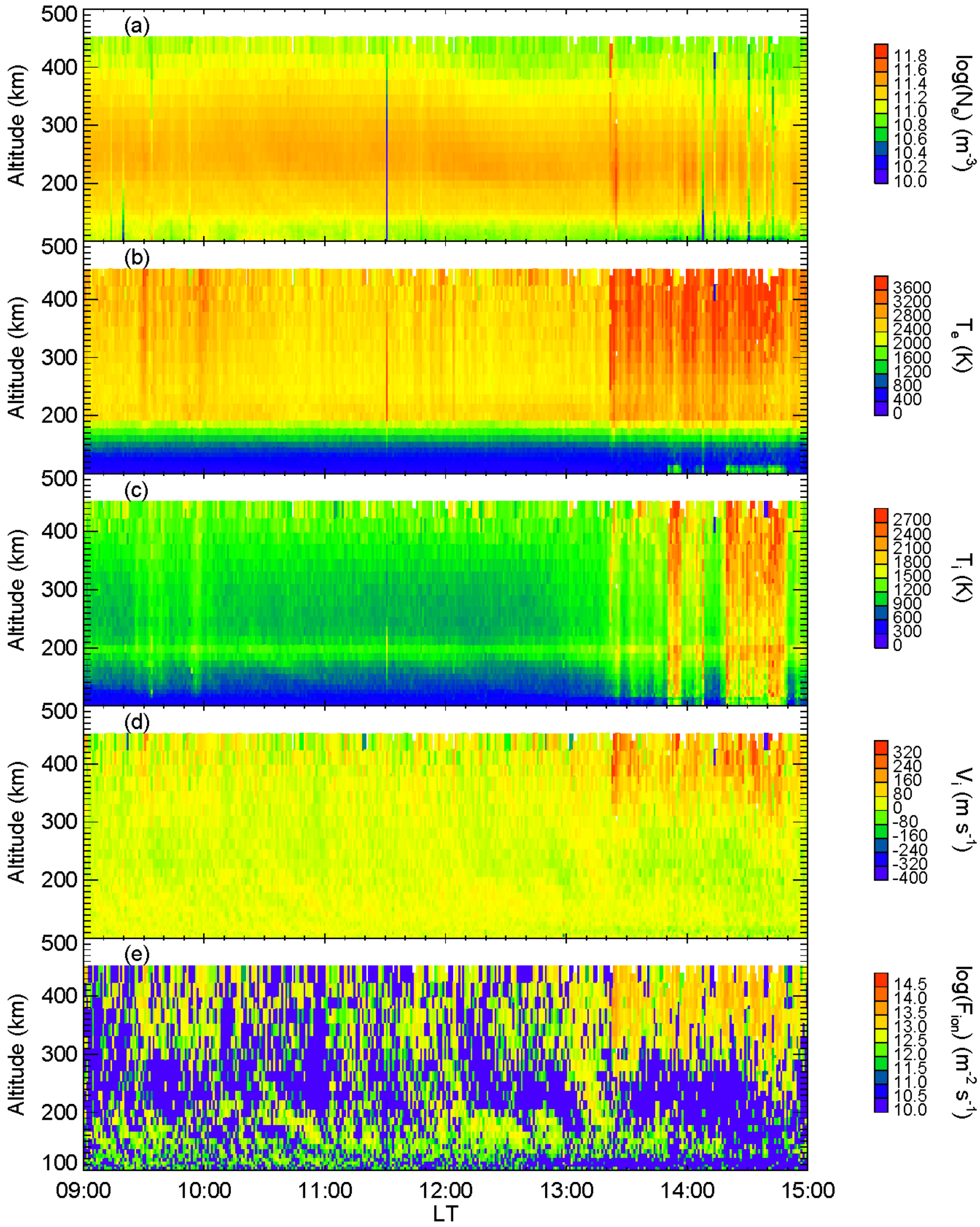

Figure 5.22: ESR parameter plot showing an example of medium duration ion upflow events observed on the dayside on June 17, 2007. The panels' format is the same as outlined in Figure 5.2.

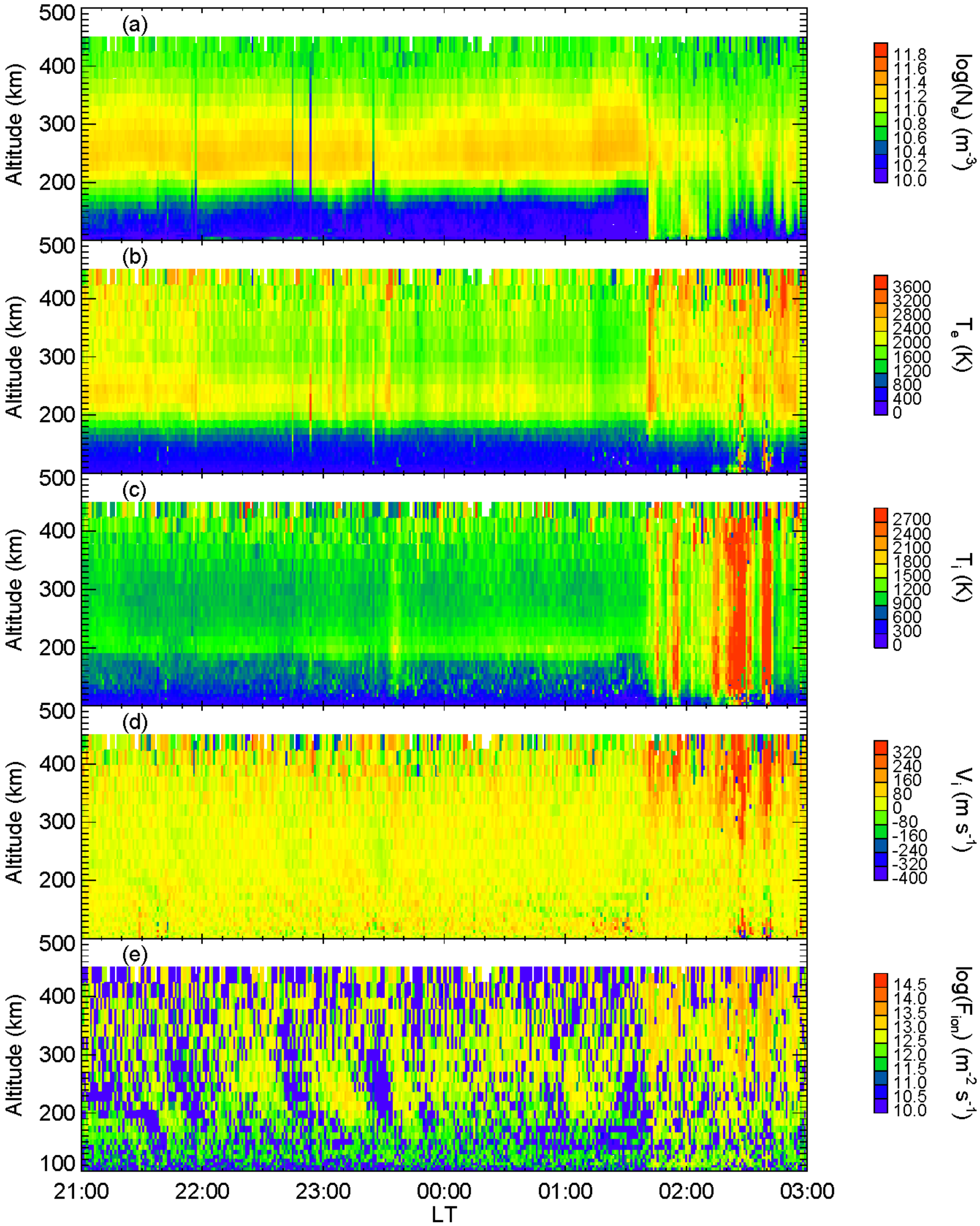

Figure 5.23: ESR parameter plot showing an example of medium duration ion upflow events observed on the nightside on April 14, 2007. The panels' format is the same as outlined in Figure 5.2.

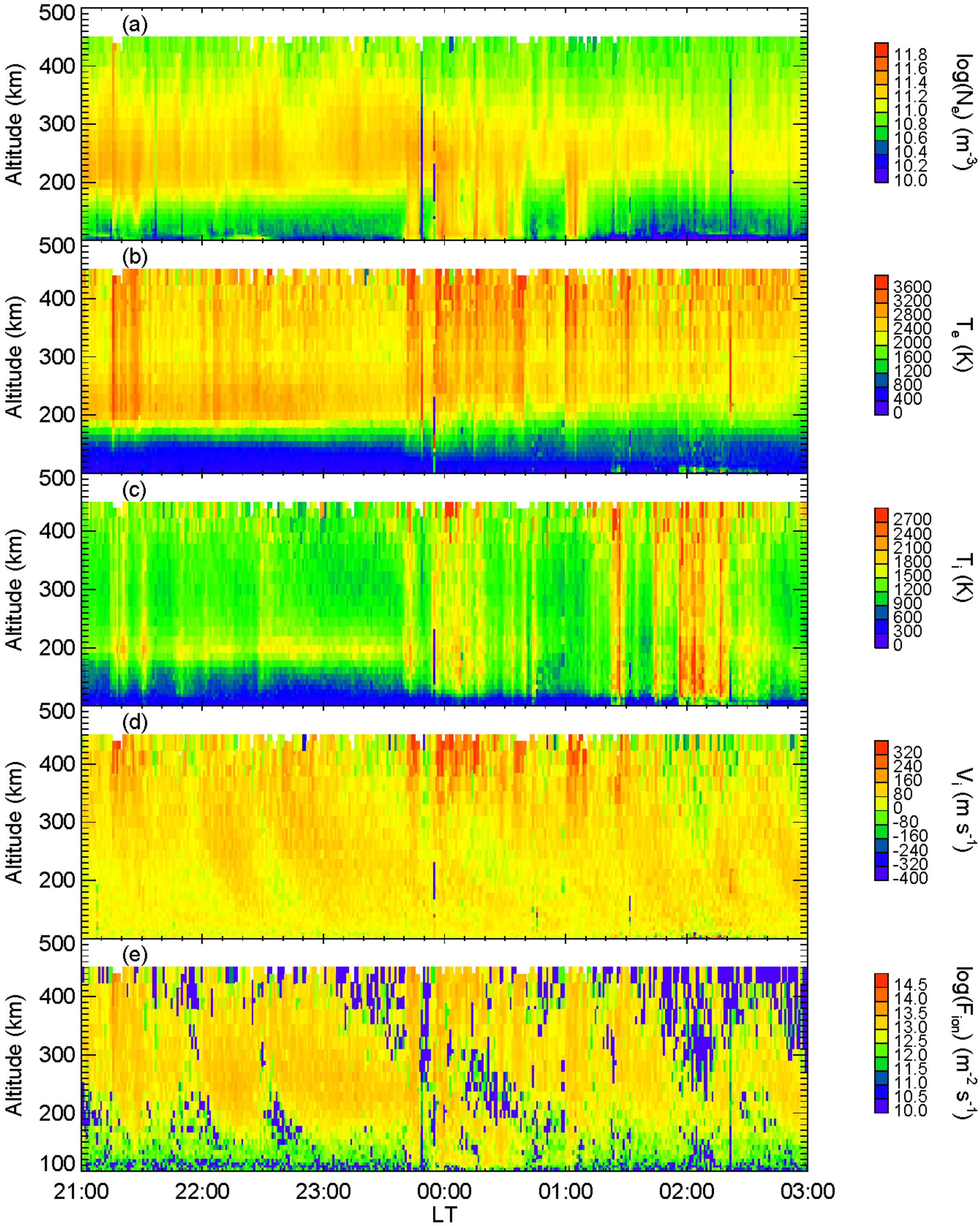

Figure 5.24: ESR parameter plot showing an example of long duration ion upflow events observed on the nightside on August 6, 2007. Figure 5.14 is an example of dayside equivalent. The panels' format is the same as outlined in Figure 5.2.

The occurrence of events classified with respect to time duration is presented in Figure 5.25, where the short, medium and long duration events record 42.5%, 25.2% and 32.4% respectively. Further analysis is done to investigate the occurrence on the dayside (green fill) and nightside (amber fill) sectors as well as those that traverse both (red fill) sectors. It is observed that about 40.9% of the total events occur on the dayside while 45.5% occur on the nightside. About 13.6% of the total events traverse both sectors. Analyses also show that 17.3% of the total events are short duration and dayside events only, while 23.7% are short duration and nightside events only. Percentage of events that traverse both sectors for short duration classification only is 1.5%. The figure shows that 13.5% and 9.4% of the total events are the respective medium duration events that occur on the dayside and nightside only, while events that traverse both sector for medium duration is 2.3%. The long duration occurrence with respect to dayside only, nightside only and both sectors simultaneously is 10.1%, 12.4% and 9.8% respectively. Table 5.2 shows the summary of the statistics. Overall the nightside seems to be the sector where most of the events occur, likely due to auroral activities accelerating the particles during substorms activities, and the nightside short duration is the most frequent.

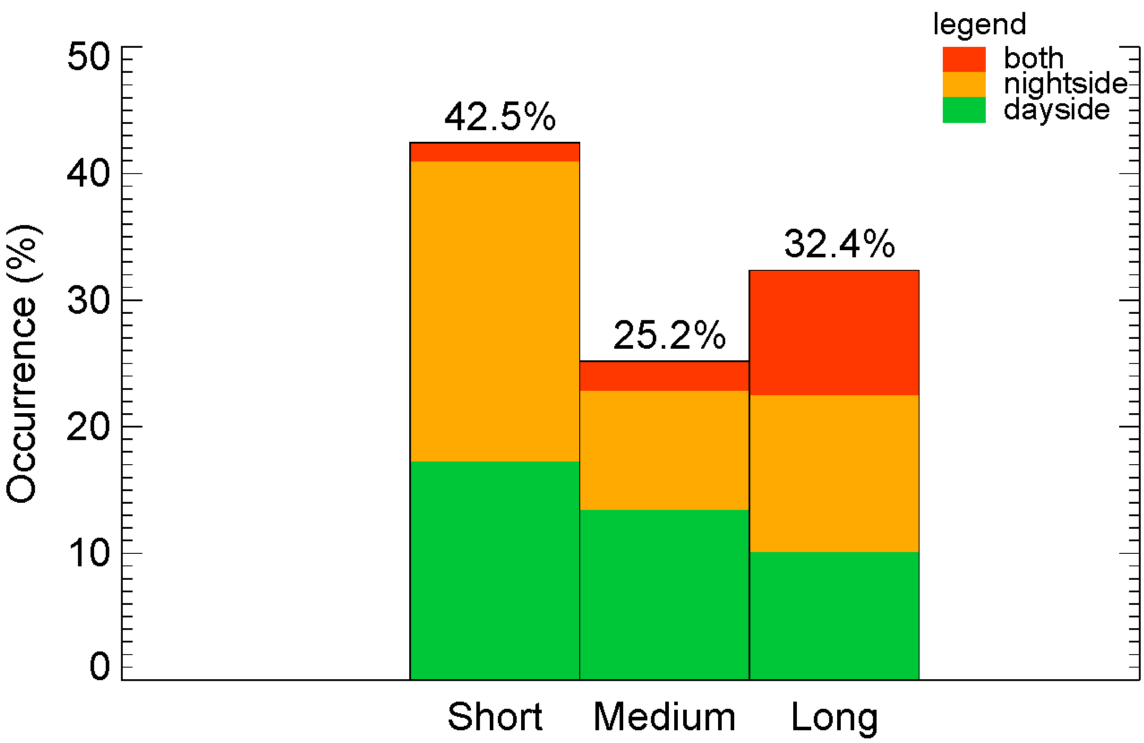

Figure 5.25: Histogram showing the classification of events by duration and its occurrence on the dayside, nightside, and those that traverse both sectors.

Table 5.2: Duration of upflow events against time sectors.

	Duration	Time sector (%)			
		Dayside	**Nightside**	**Both**	**Total**
i.	Short	17.3	23.7	1.5	**42.5**
ii.	Medium	13.5	9.4	2.3	**25.2**
iii.	Long	10.1	12.4	9.8	**32.4**
	Total	**40.9**	**45.5**	**13.6**	**100.0**

The main mechanisms driving the upflow, namely the ambipolar electric field and Joule heating are also analysed to investigate the dominant driver of the upflow. Figure 5.26 shows that about 59.3% of the upflow are solely driven by ambipolar electric field, while the Joule heating predominantly drives about 8.8% of the events. Moreover, period when both mechanisms contribute substantially to the upflow driving is estimated to be around 31.9%. Furthermore, the dominance of the drivers in relation to events classification by duration is presented. Short duration is indicated by green fill on the figure, while amber and red fills indicate medium and long duration respectively. Statistical analysis of the occurrence for the short, medium and long duration events that are predominantly driven by ambipolar electric force is about 45.2%, 27.9% and 26.9% of the 59.3% (i.e., 26.8%, 16.5% and 16.0% of the total) respectively. On the part of the Joule heating as the predominant driver, it is analysed that 56.7% of the overall 8.8% events that it drives (i.e., 5.0% of the total) are short duration events, while 16.7% and 26.7% of the 8.8%, which amount to a total of about 1.5% and 2.3%, are the respective occurrence for the medium and long duration classes. The occasions on which the ambipolar electric field and the Joule heating play effective role in ion upflow with respect to classification by duration have 33.5%, 22.5% and 44.0% occurrences of the 31.9% (i.e., 10.7%, 7.2% and 14.0% of the total) during the short, medium and long durations respectively. These are summarized in Table 5.3 below. The ambipolar electric force therefore seems to be the dominant mechanism of ion upflow, and its occurrence is significant in any classification by duration. In addition, the conjunction of both mechanisms is most significant during long duration events.

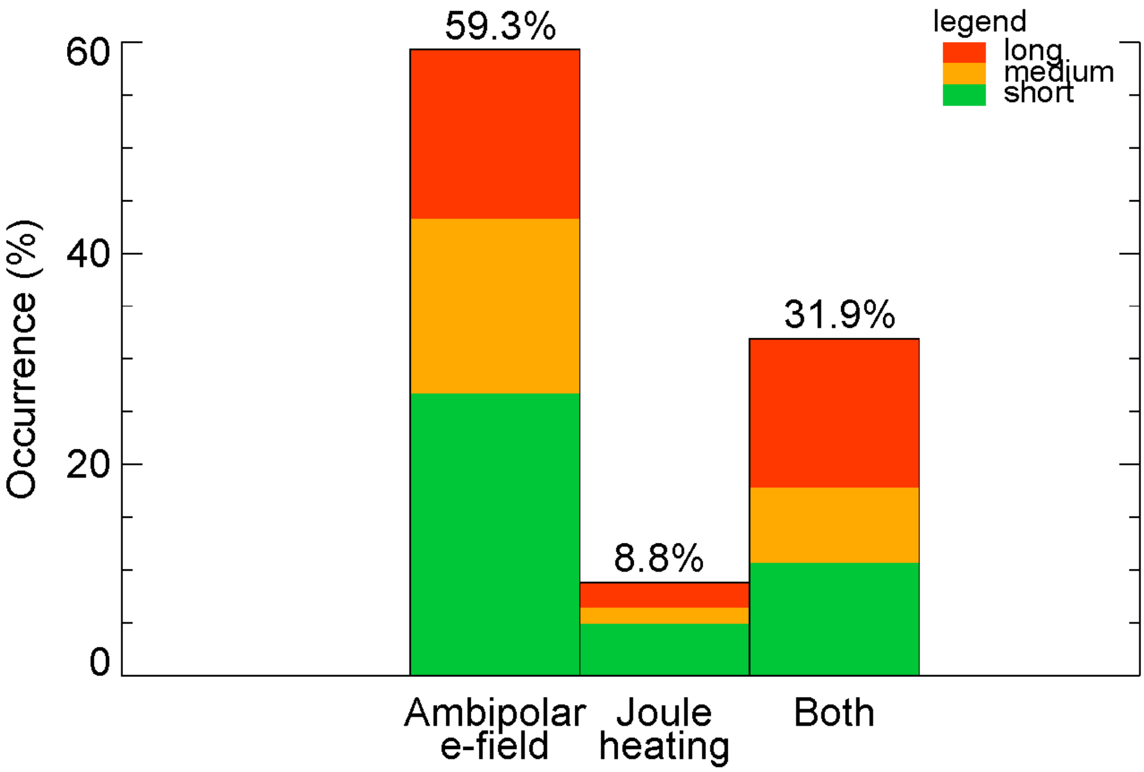

Figure 5.26: Histogram showing the driving mechanism(s) of ion upflows and its occurrence by duration of events.

Table 5.3: Duration of upflow events against the driving mechanisms. Percentage of the total events in red, and black is the percentage of the duration in the driver(s).

	Duration	**Driving mechanism (%)**		
		Ambipolar force	**Joule heating**	**Both**
i.	Short	45.2 (26.8)	56.7 (5.0)	33.5 (10.7)
ii.	Medium	27.9 (16.5)	16.7 (1.5)	22.5 (7.2)
iii.	Long	26.9 (16.0)	26.7 (2.3)	44.0 (14.0)

5.5.2 Summary

Examples of short, medium and long duration events on the dayside and nightside have been investigated. The short duration events take between 10 – 60 minutes to occur, while the medium and long are classified between 61 – 120 minutes and > 120 minutes respectively. Analysis shows that short duration events are most frequent and cover about 17.3% and 23.7% on the dayside and nightside respectively, while about 1.5% traverse both sectors. Furthemore, about 26.8% of the total events are short duration that are principally driven by ambipolar electric force only, while the Joule heating predominate in about 5.0% of the short duration events. The ambipolar electric force predominantly drives about 59.3% of the total events including short, medium and long duration which is about seven times the total events driven by the Joule heating only.

5.6. Case study of ion outflow identified by the Fast satellite

5.6.1 Introduction

The Fast Auroral SnapshoT (FAST) satellite is one of the Small Explorer (SMEX) missions launched by NASA. The spacecraft database has assisted scientists in reviewing theories about the nature of Earth's aurora. Details about the FAST spacecraft and key scientific questions that its data has helped to explore are reported in Chapter 3. This section examines data during conjunctions of the FAST spacecraft and the 42 m dish EISCAT Incoherent Scatter Radar (ISR) at Longyearbyen, Svalbard. During the FAST satellite mission (1996-2009), no suitable conjunction was found during the IPY campaign. However a year before the campaign, there was a suitable conjunction of the FAST satellite, ESR and CUTLASS ground-based radars on March 18, 2006. Table 5.4 shows the orbit, time, altitude and the coordinates of the FAST satellite during the period that ion outflow occurred.

Table 5.4: The ion outflow event observed by the FAST satellite.

FAST Orbit	Date	UT	Alt (km)	MagLat (°)	GGLat (°)	GGLon (°)
38508	2006-03-18	08:09:23	3728	74.111	77.78	20.058

This chapter mainly focuses on the ESR observations of the initial ionospheric upflows that eventually led to the ion outflow observed by the FAST satellite. The maximum upflow along the field line is also evaluated to validate the Wahlund and Opgenoorth (1989) threshold, $10^{13}\ \mathrm{m}^{-2}\ \mathrm{s}^{-1}$, used in this research work. Moreover, the ion momentum equation (equation 2.8) is investigated to infer the dominant mechanism that drives the 2006-03-18 event. In addition, the geophysical conditions are also studied to examine the dayside magnetic activity for the event.

5.6.2 Instrument and data source

The data used in this section consists of the fixed field-aligned antenna of 42 m diameter of the EISCAT Svalbard radar (ESR), beam 9 of the Cooperative UK Twin Located Auroral Sounding System (CUTLASS) radar located at Hankasalmi, Finland, the FAST satellite data, and the high-resolution global storm indices from OMNIweb. It should be mentioned that the ESR experiments operated during the 2006-03-18 event is steffe under the common programmes (CP-1). The experiment allows wider altitudinal coverage spanning up to about 1000 km. The reader is referred to Chapter 3 for details on different programmes and experiments run by EISCAT Scientific Association.

5.6.3 Results and Discussion

The March 18, 2006 ion outflow event identified by the FAST spacecraft at about 08:09:21 UT, which is around cusp at Longyearbyen (LT = UT + 2hours), is investigated. Figure 5.27 shows the ESR parameter plot, while the OMNI data, the ion momentum plots, and the FAST measurements are presented in Figures 5.28, 5.29, and 5.30 respectively.

5.6.3.1 ESR parameter plot

Figure 5.27 shows the ESR parameter plot for the March 18, 2006 event. The panels' format is the same as outlined in Figure 5.2 and the black dashed line indicates the FAST – ESR conjunction. Moderate precipitation to the E region is observed on the first panel of Figure 5.27 from 08:00 LT and lasted until the rest of the period shown on the plot. ESR data indicate moderately intense precipitation to the F1 region (to an altitude about 150 km) immediately before conjunction. However, strong electron temperature dominates the entire period from above 200 km as shown on the second panel. At conjunction, the third panel shows a strong ion temperature elevation which coincides with high field-aligned flow as shown on the fourth panel, indicating a clear relationship between strong ion velocity and elevated ion temperature (St.-Maurice and Hanson, 1982). The combined pressure gradient simultaneously created at FAST – ESR conjunction by both electron and ion species, results in field-aligned ion acceleration and hence ion upflow. A number of intervals of ion upflow are evident on the last panel of the figure, most obviously between 08:00 LT to 10:20 LT as well as 11:00 LT to 12:00 LT. However, more detailed investigation reveals that ion temperature above 3000 K and upward velocities up to about 400 m s^{-1} occur at the time of conjunction. According to Wahlund and Opgenoorth (1989) and Wahlund et al. (1992), the characteristics displayed by this event may classify it as a Type-1 auroral bulk upflow. The peak flux around conjunction for the March 18, 2006 event is about $4.2 \times 10^{13}\ m^{-2}\ s^{-1}$. Analysis shows that between a minute before and after conjunction, about 8.5% occurrence is observed in the low flux category while 4.3% and 0% belong to the medium and high classes of flux respectively. Further investigation at altitudes above 300 km for the time interval above reveals that there is no high flux occurrence, whereas, the low and medium fluxes have occurrence increased to 17.4% and 8.7% respectively. The implication is that large percentage (about 73.9%) of downflow and flux below threshold are observed in the March 18, 2006 event, which could be typical of the period during solar cycle 23.

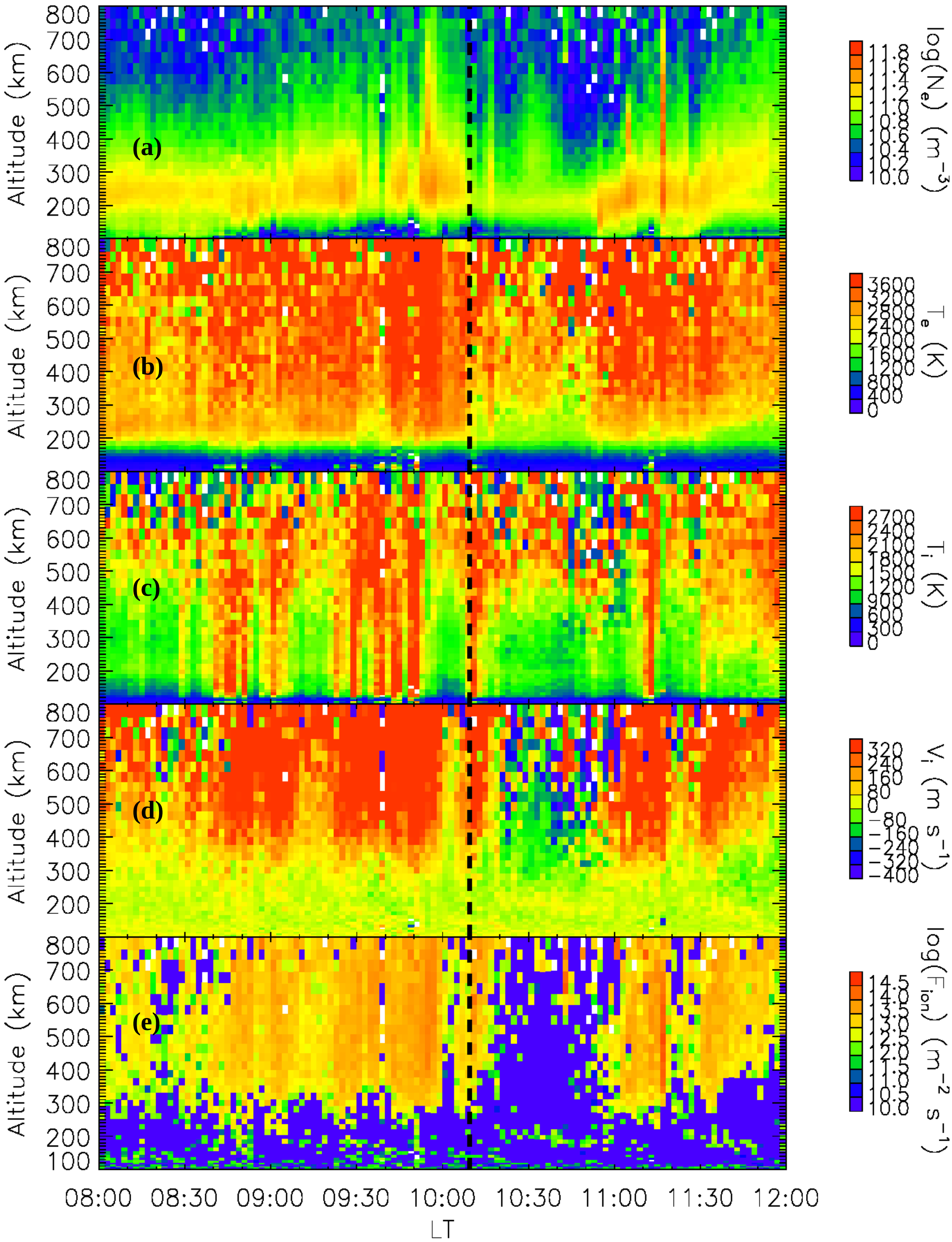

Figure 5.27: Plot showing the ESR parameter plot during FAST – ESR conjunction on March 18, 2006. The panels' format is the same as outlined in Figure 5.2. The black dashed line indicates the FAST – ESR conjunction.

5.6.3.2 OMNI measurements

The OMNI record of the March 18, 2006 dayside event is presented in Figure 5.28, the dashed lines representation is again the FAST-ESR conjunction and its panels' format is the same as outlined in Figure 5.4. The response of the magnetosphere as seen on the first panel of Figure 5.28 by the ring current index, Sym-H, indicates a quiet phase that gradual develops and causing weak depletion in the earth's magnetic field as the ring current builds up and opposes the earth's magnetic field thereby. However, a further development of the ring current, following a two-step storm which is a common phenomenon when there are two southward turning of IMF of approximately equal strength at a close interval, is described by Sym-H (Kamide et al, 1998). The IMF B_z on the penultimate panel showing a long period of southward B_z is likely during reconnection. In addition, a negatively strong B_z will enhance reconnection leading to open field lines in the polar cap region, thereby allowing the transfer of mass, energy and momentum. Reconnection causes electron precipitation in or near the cusp leading to heating and upwelling as a result. It is obvious that there is a geomagnetic disturbance as seen from the IMF B_z panel, and in the response of AL and AU indices on the second panel. Due to geomagnetic disturbances, the thermosphere is heated up leading to changes in the thermospheric composition that may result in negative ionospheric storm (Liu et al., 2010).

Sudden changes in the solar wind dynamic pressure and, more frequently, northward turnings of the IMF as indicated on panels d, f and g between 09:30 LT and 10:00 LT, can trigger the sudden unloading of stored energy (Kivelson and Russell 1995 and the references therein). For this sudden onset of dissipation to take place, it has been found that the IMF must have been southward for about an hour prior to the triggering event (Kivelson and Russell 1995) and this is clearly represented on the penultimate panel of the figure.

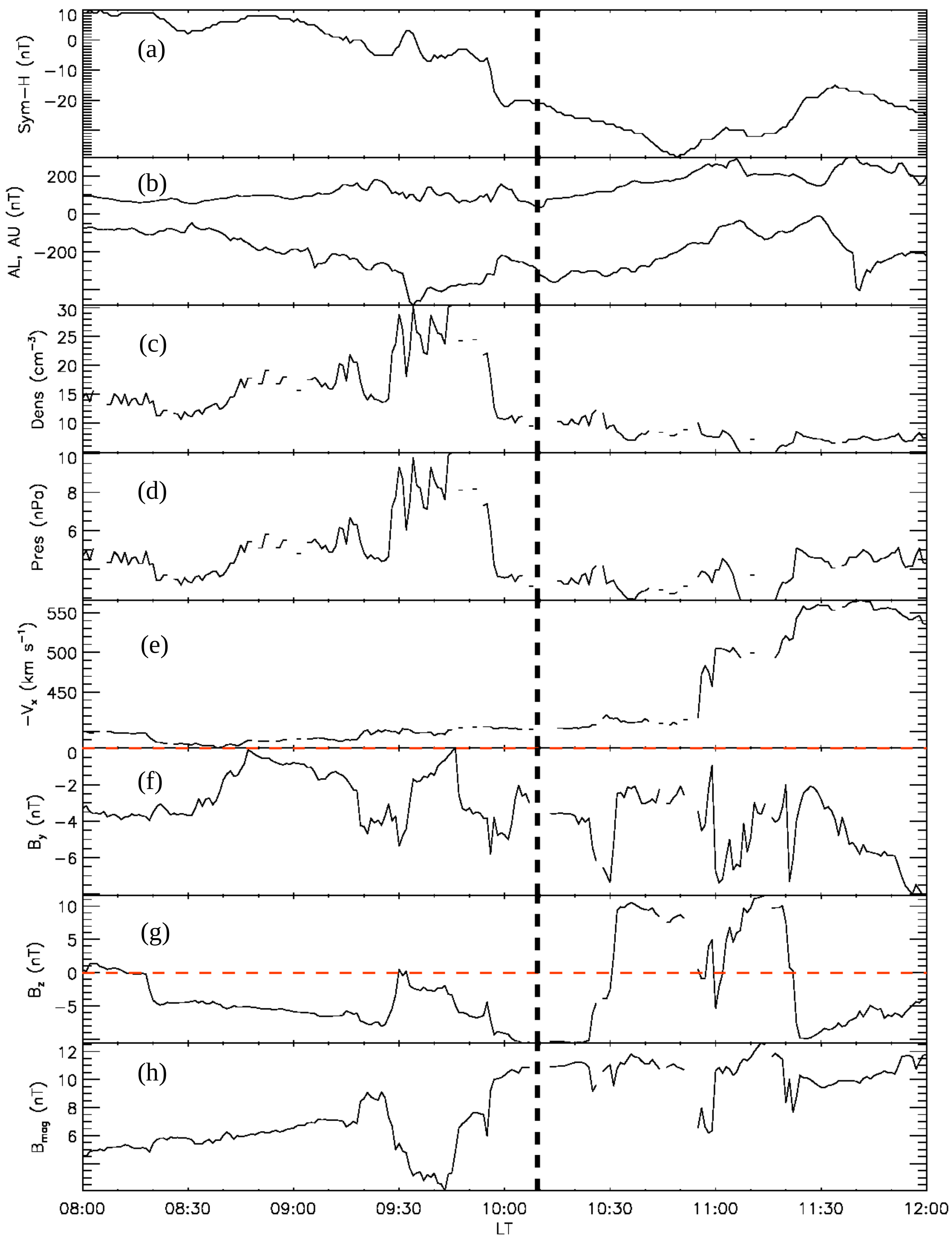

Figure 5.28: Plot showing the OMNI measurements for the ion outflow event on March 18, 2006. The panels' format is the same as outlined in Figure 5.24. The black dashed line indicates the FAST – ESR conjunction.

5.6.3.3 Ion momentum plot

Figure 5.29 presents the ion momentum plot for the March 18, 2006 outflow event observed by the ESR and has the same panels' format as described for Figure 5.6. The black dashed line again indicates conjunction of the FAST spacecraft and ESR. Intermittently moderate ambipolar force between $2.0 - 4.0 \times 10^{-14}\, Nm^{-3}$ is observed on the first panel along the field line at conjunction. However, the ion pressure gradient on the second panel is low in magnitude compared to the ambipolar electric force, yet their combined effect at conjunction still result in an upward flow over gravity as shown on the third panel. A high poleward flow speed away from the radar, which is a characteristic of the cusp, is indicated by the SuperDARN radar data on the fourth panel. The line-of-sight velocity during the time of conjunction is above 800 m s^{-1} indicating that data from the CUTLASS Finland radar signal strong cusp signatures during the 2006 event. A significant phenomenon about 30 – 40 minutes before conjunction appears in the first four panels. It is observed that elevated ambipolar force, the ion pressure gradient and the net force from the first three panels respectively, couple with velocity shear resulting from convection reversal on the fourth panel could have been triggered by the conditions in the solar wind between about 09:30 – 10:00 LT. There was corotating interacting region (CIR) of fast and slow solar wind streams, which can lead to magnetospheric disturbances, as seen from the sharp increase in the solar wind dynamic pressure and density within the time interval as shown in Figure 5.28. The convection reversal observed in the plasma flow on the fourth panel of Figure 5.29 from 9:30 to 10:00 LT between magnetic latitude 65 – 70° indicates wave activity in the magnetic field around conjunction. The fifth panel indicates that upflow satisfying the threshold is present at conjunction and on the last panel reconnection is indicated by the strong southward IMF B_z.

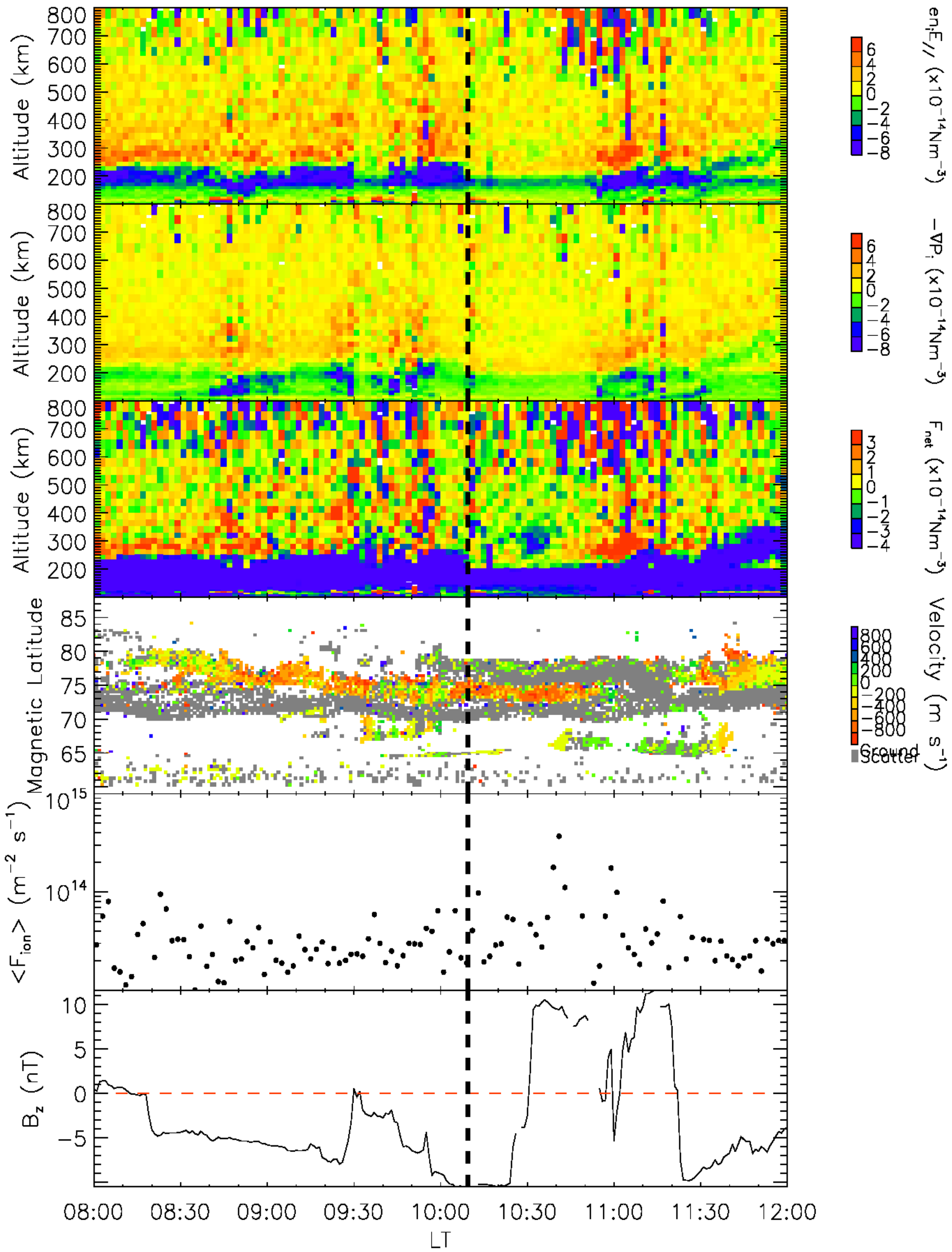

Figure 5.29: Plot showing the drivers and geophysical conditions during the March 18, 2006 outflow event. The panels' format is the same as outlined in Figure 5.6. The black dashed line indicates the FAST – ESR conjunction.

5.6.3.4 FAST measurements

The FAST satellite data is presented in Figure 5.30 for the March 18, 2006 outflow event and the FAST-ESR conjunction is indicated by the vertical dashed line. The first panel, representing a radio emission at a local ion plasma frequency, signals an elevated AC electric field of about 2 kHz from around 08:08 UT (10:10 LT) until about few seconds to the conjunction, which may be capable of generating an $E_{\parallel}$ high enough to accelerate the particles along the field. Precipitation of low energy electron fluxes and an ion population of few hundreds eV from the magnetosheath are indicated respectively on the second and fourth panels. The fifth panel shows that an ion conic (explained in detail in Chapter 2) is observed by the FAST satellite during the passage over Svalbard. It is observed that the ion outflow is peaked at an oblique angle to the magnetic field line, which is a characteristic of the ion conics. The last panel of Figure 5.30 indicates a weak magnetic perturbation at conjunction which in the presence of the perpendicular energization by the electric field could still carry a significant Poynting flux in addition to the precipitating flux, for a stronger acceleration of the ions.

During the period that FAST measurements indicated an ion outflow, elevated electron and ion temperatures, indicating heating, were observed by the ESR, while the fast plasma flow observed by CUTLASS radar indicated that the 2006 event was cusp related. The long period of southward B_z indicated reconnection causing electron precipitation and plasma heating as a result. Magnetospheric disturbance as a result of a CIR signalled by the sharp increase in the ram pressure also preceded the 2006 event. The fluxes observed by the ESR at the time that FAST identified the outflow was estimated to peak at $4.2 \times 10^{13}\ \mathrm{m}^{-2}\ \mathrm{s}^{-1}$, validating the Wahlund and Opgenoorth (1989) threshold. The increase in plasma pressure gradient and the wave activity indicated on the ion momentum plot show energization of the ionospheric ions, which coupled with the geophysical conditions results in an ion outflow identified by the FAST satellite.

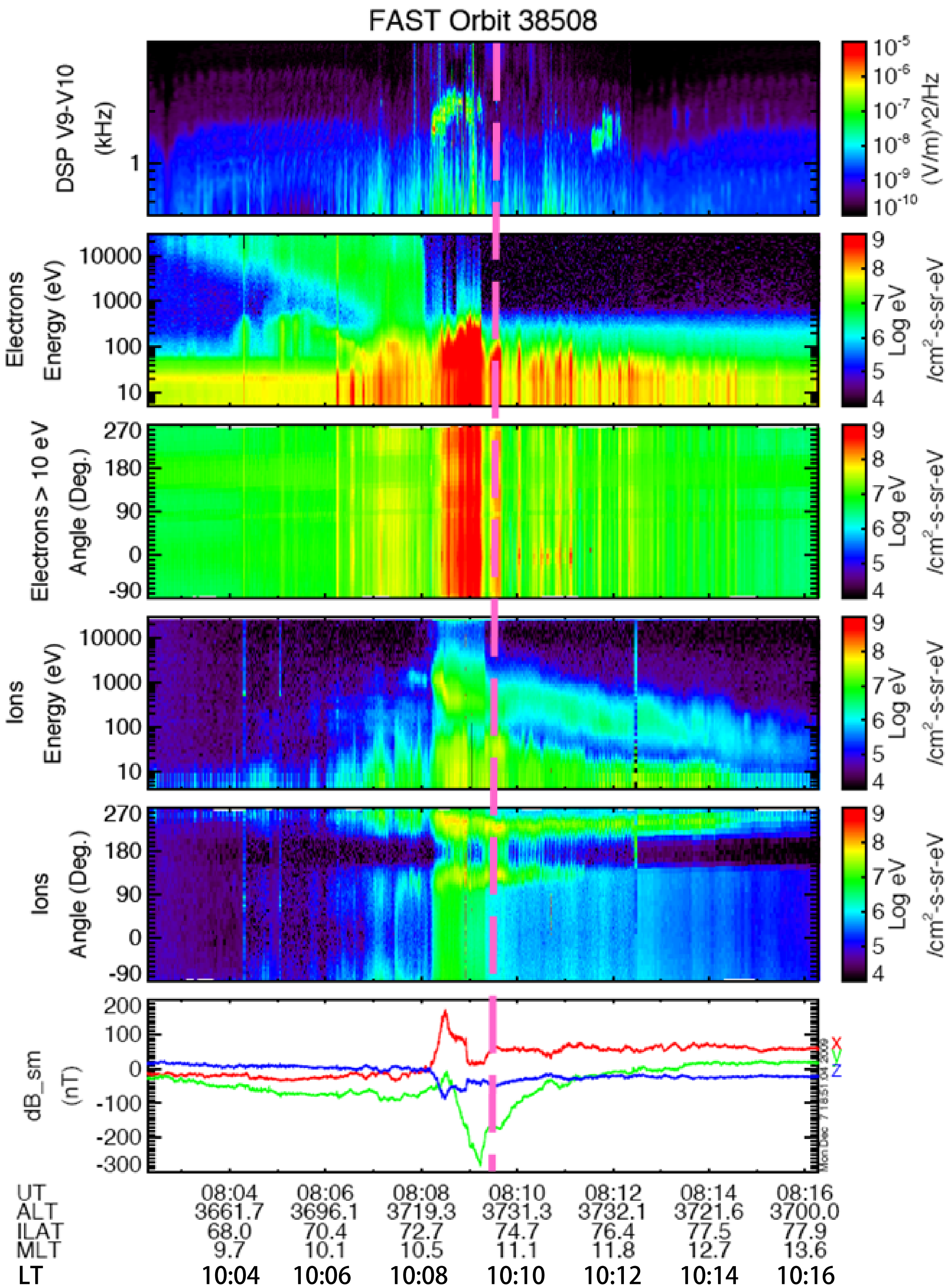

Figure 5.30: Plot showing FAST measurements during the March 18, 2006 ion outflow event. (a) AC electric field, (b) electron flux resolved in energy, (c) pitch angle, (d) ion flux resolved in energy, (e) pitch angle and (f) residual magnetic field components. The pink dashed line indicates the FAST – ESR conjunction.

5.7. Conclusion

Ion upflow flux from the Earth's upper atmosphere during the international polar year (IPY) 2007 campaign, which coincides with solar minimum, has been investigated using the ionospheric basic parameters as observed by the EISCAT Svalbard Radar (ESR). The study is carried out in order to determine the primary mechanisms driving the upflow, i.e., the ambipolar electric force and Joule heating. A case study of ion outflow identified by FAST satellite was also discussed. Also included in the study is analysis of the duration of events as well as the local time sector, and the main results are summarized below:

- The ion momentum plot, introduced for the first time in this study, shows that ion upflow can be simultaneously or independently driven by the ambipolar electric force and/or Joule heating mechanism(s).
- The average upflow is generally higher if both mechanisms are simultaneously present compared to only one mechanism.
- The ambipolar electric force alone may drive upflow about seven times as often as the Joule heating, making the ambipolar force the dominant mechanism.
- In contrast to the proposition that there cannot be any remarkable outflow irrespective of the amount of the Poynting flux as long as the precipitating flux is zero, the September 11, 2007 event shows that strong Joule heating can drive significant ion upflow without any accompanying precipitating flux.
- Ion upflows are shown to occur during both southward and northward B_z, however, the occurrence is higher during the southward orientation.
- Short duration event are most common with 17.3% and 23.7% on the dayside and nightside respectively, while 1.5% traverse both sectors.
- Ion upflow is predominantly observed at altitudes ≥ 300 km. However, during wide range of intense electron precipitation, the upflow flux can be observed below 200 km, as shown in the April 18, 2007 event, for instance.
- 21.7% of the total events occur around local noon, 80.4% of which are cusp related.

- 30.2% of the total events occur around midnight, 65.5% of which are related to substorm activity.

The ambipolar electric force played a role in 91.2% of the total events investigated, while the Joule heating was involved in 40.7%. Furthermore, the ambipolar force acting alone drove about 59.3% of the upflow, while the Joule heating did so alone for about 8.8% of the events. It could therefore be concluded that the ambipolar electric force is the dominant driver of initial ionospheric upwelling from the Earth's upper atmosphere. A key result from the study showed that, though rare, the Joule heating, in the absence of any precipitating flux, could still carry the Poynting flux that could drive sufficient flux density to meet the threshold for potential ion outflow.

Ion upflow flux was shown to be largely independent of the interplanetary magnetic field (IMF) orientation, however, more events were observed during southward orientation of the IMF. It was also found that over 50% of the events occurred around local noon and midnight, 71.8% of which are either cusps or substorms related. The main region of ionospheric upflow was found to be the F2-region, but could extend down to F1-region during times of wider altitudinal coverage of intense precipitation.

The most frequent class of upflow was found to be the short duration which did not exceed an hour. However, the long duration events were most common on the night side. Furthermore, though simultaneous heating from both mechanisms leading to ion upflow can occur during both dayside and nightside, it was during the long duration events that both driving mechanisms simultaneously played the major role in ion upflow.

In order to ascertain that the threshold set for upflow flux used in this work accurately represents the true picture during ion outflow, a case study of an outflow identified by the FAST satellite on March 18, 2006 was carried out. Heating of the plasma was indicated by the enhanced electron and ion temperatures observed by the ESR, with a cusp signature indicated by CUTLASS radar. Reconnection and magnetospheric disturbance were respectively indicated by the long period of southward B_z and a CIR that preceded the 2006 event. The fluxes observed by the

ESR during the ion outflow event peaked at $4.2 \times 10^{13}\ \mathrm{m^{-2}\ s^{-1}}$. The flux distribution of ion conics peaked at an oblique angle to the geomagnetic field was identified by the FAST satellite. Both the ambipolar electric force and the Joule heating played a role in the outgoing ions, the ion momentum plot showed that the former was the dominant driver. It could therefore be concluded that the role of the geomagnetic conditions, the elevation of T_e and T_i and wave activity are important in ion outflow. Also the Wahlund and Opgenoorth (1989) threshold used in filtering the data in this work is a valid threshold for outflow.

CHAPTER 6

Statistical analysis of ion upflow flux in relation to solar wind plasma and basic ionospheric parameters during the IPY-ESR 2007 observations

6.1. Introduction

As discussed in Chapter 4, the EISCAT Svalbard Radar (ESR) observed about 312,444 field aligned profiles during the international polar year (IPY) 2007 campaign. Several studies (Foster et al., 1998; Endo et al., 2000; Buchert et al., 2004; Ogawa et al., 2009; Skjæveland et al., 2014) have performed various types of statistical analyses on ion upflow for field-aligned observations. Foster et al. (1998) examined the diurnal variation of ion upflow as well as its dependence on season and solar cycle, while Howarth and Yau (2008) have investigated the behaviour of ion flux during dawnward and duskward movement of the cusp due to the interplanetary magnetic field (IMF) B_y. Investigation by Ogawa et al. (2009) have shown that there is high correlation between ion upflow ocurrence and upstream solar wind density, while Skjæveland et al. (2014) found out that there is a low correlation between ion upflow and local terrestrial ionospheric electron density. These previous studies examined data ranging from about 300 profiles for some hours observation, to a hundred thousand profiles, for the complete solar cycle. The current study accesses a large dataset of over three hundred thousand field-aligned profiles within a year during solar minimum of 2007. This provides both qualitative and quantitative data for robust statistical analysis. In this study, identification of ion upflow as observed by the ESR during the IPY 2007 campaign has been grouped into three classes as outlined in Chapter 4.

The main focus of this chapter is to analyse the relationship of ion upflow flux with the upstream solar wind plasma parameters and the downstream terrestrial magnetic activity for a whole year of near-continuous ESR data. The correlation of ion upflow flux with the basic ionospheric parameters observed by the ESR is also investigated with respect to classes of upflow flux during the period under investigation. As noted in Chapter 4, ESR observation of an ion flux threshold of $10^{13}\ \mathrm{m^{-2}\ s^{-1}}$ along the field line that satisfies the filtering analysis described therein under section 4.2.2 is regarded as an event in this chapter. ESR observation that falls in the low upflow categories is about 82,852, while the medium and the high upflow categories are 9,810 and 1,131 observations respectively. The upper and lower limits of each class boundaries of the ion upflow flux are listed in Table 4.1 in Chapter 4.

6.2. Statistical Data Source

The database employed in this study consists of:

a) The one minute resolution upstream solar wind plasma parameters from OMNIweb comprising the solar wind speed, v_{sw}, the solar wind number density, n_{sw}, the dynamic pressure, P_{dyn}, the IMF components, B_x, B_y and B_z, as well as the downstream geomagnetic ring current index (Sym-H) and lower and upper auroral electrojet indices (SML and SMU) from SuperMAG.

b) The four key ionospheric parameters derived from the ESR data namely, ionospheric electron density, n_e, ion temperature, T_i, electron temperature, T_e, and the ion drift velocity v_i, and the derived ion flux from two basic parameters, i.e., electron density and ion velocity.

6.3. Upstream plasma parameter relationship with ion upflow occurrence

Six figures (Figures 6.1 – 6.6) are presented in this section and each figure comprises three panels. The first panel corresponds to the low flux category while the second and third panels show the medium and high flux classes respectively. The plots investigate the relationship between ion upflow occurrence in relation to solar wind plasma parameters. The occurrence frequency in this section is calculated from the ratio of the event points to the total observations in corresponding bins for each parameter, with respect to the upflow classes. The scale used on the ordinate for different parameters and upflow classes varies; it reflects the percentage occurrence for each parameter and class. It should be noted that the correlation coefficient is calculated in the region where the data is less scattered.

6.3.1 Solar wind speed with ion upflow occurrence

Figure 6.1 shows the occurrence of the ion upflow with respect to solar wind speed. The data is binned at every speed interval of 1 km s^{-1} and the number of ion flux in each upflow class is counted which is then plotted against the corresponding solar wind speed. In the first panel, which corresponds to the low flux, a total of 483 data points are plotted. It is observed that as the solar wind speed increases, the occurrence frequency of the low flux also increases with a linear Pearson correlation coefficient (ρ) of about 0.581. It is observed in the low flux that below the average solar wind speed of around 400 km s^{-1}, the occurrence frequency is predominantly less than or equal to about 5%, whereas at a speed above 700 km s^{-1}, the occurrence frequency can reach up to about 15%. The second panel of Figure 6.1 presents the medium flux which indicates data points totalling 452. Although the occurrence frequency of the medium class also increases with an increase in solar wind speed, the gradient is shallow compared to that in the low flux. However, a linear Pearson correlation coefficient of about 0.607 is observed in the medium flux and the occurrence frequency is also at maximum when solar wind speed is above 700 km s^{-1}. For solar wind speed less than ~ 650 km s^{-1}, there is a good linear trend in the low and medium-flux upflows. The last panel of Figure 6.1 showing the high flux indicates a lesser correlation among the 331 data points compared to that in both low and medium classes. On the other hand, it is observed that unlike in the low and medium flux categories, sufficient data points begin to emerge in the high flux when solar wind speed has reached about 300 km s^{-1}. I could infer from this that a higher threshold is required in the solar wind for a high flux to occur. Another intriguing fact in the high flux is that no occurrence is observed at about 700 km s^{-1} and above. Ogawa et al. (2009) reported an increase in the correlation between the occurrence frequency and the solar wind speed until about 700 km s^{-1} after which it plummeted. This study could draw conclusion that the sharp decrease they observed could largely be due to the little or no contribution from the high flux, which indicates no occurrence above the speed in question. The linear Pearson correlation coefficient obtained in the high flux is about 0.346, which shows that the correlation of ion upflow occurrence with solar wind speed decreases as the ion flux magnitude increases.

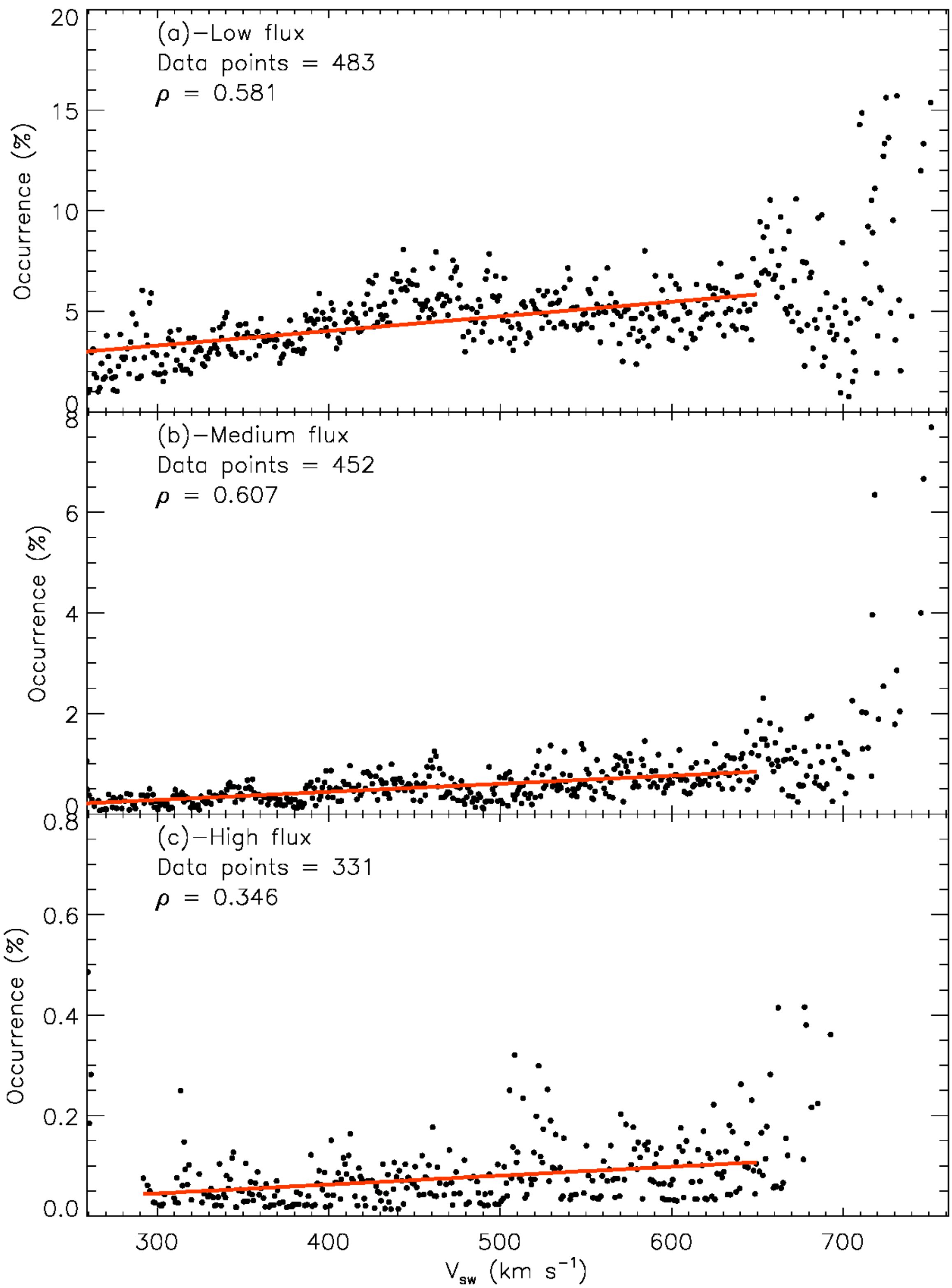

Figure 6.1: Plot showing the relationship between upflow occurrence and solar wind speed. The first panel shows the low flux class, while the second and the last show the respective medium and high classes of flux.

6.3.2 Solar wind number density with ion upflow occurrence

In Figure 6.2, occurrence of the ion upflow is plotted in relation to the number density (n_{sw}) of plasma in the solar wind. The bin interval chosen for the number density is 0.1 cm^{-3}. The low flux as shown in the first panel of Figure 6.2 presents a total number of 489 data points. A clear trend is observed when the number density is less than about 20.0 cm^{-3} and thereafter, greater scatter is observed. Although the number density in the low flux category goes above 60.0 cm^{-3}, the plot shows that high occurrence is observed around number density of 30.0 – 50.0 cm^{-3}. Moreover, the plot shows that maximum occurrence of about 50% is obtainable in the low flux. The linear Pearson correlation coefficient obtained for this class of upflow where the points are less scattered is about 0.611 to three significant figures. The medium and high flux classes presented in the second and third panels of Figure 6.2 show the occurrence frequency of the ion upflow flux which begins with a predominantly low and constant occurrence frequency in both cases when the number density is below about 20.0 cm^{-3}. The respective averages of the medium and high flux occurrence observed before 20.0 cm^{-3} are less than 1.0% and 0.1% with respective linear Pearson correlation coefficients of 0.263 and 0.563. However, at about 20.0 cm^{-3} and thereafter, a steep increase is observed in the number density, making the medium and high-flux upflows attain occurrence percentage up to about 20% and 4% respectively. Ogawa et al. (2009), though without giving any correlation coefficient, reported that they have observed high correlation between ion upflow occurrence and solar wind density however, in this study, it has been found that the overall correlation of the upflow occurrence (all classes data points) with the solar wind density is about 51.5%. In addition, there seems to be a threshold n_{sw} of 15 – 25 cm^{-3} before a change in behaviour from linear to randomness is observed in the upflow occurrence and n_{sw} relationship. A steep increase in the occurrence frequency from about 25% to above 50%, when solar wind density is above 30.0 cm^{-3}, was reported by Ogawa et al. (2009) from the analysis of one third of their data set (0800 – 1600 MLT). However, the large data set analyse in the present study shows that the increase could take place even at solar wind density above about 20.0 cm^{-3}. It is also observed that appreciable occurrence is seen at high number density of the solar wind plasma, which could have caused more precipitation and heating as a result.

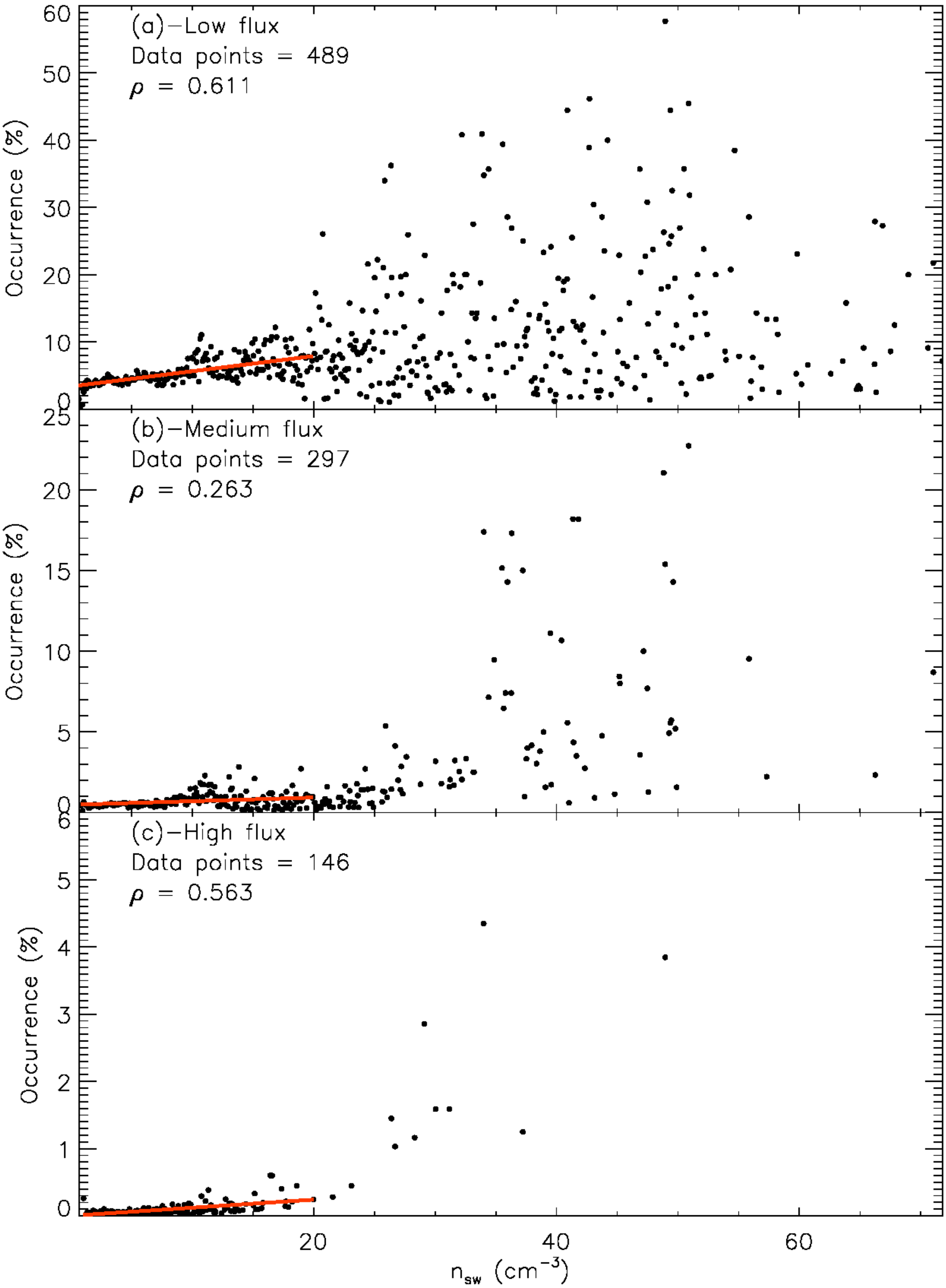

Figure 6.2: Plot showing the relationship between upflow occurrence and solar wind number density. The panels' format is the same as outlined in Figure 6.1.

6.3.3 *Solar wind dynamic pressure with ion upflow occurrence*

The relationship between upflow occurrence and the dynamic pressure as shown in Figure 6.3 indicates a similar trend as in the case of the solar wind number density. This should be expected as the solar wind pressure has a direct relationship with the mass density (product of proton mass and number density) in the solar wind as shown in equation (6.1) below.

$$P_{sw} = \rho_{sw} v_{sw}^2 \tag{6.1}$$

where P_{sw} is the plasma pressure of the solar wind,

ρ_{sw} is the mass density of the solar wind and

v_{sw} is the solar wind speed.

The first panel in Figure 6.3 shows that up to dynamic pressure of about 6 nPa, there is a monotonic increase in the occurrence frequency observed in the low flux. Thereafter, a more random distribution is observed. A similar trend, but of shallower slope is indicated in the medium flux up to dynamic pressure of about 5 nPa. However, significant increase in the occurrence frequency is not noticed in the medium flux until the dynamic pressure attains about 13 nPa. The solar wind pressure is typically ~ 1 nPa in the rarefaction regions and goes up to tens of nPa in compression regions. This implies that CIR of fast and slow solar wind streams tends to increase the occurrence frequency. The third panel on the other hand is less random, and seems to predominantly indicate increasing occurrence in high flux as the pressure increases. However, the linear Pearson correlation coefficient until about 6 nPa, after which departure from linear trend is largely observed, is greatest in the low flux with a value of 0.930, while in medium and high fluxes are 0.721 and 0.646 respectively. The data here is also binned at 0.1 nPa interval and the total data points obtained for the low, medium and high classes are respectively 174, 133 and 69.

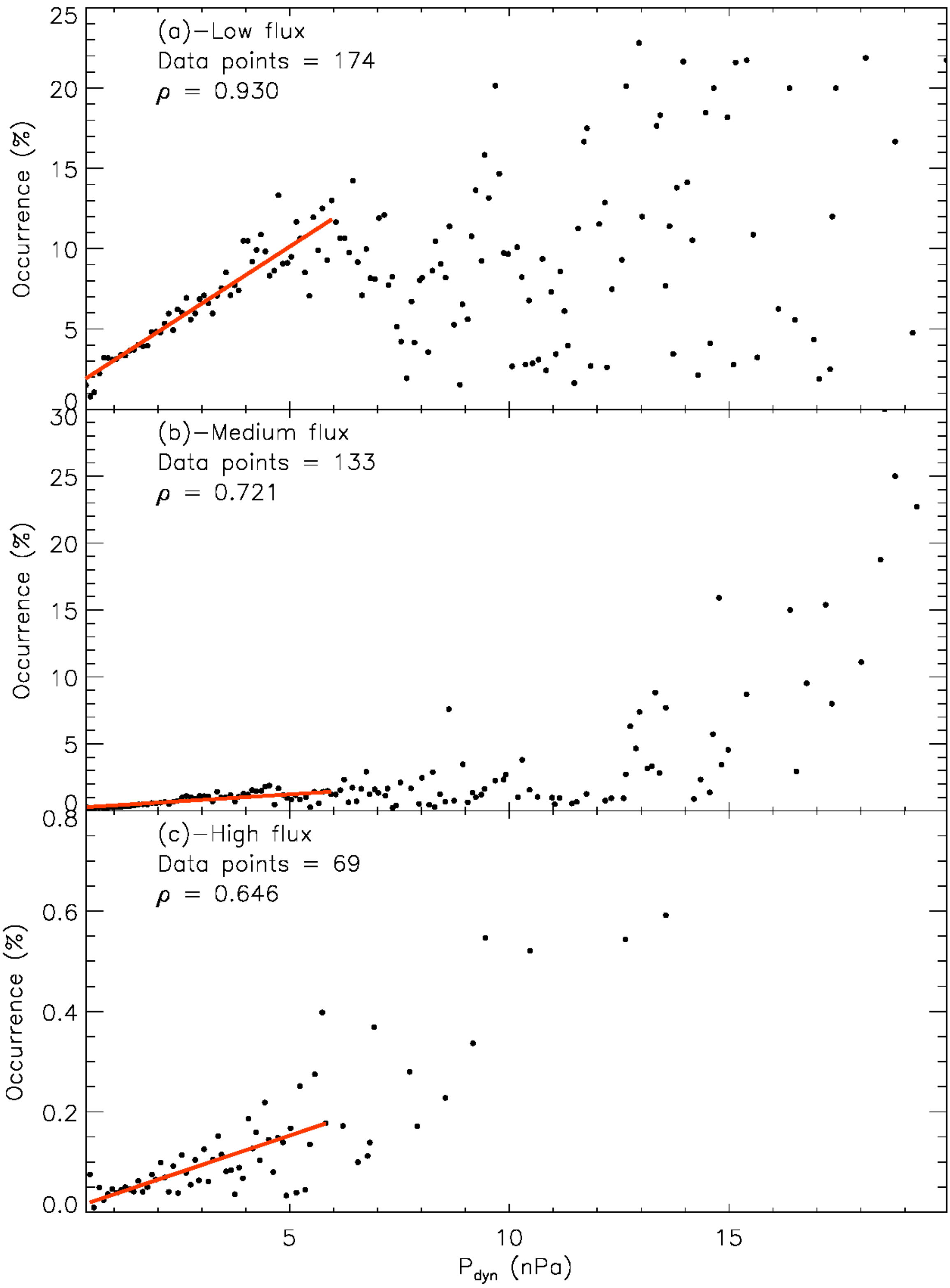

Figure 6.3: Plot showing the relationship between upflow occurrence and solar wind dynamic pressure. The panels' format is the same as outlined in Figure 6.1.

6.3.4 IMF B_{mag} with ion upflow occurrence

Figure 6.4 presents the occurrence of the ion upflow with respect to magnitude of the interplanetary magnetic field (IMF). The IMF B_x, B_y and B_z components obtained from OMNIweb are used to calculate the field strength via equation (6.2) as shown below.

$$B_{mag} = \left(B_x^2 + B_y^2 + B_z^2\right)^{1/2} \tag{6.2}$$

The IMF magnitude data is binned at interval of 0.1 nT and a total of 200 data points are obtained for the low flux shown in the first panel of Figure 6.4. The plot shows that occurrence frequency of the low flux increases as the magnitude of the IMF increases and has about 93% linear Pearson correlation coefficient until 13 nT where the scatter is less random. It is observed that the occurrence scatter grows as the IMF magnitude grows; below 5 nT, the data points highly fit on the line of best fit and between 5 and 10 nT, a moderate dispersion is observed, whereas, at above 10 nT the data points disperse widely from the line of best fit. On the other hand, a good fit up to about 11 nT is observed in the medium class of flux. However, a gentle slope beginning with a little or no occurrence until about 5 nT when a small increase in the occurrence becomes noticeable is indicated in the medium-flux upflow. Above 12 nT, occurrence frequency up to 6% is observed in comparison to occurrence peak of about 1.5% observed before 12 nT. A total of 174 data points with a linear Pearson correlation coefficient of 0.716 is observed in the medium flux before 13 nT. The third panel shows the high flux with maximum occurrence around IMF magnitude of about 15 nT. Appreciable increase in the occurrence frequency begins to be noticeable when IMF strength is around about 10 nT and above. An interesting feature observed in all classes of flux is that the occurrence peak is between 15 – 16 nT bin of the IMF magnitude. The occurrence peaks which decrease as the flux magnitude increases from low to high flux class are about 24.0%, 9.3% and 1.3% respectively. Furthermore, the low flux correlates more with the IMF magnitude than any other class.

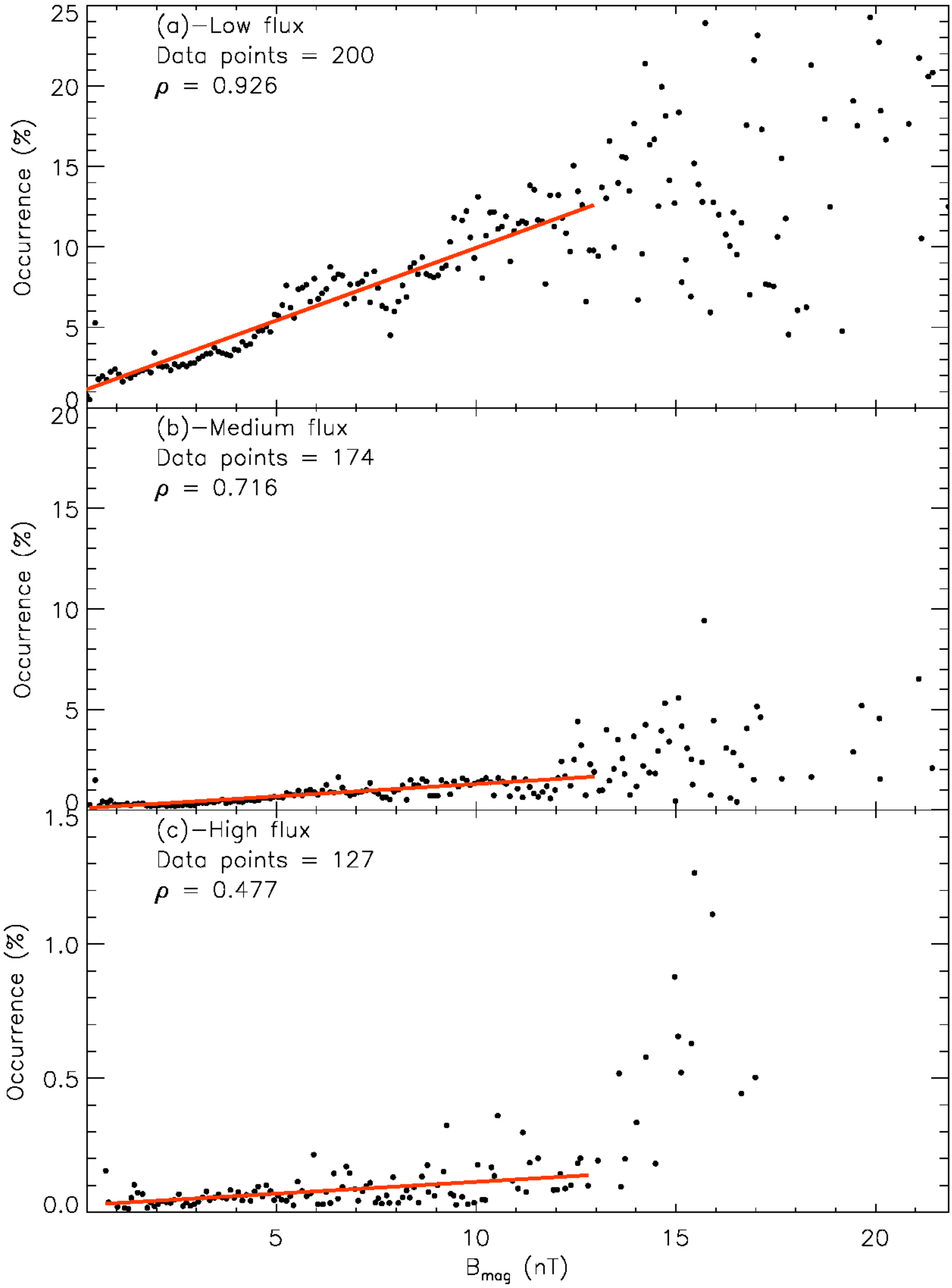

Figure 6.4: Plot showing the relationship between upflow occurrence and IMF magnitude. The panels' format is the same as outlined in Figure 6.1.

6.3.5 Solar wind clock angle with ion upflow occurrence

The clock angle is defined as "the angle between the IMF vector projected into the GSM Y-Z plane and the Z-axis". It is calculated from the arc tangent of the ratio of the IMF B_y to IMF B_z as shown in equation (6.3) below and ensures that the quadrants of B_y and B_z are taking into account. The data is binned at 1° interval and about 360 data points are obtained for the low and medium fluxes while high flux has about 326. The occurrence value in each bin is normalized by the highest value across all bins for each class of ion upflow.

$$\theta = \tan^{-1}\left(\frac{B_Y}{B_Z}\right) \tag{6.3}$$

The low, medium and high upflow classes in Figure 6.5 show the normalized occurrence plots which have been smoothed over 10°. The dashed lines in Figure 6.5 also indicate the partition of the clock angle into the four quadrants in a clockwise direction. It is observed that occurrence maximizes between 90° and 270° in all classes of upflow flux. This is in good agreement with existing theory that the IMF's geo-effectiveness is higher when the clock angle is southward. Moreover, it is also observed that during the southward excursion of the clock angle, there is preference for higher occurrence in the South-East direction (second quadrant) than the South-West in all the three classes of upflow. This implies that there is preference for upflow occurrence when the cusp is duskward than when it is dawnward, which is in good agreement with Howarth and Yau (2008) investigation of ion outflow into the plasma sheet. On the other hand it is observed that occurrence predominantly tends to minimum as the clock angle tends to absolute north direction, that is, at 0°or 360°.

6.3.6 Solar wind coupling function with ion upflow occurrence

Figure 6.6 presents the relationship between the upflow occurrence and the solar wind coupling function, a measure of energy delivered by the solar wind to the magnetosphere. There are many coupling function formulas relating the quantity of energy extracted from the solar wind, but in this work the Milan et al. (2012) approach is employed due to its high Pearson correlation coefficient of about 0.972. The required solar wind plasma parameters from OMNIweb are combined with equation (6.4) below to generate the values of the coupling function at every minute. Equation (6.4) and the notations have been defined after Milan et al. (2012).

$$\Phi_D = \Lambda V_x^{4/3} B_{YZ}\, sin^{9/2}\frac{1}{2}\theta \tag{6.4}$$

where Φ_D is 'the dayside coupling function',

V_x is the speed of the solar wind along the sun-earth line,

$B_{YZ}^2 = B_Y^2 + B_Z^2$ is 'the transverse component of the IMF',

θ is 'the clock-angle; the angle between the IMF vector projected into the GSM Y-Z plane and the Z-axis', i.e., $\theta = \tan^{-1}(\frac{B_Y}{B_Z})$, and

Λ is 'the coefficient of proportionality' given by $3.3 \times 10^5\ m^{2/3}\ s^{1/3}$.

The first panel of the figure indicates a linear correlation of ρ = 0.562 between the low flux occurrence and coupling function relationship, with an increasing occurrence as Φ_D increases. This implies that the higher the energy available for the solar wind-magnetosphere-ionosphere dynamics, the higher the tendency of ion upflow. At about $\Phi_D \geq 100$ kV, occurrence up to about 40% is reached in the low flux. On the second and third panels of Figure 6.6, the medium and high flux classes indicates a threshold of between 20 – 30 kV for coupling value before any substantial occurrence and correlation could be observed between upflow occurrence and coupling function whereas, at low coupling value (about 0 kV), low flux is still achievable. It could be inferred form Figure 6.6 that without any external driver, it is likely that as the field and ionospheric plasma rotate around the planet, corotation could drive the low flux category whereas enhanced convection is required for the medium and high flux classes. In addition, the study by Milan et al. (2012) shows that during reconnection activity at the nightside, viscous interaction could excite an offset of the order 25 kV without the occurrence of dayside reconnection. The threshold observed in the medium and high fluxes where minimum coupling function of about 20 – 30 kV is required could also be the offset needed to drive these classes of upflow flux.

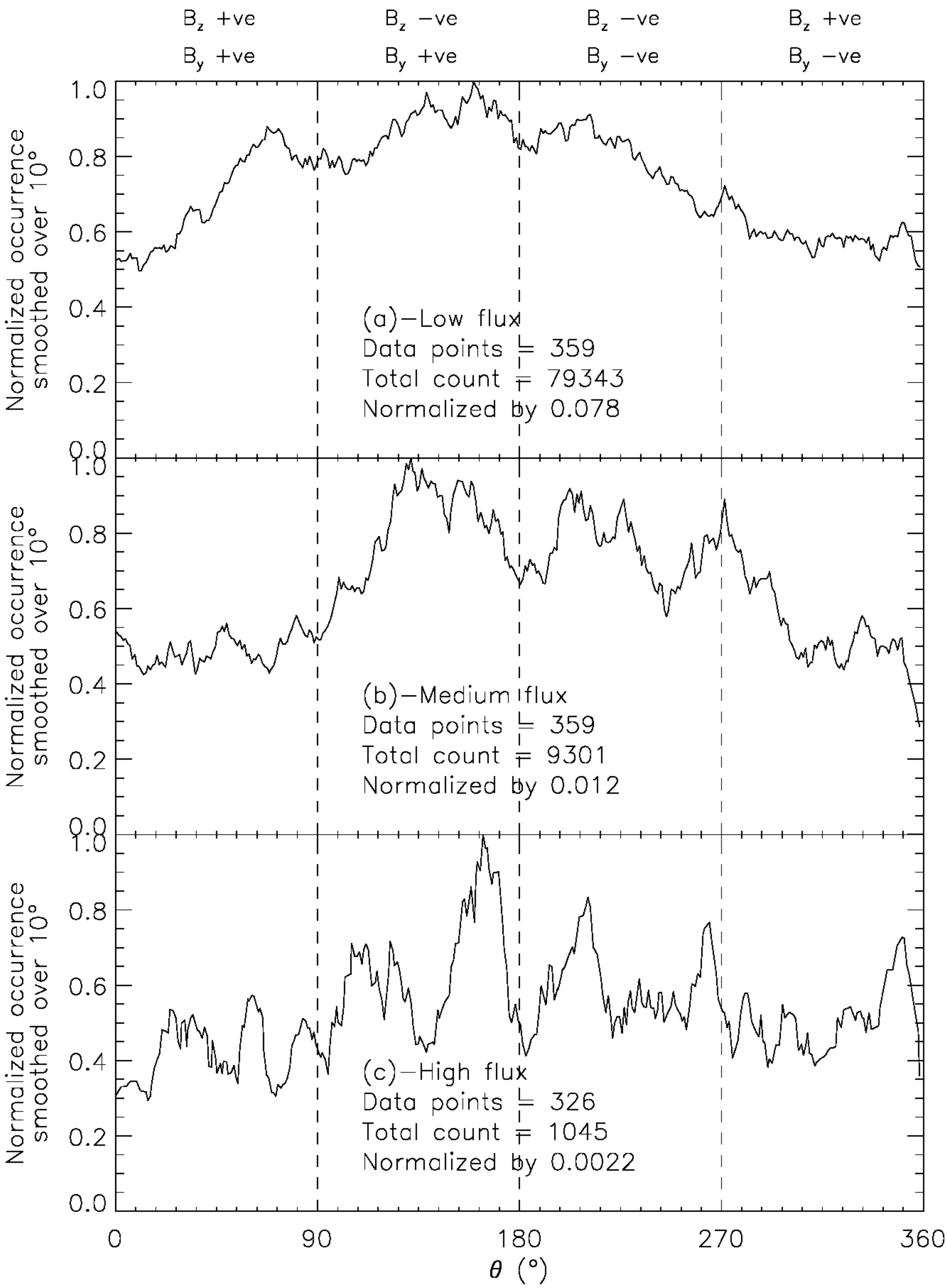

Figure 6.5: Plot showing the relationship between upflow occurrence and solar wind clock angle. The panels' format is the same as outlined in Figure 6.1. The dotted lines indicate the partitioning of the clock angle into the four quadrants in clockwise direction.

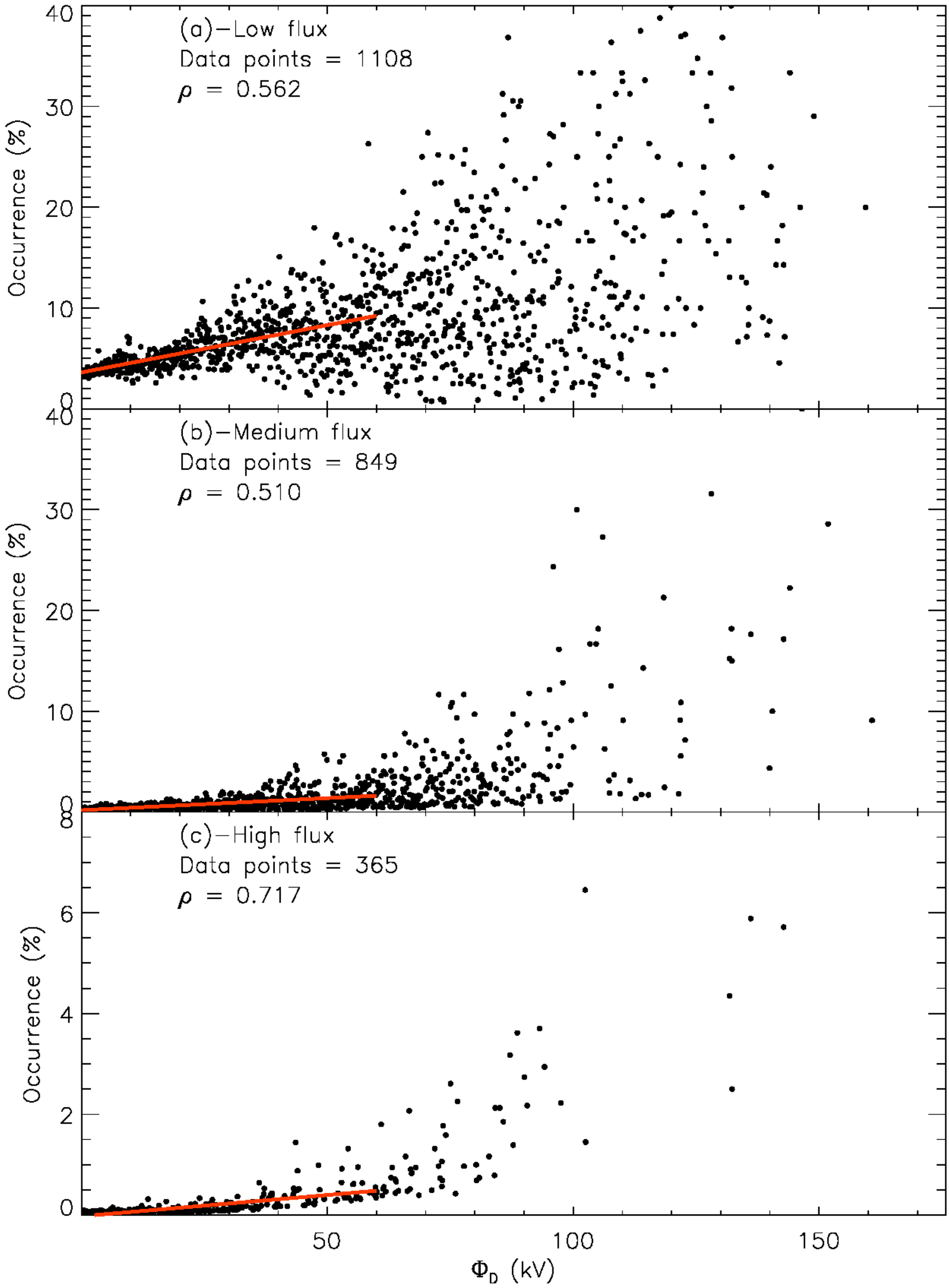

Figure 6.6: Plot showing the relationship between upflow occurrence and solar wind coupling function. The panels' format is the same as outlined in Figure 6.1.

6.4. Downstream magnetic activity relationship with ion upflow occurrence

In this section, the perturbation of the Earth's magnetic field caused by the eastward and westward current electrojets respectively measured as upper and lower auroral electrojet indices (SMU and SML), and the depletion of the earth's magnetic field caused by the ring current as measured by the Sym-H index is explored in relation to upflow occurrence. Each of the figures in this section also shows three panels consisting of the low, medium and high classes of flux in a respective order.

6.4.1 Ring current index (Sym-H) with ion upflow occurrence

Figure 6.7 shows the relationship between the upflow occurrence and the ring current index, Sym-H. A bin interval of 0.1 nT is chosen and the parameter is averaged over the interval. Detailed analysis of the ring current classification as stated in Chapter 5 indicates no intense geomagnetic activity throughout the IPY campaign period, consistent with being at solar minimum. However, the ring current index data indicates that geomagnetically quiet (see Vieira et al., 2001) activity dominates the period with about 96.6% of the Sym-H data. The first panel of Figure 6.7 presents the low flux showing about 120 data points for which $\rho = -0708$ between 0 to -35 nT. However, the magnitude of ρ is about 2% for the overall data points, which implies that the low class of upflow is not necessarily tied to geomagnetic storms. Moreover, distinct minimum is observed around absolute quietness (0 nT) and the occurrence did not go beyond about 4% whereas, on the left flank about 12 - 13% occurrence is observed. The medium and high classes of flux on the respective second and third panels of Figure 6.7 show linear Pearson correlation coefficients (ρ) of about 80% and 68% respectively. The negative value in ρ indicates an increasing occurrence as the opposing magnetic field due to the ring current gets stronger than the earth's magnetic field, thereby causing depletion in the earth's magnetic field. The magnitude of ρ for all the data points is about 30% and 35% respectively for the medium and high fluxes. Occurrence during positive value of Sym-H in all classes of upflows as shown in Figure 6.7 indicates that during the compression of the magnetosphere, the dynamics of magnetosphere-ionosphere system can as well support ion upflow to a certain extent.

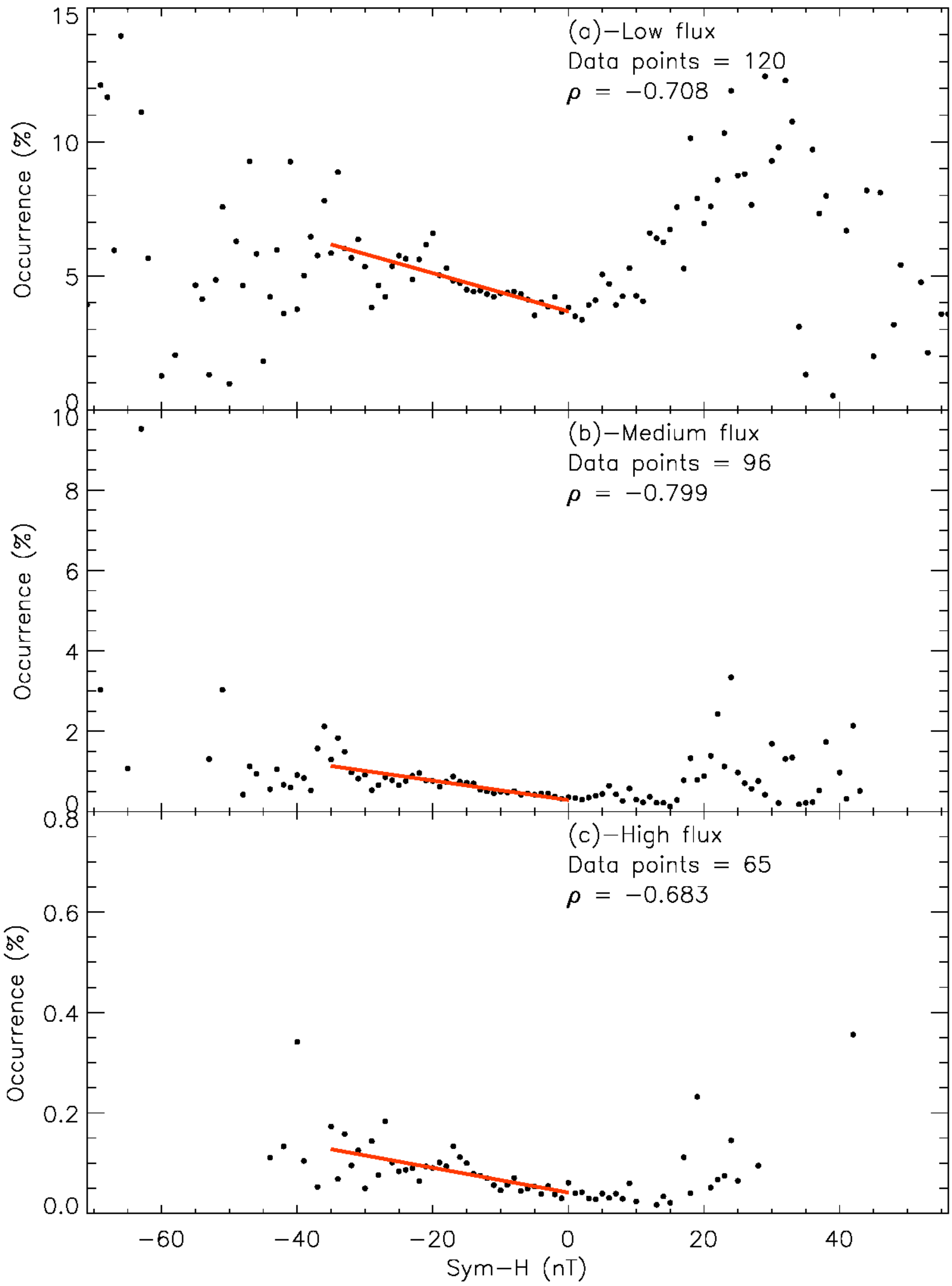

Figure 6.7: Plot showing the relationship between upflow occurrence and downstream terrestrial magnetic activity measured by the ring current index. The panels' format is the same as outlined in Figure 6.1.

6.4.2 SuperMAG lower auroral electrojet index with ion upflow occurrence

The relationship between the occurrence of the ion upflow and the SuperMAG lower auroral electrojet (SML) is presented in Figure 6.8. The data is binned at 1 nT interval and a total of 2,082 data points are obtained. The low flux is shown on the first panel with a total number of 908 data points spanning between -1200 nT and 0 nT. The negative slope and the linear Pearson correlation coefficient of -0.706 suggest that the upflow occurrence decreases as the magnitude of the earth's magnetic perturbation decreases from the baseline. There is almost a monotonic increase before about -250 nT and almost all the data points fit well on the line of best fit. Thereafter, the dispersion of the data points grows as the electrojet grows in magnitude. Low flux up to about 40% occurrence is observed when the magnitude of SML is above 800 nT whereas, occurrence frequencies of about 7% or less are very common before about -250 nT. The second panel of Figure 6.8 showing the medium flux indicates that a threshold magnitude of about -200 nT is required before significant occurrence could be observed. The 784 data points investigated in the medium class of upflow shows a linear Pearson correlation coefficient of -0.604. The negative slope and correlation as before also indicate an increasing occurrence the more the southward perturbation by the westward current electrojet increases below the baseline. The threshold for significant occurrence shown by high flux on the third panel is over -400 nT and only about 12% of the 390 data points plotted show above 0.5% occurrence. However, increase in occurrence with respect to SML is also as indicated in the low and medium classes of upflow. The high-flux upflow has a $\rho = -0.616$, about the order observed in the medium flux.

I have also looked at the lower auroral electrojet (AL) obtained from OMNIweb and observed that both behave in the same way and the result is almost identical. I have chosen to present the SuperMAG plot because of its large coverage of more ground-based magnetometers and it also contains more data points before and after the average analysis.

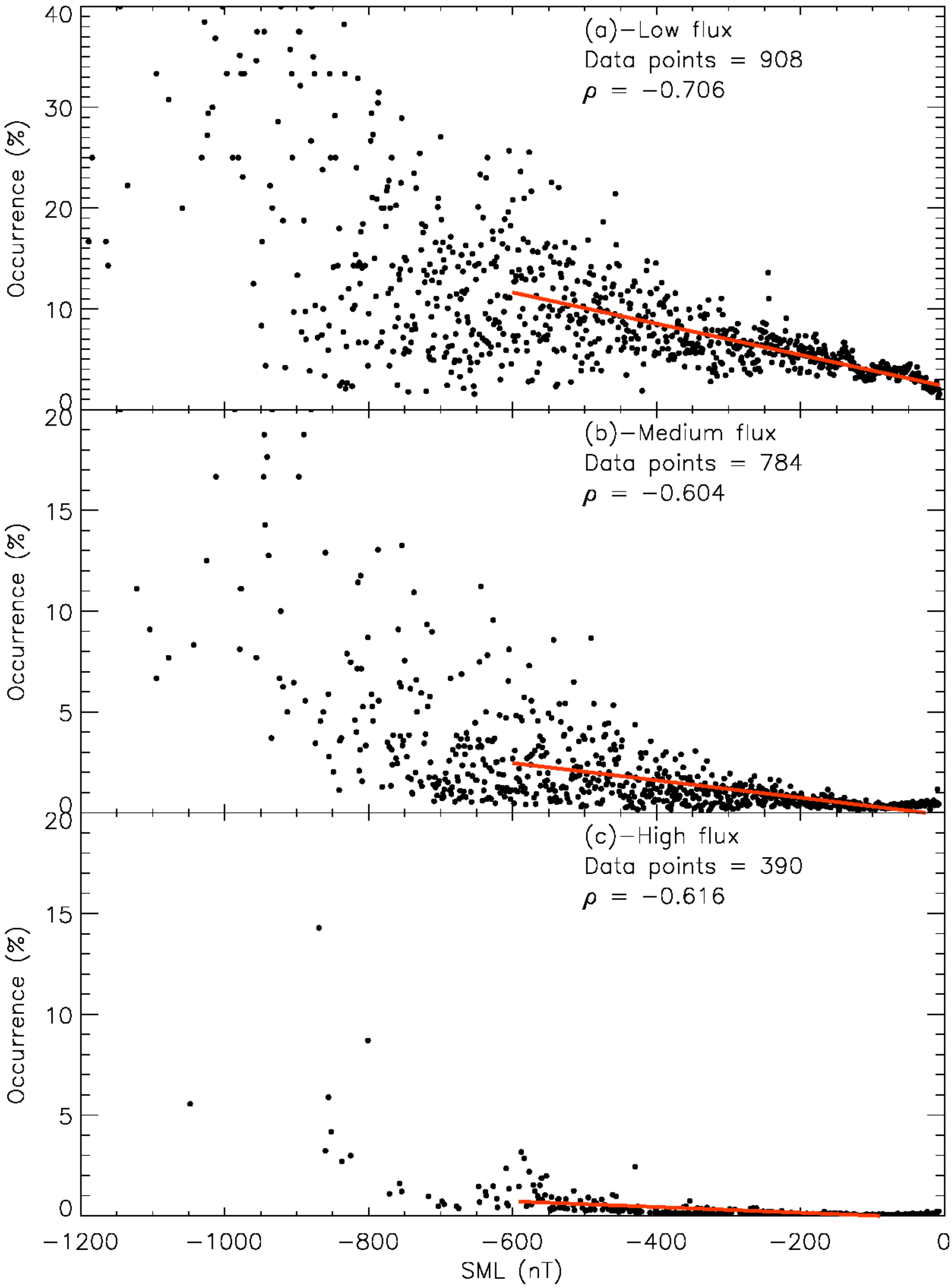

Figure 6.8: Plot showing the relationship between upflow occurrence and earth's horizontal magnetic field perturbation measured by the SuperMAG lower electrojet index. The panels' format is the same as outlined in Figure 6.1.

6.4.3 SuperMAG upper auroral electrojet index with ion upflow occurrence

Analysis of the relationship between upflow occurrence and the SuperMAG upper auroral electrojet (SMU) is presented in Figure 6.9. The data is binned at 1 nT interval and the SML is averaged in each bin. A total of 499 data points shown on the first panel is presented for the low flux. The points have a linear Pearson correlation coefficient of 0.769 until 300 nT after which more randomness is observed. A well-defined pattern is observed when SMU is below 200 nT, after which variation in dispersion of the data points from the line of best fit gets bigger with increase in SMU. A noticeable feature is a prominent drop in the occurrence frequency after about 300 nT. This drop in occurrence becomes more pronounced between about 350 – 400 nT and has no conjugate data points at the other side if the line of best fit is projected. Such a feature is not observed in SML and makes it a better parameter that can influence the upflow occurrence at higher values than the SMU. On the second panel of Figure 6.9 is the medium flux which shows 405 data points. At about 250 nT, the rising occurrence begins to fall until about 400 nT creating another dip as in the low flux. However, the slope of the medium flux up to 300 nT is shallower than in the low flux and its value for ρ is 0.447. The high flux on the third panel of Figure 6.9 starts with a very low and almost constant occurrence until about 120 nT, and thereafter begins to increase as SMU increases. Unlike the low and medium flux, there is no prominent dip observed in the high flux and linear correlation coefficient of 0.475 is observed in the high-flux upflow for data up to 300 nT.

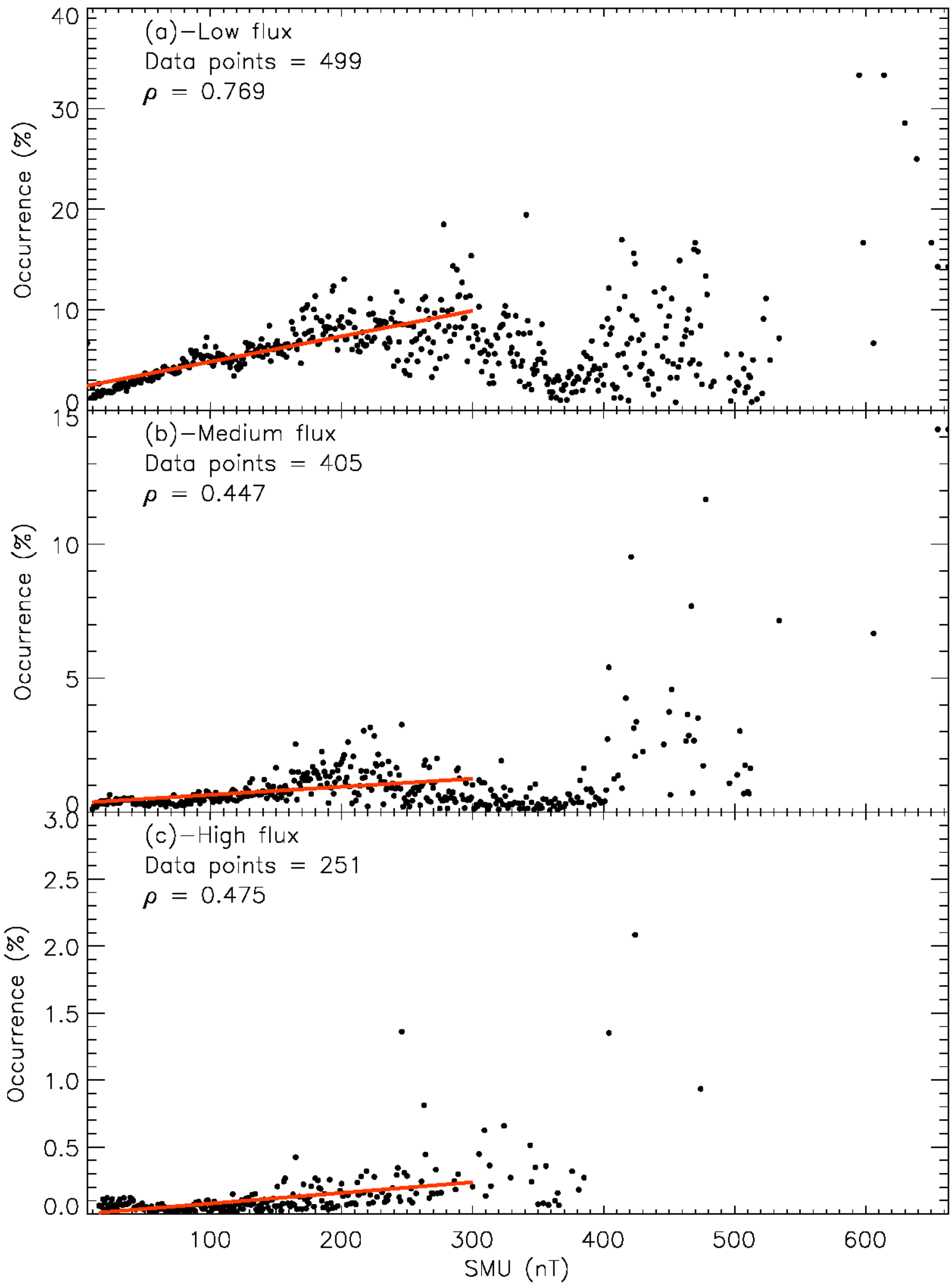

Figure 6.9: Plot showing the relationship between upflow occurrence and earth's horizontal magnetic field perturbation measured by the SuperMAG upper electrojet index. The panels' format is the same as outlined in Figure 6.1.

6.5. Effect of the solar wind on upflow flux

In this section, the total upflow flux satisfying the threshold of $10^{13}\ \mathrm{m^{-2}\ s^{-1}}$ is counted in a bin interval of $1\ \mathrm{km\ s^{-1}}$ for the solar wind speed, while $0.1\ \mathrm{cm^{-3}}$, 0.1 nT and 1° intervals are chosen for solar wind number density, IMF and clock angle respectively. The solar wind parameters are averaged in each bin and the number of upflow in each bin is normalized by the highest value across all bins. The normalized upflow flux is plotted (Figures 6.10 – 6.15) against the corresponding averaged solar wind parameters. Six parameters namely, solar wind speed, solar wind number density, IMF B_y, IMF B_z, IMF B_{mag} and the clock angle and the relationship with the total flux is investigated in this section and presented in Figures 6.10 – 6.15. Each of the figures in this section also shows three panels consisting of the low, medium and high classes of flux in a respective order. Table 6.1 shows the summary of the key results for the plots in this section. The number of upflow in each bin is given as expressed in equation (6.5) below:

$$number\ of\ upflow\ in\ bin = \text{normalized count} \times \text{normalization factor} \quad (6.5)$$

6.5.1 Upflow flux dependence on solar wind speed

In this section the relationship between the total number of upflow flux and the solar wind speed is presented in Figure 6.10. The first panel presenting the low flux of total count close to about 71,000 which when averaged over $1\ \mathrm{km\ s^{-1}}$ gives an array of 483 data points that are smoothed over $5\ \mathrm{km\ s^{-1}}$. The upflow flux peaks at about 670 units (1.0 on normalized axis) at a solar wind speed (v_{sw}) of about $440\ \mathrm{km\ s^{-1}}$ and tends to zero where $v_{sw} \geq 700\ \mathrm{km\ s^{-1}}$. The medium flux on the second panel also indicates peak flux in the range $v_{sw} = 440\ \mathrm{km\ s^{-1}}$ to $460\ \mathrm{km\ s^{-1}}$ with a peak upflow of about 71. On the third panel is the high flux of peak upflow flux of about 10 around $v_{sw} = 410\ \mathrm{km\ s^{-1}}$. Comparison between Figure 6.10 and Figure 6.1 shows that there are some few high flux upflow when $v_{sw} \geq 700\ \mathrm{km\ s^{-1}}$ but the occurrence is negligible. It can be concluded from Figure 6.10 that upflow flux is mostly frequent between about $400 \leq v_{sw} \leq 450\ \mathrm{km\ s^{-1}}$ which could be linked to average value of solar wind speed especially during solar minimum as it is the case in this study.

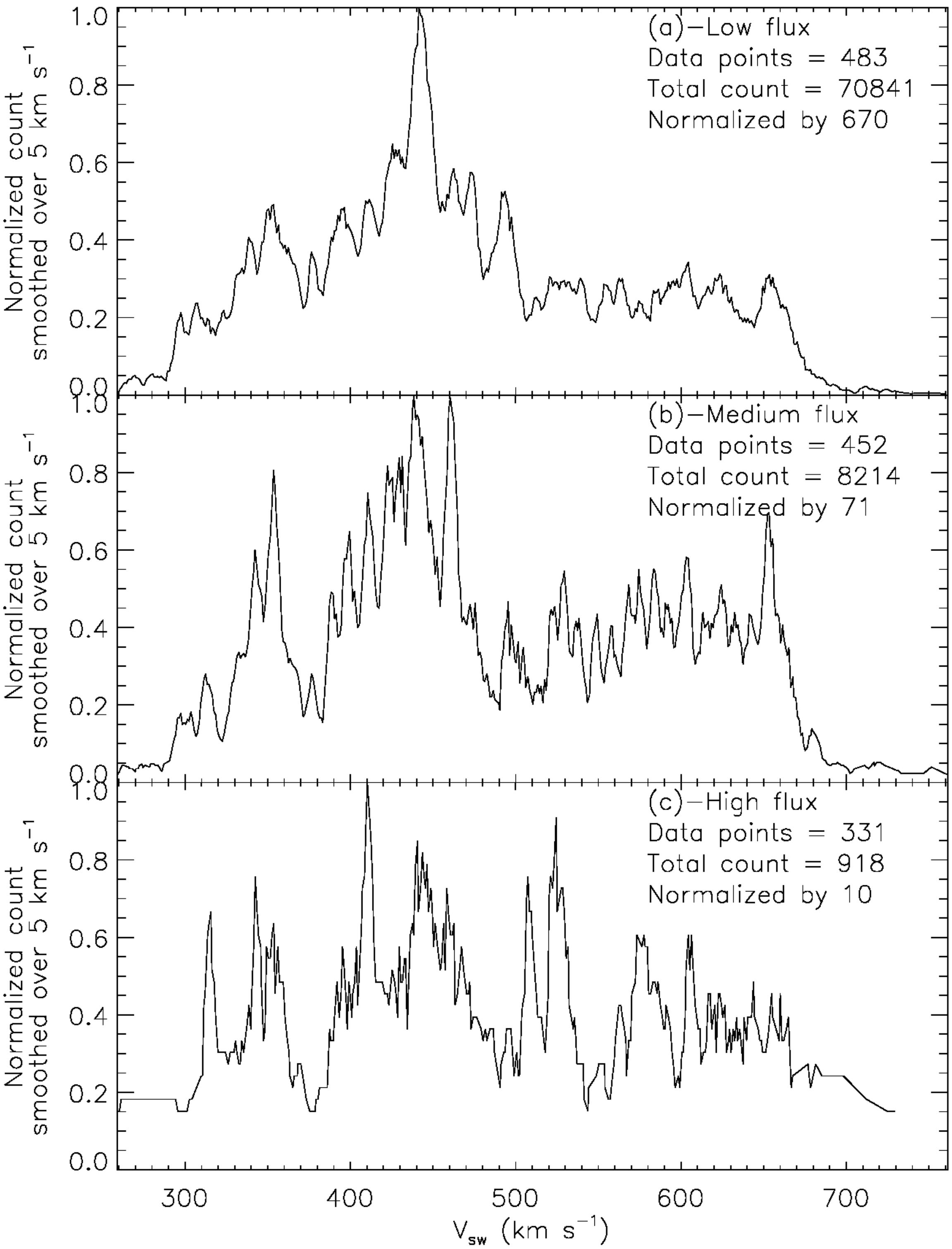

Figure 6.10: Plot showing the total number of upflow flux in 1 km s^{-1} bin interval of solar wind speed. The panels' format is the same as outlined in Figure 6.1.

6.5.2 *Upflow flux dependence on solar wind number density*

Figure 6.11 shows the relationship between the number of ion upflow and solar wind number density smoothed over $2\ \mathrm{cm}^{-3}$. The normalized count shows a rising value from about $0.68\ \mathrm{cm}^{-3}$ to a peak at $3.04\ \mathrm{cm}^{-3}$ in all classes of flux and thereafter an almost exponential decay of the normalized count follows. Over 1800 low flux counts are observed at the solar wind number density of about $3.04\ \mathrm{cm}^{-3}$ while about 187 and 35 upflow flux counts belong to medium and high fluxes respectively at about the same number density. Further analysis shows that count asymptotically goes to zero at number density predominantly above $20\ \mathrm{cm}^{-3}$. The likelihood of the low number density of about $3\ \mathrm{cm}^{-3}$ could be traced to the deep solar minimum of the period under investigation hence, it is expected that during solar maximum, higher number density could be attributed to maximum number of upflow. This is left opened to future research for confirmation.

6.5.3 *Upflow flux dependence on IMF B_y*

The number of upflow per 0.1 nT bin interval of the IMF B_y is presented in Figure 6.12. Upflow flux close to about 80,000 are grouped into 308 bins for the low flux, while about 9,300 and a little above 1,000 are grouped into 265 and 158 bins for the medium and high fluxes respectively. It is observed that as the magnitude of B_y decreases the number of upflow predominantly increases. Notable feature observed is the depression around $B_y = 0$ nT and elevated total number of upflow flanking the absolute zero value in all classes of upflow. An inference drawn from this is that there is preference for upflow during asymmetry of the cusp. In addition, the preference is also shown to be in favour of the duskward side.

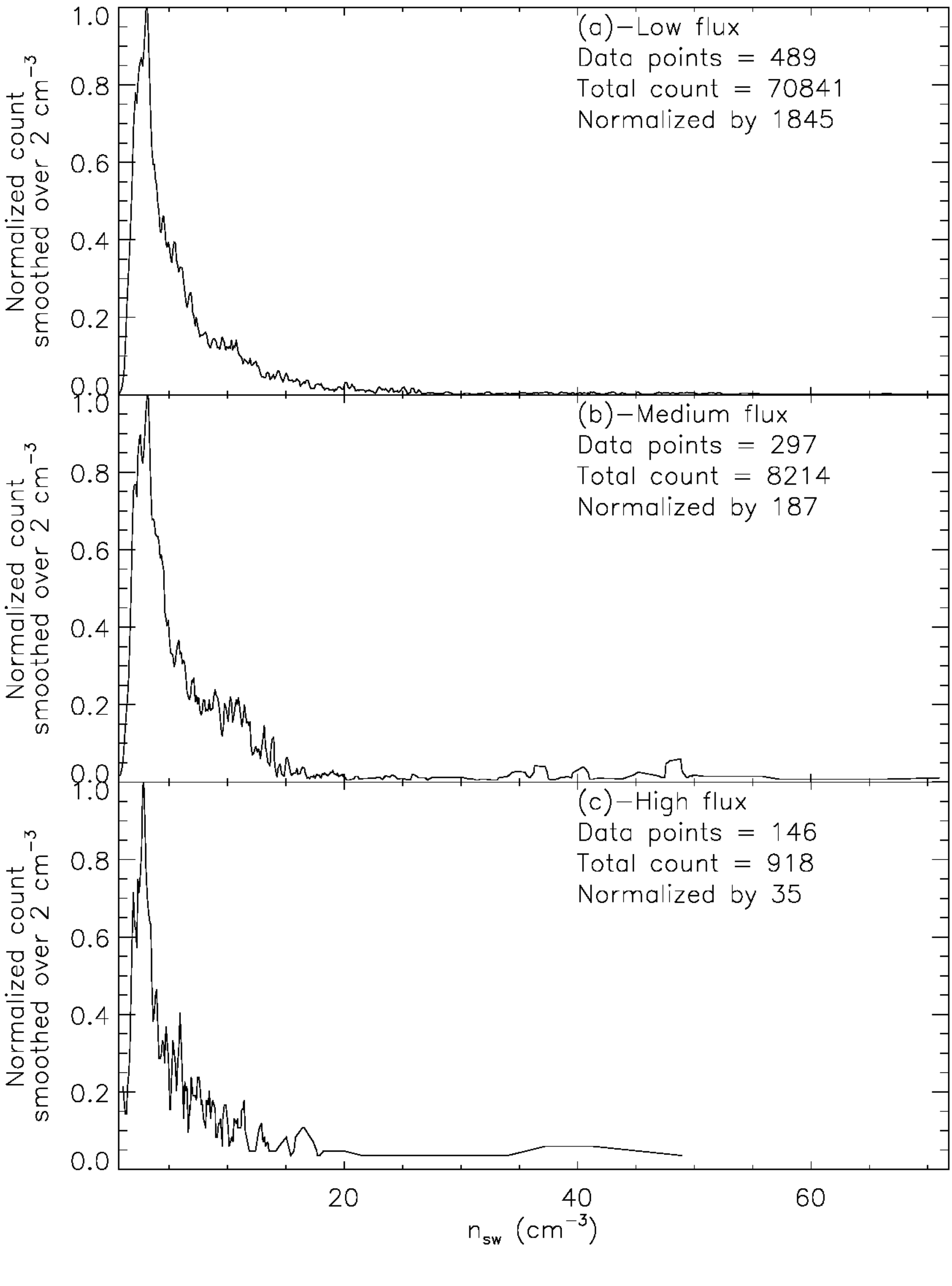

Figure 6.11: Plot showing the total number of upflow flux in 0.1 cm^{-3} bin interval of solar wind number density. The panels' format is the same as outlined in Figure 6.1.

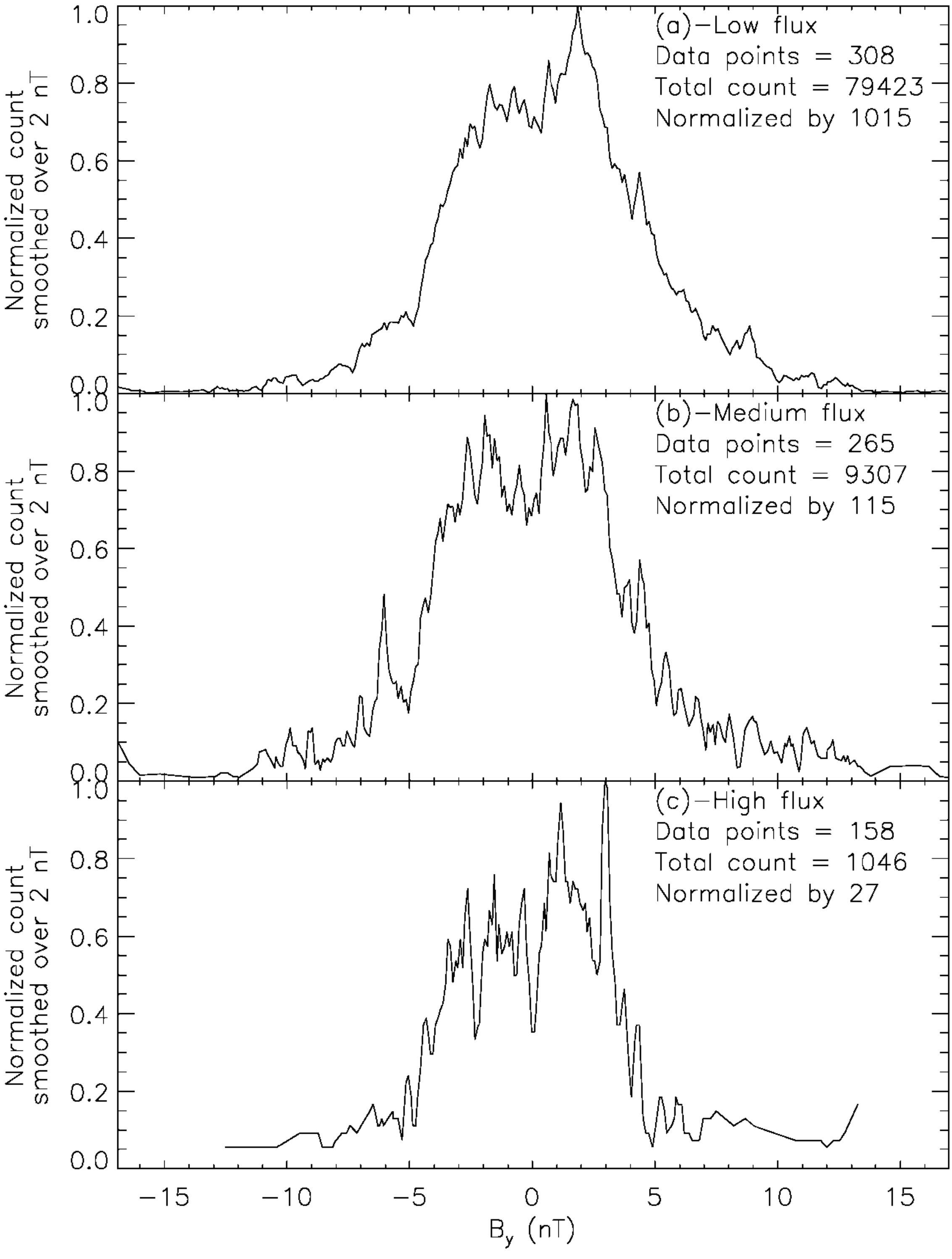

Figure 6.12: Plot showing the total number of upflow flux in 0.1 nT bin interval of IMF B_y. The panels' format is the same as outlined in Figure 6.1.

6.5.4 Upflow flux dependence on IMF B_z

The plot shown in Figure 6.13, which is smoothed over 2 nT, presents the dependence of upflow flux on IMF B_z. The upflow is binned in the same way as IMF B_y above and the same total number of upflow flux is investigated in all classes of flux in both cases. However, the number of data points in each bin varies for the two orientations of IMF. It is observed that the number of upflow in bins predominantly drops as the magnitude of IMF B_z increases. Moreover, a sharp decrease is observed for low flux, but less for medium flux. The high flux on the other hand shows a more variable drop especially when B_z is negative. This could mean that high flux is triggered when geomagnetic activity increases. It is noted in Chapter 5 that ion upflow can be observed during southward and northward turning of IMF B_z. Detailed analysis of the areas under the curves in Figure 6.13 shows the total number of upflow when B_z is southward or northward. The dashed line on the plot is the zero reference before and after which the area is calculated for southward and northward B_z respectively. The low flux shows about 42,717 and 35,062 upflows during southward and northward B_z respectively, while the medium and high classes of flux indicate about 5,417 and 597 during southward B_z and 3,707 and 424 during northward B_z respectively. Although there is less activity due to solar minimum at the period under investigation, yet the number of upflow in all classes of flux is slightly greater during southward B_z than northward B_z.

6.5.5 Upflow flux dependence on IMF B_{mag}

Figure 6.14 is smoothed over 2 nT and it shows the dependence of the ion upflow on the magnitude of the interplanetary magnetic field. Data is grouped at a spacing of 0.1 nT into about 200 bins from the 79,423 low flux shown on the first panel. The number of upflows in each bin is counted and plotted against the average IMF B_{mag} in the corresponding bin. Similarly, about 174 and 127 data bins from medium and high fluxes, of about 9,307 and 1,046 upflows, are plotted as shown on the second and third panels respectively. Observation shows that the number of upflows grows predominantly as the interplanetary magnetic field strength increases from 0 to about 3 nT in all classes of upflow and largely sustained until around 5 nT. Thereafter, a quick down turn to about 20% of the upflow flux peak is observed

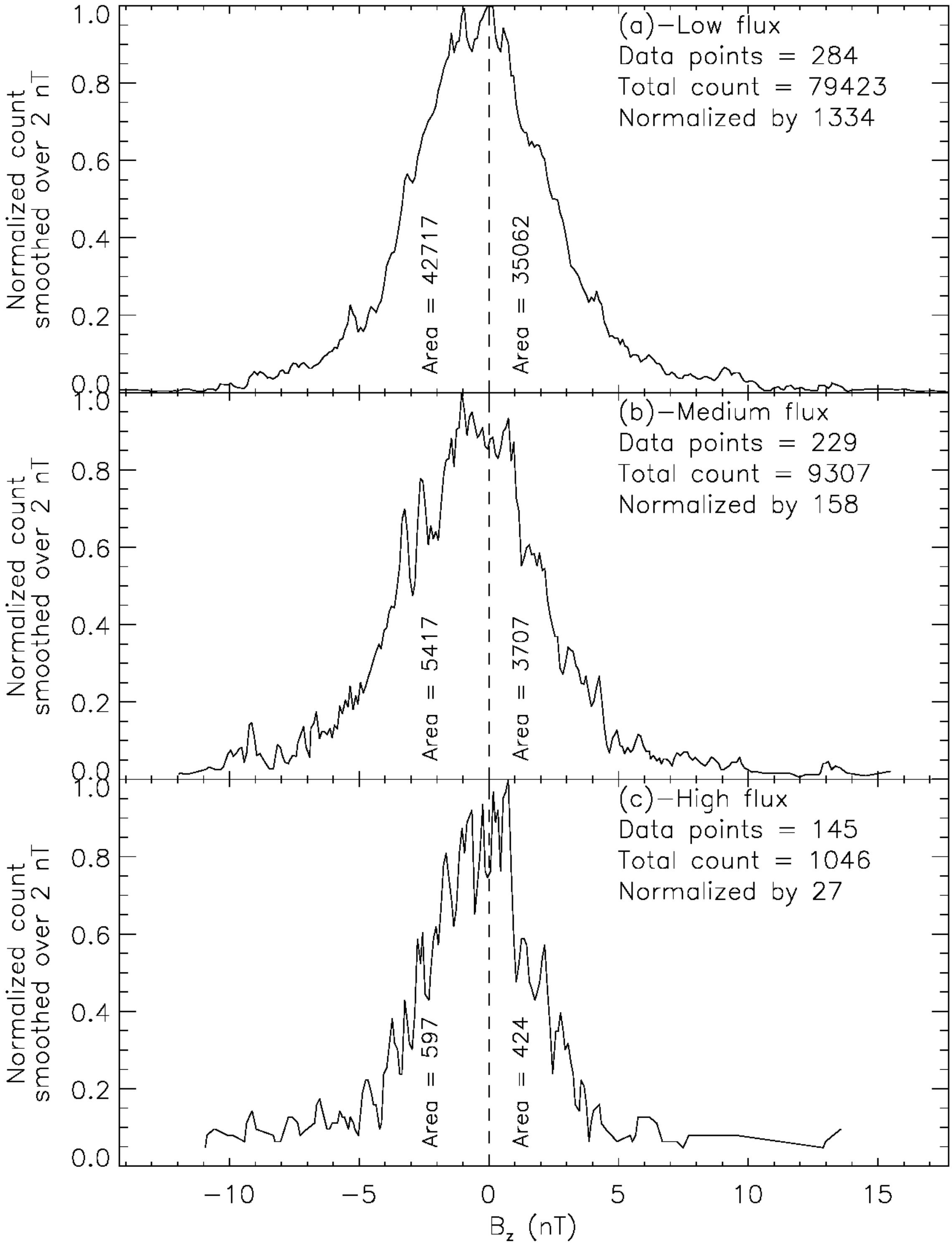

Figure 6.13: Plot showing the total number of upflow flux in 0.1 nT bin interval of IMF B_z. The panels' format is the same as outlined in Figure 6.1.

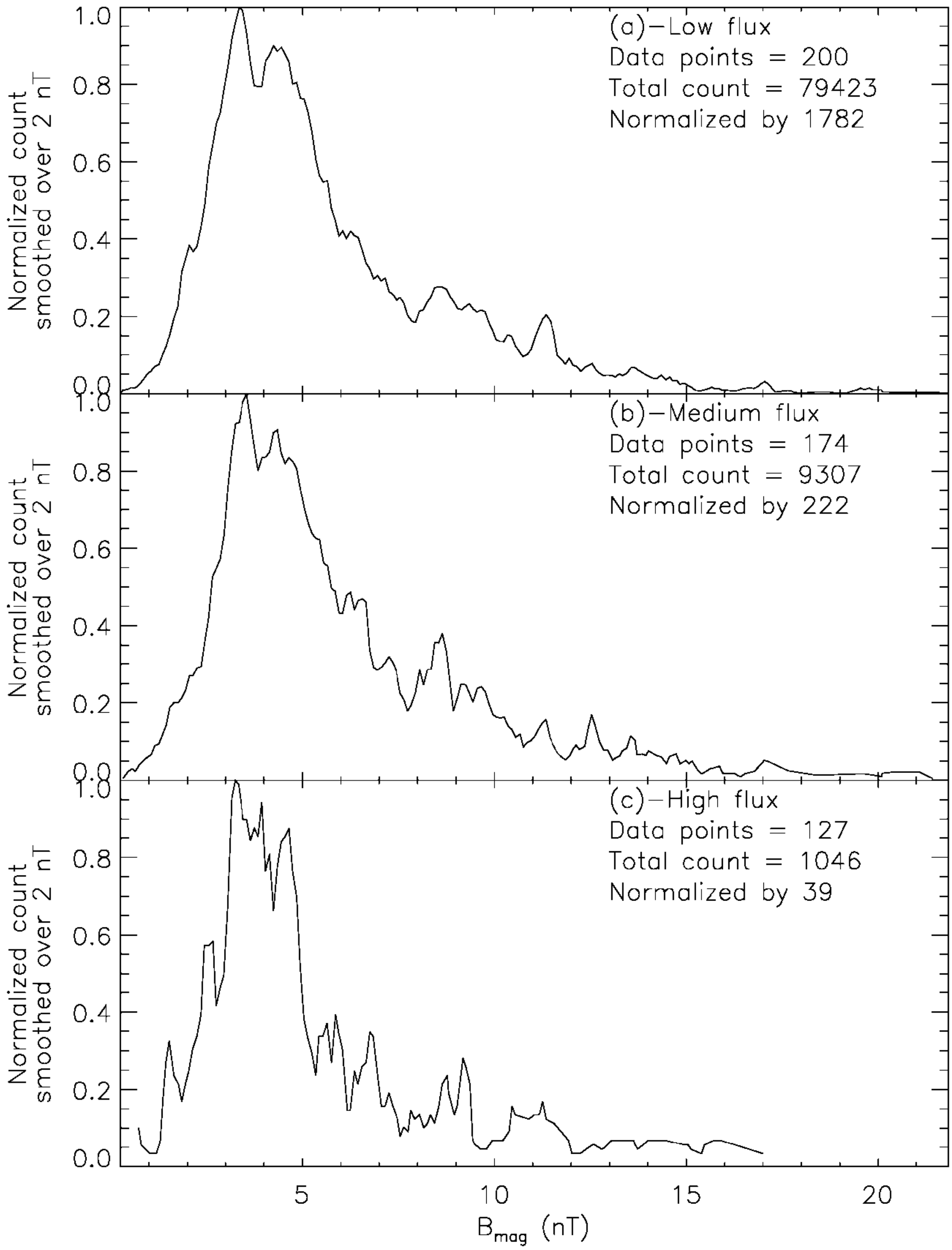

Figure 6.14: Plot showing the total number of upflow flux in 0.1 nT bin interval of IMF B_{mag}. The panels' format is the same as outlined in Figure 6.1.

around 8 nT in the low flux and oscillates to about 0.05% around 14 nT after which it predominantly approaches about 0% at higher IMF B_{mag}. However, the sharp decrease in the medium and high flux classes is short-lived (i.e., less than 1 nT), but thereafter the amplitude percentage decay faster in medium flux in comparison to the high flux. Further analysis reveals that a minimum of about 0.7 nT of IMF strength is required before a high upflow could occur, whereas as low as about 0.2 nT and 0.3 nT are observed in the low and medium fluxes respectively.

6.5.6 Upflow flux dependence on clock angle

Figure 6.15 presents the relationship between the clock angle and the number of upflows in their respective classes during the period of investigation. The data is binned at 1° interval and about 80,000 low upflows are binned into about 360 bins while the medium and high fluxes have about 9,289 and 1,045 numbers of upflows that are binned into about 360 and 326 bins respectively. The first to third panels of Figure 6.15 show smoothed plots over 10° for the low, medium and high upflow classes respectively. It can be seen that minimum number of upflow flux is observed in all the panels when the clock angle is around 0°, indicating northward B_z, during which reconnection is less likely to be geoeffective, and the number of upflow is reduced. In addition, turning points are observed in the low flux when the clock angle is in the south-west and north-east direction in both flanks however, with preference to the large number of upflows in the north-east direction. The medium flux on the second panel shows almost symmetric upflows in both flanks of $\theta = 0^{\circ}$ and maxima are observed around south-west and south-east directions of IMF projection into the GSM Y-Z plane. Similarly, the high flux like the medium flux also show a symmetry on both sides of $\theta = 0^{\circ}$. On the other hand intermittent peaks are observed across a wide range of θ in the high flux than the other classes.

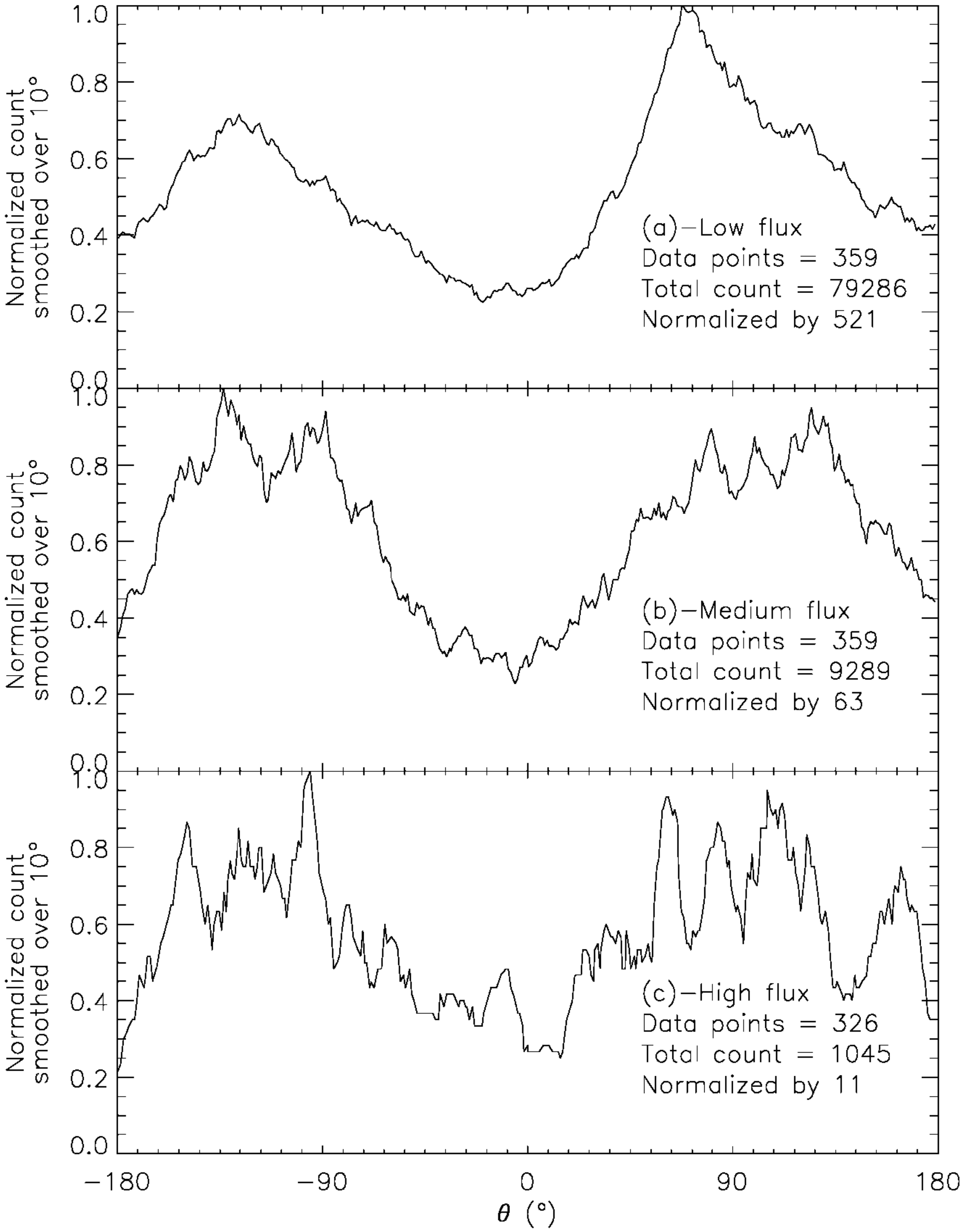

Figure 6.15: Plot showing the total number of upflow flux in 1° bin interval of solar wind clock angle. The panels' format is the same as outlined in Figure 6.1.

Table 6.1: Key results of Figures 6.10 – 6.15. Peak value of the solar wind and upflow flux relationship in black, and its standard deviation in red.

	Solar wind parameters	Flux		
		Low	Medium	High
i.	v_{sw} (km s^{-1})	441.47 (139.98)	438.42 (132.55)	410.28 (113.79)
ii.	n_{sw} (cm^{-3})	3.10 (17.40)	3.15 (13.95)	2.84 (8.46)
iii.	B_y (nT)	1.86 (9.07)	0.56 (7.98)	2.96 (5.46)
iv.	B_z (nT)	0.15 (8.39)	−1.05 (7.09)	0.75 (5.16)
v.	B_{mag} (nT)	3.35 (5.98)	3.55 (5.31)	3.25 (4.23)
vi.	θ (°)	67.49 (103.78)	−133.56 (103.77)	−95.38 (104.73)

6.6. Ion upflow flux dependence on ionospheric parameters

The correlation of ion upflow flux with the ionospheric parameters derived from the ESR is now investigated with respect to the classes of the upflow flux and season. Apart from the four basic ionospheric parameters measured by ESR namely, ionospheric electron density, n_e, ion temperature, T_i, electron temperature, T_e and the ion drift velocity v_i, the derived "average plasma temperature", $< T_p >$, defined by Skjæveland et al. (2014) as shown in equation (6.6) below is also investigated in order to observe the behaviour of the plasma temperature in comparison to the ion and electron temperatures.

$$< T_p > = (T_i + T_e)/2 \qquad (6.6)$$

Figures 6.16 – 6.20 are presented in this section, each having four panels showing the seasons of the year and the ion flux is on a logarithm scale.

6.6.1 *Upflow flux dependence on field-aligned ion velocity*

Figure 6.16 shows the relationship between the ion upflow flux and the field-aligned ion velocity. In all the seasons, it is observed that the slope is positive as seen in the positive linear Pearson correlation coefficients, suggesting that flux increases as ion velocity increases. However, the correlation is below 40% in every season at all classes of upflow flux. Moreover, the lowest correlation in low and high classes of flux is observed in winter. In addition, clutter is observed to be predominant in winter where velocity around 10 km s^{-1} is observed. On the other hand, correlation is highest in the high flux category among the classes of upflow across the seasons, and it ranges between about 28 – 40% with the least correlation occurring in winter. It is observed that apart from summer period, the high flux predominantly requires a threshold of about 100 m s^{-1} to occur. However, further analysis shows that low and medium fluxes predominantly require a threshold velocity of about 15 m s^{-1} and 20 m s^{-1} respectively. Table 6.2 shows the analysis of the upflow flux throughout the IPY campaign, where about 77% of the upflows occur between 50 – 300 km s^{-1}.

Table 6.2: Upflow flux in different velocity regimes.

	Field-aligned velocity $(\mathrm{m\ s^{-1}})$	**Number of upflow flux**	**Percentage of upflow flux (%)**
i.	$50 \leq v_i < 100$	31,876	33.99
ii.	$100 \leq v_i < 200$	28,708	30.61
iii.	$200 \leq v_i \leq 300$	11,814	12.60

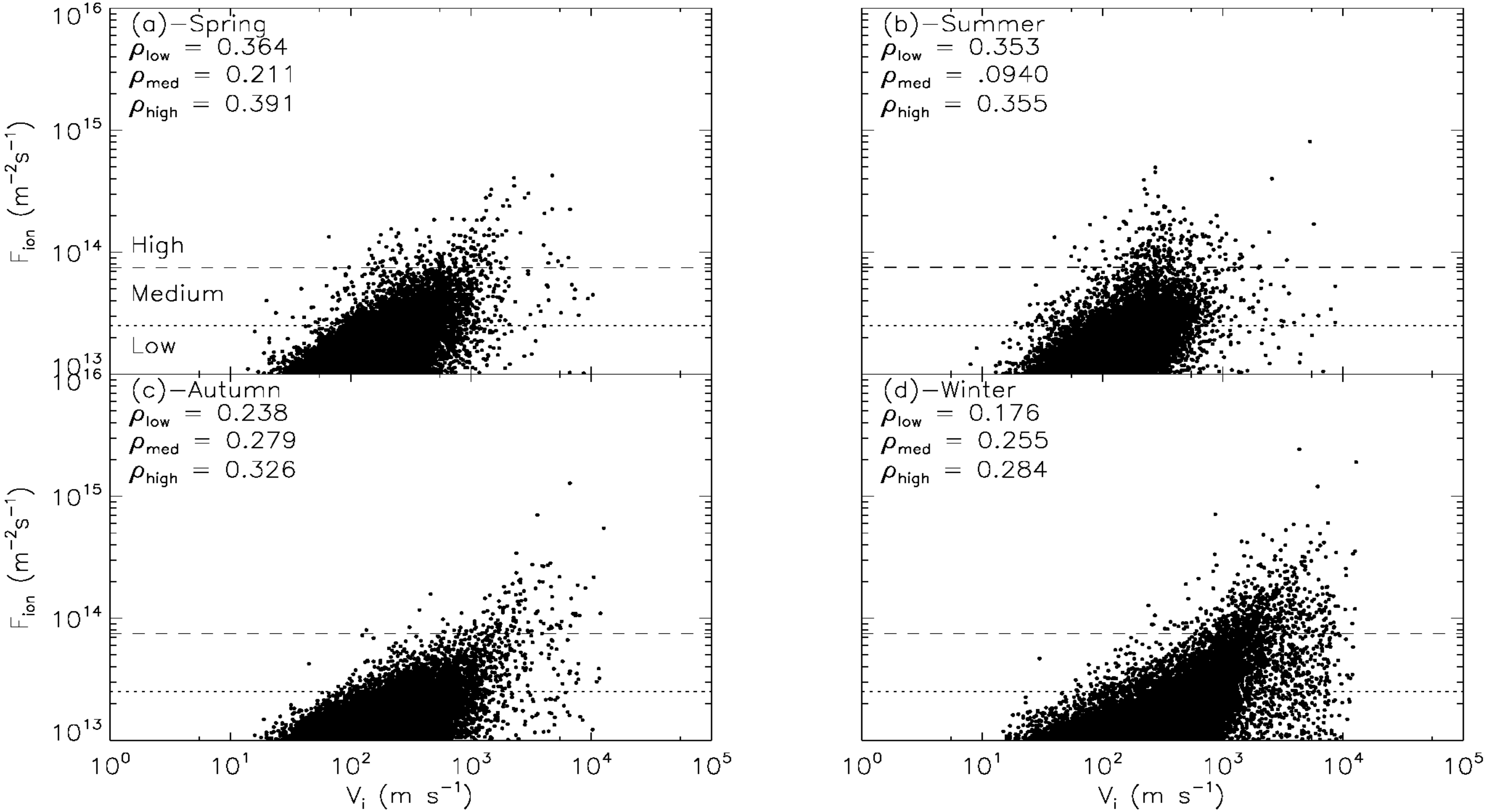

Figure 6.16: Plot showing seasonal upflow flux dependence on field-aligned ion velocity on a log-log scale. The top two panels labelled (a) and (b) indicate spring and summer, while the bottom panels (c) and (d) indicate spring and winter respectively. The dotted and dashed lines on the panels show the upper boundaries of the low and medium fluxes as marked. Above the dotted lines is the high-flux upflow

6.6.2 Upflow flux dependence on ionospheric electron density

In Figure 6.17, the relationship between the upflow flux and ionospheric electron density is investigated. All the panels in the figure show that the relationship is predominantly dome shaped and hence, low correlation. This is in agreement with Skjæveland et al. (2014) in their study of 6 hours data from ESR observation on December 20, 1998 that there is poor correlation between ion upflow and ionospheric electron density. The present study extends the investigation beyond winter and observed that apart from summer, anti-correlation is seen in other seasons. For the high flux, the ion flux is driven by high n_e in summer, while n_e seems to be poorest in winter where the distribution shifted to lower n_e due to the small amount of solar flux reaching the Earth at the period coupled with little or no direct production as a result of winter night. The occurrence of ionospheric electron density above 10^{12} m^{-3} leading to ion upflow is predominant in summer and analysis shows that about 57% of the summer upflow flux due to the high n_e result in high flux, and none in winter for same class of upflow. However, further analysis shows that when $n_e \geq 10^{12}$ m^{-3} in summer, about 29.1% of it results in ion upflow while only 2.3% do in winter (only medium-flux upflow). Moreover, about 0.34% of the total event points during the IPY campaign are in this higher density regime, 13.5% of which resulted in an upflow flux. Highest correlation between the ion upflow and electron density in the high flux class appears to be in winter, but it should be noted that clutter in the velocity, which directly relates to ion flux, is largely observed in winter and could as a result bias the result in winter.

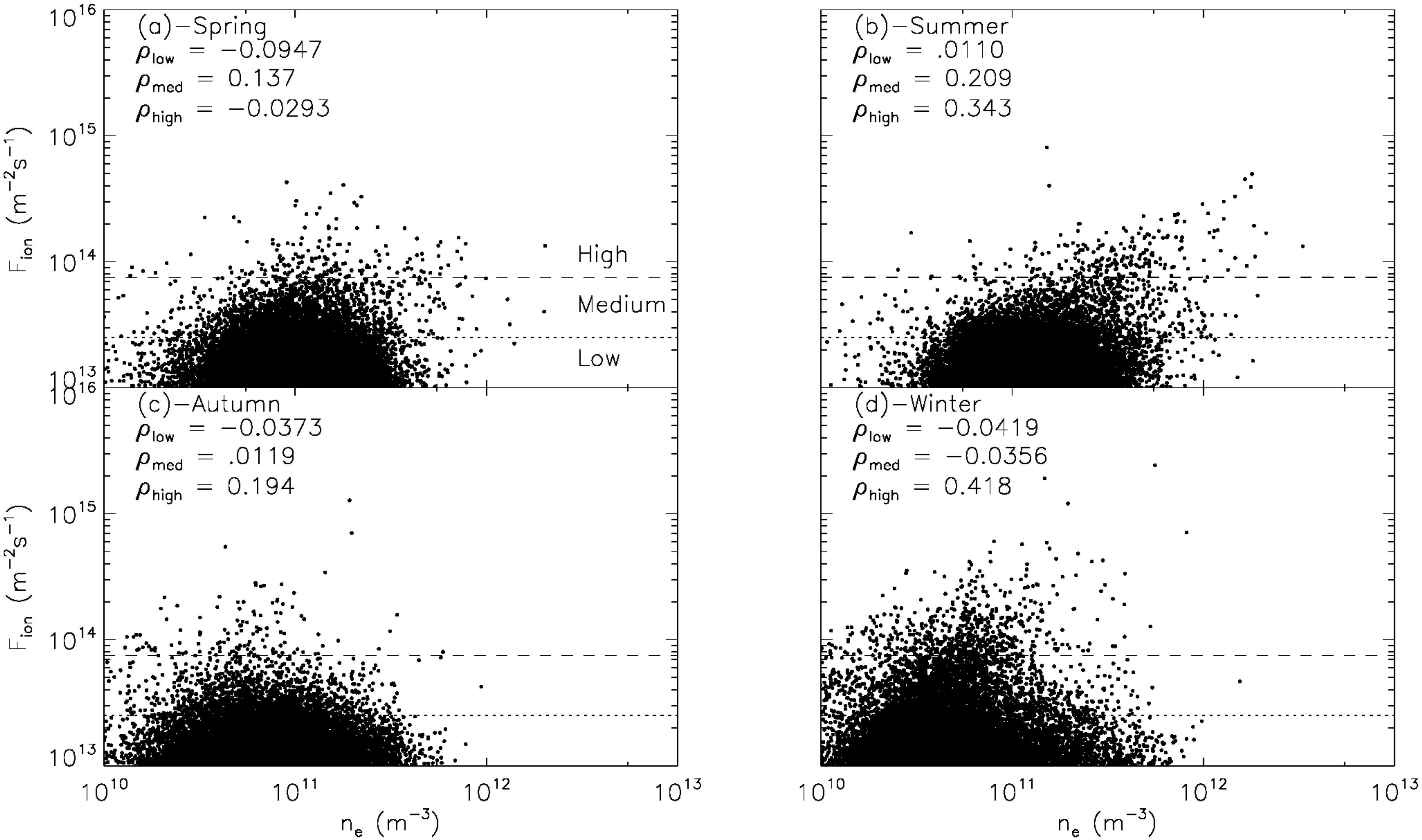

Figure 6.17: Plot showing seasonal upflow flux dependence on ionospheric electron density on a log-log scale. The panels' format is the same as outlined in Figure 6.16.

6.6.3 Upflow flux dependence on ion temperature

Ion upflow is a function of plasma temperature and it is a dominant mechanism that drives the heating responsible for an increase in the ion scale height and ion upwelling as a result (Wahlund et al., 1992; Skjæveland et al., 2014). Figure 6.18 presents the relationship between the ion upflow flux and ion temperature. In autumn and winter, very low correlation between 0.01 and 0.09 is observed, while low correlations up to about 0.32 and 0.22 are respectively observed in spring and summer respectively. A high correlation of up to 0.75 was reported by Skjæveland et al. (2014), but that was due to selective period investigated (December 20, 1998). In comparison to their result, colder plasma is observed to be predominant in winter than any other season especially in the low flux and reduces in number as the flux magnitude increases. For the high flux, a distinct peak is observed in the summer distribution at $T_i \sim 1000$ K and analysis shows that about 27.5% of the high-flux upflow occur at $T_i = (1000 \pm 150)$ K around local midday and 1.8% around local midnight. However at $T_i \geq 1000$ K, about 18.5% and 37.5% of the total ion flux upflow during the campaign occur around local midday and midnight respectively. This shows that in general, the dynamics around the local midnight heats the ions almost as twice as the energization processes around midday.

6.6.4 Upflow flux dependence on electron temperature

The plot shown in Figure 6.19 presents the relationship between the ion upflow flux and electron temperature. The figure indicates that, though low, a better correlation is observed with T_e than T_i . In both summer and spring, correlation coefficients above about 0.40 are observed in the high flux, while less than about 0.11 and 0.07 are observed in autumn and winter respectively. In general, the linear correlation coefficient observed across the board with respect to T_e is greater than that observed with respect to T_i in all seasons and predominantly in all class of upflow. As earlier reported in Chapter 5 of this study, under section 5.6.2, the dominant mechanism identified is the electron precipitation which, it is suggested, leads to the creation of an ambipolar electric field, and hence resulting in ion upflow. Another feature in the T_e distribution different from T_i is the somewhat cut-off before 10^4 K observed. Apart from winter, only about 0.5% of the distribution goes beyond the precise cut-off of 7.5×10^3 K, whereas about 1.3% observation was made for winter alone by the ESR. The reason for this shape in T_e is yet unclear, but the result does show that except from winter, T_e rarely go above a threshold of 7.5×10^3 K.

6.6.5 *Upflow flux dependence on plasma temperature*

Figure 6.20 shows the dependence of ion upflow on the average plasma temperature, $< T_p >$, calculated from equation (6.6). It is observed that there is a good similarity between $< T_p >$ and T_e than T_i as shown from Figures 6.18 – 6.20. The plasma temperature, T_p, shows almost same correlation with the ion flux upflow as does the electron temperature, T_e. This is in good agreement with the fact that electron plasma frequency is the characteristic frequency of the plasma as explained in detail from equations (2.9) – (2.12) in Chapter 2.

It is also observed that T_p, T_e, and T_i indicate that cold plasma is prevalent in winter and least in summer, whereas the equinoctial seasons are somewhat similar and their degree of cold plasma is in between summer and winter.

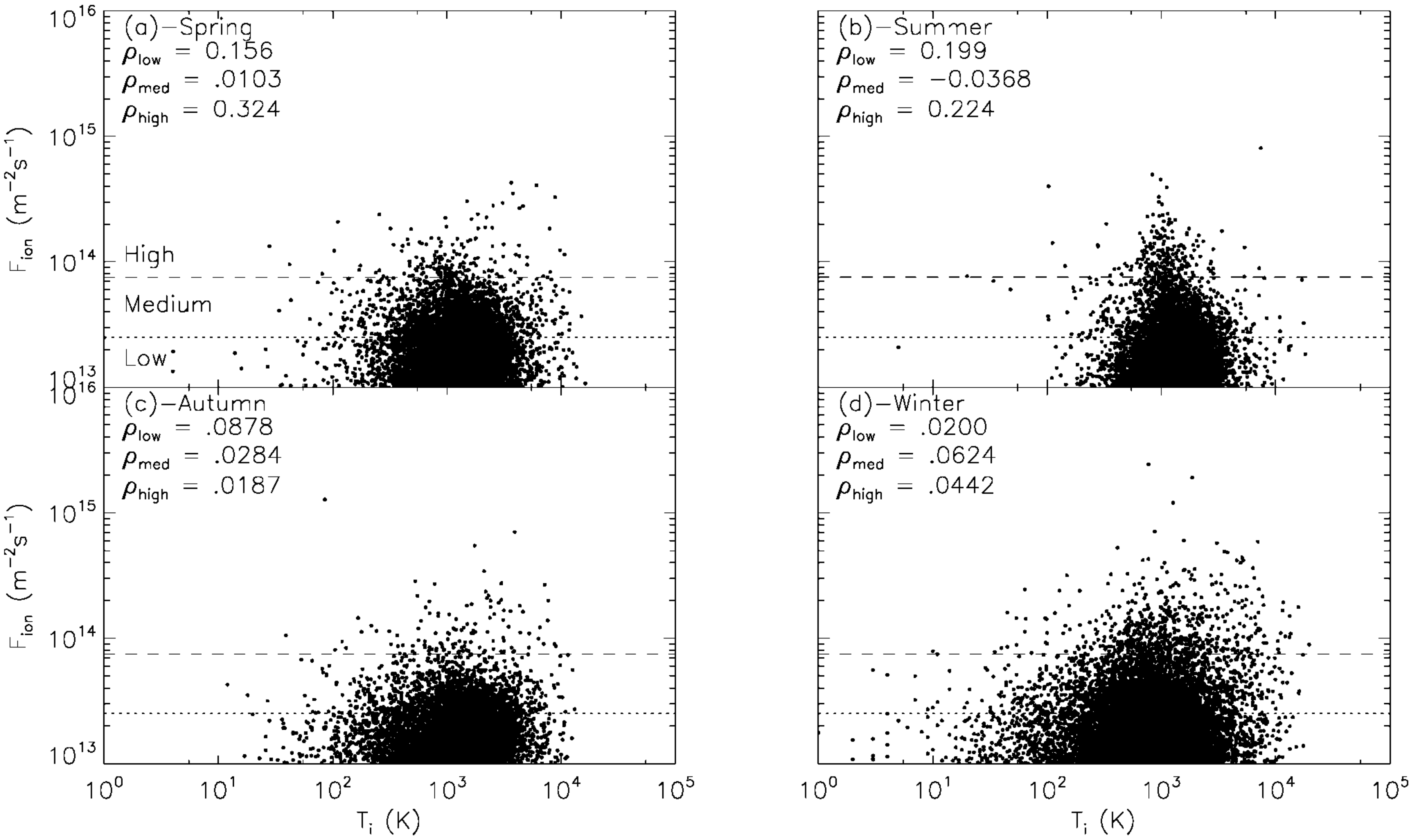

Figure 6.18: Plot showing seasonal upflow flux dependence on ion temperature on a log-log scale. The panels' format is the same as outlined in Figure 6.16.

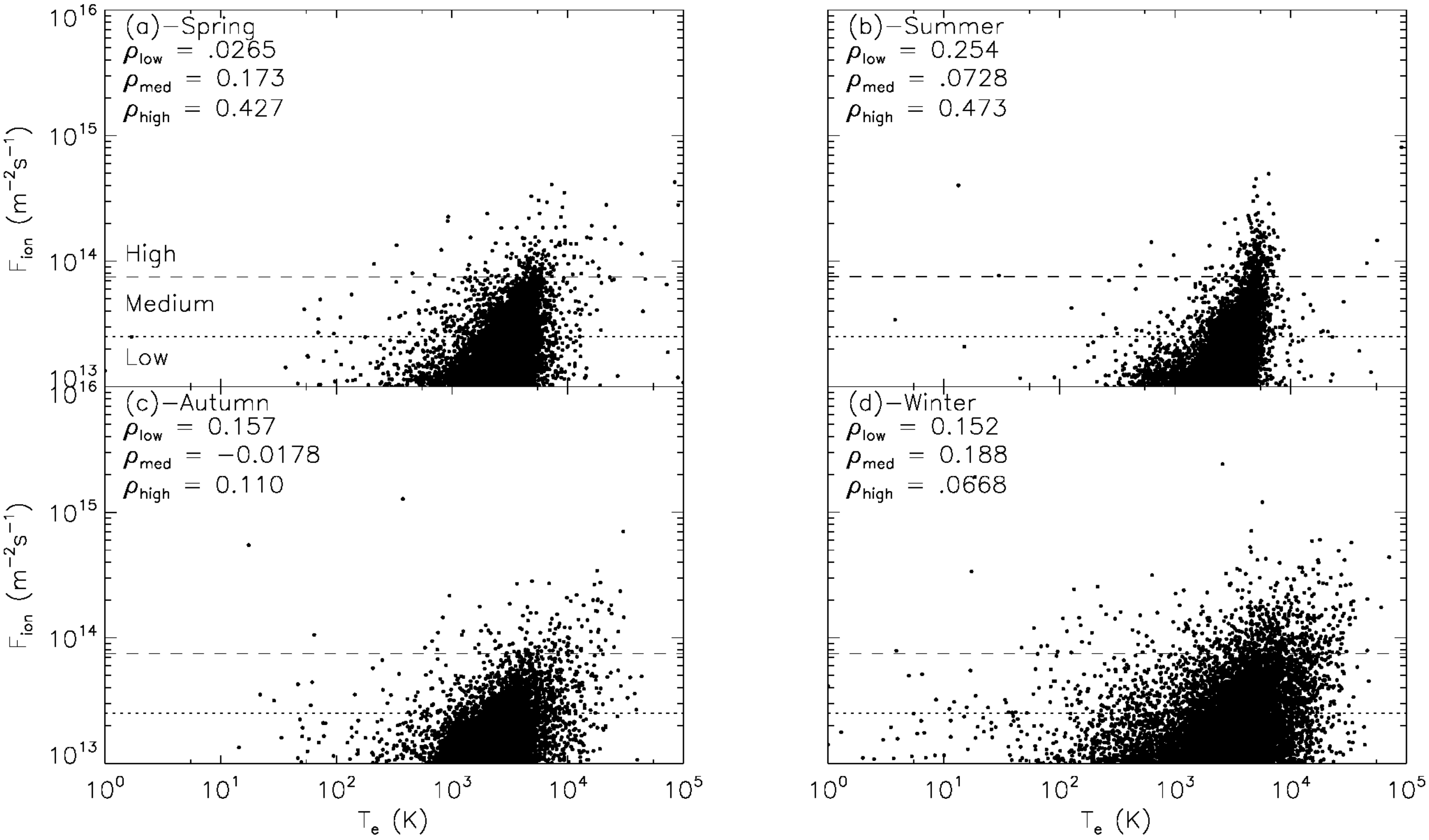

Figure 6.19: Plot showing seasonal upflow flux dependence on electron temperature on a log-log scale. The panels' format is the same as outlined in Figure 6.16.

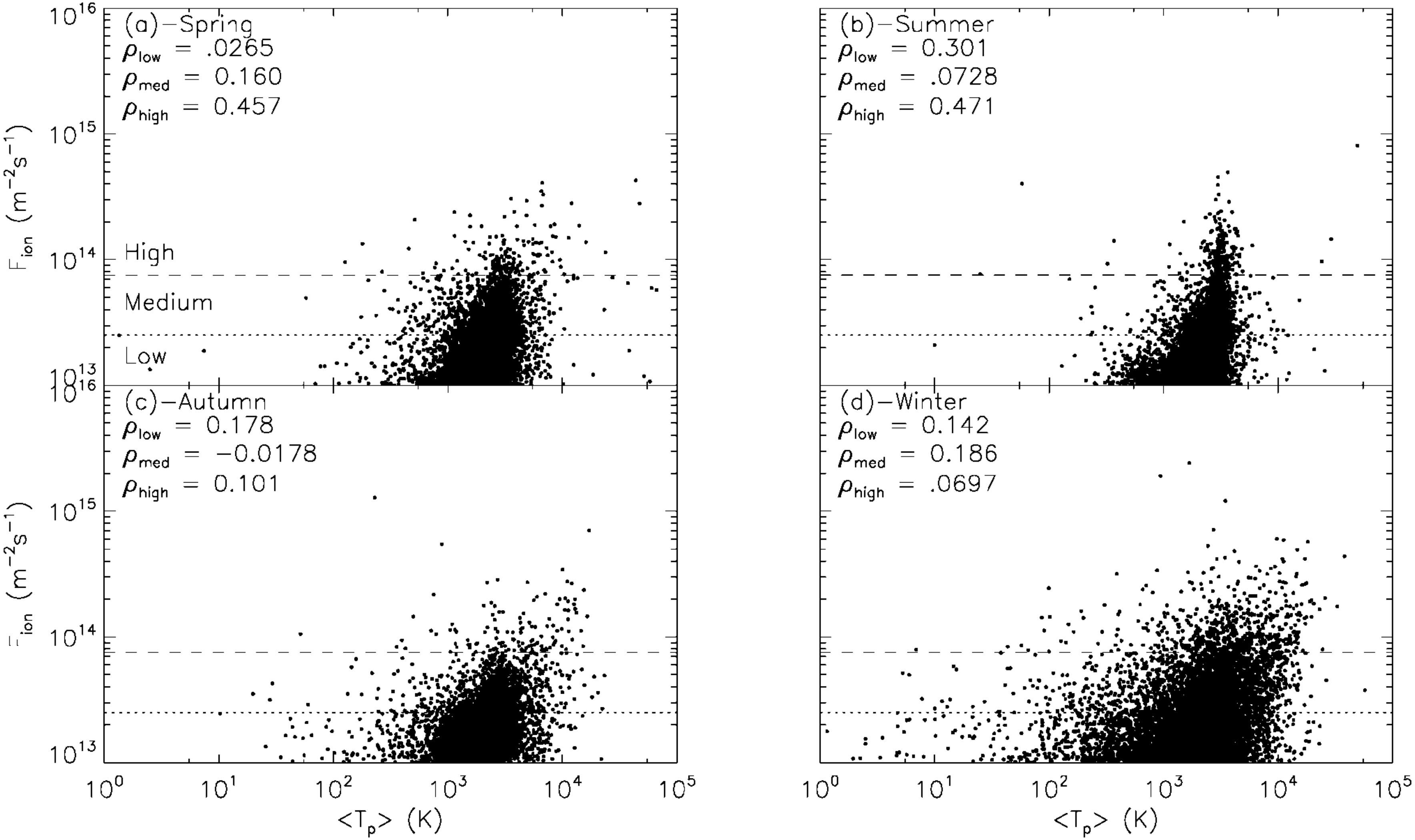

Figure 6.20: Plot showing seasonal upflow flux dependence on plasma temperature on a log-log scale. The panels' format is the same as outlined in Figure 6.16.

6.7. Conclusion

A statistical analysis of ion upflow flux campaign has been carried out to determine its occurrence in relation to solar wind plasma parameters as well as basic ionospheric parameters as observed by the EISCAT Svalbard Radar (ESR) during the international polar year (IPY) 2007. The Pearson correlation coefficient, ρ, which is a measure of linear correlation between variables, was also computed in all cases. The occurrence of ion upflow flux was found to fit better with solar wind density, especially in the high and medium-flux upflows, than with the solar wind speed. As ion flux magnitude increases, the correlation of its occurrence with solar wind speed decreases. Occurrence rarely goes beyond 10% unless at higher velocity ($v_{sw} \geq 650\ \mathrm{km\ s^{-1}}$) and significant occurrence was achieved when $n_{sw} \geq 20\ \mathrm{cm^{-3}}$. The higher number density likely enhanced precipitation and aided ambipolar electric field in driving the ion upflow.

The occurrence of the ion upflow with respect to the coupling function showed a curvilinear trend especially in the high-flux upflow. This shows the complexity of the coupling function as a function of many parameters. There are also two regimes going on regarding the n_{sw} and P_{dyn}, with a threshold of $15 - 20\ \mathrm{cm^{-3}}$ and $5 - 10\ \mathrm{nPa}$ respectively before a change in behaviour. During high solar wind dynamic pressure ($P_{dyn} \geq 10\ \mathrm{nT}$) which can create a compression region leading to strong disturbances in the magnetosphere, ion upflow occurrence reached its maximum peak.

Ion upflow occurrence increased as the IMF strength increases in all classes with a good fit of about 77% in the low-flux upflow and 56% overall. The occurrence in all the upflow flux classes was highest when the orientation of the IMF clock angle indicated a southward B_z. However during conditions of southward IMF, occurrence was also higher when cusp is post-noon (positive B_y) than when dawnward (negative B_y) in all classes of ion flux upflows. The reconnection rate measured by the coupling function showed a goodness of fit, ρ, from 0.55 to 0.64 that increased as the flux magnitude increased. This showed that the higher the magnitude of the flux, the more it depends on reconnection.

There is poor correlation in all classes between the upflow occurrence and ring current index. However, the southward (negative) perturbation of the Earth's magnetic field by the westward current electrojet showed correlation up to about 63%. This showed that the auroral electrojet index is better to estimate the downstream magnetic contribution to ion upflow. Below about 300 nT, the occurrence rarely goes beyond 10%, however, as the perturbation reached about 500 nT, more than 20 – 40% occurrence is attainable.

Regarding the effect of solar wind parameters on the magnitude of the upflow flux, it was found that ion upflow flux was prevalent between $400 \leq v_{sw} \leq 450\ \mathrm{km\ s^{-1}}$. Comparison between ion upflow flux and its occurrence (Figures 6.1 and 6.10) showed that although flux is minimum at higher velocity ($v_{sw} \geq 650\ \mathrm{km\ s^{-1}}$), the occurrence probability is higher at such solar wind speed. Similarly at low n_{sw} around $3\ \mathrm{cm^{-3}}$, the upflow flux attains maximum but the occurrence is insignificant (Figures 6.2 and 6.11). It could therefore be conceived that a higher solar wind speed and number density are strong driver of ion upflow occurrence.

The relationship between upflow flux and the interplanetary magnetic field showed that all fluxes indicated a peak near $\mathrm{B_z} = 0$ nT with the distribution skewed towards $\mathrm{B_z} < 0$ nT. The implication of this is that reconnection is not absolutely essential for ion flux to occur, however, occurrence increases when it does. Moreover, upflow can take place during northward and southward $\mathrm{B_z}$, but the areas under the curve for all cases in Figure 6.13 agree with the result in Chapter 5 that flux is dominant during southward than northward $\mathrm{B_z}$. IMF $\mathrm{B_y}$ on the other hand, showed that ion upflow flux is dominant during post-noon cusp compared to pre-noon or noon cusp. However unlike the case for $\mathrm{B_z}$, a positive offset was noticed in $\mathrm{B_y}$ indicating a preference for upflow flux during duskward movement of the cusp. Furthermore, the upflow flux and its occurrence in all classes attained minimum value when the clock angle is around zero (or 360°). There was substantial increase especially in the low-flux upflow during north-east orientation ($65 - 70^{\circ}$), which could lead to reconnection at the open field lines, the upflow occurrence is still greater during southward orientation of the clock angle. This again confirmed that reconnection is not compulsory for upflow flux, but only enhances its occurrence.

In general, highest occurrence of upflow was observed to be strongly driven during conditions of southward B_z, positive B_y, and a stronger magnitude of IMF coupled with fast solar wind speed and higher number density. However, significant and peak upflow fluxes are also observed at lower values of these solar wind plasma parameters. Moreover, correlation is less than 100% in each of these parameters, suggesting that upflow occurrence is likely not related to just one parameter.

It was found from upflow flux dependence on ionospheric parameters that higher plasma density occurred 318 times (0.34% of the total fluxes), of which 13.5% resulted in an upflow, whereas, for higher field-aligned flow $v_i \geq 1000 \text{ m s}^{-1}$ about 4145 times (4.42% of the total fluxes), 73.6% of which became an upflow. Furthermore, at a maximum threshold of 1 km s^{-1} for field-aligned flow velocity, 7895 fluxes occurred between 500 – 1000 km s^{-1}, of which 75.2% resulted in an ion upflow. It can therefore be conceived that faster field-aligned ion upflow velocity is a better driver of ion upflow flux compared to higher density.

The plasma temperature showed that in summer, the high-flux upflow has a plasma temperature clustered around $T_i \sim 1000$ K and analysis showed that this class of upflow was driven around local midday and midnight at a ratio of about 15:1 around this temperature. However, it was shown that in general, the dynamics around the local midnight heats the ions almost as twice as the energization process around midday throughout the campaign. It could therefore be envisaged that apart from the high-flux upflow in summer, midnight activity are more responsible for upwelling of the ions. On the other hand, the correlation of ion upflow flux was better with T_e than T_i across the seasons and classes of upflows. This agreed with Chapter 5 that the ambipolar electric field which increases from a growing pressure gradient is the key mechanism leading to upflow. Furthermore, it was found that the electron temperature rarely exceeds a threshold of 7.5×10^3 K except in winter.

CHAPTER 7

Summary and Future Work

7.1. Summary

Ionospheric ions from the Earth's upper atmosphere outflow into the overlying magnetosphere under the right geophysical conditions. An extensive study of ionospheric upwelling ions from the Earth's upper atmosphere has been carried out with a large data set observed by the 42 m dish EISCAT Svalbard Radar (ESR) at Longyearbyen, Svalbard, during the International Polar Year (IPY) 2007 campaign at a period of deep solar minimum. Over 300,000 field-aligned profiles were considered and analysed. A flux threshold of $10^{13}\ \mathrm{m^{-2}\ s^{-1}}$, put forward by Wahlund and Opgenoorth (1989), forms the basis for the upflows considered in this study. In addition, this study took a further step for the first time in categorizing the upflows into low, medium and high fluxes. The total upflow flux in the low flux category maximizes on the nightside, while the medium and the high fluxes are peaked around noon. On the other hand, the occurrence of all categories of upflows was found to maximize around local noon at all levels of geomagnetic activity, that is, low medium and high geomagnetic disturbances. However, whereas occurrence magnitude was found to increase as the level of geomagnetic disturbance increases, it decreases with increasing flux intensity. In agreement with previous studies, ion upflow occurs at all local times even during solar minimum, however, the temporal variation is higher in summer than in winter.

The two principal mechanisms driving ion upflow, namely the ambipolar electric force and Joule heating are investigated. For the first time in a long data set, terms in the ion momentum equation were used to explore the dominant mechanism of ion upflow. It was found that though both mechanisms can drive ion upflow separately, their conjunction drives upflow of greater magnitude. The ambipolar electric force was found to be the dominant (more frequently effective) mechanism, predominantly driving about seven times of the total events as the Joule heating. The study demonstrated that contrary to the previous proposition that no substantial outflow could be observed in the absence of precipitating flux (irrespective of the strength of the Poynting flux), the September 11, 2007 event has upflows around a maximum of about $4.67 \times 10^{13}\ \mathrm{m^{-2}\ s^{-1}}$ dominating the altitudes from about 300 km and above.

Furthermore, a statistical analysis of the ESR observations was carried out with respect to solar wind plasma parameters and the downstream terrestrial magnetic activities. It was identified that the upflow occurrence correlates better with solar wind number density than the solar wind speed. A linear Pearson correlation coefficient (ρ) of about 0.52 was found to exist between upflow occurrence and solar wind number density. Furthermore, occurrence fits better for a number density and dynamic pressure below about $20\ \mathrm{cm^{-3}}$ and 6 nPa respectively. Moreover, an increasing occurrence with a positive ρ respectively peaking at about 93% or 72% was observed when either the IMF strength or the coupling function increased whereas correlation with ring current and auroral electrojet indices showed a negative ρ, indicating that occurrence increased as magnetic perturbation increases. As expected, it was found that occurrence maximizes when the IMF clock angle was southward. However, analysis showed variation in occurrence with respect to cusp asymmetry giving preference for duskward cusp (South-East clock angle) in comparison to dawnward's (South-West clock angle).

Finally, a case study of the initial upwellings observed by the ESR and the geophysical conditions at a time that ion outflows were identified by the Fast Auroral SnapshoT (FAST) spacecraft was investigated. The study agrees with Wahlund and Opgenoorth (1989) that an upflow threshold, $10^{13}\ \mathrm{m^{-2}\ s^{-1}}$, must be attained during ion outflow events. Peak upflow flux observed during the event was $4.2 \times 10^{13}\ \mathrm{m^{-2}\ s^{-1}}$. In addition, the ambipolar force was predominant over the Joule heating during the March 18, 2006 ion outflow event.

7.2. Future Work

The study of ion upflow during a solar minimum with a large database has been extensively explored in this work. It is appealing to investigate upflow structure during a solar maximum and see the effect of geophysical conditions on it. Recommendation for a future campaign also lasting about a year around solar maximum would be suggested for comparison between the two aforementioned periods in a solar cycle. The work by Endo et al. (2000) and Ogawa et al. (2009) covering half a solar cycle and about a full solar cycle respectively have fewer field-aligned profiles to investigate compared to the IPY period as reported in Chapter 4. A campaign by the international scientific community will really help to justify the comparison.

It is also of interest to look at the upflow flux with respect to the range gates and also to separate the ionosphere into its respective layers based on composition/density structure. This would enable us to see clearly, the altitude or ionospheric layer(s) contributing largely to the upflow occurrence.

The result in Chapter 5 has shown that the ambipolar electric force is dominant over the Joule heating to drive the initial ionospheric upflow. It might be that the EISCAT Svalbard Radar (ESR), being close to the polar cap, misses some of the auroral activity and as a result the current closure in the Pedersen layer leading to Joule heating. It would be of interest to explore the Tromsø radar, which is more equatorward than the ESR, and compare the results.

The non-availability of suitable conjunction of ground-based and satellite measurements has limited the number of ion outflow case study considered in this work. With the advent of the Enhanced Polar Outflow Probe (e-POP) that was launched about three years ago into a perigee and an apogee of 325 km and 1500 km respectively (Yau and James, 2015), it is hopeful that more outflow would be targeted and a large data set for robust statistical analysis of upflow-outflow conjunction would be possible. An additional area of further work will be to utilize these measurements to constrain models of the ion outflows.

References

Akbari, H., Bhatt, A., La Hoz, C. (2017). 'Incoherent Scatter Plasma Lines: Observations and Applications', *Space Science Reviews*, doi:10.1007/s11214-017-0355-7.

Alcaydé, D. (1997). 'Incoherent Scatter Theory, Practice and Science, Collection of lectures given in Cargese, Corsica, 1995', *EISCAT Tech Rep 97/53, 1995*.

André, M. and Yau, A. (1997). 'Theories and Observations of Ion Energization and Outflow in the High Latitude Magnetosphere', *Space Science Reviews,* **80**(1-2), pp. 27-48.

Aruliah, A. (2016). E-mail conversation with Timothy David, 2 December.

Axford, W.I. (1968). 'The Polar Wind and the Terrestrial Helium Budget', *Journal of Geophysical Research*, **73**, pp. 6855.

Baker, D.N., Chin, G. and Pfaff, R.F. (1991). 'NASA Small Explorer Program', *Physics Today,* **44**(12), pp. 44-51

Ball, L. (1989). 'Can Ion Acceleration by Double-Cyclotron Absorption Produce O^+ Ion Conics?', *Journal of Geophysicsical Research* **94**(A11), pp. 15,257-15,264.

Ball, L. and André, M. (1991). 'Heating of O^+ Ions in the Cusp/Cleft: Double-Cyclotron Absorption Versus Cyclotron Resonance', *Journal of Geophysical Research*, **96**(A2), pp. 1429-1437.

Baumjohann, W. and Treumann, R.A., eds. (1997). *Basic Space Plasma Physics*, 1997 edn. Singapore: Imperial College Press.

Blelly, P.L. and Alcaydé, D. (1994). 'Electron Heat Flow in the Auroral Ionosphere Inferred from EISCAT-VHF Observations', *Journal of Geophysical Research,* **99**(A7), pp. 13,181-13,188.

Blelly, P.L., Robineau, A. and Alcaydé, D. (1996). 'Numerical Modelling of Intermittent Ion Outflow Events Above EISCAT', *Journal of Atmospheric and Terrestrial Physics*, **58**(1-4), pp. 273-285.

Bowles, K.L. (1958). 'Observations of Vertical Incidence Scatter from the Ionosphere at 41 Mc s^{-1}', *Physical Review Letters*, **1**(12), pp. 454-455.

Bowles, K.L. (1961). 'Incoherent Scattering by Free Electrons as a Technique for Studying the Ionosphere and Exosphere: Some Observations and Theoretical

Considerations', *Journal of Research of the National Bureau of Standards-D. Radio Propagation*, **65D**(1), pp. 1-14.

Brekke, A., ed. (2013). *Physics of the Upper Polar Atmosphere*, Second edn. Praxis Publishing, Chichester, UK: Springer Science & Business media. ISBN 978-3-642-27400-8.

Brinton, H.C., Grebowski, J.M. and Mayr, H.G. (1971). 'Altitude Variation of Ion Composition in Midlatitude Trough Region - Evidence for Upward Plasma Flow', *Journal of Geophysical Research*, **76**(16), pp. 3738-3745.

Buchert, S.C., Ogawa, Y., Fujii, R. and van Eyken, A.P. (2004). 'Observations of Diverging Field-Aligned Ion Flow with the ESR', *Annales Geophysicae*, **22**, pp. 889-899.

Cai, L., Aikio, A.T., Nygrén, T. (2014). 'Solar Wind Effect on Joule Heating in the High-Latitude Ionosphere', *Journal of Geophysical Research-Space Physics*, **119**, pp. 10440-10455, doi:10.1002/2014JA020269.

Carlson, C.W., Mcfadden, J.P., Turin, P., Curtis, D.W. and Magoncelli, A. (2001). 'The Electron and Ion Plasma Experiment for FAST', *Space Science Reviews*, **98**(1-2), pp. 33-66.

Caton, R., Horwitz, J.L., Richards, P.G. and Liu., C. (1996). 'Modeling of F-region Ionospheric Upflows Observed by EISCAT', *Geophysical Research Letters*, **23**(12), pp. 1537-1540.

Chang, T., Crew, G.B., Hershkowitz, N., Jasperse, J.R., Retterer, J.M. and Winningham, J.D. (1986). 'Transverse Acceleration of Oxygen Ions by Electromagnetic Ion Cyclotron Resonance with Broadband Left-Hand Polarized Waves', *Geophysical Research Letters*, **13**(7), pp. 636-639.

Chappell, C.R., Giles, B.L., Moore, T.E., Delcourt, D.C., Craven, P.D. and Chandler, M.O. (2000). 'The Adequacy of the Ionospheric Source in Supplying Magnetospheric Plasma', *Journal of Atmospheric and Solar-Terrestrial Physics*, **62**(6), pp. 421-436.

Chappell, C.R., Moore, T.E. and Waite, J.H. (1987). 'The Ionosphere As a Fully Adequate Source of Plasma for the Earth's Magnetosphere', *Journal of Geophysical Research*, **92**(A6), pp. 5896-5910.

Chisham, G., Lester, M., Milan, S.E., Freeman, M.P., Bristow, W.A., Grocott, A., Mcwilliams, K.A., Ruohoniemi, J.M., Yeoman, T.K., Dyson, P.L., Greenwald, R.A., Kikuchi, T., Pinnock, M., Rash, J.P.S., Sato, N., Sofko, G.J., Villain, J.-P.

and Walker, A.D.M. (2007). ‘A Decade of the Super Dual Auroral Radar Network (SuperDARN): Scientific Achievements, New Techniques and Future Directions’, *Surveys in Geophysics*, **28**(1), pp. 33-109.
Cowley, S.W.H. (2000). ‘Magnetosphere-Ionosphere Interactions: A Tutorial Review’, in: *Magnetospheric Current Systems, Geophysical Monograph*, vol. 118, edited by S. Ohtani, R. Fujii, M. Hesse, R.L. Lysak, American Geophysical Union, pp. 91-106.

Cowley, S.W.H. (2014). *Departmental Training Course* [Lecture to Ph.D. Students], *Kinetic Theory of Collisionless Plasmas*. University of Leicester, 12 November 2014.

Cowley, S.W.H. (2016). E-mail conversation with Timothy David, 16 September.

Cowley, S.W.H. (2017). Oral conversation with Timothy David, 10 July.

Dandouras, I. (2013). ‘Detection of a Plasmaspheric Wind in the Earth's Magnetosphere by the Cluster Spacecraft’, *Annales Geophysicae*, **31**(7), pp. 1143-1153.

David, T.W. (2013), ‘Investigation into Quiet and Magnetic Storms Periods Above Magadan During October - December 2003’, *Indian Journal of Radio & Space Physics*, **42**, pp. 89-96.

Demars, H.G., Barakat, A.R. and Schunk, R.W. (1996), ‘Effect of Centrifugal Acceleration on the Polar Wind’, *Journal of Geophysical Research*, **101**(A11), 24565–24571, doi:10.1029/96JA02234.

Dessler, A.J. and Hanson, W.B. (1961). ‘Possible Energy Source for the Aurora’, *Astrophysical journal*, **134**, pp. 1024-1025.

Dessler, A.J. and Michel, F.C. (1966). ‘Plasma in the Geomagnetic Tail’, *Journal of Geophysical Research*, **71**, pp. 1421-1426.

Dougherty, J.P. and Farley, D.T. (1960). ‘A Theory of Incoherent Scattering of Radio Waves by a Plasma’, *Proceedings Royal Society of London series A*, **259**(1296), pp. 79-99.

Dungey, J. (1961). ‘Interplanetary Magnetic Field and the Auroral Zones’, *Physical Review Letters*, **6**(2), pp. 47-48

EISCAT (2015). *Pictures of the ESR Dishes.* Available at: https://www.eiscat.rl.ac.uk/radars/esr/esrpics/ (Accessed: 8 May 2015).

EISCAT (2016). *What is EISCAT*? Available at: https://www.eiscat.se/about/whatiseiscat_new (Accessed: 17 October 2016).

EISCAT and NSF (2016). *International Incoherent Scatter Radar School 2016*, [Lectures to ISR Trainee], Hosted at Sodankylä Geophysical Observatory, Finland. Available at: https://wikis.mit.edu/confluence/display/ASGScience/2016ISRSchool (Accessed: 24 - 30 July 2016).

Endo, M., Fujii, R., Ogawa, Y., Buchert, S.C., Nozawa, S., Watanabe, S., Yoshida, N. (2000). 'Ion Upflow and Downflow at the Topside Ionosphere Observed by the EISCAT VHF Radar', *Annales Geophysicae*, **18**, 170-181.

Ergun, R.E., Carlson, C.W., Mozer, F.S., Delory, G.T., Temerin, M., Mcfadden, J.P., Pankow, D., Abiad, R., Harvey, P., Wilkes, R., Primbsch, H., Elphic, R., Strangeway, R., Pfaff, R. and Cattell, C.A. (2001). 'The FAST Satellite Fields Instrument', *Space Science Reviews*, **98**(1-2), pp. 67-91.

ESA (2013). *Cluster Ion Spectrometer (CIS) – Scientific Objectives*. Available at: http://www2011.mpe.mpg.de/CLUSTER/CIS-Pages/scien_object_cis.html (Accessed: 11 December 2013).

Evans, J.V. (1969). 'Theory and Practice of Ionosphere Study by Thomson Scatter Radar', *Proceedings IEEE*, **57**(4), pp. 496-530.

Fälthammar, C.G. (1986). 'Magnetosphere Ionosphere Interactions - Near-Earth Manifestations of the Plasma Universe', *IEEE Transactions on Plasma Science*, **14**(6), pp. 616-628

Farley, D. T. (1966). 'A Theory of Incoherent Scattering of Radio Waves by a Plasma, 4. The Effect of Unequal Ion and Electron Temperatures', *Journal of Geophysical Research*, **71**(17), pp. 4091-4098.

Fejer, J.A. (1960). 'Radio-Wave Scattering by an Ionized Gas in Thermal Equilibrium', *Journal of Geophysical Research*, **65**(9), pp. 2635-2636.

Foster, C., Lester, M. and Davies, J.A. (1998). 'A Statistical Study of Diurnal, Seasonal and Solar Cycle Variations of F-region and Topside Auroral Upflows Observed by EISCAT Between 1984 and 1996', *Annales Geophysicae*, **16**, pp. 1144–1158.

Fu, H.Y., Scales, W.A., Bernhardt, P.A., Briczinski, S.J., Kosch, M.J., Senior, A., Rietveld, M.T., Yeoman, T.K. and Ruohoniemi, J.M. (2015). 'Stimulated Brillouin Scattering During Electron Gyro-Harmonic Heating at EISCAT', *Annales Geophysicae*, **33**, pp. 983–990.

Gillies, R.G., Hussey, G.C., Sofko, G.J. and McWilliams, K.A. (2012). 'A Statistical Analysis of SuperDARN Scattering Volume Electron Densities and Velocity Corrections Using a Radar Frequency Shifting Technique', *Journal of Geophysical Research-Space Physics,* **117**, pp. A08320.

Gjerloev, J.W. (2009). 'A Global Ground-Based Magnetometer Initiative', *Eos Transactions American Geophysical Union*, **90**(27), pp. 230–231, doi:10.1029/2009EO270002.

Gjerloev, J.W. (2012). 'The SuperMAG Data Processing Technique', *Journal of Geophysical Research*, **117**(A09213), doi:10.1029/2012JA017683.

Glocer, A., Toth, G., Gombosi, T. and Welling, D. (2009). 'Modeling Ionospheric Outflows and Their Impact on the Magnetosphere, Initial Results', *Journal of Geophysical Research*, **114**, pp. A05216.

Gonzalez, W.D., Clúa de Gonzalez, A.L., Sobral, J.H.A., Dal Lago, A. and Vieira, L.E. (2001). 'Solar and Interplanetary Causes of Very Intense Geomagnetic Storms', *Journal of Atmospheric and Solar-Terrestrial Physics*, **63**(5), pp. 403-412.

Gonzalez, W.D., Tsurutani, B.T., Gonzalez, A.L.C., Smith, E.J., Tang, F. and Akasofu, S.I. (1989). 'Solar Wind-Magnetosphere Coupling During Intense Magnetic Storms (1978-1979)', *Journal of Geophysical Research*, **94**(A7), pp. 8835-8851.

Gordon, W.E. (1958). 'Incoherent Scattering of Radio Waves by Free Electrons with Applications to Space Exploration by Radar', *Proceedings of the IRE*, **46**(11), pp. 1824 – 1829.

Greenwald, R.A., Baker, K.B., Dudeney, J.R., Pinnock, M., Jones, T.B., Thomas, E.C., Villain, J.-P., Cerisier, J.-C., Senior, C., Hanuise, C., Hunsucker, R.D., Sofko, G., Koehler, J., Nielsen, E., Pellinen, R., Walker, A.D.M., Sato, N., Yamagishi, H. (1995). 'Darn/Superdarn: A Global View of the Dynamics of High-Lattitude Convection', *Space Science Reviews*, **71**(1-4), pp. 761-796.

Harvey, P.R., Curtis, D.W., Heetderks, H.D., Pankow, D., Rauch-Leiba, J.M., Wittenbrock, S.K. and Mcfadden, J.P. (2001). 'The FAST Spacecraft Instrument Data Processing Unit', *Space Science Reviews*, **98**(1-2), pp. 113-149.

Hoffman, J.H., Dodson, W.H., Lippincott, C.R. and Hammack, H.D. (1974). 'Initial Ion Composition Results from Isis 2 Satellite', *Journal of Geophysical Research,* **79**(28), pp. 4246-4251.

Horwitz, J.L., Ho, C.W., Scarbro, H.D., Wilson, G.R. and Moore T.E. (1994). 'Centrifugal Acceleration of the Polar Wind', *Journal of Geophysical Research,* **99**(A8), pp. 15,051-15,064.

Howarth, A. and Yau, A.W. (2008). 'The Effects of IMF and Convection on Thermal Ion Outflow in Magnetosphere-Ionosphere Coupling', *Journal of Atmospheric and Solar-Terrestrial Physics*, **70**(17), pp. 2132-2143.

Hultqvist, B., Øieroset, M., Paschmann, G. and Treumann, R., eds. (1999). *Magnetospheric Plasma Sources and Losses*, 1999 edn. Dordrecht/Boston/London: Kluwer Academic Publishers.

Jones, G.O.L., Williams, P.J.S., Winser, K.J., Lockwood, M. and Suvanto, K. (1988). 'Large Plasma Velocities Along the Magnetic-Field Line in the Auroral-Zone', *Nature*, **336**(6196), pp. 231-232.

Jones, T.B., Lester, M., Milan, S.E., Robinson, T.R., Wright, D.M., Dillon, R.S. (2001). 'Radio Wave Propagation Aspects of the CUTLASS Radar', *Journal of Atmospheric and Solar-Terrestrial Physics*, **63**, pp. 99-105.

Kamide, Y. and Kokubun, S. (1996). 'Two-Component Auroral Electrojet: Importance for Substorm Studies', *Journal of Geophysical Research,* **101**(A6), 13027–13046, doi:10.1029/96JA00142.

Kamide, Y., Yokoyama, N., Gonzalez, W., Tsurutani, B.T., Daglis, I.A., Brekke, A. and Masuda, S. (1998). Two-step Development of Geomagnetic Storms, *Journal of Geophysical Research*, **103**(A4), 6917–6921, doi:10.1029/97JA03337.

Keating, J.G., Mulligan, F.J., Doyle, D.B., Winser, K.J. and Lockwood, M. (1990). 'A Statistical Study of Large Field-Aligned Flows of Thermal Ions at High Latitudes', *Planetary and Space Science,* **38**(9), pp. 1187-1201.

Khazanov, G.V., Liemohn, M.W., Krivomtsky, E.N. and Moore, T.E. (1998). 'Generalized Kinetic Description of a Plasma in an Arbitrary Field-Aligned Potential Energy Structure', *Journal of Geophysical Research*, **103**(A4), pp. 6871-6889.

Kintner, P.M., Bonnel, J., Arnoldy, R., Lynch, K., Pollock, C. and Moore, T. (1996). 'SCIFER – Transverse Ion Acceleration and Plasma Waves', *Geophysical Research Letters*, **23**, 1873–1876.

Kivelson, M.G., and Russell, C.T., eds. (1995). *Introduction to Space Physics*, First edn. United Kingdom, University of Cambridge: Cambridge University Press.

Lemaire, J. and Schunk, R.W. (1992). ‘Plasmaspheric Wind’, *Journal of Atmospheric and Terrestrial Physics*, **54**(3-4), pp. 467-477.

Lester, M. (2013). ‘The Super Dual Auroral Radar Network (SuperDARN): An Overview of its Development and Science’, *Journal of Advances in Polar Science,* **24(1)**, pp. 1-11.

Liu, C., Horwitz, J.L. and Richards, P.G. (1995). ‘Effects of Frictional Ion Heating and Soft Electron Precipitation on High-Latitude F-region Upflows’, *Geophysical Research Letters,* **22**(20), pp. 2713-2716.

Liu, J., Zhao, B. And Liu, L. (2010). ‘Time Delay and Duration of Ionospheric Total Electron Content Responses to Geomagnetic Disturbances’, *Annales Geophysicae,* **28**(3), pp. 795-805.

Liu, W. and Fujimoto, M., eds. (2011). *The Dynamic Magnetosphere,* vol. 3 edn. Springer Dordrecht Heidelberg London New York, doi:10.1007/978-94-007-0501-2, ISBN 978-94-007-0500-5.

Lockwood, M., Chandler, M.O., Horwitz, J.L., Waite Jr., J.H., Moore, T.E., Chappell, C.R. (1985). ‘The Cleft Ion Fountain’, *Journal of Geophysical Research,* **90**(A10), pp. 9736-9748.

Lockwood, M., Cowley, S.W.H., Todd, H., Willis, D.M., Clauer, C.R. (1988). ‘Ion Flows and Heating at a Contracting Polar-Cap Boundary’, *Planetary and Space Science,* **36**(11), pp. 1229-1253.

Loranc, M., Hanson, W.B., Heelis, R.A. and St.-Maurice, J.-P. (1991). ‘A Morphological Study of Vertical Ionospheric Flows in the High-Latitude F-region’, *Journal of Geophysical Research*, **96**(A3), pp. 3627-3646.

Milan, S.E. (2014a). *Space Plasmas, PA 4319*. Available at http://www.ion.le.ac.uk/~ets/spaceplasmas/ University of Leicester, (Accessed: 13 October 2014).

Milan, S.E. (2014b). *Departmental Training Course* [Lecture to Ph.D. Students], *Magnetospheric Dynamics*. University of Leicester, 21 June 2014.

Milan, S.E., Gosling, J.S. and Hubert, B. (2012). ‘Relationship Between Interplanetary Parameters and the Magnetopause Reconnection Rate Quantified from Observations of the Expanding Polar Cap’, *Journal of Geophysical Research,* **117**, A03226, doi:10.1029/2011JA017082.

Milan, S.E., Yeoman, T.K. and Lester, M. (1998). 'The Dayside Auroral Zone As a Hard Target for Coherent HF Radars', *Geophysical Research Letters*, **25**(19) pp. 3717–3720.
Milan, S.E., Yeoman, T.K., Lester, M., Thomas, E.C. and Jones, T.B. (1997). 'Initial Backscatter Occurrence Statistics from the CUTLASS HF Radars', *Annales Geophysicae*, **15**, pp. 703-718.

Moore, T.E., Chandler, M.O., Pollock, C.J., Reasoner, D.L., Arnoldy, R.L., Austin, B., Kintner, P.M. and Bonnell, J. (1996). 'Plasma Heating and Flow in an Auroral Arc', *Journal of Geophysical Research*, **101**(A3), pp. 5279-5297.

Moore, T.E., Chandler, M.O., Chappell, C.R., Comfort, R.H., Craven, P.D., Delcourt, D.C., Elliott, H.A., Giles, B.L., Horwitz, J.L., Pollock, C.J. and Su, Y.-J. (1999). 'Polar/TIDE Results on Polar Ion Outflows', in: *Sun-Earth Plasma Connections*, *Geophysical Monograph*, vol. 109, edited by J.L. Burch, R.L. Carovillano, and S.K. Antiochos, American Geophysical Union, pp. 87-101.

Moore, T.E. and Delcourt, D.C. (1995). 'The Geopause', *Reviews of Geophysics*, **33**(2), pp. 175 – 209.

Moore, T.E., Fok, M.-C. and Garcia-Sage, K. (2014). 'The Ionospheric Outflow Feedback Loop', *Journal of Atmospheric and Solar-Terrestrial Physics*, **115-116**, pp. 59–66.

Nagy, A. F., Balogh, A., Cravens, T. E., Mendillo, M. and Müller-Wodarg, I, eds. (2008). 'Comparative Aeronomy', *Space Sciences Series of ISSI*, **29**, Dordrecht, Netherlands: Springer Science & Business media. ISBN 978-0-387-87825-6.

NASA (2013). *The Earth's Plasmasphere*. Available at: http://plasmasphere.nasa.gov/ (Accessed: 20 December 2013).

NASA (2014). *Regions of the Magnetosphere*. Available at: http://helios.gsfc.nasa.gov/magnet.html (Accessed: 6 March 2014).

NASA (2015a). *Shape of the Magnetosphere*. Available at: https://commons.wikimedia.org/wiki/File:Magnetosphere_rendition.jpg (Accessed: 7 May 2015).

NASA (2015b). *The Fast Auroral SnapshoT (FAST)*. Available at: https://commons.wikimedia.org/w/index.php?curid=2793679 (Accessed: 8 May 2015).

Newell, P.T., Greenwald, R.A. and Ruohoniemi, J.M. (2001). 'The Role of the Ionosphere in Aurora and Space Weather', *Reviews of Geophysics*, **39**(2), pp. 137-149.

Ogawa, Y., Buchert, S.C., Fujii, R., Nozawa, S. and van Eyken, A.P. (2009). 'Characteristics of Ion Upflow and Downflow Observed with the European Incoherent Scatter Svalbard Radar', *Journal of Geophysical Research*, **114**, A05305, doi:10.1029/2008JA013817.

Peterson, W.K., Abe, T., Fukunishi, H., Greffen, M.J., Hayakawa, H., Kasahara, Y., Kimura, I., Matsuoka, A., Mukai, T., Nagatsuma, T., Tsuruda, K., Whalen, B.A. and Yau, A.W. (1994). 'On the Sources of Energization of Molecular-Ions at Ionospheric Altitudes', *Journal of Geophysical Research*, **99**(A12), pp. 23257-23274.

Pfaff, R., Carlson, C., Watzin, J., Everett, D. and Gruner, T. (2001). 'An Overview of the Fast Auroral Snapshot (FAST) Satellite', *Space Science Reviews*, **98**(1-2), pp. 1-32.

Pham, K.H., Lopez, R.E. and Bruntz, R. (2016). 'The Effect of a Brief Northward Turning in IMF B_z on Solar Wind-Magnetosphere Coupling in a Global MHD Simulation', *Journal of Geophysical Research-Space Physics*, **121**(5), pp. 4291-4299.

Pharnell, C. (1999). 'Peeling Back the Sun, *Solar Physics*', *Letter to the Editor 1999 Physics Education IOPscience*, **34**(3), pp. 108-112.

Ribeiro, A.J., Ponomarenko, P.V., Ruohoniemi, J.M., Baker, J.B.H., Clausen, L.B.N., Greenwald, R.A. and De Larquier, S. (2013a). 'A Realistic Radar Data Simulator for the Super Dual Auroral Radar Network', *Radio Science*, **48**(3), pp. 283-288.

Ribeiro, A.J., Ruohoniemi, J.M., Ponomarenko, P.V., Clausen, L.B.N., Baker, J.B.H., Greenwald, R.A., Oksavik, K. and De Larquier, S. (2013b). 'A Comparison of SuperDARN ACF Fitting Methods', *Radio Science*, **48**(3), pp. 274-282.

Richmond, A.D. (1998). 'The Ionosphere and Upper Atmosphere', in: *From the Sun: Auroras, Magnetic Storms, Solar Flares, Cosmic Rays*, 1998 edn., edited by S.T. Suess and B.T. Tsurutani, eds, American Geophysical Union, pp. 35-44.

Rishbeth, H. (1985). 'Coherence from Incoherence', *Nature*, **313**, pp. 431 – 432.

Rishbeth, H. (1988). 'Basic Physics of the Ionosphere: A Tutorial Review', *Journal of the Institution of Electronic and Radio Engineers*, **58**(6), pp. S207-S223.

Rishbeth, H. and Williams, P.J.S. (1985). 'The EISCAT Ionospheric Radar - The System and its Early Results', *Royal Astronomical Society, Quarterly Journal* (ISSN 0035-8738), **26**, pp. 478-512.

Roger, V. (2016) *Group Experimental work* [Lecture During ISR 2016 Experiment], *Ambipolar Electric Force*. Sodankylä Geophysical Observatory, Finland, 28 July 2016.

Shelley, E.G., Peterson, W.K., Ghielmetti, A.G. and Geiss, J. (1982). 'The Polar Ionosphere as a Source of Energetic Magnetospheric Plasma', *Geophysical Research Letters*, **9**(9), pp. 941-944.

Shelley, E.G., Sharp, R.D. and Johnson, R.G. (1972). 'Satellite Observations of Energetic Heavy-Ions During a Geomagnetic Storm', *Journal of Geophysical Research*, **77**(31), pp. 6104-6110.

Skjæveland, Å., Moen, J. and Carlson, H.C. (2014). 'Which Cusp Upflow Events Can Possibly Turn into Outflows?', *Journal of Geophysical Research-Space Physics*, **119**, 6876–6890, doi:10.1002/2013JA019495.

St.-Maurice, J.-P. and Hanson, W.B. (1982). 'Ion Frictional Heating at High-Latitudes and its Possible Use for an In Situ Determination of Neutral Thermospheric Winds and Temperatures', *Journal of Geophysical Research*, **87**(A9), pp. 7580-7602.

Strangeway, R.J., Ergun, R.E., Su, Y.J., Carlson, C.W. and Elphic, R.C. (2005). 'Factors Controlling Ionospheric Outflows as Observed at Intermediate Altitudes', *Journal of Geophysical Research*, **110**(A3), pp. A03221.

Tam, S.W.Y., Yasseen, F., Chang, T. and Ganguli, S.B. (1995). 'Self-Consistent Kinetic Photoelectron Effects on the Polar Wind', *Geophysical Research Letters*, **22**(16), pp. 2107-2110.

Tjulin, A. (2017). *EISCAT Experiments*. Available at: https://www.eiscat.se/wp-content/uploads/2017/04/Experiments.pdf (Accessed: 9 June 2017).

Tsurutani, B.T., Gonzalez, W.D., Tang F., Akasofu S.I. and Smith E.J. (1988). 'Origin of Interplanetary Southward Magnetic Fields Responsible for Major Magnetic Storms near Solar Maximum (1978 – 1979)', *Journal of Geophysical Research*, **93**, 8519 – 8531

University of California, Berkeley (2014). *FAST Education and Public Outreach*. Available at: http://cse.ssl.berkeley.edu/fast_epo/ (Accessed: 15 June 2014).

University of California, Los Angeles (2013). *Magnetosphere-Ionosphere Coupling*. Available at: http://esp.ess.ucla.edu/images/ionosphereprocesses.jpg (Accessed: 20 December 2013).

University of California, Los Angeles (2017). *Experimental Space Physics*. Available at: http://esp.igpp.ucla.edu/research.html (Accessed: 12 May 2017).

University of Leicester (2017a). *Electron concentration*. Available at: http://www.ion.le.ac.uk/ionosphere/profile.html#gases (Accessed: 12 May 2017).

University of Leicester (2017b). *Co-operative UK Twin Auroral Sounding System*. Available at: http://www.ion.le.ac.uk/cutlass/cutlass.html (Accessed: 12 June 2017).

Vieira, L.E.A., Gonzalez, W.D., Clua de Gonzalez, A.L. and Dal Lago, A. (2001). 'A Study of Magnetic Storms Development in Two or More Steps and Its Association with the Polarity of Magnetic Clouds', *Journal of Atmospheric and Solar-Terrestrial Physics*, **63**(5), pp. 457-461.

Vlasov, A., Kauristie, K., van de Kamp, M., Luntama, J.P. and Pogoreltsev, A. (2011). 'A Study of Traveling Ionospheric Disturbances and Atmospheric Gravity Waves Using EISCAT Svalbard Radar IPY-Data', *Annales Geophysicae*, **29**, pp. 2101–2116.

Wahlund, J.E. and Opgenoorth, H.J. (1989). 'EISCAT Observations of Strong Ion Outflows from the F-region Ionosphere During Auroral Activity - Preliminary-Results', *Geophysical Research Letters*, **16**(7), pp. 727-730.

Wahlund, J.E., Opgenoorth, H.J., Haggstrom, I., Winser, K.J. and Jones, G.O.L. (1992). 'EISCAT Observations of Topside Ionospheric Ion Outflows During Auroral Activity – Revisited', *Journal of Geophysical Research*, **97**(A3), pp. 3019-3037.

Waite, J.H., Nagai, T., Johnson, J.F.E., Chappell, C.R., Burch, J.L., Killeen, T.L., Hays, P.B., Carignan, G.R., Peterson, W.K. and Shelley, E.G. (1985). 'Escape of Suprathermal O^+ Ions in the Polar-Cap', *Journal of Geophysical Research*, **90**(A2), pp. 1619-1630.

Wannberg, G., Wolf, I., Vanhainen, L.-G., Koskenniem, K., Röttger, J., Postila, M., Markkanen, J., Jacobsen, R., Stenberg A., Larsen, R., Eliassen, S., Heck, S., and Huuskonen, A. (1997). 'The ElSCAT Svalbard Radar: A Case Study in Modern Incoherent Scatter Radar System Design', *Radio Science*, **32**(6), pp. 2283-2307.

Wikimedia Commons (2017). *The diagram of the Sun*. Available at: https://commons.wikimedia.org/w/index.php?curid=23371669 (Accessed: 11 September 2017).

Williams, P.J.S. (1995). 'A Multi-Antenna Capability for the EISCAT Svalbard Radar', *Journal of Geomagnetism and Geoelectricity*, **47**, pp. 685-698.

Winser, K.J., Jones, G.O.L. and Williams, P.J.S. (1988). 'Large Field-Aligned Velocities Observed by EISCAT', *Journal of Atmospheric and Terrestrial Physics*, **50**(4-5), pp. 379-382.

Wright, D.M., Yeoman, T.K., Baddeley, L.J., Davies, J.A., Dhillon, R.S., Lester, M., Milan, S.E. and Woodfield, E.E. (2004). 'High Resolution Observations of Spectral Width Features Associated with ULF Wave Signatures in Artificial HF Radar Backscatter', *Annales Geophysicae*, **22**(1), pp. 169-182

Yau, A.W. and André, M. (1997). 'Sources of Ion Outflow in the High Latitude Ionosphere', *Space Science Reviews*, **80**(1-2), pp. 1-25.

Yau, A.W., Peterson, W.K. and Abe, T. (2011). 'Influences of the Ionosphere, Thermosphere and Magnetosphere on Ion Outflows', in: *The Dynamic Magnetosphere, IAGA Special Sopron Book Series*, vol. 3, edited by W. Liu, M. Fujimoto, Springer, Netherlands, pp. 283–314, doi:10.1007/978-94-007-0501-2_16.

Yau, A.W., Shelley, E.G., Peterson, W.K. and Lenchyshyn, L. (1985). 'Energetic Auroral and Polar Ion Outflow at DE-1 Altitudes - Magnitude, Composition, Magnetic Activity Dependence, and Long-Term Variations', *Journal of Geophysical Research*, **90**(A9), pp. 8417-8432.

Yau, A.W. and James, H.G. (2015). 'CASSIOPE Enhanced Polar Outflow Probe (e-POP) Mission Overview', *Space Science Reviews*, **189**(1-4), pp. 3-14.

Yeoman, T.K., Klimushkin, D.Y. and Mager, P.N. (2010). 'Intermediate-m ULF Waves Generated by Substorm Injection: A Case Study', *Annales Geophysicae*, **28**(8), pp. 1499-1509

Yu, Y., and Ridley, A.J. (2013), Exploring the Influence of Ionospheric O^+ Outflow on Magnetospheric Dynamics: Dependence on the Source Location, *Journal of Geophysical Research-Space Physics*, **118**, pp. 1711–1722.